Incorporating size fractionation into an organoid production bioprocess

Nuria Abajo Lima

A thesis submitted to Cardiff University for the degree of Doctor of Philosophy (Ph. D)

Cardiff School of Bioscience

Sept 2016-July 2020

Acknowledgements

I would like to thank my first supervisor Dr. Marianne Ellis for giving me the opportunity to pursue this research, as well as her support throughout. Also, to my second supervisor Prof. Trevor Dale for your time and effort in guiding the progress of the biological part of this thesis, your valued scientific input has been very helpful to fill in the gaps in my biology knowledge.

I also want to thank the ITN Marie Skłodowska-Curie programme PolarNet for funding my research. In particular, to our coordinator Dr. Mike Boxem, who minded for our scientific development throughout the years.

Thank you to Angela Marchbank and Dr. Sumukh Deshpande for helping me with the sequencing and bioinformatics analysis, respectively.

To all members of the Dale lab (Dr. Eider Valle-Encinas, Dr. Anika Offergeld, Dr. Kenneth Ewan, Dr. Andrew Hollins, Carmen Velasco Martinez and Matt Zverev) for your help and advice provided during the lab meetings. Especially, to my friend Eider for your huge help and support all along. Also, to Carmen for your friendship during the last year of my thesis.

My gratitude is extended to the Cellesce team (Dr. Victoria Marsh Durban, Dr. Mairian Thomas, Dr. Kim Luetchford, Liz Fraser, Jessica Lucena-Thomas and William Newell). In particular, to Liz and Jessica for your relaxed chats after long hours in the lab.

Finally, I would like to thank my family and Klaus. Muchas gracias Klaus por ayudarme tanto, por animarme en los momentos difíciles y ahora ya nos toca vivir una vida feliz juntos. Muchas gracias a mis padres y a mi hermana por vuestros ánimos y apoyo constante, por enseñarme que sin esfuerzo no hay recompensa y cuidarme tanto cuando vuelvo a casa.

Abstract

Recent studies showing that cancer organoids recapitulate the biology of primary cancers have driven tremendous excitement in their potential to revolutionize drug discovery and personalized medicine. Tumour heterogeneity at the genetic and phenotypic level drives differential responses to therapeutic agents, and this heterogeneity is preserved in organoids grown from colorectal cancers. The use of organoids as an alternative model system to 2D cultures is growing in popularity but there is a bottleneck to their widespread utilization. Organoids need to be produced on a large enough scale to adequately supply end users, from university researchers to pharmaceutical companies. In addition, the reproducibility of data from organoid experiments needs to be improved, in particular batch-to-batch variation needs to be minimized. Currently, manual processing results in organoids of varied size and while the majority are suitably functional, this means some organoids are too small to polarize, and some have necrotic cores and are effectively too big. The first aim of this thesis was to fractionate colorectal organoid subpopulations based on their size through the design of a fluidised bed in order to generate a consistent product that should improve drug screening assay reproducibility. The second aim was to study the molecular mechanisms underlying organoid phenotypic heterogeneity using biophysically-purified organoid subpopulations to assess whether organoid transcriptome is altered by their size.

This work resulted in a fluidised bed design that was able to remove single cells from a heterogeneously-sized organoid population, however the current design will need to be improved if it were to be commercially applied.

Fractionated colorectal cancer organoids responded to known colorectal cancer targeting compounds (LGK974, 5-FU and Trametinib) and drug response variability was reduced when a size-based fractionation step was included after cell expansion. The effects of organoid size on biology were studied by RNA-seq. Hypoxia appeared to be the main contributor to differences in gene expression between large and small organoids, which might indicate that oxygen and nutrients are reduced at the centre of large organoids. In addition, the data suggested that energy production and lipid metabolism pathways were selectively upregulated in larger organoids. Taken together, these findings showed that organoid biology is affected by their size and reinforces the importance of considering organoid size during the selection of drug testing assays and in the interpretation of the mechanism of action of candidate compounds.

Abbreviations

2D	Two-dimensional
3D	Three-dimensional
5-FU	5-Fluorouracil
ACA	Anti clumping agent
adj	adjusted
ADMET	Absorption, distribution, metabolism, elimination and toxicity
ANOVA	Analysis of variance
APC	Adenomatous polyposis coli
ATCC	American Type Culture Collection
ATP	Adenosine triphosphate
BME	Basement membrane extract
BMP	Bone morphogenetic protein
BSA	Bovine serum albumin
CA9	Carbonic anhydrase IX
cAMP	cyclic adenosine monophosphate
CBP	CREB-binding protein
CDK1	Serine/threonine kinase-1
cDNA	complementary deoxyribonucleic acid
CDX	Cell line-derived xenograft
CREB	cAMP response element-binding
CFD	Computational fluid dynamics
CI	Confidence interval
CPM	Counts per million
CRC	Colorectal cancer
CRO	Contract research organisation
CTC	Circulating tumour cell
D3	Day 3 of culture
D5	Day 5 of culture
D8	Day 8 of culture
DLD	Deterministic lateral displacement
DMEM	Dulbecco's modified eagle medium

DMSO	Dimethyl sulfoxide
DNA	Deoxyribonucleic acid
DS	Dextran sulphate
Dvl	Dishevelled
ECM	Extracellular matrix
EDTA	Ethylenediaminetetraacetic acid
EGF	Epidermal growth factor
ESC	Embryonic stem cell
FABP	Fatty-acid-binding protein
FACS	Fluorescent-activated cell sorting
FAP	Familial adenomatous polyposis
FASN	Fatty acid synthase
FB	Fluidised bed
FBB	Fluidised bed bioreactors
FBS	Foetal bovine serum
FBTT	From bottom to top
FC	Fold change
FDA	Food and Drug Administration
FDR	False discovery rate
FIH	Factor inhibiting HIF1
FPKM	Fragments per kilobase of transcript per million mapped reads
GLUT	Glucose transporter
GO	Gene ontology
GSK3	Glycogen synthase kinase-3
HAP	Hypoxia-activated prodrug
HEPA	High-efficiency particulate air
HIF	Hypoxia-inducible transcription factor
HRE	Hypoxic responsive element
HTS	High-throughput screening
IPA	Ingenuity pathway analysis
iPSC	Induced pluripotent stem cell
IRC	Inverted reflux classifier
LDHA	Lactate dehydrogenase A

LEF	Enhancer-binding factor
LFC	log2 fold changes
Lrp	Lipoprotein receptor-related protein
MAPK	Mitogen-activated protein kinase
MCT	Monocarboxylate transporter
MCTS	Multicellular tumour spheroid
mRNA	messenger ribonucleic acid
MRP	Mitochondrial ribosomal protein
MS3	Multisizer 3
NF	Non-fractionated
NGS	Next generation sequencing
ODX	Organoid-derived xenograft
PBS	Phosphate-buffered saline
PC	Principal component
PCA	Principal component analysis
PCR	Polymerase chain reaction
PDH	Pyruvate dehydrogenase
PDK1	Pyruvate dehydrogenase kinase 1
PDX	Patient derived xenograft
PDXO	Patient-derived xenograft organoid
PEG	Polyethylene glycol
PF-68	Pluronic F-68
PHD	Prolyl hydroxylase domain protein
pH_i	Intracellular pH
PIV	Particle image velocimetry
PLA	Polycaprolactone
PLG	Polylactide-co-glycolide
PS	PluriStrainer
PSD	Particle size distribution
PTFE	Polytetrafluoroethylene
PVA	Polyvinyl alcohol
PVC	Polyvinyl chloride
PXR	Pregnane X receptor

qRT-PCR	quantitative reverse transcription polymerase chain reaction
R&D	Research and development
RC	Reflux classifier
RIN^e	RNA integrity number equivalent
RNA	Ribonucleic acid
RNA-seq	RNA-sequencing
ROS	Reactive oxygen species
RXR	Retinoid X receptor
TA	Transit-amplifying
TAE	Tris base, acid acetic and EDTA
TCA	Tricarboxylic acid
TCF	T cell factor
TIMM	Translocase of inner mitochondrial membrane
TME	Tumour microenvironment
TOMM	Translocase of outer mitochondrial membrane
VDT	Volume doubling time
VHL	von Hippel-Lindau
WWT	Wastewater treatment

Symbols (SI units)

A	Cross-sectional area of the column (m^2)
A_{lv}	Surface area of liquid-vapor interface (m^2)
A_{sl}	Surface area of solid-liquid interface (m^2)
A_{sv}	Surface area of solid-vapor interface (m^2)
Ar	Archimedes number (-)
C_T	Threshold cycle (-)
C_v	Volumetric concentration (%)
CV	Coefficient of variation (%)
D	Tubing diameter (m)
d_*	Dimensionless particle diameter (-)
d_{50}	Particle size at which 50% of the solids are finer (mm)
D_c	Column diameter (m)
d_{cell}	Diameter of a single cell (m)
d_{org}	Diameter of an organoid (m)
d_p	Particle diameter (m)
d_{sauter}	Sauter mean diameter (m)
E	Enrichment (-)
$E_{surface}$	Surface energy (J/m^2)
F_L	Durand velocity factor (-)
g	Gravitational acceleration (m/s^2)
H	Bed height (m)
H_0	Final bed height (m)
IC_{50}	Half maximal inhibitory concentration (M)
ID	Interior diameter (m)
L	Length (m)
l	Height of the bed (m)
M	Mass of particles (kg)
N	Number of biological replicates (-)
n	Number of technical replicates (-)
$N_{cell/org}$	Number of cells per organoid (-)

OD	Outside diameter (m)
P	Purity (%)
Q	Flow rate (m^3/s)
r	Radius of the tubing (m)
Re	Reynolds number (-)
Re_{mf}	Reynolds number at minimum fluidisation velocity (-)
Re_t	Reynolds number at terminal falling velocity (-)
R^2	Coefficient of determination (-)
RPM	Revolutions per minute (min^{-1})
s	Standard deviation
SE	Separation efficiency (%)
$s_{\Delta P_B}$	Standard deviation of the pressure drop of the background (Pa)
$s_{\Delta P_W}$	Standard deviation of the pressure drop of the whole system (Pa)
t	Cultivation time (days)
u	Superficial velocity (m/s)
u_*	Dimensionless terminal velocity (-)
u_0	Terminal falling velocity (m/s)
u_{cf}	Complete fluidisation of the whole set of particles in the mixture (m/s)
u_{if}	Incipient fluidisation of the most fluidisable particles (m/s)
u_m	Minimum flow velocity required to suspend particles in horizontal pipe flow (m/s)
u_{mf}	Minimum fluidisation velocity (m/s)
V	Volume (m^3)
V_{cell}	Volume of a single cell (m^3)
V_{org}	Organoid volume (m^3)
α	Constant growth rate ($days^{-1}$)
γ_{lv}	Surface free energy of liquid-vapor interface (J/m^2)
γ_{sl}	Surface free energy of solid-liquid interface (J/m^2)
γ_{sv}	Surface free energy of solid-vapor interface (J/m^2)
$\dot{\gamma}$	Mechanical shear rate generated by the fluid (s^{-1})
ΔP	Pressure drop (Pa)
ΔP_B	Background pressure drop (Pa)
ΔP_W	Pressure drop of the whole system (Pa)

ε	Voidage (-)
ε_{mf}	Minimum fluidisation voidage (-)
θ	Contact angle of liquid on the solid surface (°)
θ_p	Angle of inclination of the tubing (°)
μ	Viscosity (Pa s)
$\mu_{\Delta P_B}$	Mean of the pressure drop of the background (Pa)
$\mu_{\Delta P_W}$	Mean of the pressure drop of the whole system (Pa)
μ_f	Fluid viscosity (Pa s)
ρ_B	Fluidised bed suspension density (kg/m^3)
ρ_f	Fluid density (kg/m^3)
ρ_p	Particle density (kg/m^3)
ρ_s	Solid density (kg/m^3)
$\emptyset_p$	Particle volume fraction (-)

Table of Contents

List of Figures

List of Tables

1. Introduction

1.1 Research and development productivity in drug discovery industry

Over the last five decades, there have been major advances in many of the scientific and technological tools used in drug research. For instance, combinatorial chemistry has allowed a huge growth in size of compound libraries that can be used in a screening campaign (Scannell et al. 2012). Also, DNA-sequencing has become easier and orders of magnitude faster, aiding the identification of new drug targets (Scannell et al. 2012). In addition, X-ray crystallography has increased 400 times the number of three-dimensional protein structure entries in databases during the last 30 years (see the RCSB Protein Data Bank database website), facilitating the identification of improved lead compounds through structure-guided strategies. Furthermore, high-throughput screening (HTS) has resulted in a ten-fold reduction in the cost of testing compound libraries against protein targets since mid-1990s (Scannell et al. 2012; Zhang et al. 2012). However, in spite of constant increases in research and development (R&D) expenditures, the number of new chemical entities that reach to the market has actually decreased. Scannell *et al*. (2012 and 2016) have named this trend as "Eroom's Law". Eroom's Law is Moore's Law backwards and explains that the number of new US Food and Drug Administration (FDA)-approved drugs per billion US dollars of R&D spending in the drug industry has halved approximately every 9 years since 1950 (Scannell et al. 2012; Scannell 2016) (Figure 1.1). The development of new drugs for human diseases is currently a long and costly process largely due to the failure in late-stage clinical studies, especially phase III, of promising drug candidates identified in initial *in vitro* screens to perform as intended *in vivo*. It usually takes an average of 12 years and $1 billion from pre-clinical testing to approval of a new drug (Van Norman 2016). There is no single reason that explains this productivity decline and some causes are given below. Firstly, Pammolli *et al*. (2011) determined that pharmaceutical companies invest in scientifically tougher areas with inherently lower probabilities of success, since these translate into lower expected number of competitors and therefore higher expected prices and revenues (Pammolli et al. 2011). Secondly, the use of new technologies and innovative treatment ideas translate into an increase of regulatory hurdles for efficacy, safety and quality (Scannell et al. 2012). Thirdly, our global state of knowledge in human biology, especially regarding the complex inter-relationships that constitute biological

pathways, is still far behind other scientific and technical areas. In most cases, a biological target that succeeded in the test tube did not have the expected results in patients when provided with a custom-designed drug in a clinical setting, or worse still, led to critical side effects, owing to the complexity of the targeted biological pathway, as well as, to effects on other biological pathways (Cook et al. 2014). Fourthly, clinical trials are time consuming, expensive and the primary source of trial failures arise from a lack of efficacy. Hwang *et al*. (2016) assessed 640 phase III trials with novel therapeutics and found that 54% failed in clinical development, with 57% of those due to inadequate efficacy, followed by 17% because of safety concerns (Hwang et al. 2016). Therefore, it is important to develop robust systems that provide the maximum amount of information about biological activity, toxicological profile, biochemical mechanisms and off-target interactions of drug-candidate leads in the earliest stage of drug discovery. In particular, since cancer is a highly heterogeneous disease, accurate prediction of efficacy is critical to get novel treatments approved (Kondo & Inoue 2019). *In vitro* biochemical assays, for example ligand-receptor binding assays, were previously the gold standard for drug screening due to their simplicity and reproducibility. However, cell-based assays have been shown to be suitable to address the early phase of drug discovery process more efficiently (Michelini et al. 2010) due to their ability to detect more biologically relevant characteristics of compounds in living systems. Available cell culture systems for cell-based assays in drug screening are described below, along with the advantages and limitations of each system.

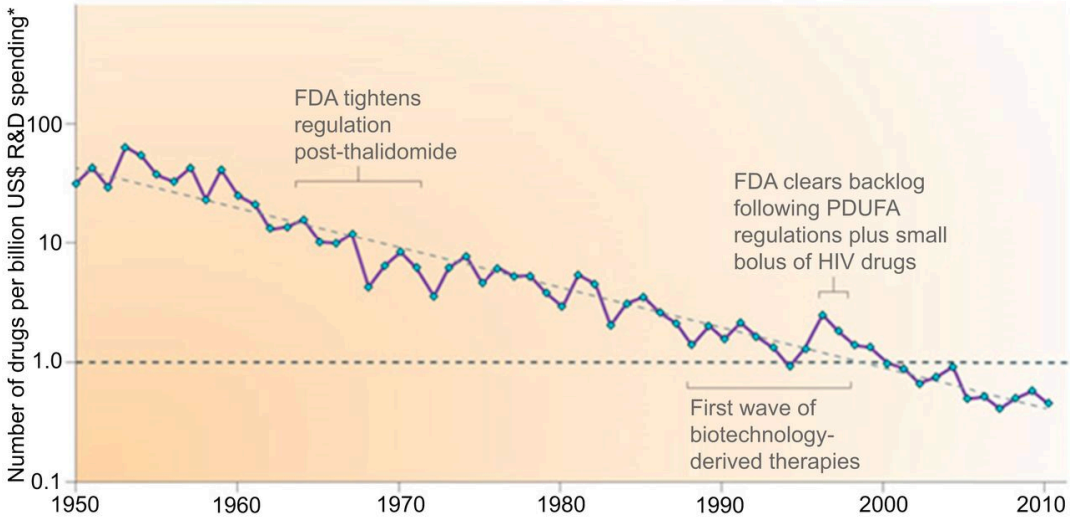

Figure 1.1 Overall trend in pharmaceutical R&D efficiency – Eroom's Law

The number of new drugs approved by the FDA per billion US dollars (inflation-adjusted) spent on R&D has halved roughly every 9 years since 1950, Figure from (Scannell et al. 2012).

1.1.1 Cell culture systems and animal models for cancer drug discovery

Historically, drug screening extensively relies on animal models as proxies for human beings in drug target validation and ADMET (absorption, distribution, metabolism, excretion and toxicity). Although these animal models provide very useful information for drug screening, they are relatively expensive, low throughput and present ethical issues. As an alternative to animal models, cell-based assays popularised in the 80's as a simpler, faster and cost-effective tool, as well as versatile and easily reproducible (Edmondson et al. 2014a). Nowadays, automated cell-based assays are a routine procedure in drug discovery for target validation and ADMET in the early stage of drug discovery, which reduce the need for large-scale and cost-intensive animal testing. The majority of cell-based HTS assays are carried out in multi-well plates as they can be easily miniaturized to increase throughput rates, in the order of 10,000 compounds tested per day (Zang et al. 2012). Currently, several types of *in vitro*, *ex vivo* and *in vivo* human models are routinely used for drug screening and they are depicted in Figure 1.2 and described below.

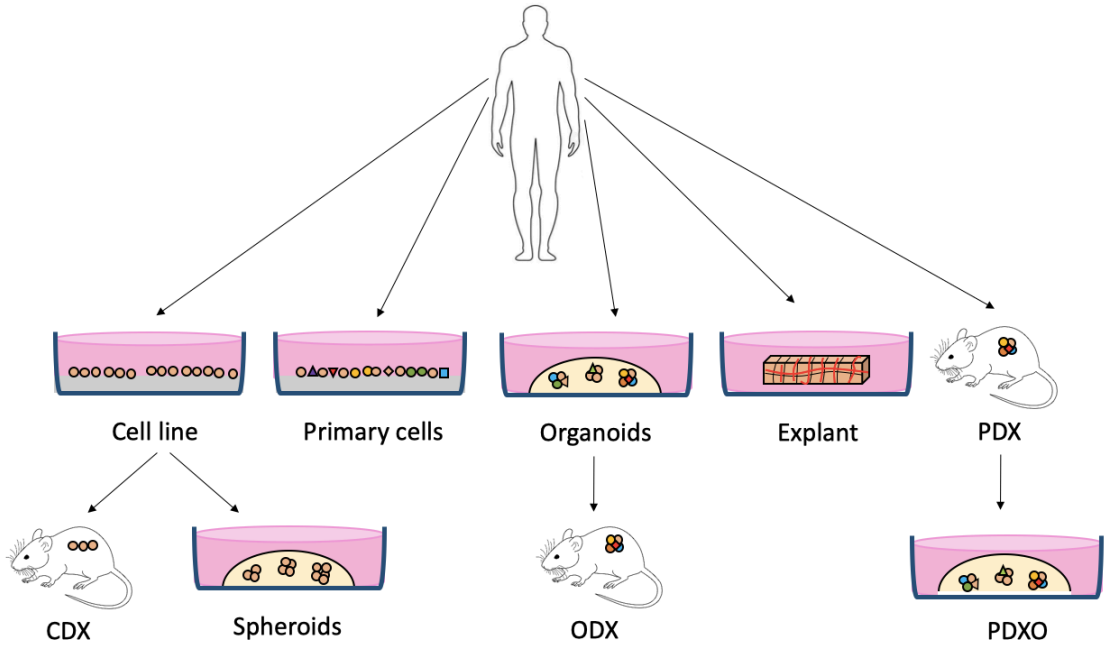

Figure 1.2 Human model systems used for cancer drug discovery

The two-dimensional *in vitro* systems include immortalised cell lines and primary cells. Three dimensional culture models can be classified as *in vitro* spheroids and organoids, and *ex vivo* explants and patient-derived xenograft organoids (PDXOs). The *in vivo* xenograft models that can be generated depending on the material implanted into the immunodeficient mouse are cell line-derived xenograft (CDX), organoid-derived xenograft (ODX) and patient-derived xenograft (PDX).

1.1.1.1 Two-dimensional (2D) cell culture systems

2D cell-based assays are the most used system because of their low cost and easy operation, and they include single cells in suspension and monolayer cells on a 2D surface. There are two different 2D cell culture systems, immortalised cell lines and primary cells.

In 1951, the first immortalised cancer line cultured, known as the HeLa cell line, was derived from cervical cancer cells taken from Henrietta Lacks (Gillet et al. 2013). Since then, immortalised human cancer-derived cell lines are the most widely used model to study the biology of cancer and improve the efficacy of cancer treatment (Gillet et al. 2013). Immortalised cell lines are generally highly proliferative, easier to culture and transfect, and they can be obtained from cell banks, such as the American Type Culture Collection (ATCC). These cells have acquired the ability to proliferate indefinitely either through random mutations as in transformed cancer cell lines, or by deliberate modification such as artificial expression of cancer genes (Kavsan et al. 2011). Most cell lines have been in culture for decades and they are well adapted to the 2D culture environment, and as a result, often differ genetically and phenotypically from their tissue origin and show a flat morphology. In order to overcome the lack of histological architecture, tumour cell lines have been implanted into an immunodeficient mouse to obtain cell line-derived xenografts (CDXs), which are further discussed in Section 1.1.1.3.

In contrast to cell lines, primary cells are isolated directly from patient tumour or biopsy and grown *in vitro* in 2D tend to be heterogeneous. Primary cells, since they have not been transformed, are considered to better represent the tumour of origin, as they provide a snapshot of the tumour of the stage collected. These models allow for the development of personalised cancer therapy as demonstrated through functional screening of chemotherapeutic drugs, modelling individual tumour response (Nelson et al. 2020). However, although an important tool in cancer research, primary cells have a finite lifespan and limited expansion capacity. As they age, they show morphological and functional changes, which is why they should ideally be used for drug discovery and preclinical studies at an early passage (Kapałczyńska et al. 2016).

The methods used for 2D cell cultures enable their preparation in large quantities at uniform quality, which is necessary for high-throughput drug screening. However, 2D cell cultures exhibit a flattened morphology and altered signalling networks compared to cancer cells in tumour tissue *in vivo*, which influences therapeutic response. Also, immortalised cell lines lack

cellular heterogeneity in addition to physiological cell-cell and cell-matrix interactions that are necessary to maintain *in situ* phenotypes. Three dimensional cell culture systems address some of these limitations and these systems are presented below.

1.1.1.2 Three-dimensional (3D) cell culture systems

Solid tumours grow with a 3D shape *in vivo*, and this suggests that adding a third dimension in 3D cultures, provides another direction for cell-cell interactions, cell migration and cell morphogenesis, which are critical in regulating cell cycle and tissue functions (Zang et al. 2012). For example, the monolayer culture of 2D systems results in unlimited access to a serum-based medium that can lead to a selection procedure for certain cell types and thus, another cause for poor translational quality to an *in vivo* tumour. *In vivo*, serum is lacking, and nutrient, oxygen, and metabolite gradients are important for the tumour development. These gradients are non-existent in 2D culture models, but 3D systems better mimic the complex natural environment (van Tienderen et al. 2019).

During the last decade, the widespread implementation of 3D cell cultures provides a more physiologically relevant platform for HTS during drug discovery due to 3D systems retaining many of the *in vivo*-like phenotypes leading to a better reflection of compound interaction with cells and tissues *in vivo*. In 3D cultures, cell-cell and cell-matrix interactions mimic more closely the natural environment found *in vivo*, so that the cell morphology closely resembles its natural shape in the body (Edmondson et al. 2014b). The main 3D culture models are *in vitro* spheroids and organoids and *ex vivo* explants.

The simplest 3D tissue culture model is a spherical aggregate of cells, called a spheroid. Some conventional 2D cell lines can be induced to form spheroids by simply seeding them in a low-attachment round-bottom plate but they tend to adhere at the bottom of untreated plastic surfaces (Kondo & Inoue 2019). The implementation of traditional techniques, such as cell culture in a spinner flask, rotation culture, and hanging drop method, promotes conventional cell lines to form spheroids as shown in Figure 1.3 (Kondo & Inoue 2019).

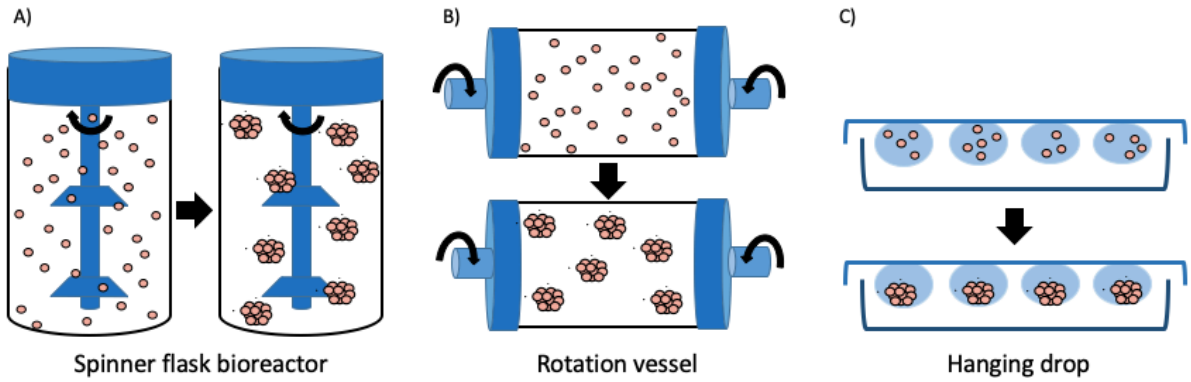

Figure 1.3 Different techniques used for spheroid cultures

A. Spinner flask bioreactor is a cell agitation approach based on stirred suspensions and the impeller mixer prevents cells sedimentation and also promotes cell-cell interaction in the culture medium. **B.** Rotatory bioreactor rotates itself to maintain cells in a continuous suspension and prevents cells to adhere to the chamber wall. **C.** Hanging drop method is based on sedimentation of the cells due to gravitational force which promotes cell-cell interactions. A small droplet containing cell suspension with volume ranging from 20 to 30 µL is seeded onto the lid of polystyrene microwell plate. After turning the plate upside down, the droplets hang and gravity allows the cells to settle at the bottom for self-assembly (Vadivelu et al. 2017).

Furthermore, biological or synthetic scaffolds that provide anchorage for the cells can be used for efficient 3D culture of established cell lines (Kondo & Inoue 2019). Commercially available products such as BD Matrigel basement membrane matrix (BD Sciences), Cultrex basement membrane extract (BME; Trevigen) and hyaluronic acid are commonly used biologically derived matrices that contain extracellular matrix (ECM) components such as laminin and collagen. Polyethylene glycol (PEG), polyvinyl alcohol (PVA), polylactide-co-glycolide (PLG) and polycaprolactone (PLA) are common materials used to form synthetic scaffolds (Edmondson et al. 2014a). Furthermore, the aforementioned gradients of nutrients, metabolites and oxygen in 3D structures are responsible of spheroids containing cells in various stages with a layered structure comprised of proliferating cells surrounding a more quiescent and hypoxic, necrotic core (Edmondson et al. 2014a). Although spheroids show improved drug responses than the corresponding 2D cell line, they frequently do not reproduce the biological heterogeneity of the cancers from which they are derived, probably because of their genetic and epigenetic adaptation to grow on plastic (Kondo & Inoue 2019). The representation of different cell populations (e.g. stem cells, transit amplifying cells and differentiated cells) is crucial to study the responses in drug development assays, as these cells may respond differently to drug treatments. This limitation has been solved with the development of 3D systems that enables the creation and growth of miniature organs called organoids. This *in vitro*

model is one of the technological advances that has become an essential tool in biomedical research and is extensively described below.

An organoid is defined as an *in vitro* 3D cellular cluster grown from primary tissue, embryonic stem cells (ESCs) or induced pluripotent stem cells (iPSCs), which consist of organ-specific cell types that are capable of self-renewal and self-organization, and exhibit similar organ functionality as the tissue of origin (Clevers 2016). The main characteristics that differentiate organoids from other systems are that organoids have never been adapted for growth on plastic and the 3D structure provides the right physical environment. In the last ten years, there has been a dramatic surge in the number of publications related to organoids, however, this field of research began many decades ago. Organoids were first described during the period of 1965-1985, mostly in classic development biology experiments that sought to describe organogenesis by cell dissociation and reaggregation experiments. A few years later, organoid popularity re-emerged in the research group of Prof. Hans Clevers in Utrecht which resulted in two important discoveries. Firstly, in 2007 Hans Clevers and Nick Barker demonstrated by lineage tracing experiments that leucine rich repeat containing G protein coupled receptor 5 (Lgr5)+ cells in the intestinal crypt had the capacity to form all different epithelial lineages over a 2 month period in the mouse (Barker et al. 2007). Once identified Lgr5 as a stem cell marker, the second important point took place in 2009 when Hans Clevers and Toshiro Sato developed the stem-cell containing organoid culture system. A robust methodology was revealed to develop organoids that not only recapitulated murine intestinal crypt physiology, but promoted the successful expansion of a stem cell compartment, including Lgr5+ stem cells, propagating their renewal and long term culture (Sato et al. 2009). Organoids are composed of stem cells, derived from the tissue of origin that facilitate long term culture, which have the capacity to differentiate into several epithelial lineages, capable of recapitulating relevant cell signalling (Yin et al. 2016). Sato *et al*. (2009) grew the first organoids by suspending mouse intestinal crypts in Matrigel (derived from Engelbreth-Holm-Swarm mouse sarcoma), which supports growth within a 3D structure and its laminin-rich nature mimics the microenvironment of the crypt base *in vivo*. In addition, the system requires the provision of culture medium including growth factors specific to the organoid type. A cocktail of epidermal growth factor (EGF), and Noggin and R-spondin provides the essential intestinal stem cell maintenance signal (Sato et al. 2009). Adding R-spondin in the medium was the key point to achieve long-term organoid cultures (discussed in Section 1.2.1.1). Furthermore, human organoid culture can now be achieved using similar culture conditions and has taken a role in the field of translational

medicine (Sato et al. 2011). To date, organoid systems have been created for growth of tissue from the small intestine (Sato et al. 2009), colon (Sato et al. 2011), stomach (Barker et al. 2010), liver (Huch, Dorrell, et al. 2013), lung (Rock et al. 2009), prostate (Karthaus et al. 2014), pancreas (Boj et al. 2015), brain (Lancaster et al. 2013), among others. Organoids can be grown from healthy but also from diseased tissues retaining the pathology such as tumour heterogeneity and tumour specific functions when cultured from cancer cells. This enables the testing of a range of therapeutic compounds in a patient-relevant model. However, organoids also present some limitations that were described by Fatehullah *et al*. (2016) (Fatehullah et al. 2016):

- The lack of stromal components, including immune cells, limits their use in modelling inflammatory responses to infection or drugs which is particularly limiting for immunotherapies.
- Organoid growth from certain tissues may be a strict dependence on growth factor/signalling gradients for maintaining balanced stem cell renewal and lineage specification, and the current system presents limitations to mimic these gradients in Matrigel matrix. To overcome this problem, microfluidic technology could be used to mimic the chemical gradient of soluble or immobilised factors that are important in stem cell research (Kim et al. 2019).
- The relative rigid ECM is a potential limitation to drug penetration because it behaves as a physical barrier that restricts drug diffusion (Kaushik et al. 2016).
- Organoid cultures are often intrinsically heterogeneous in terms of viability, size and shape, which complicates the analysis of drug toxicity and efficacy.

Despite the limitations described above, organoids represent a bridge between traditional 2D cultures and *in vivo* mouse/human models, as they are more physiologically relevant than monolayer culture models and are far more amenable to manipulation of niche components, signalling pathways and genome editing than *in vivo* models described in the following section (Fatehullah et al. 2016).

Although, organoid models have been designed to resemble *in vivo* tumour as closely as possible, especially taking tumour heterogeneity into account, organoids mimic tumour complexity only partially as they fail to fully capture tumour-stromal interactions which influence drug sensitivity and resistance and are important for immune-oncology research (Collins et al. 2020). This is due to the fact that most organoids are established through isolation of stem cells and subsequent embedding of the cells in a 3D matrix and this leads to the loss of

stromal fibroblast and infiltrating immune cells (Meijer et al. 2017). *Ex vivo* tumour explants, on the other hand, are formed by dissecting fresh tissue and placing these under defined culture conditions (Collins et al. 2020). This enables to retain the complexity of tumours *in vivo* without extensive manipulation of the tissue, often retaining multiple cell types and the surrounding donor-derived ECM and stroma (Meijer et al. 2017; Hu et al. 2017) which means that the tumour cells are surrounded by their original microenvironment, rather than artificial matrices (Meijer 2017). The use of patient-relevant material, the ability to culture the surrounding normal tissue in parallel and the preservation of the original architecture of the tissue are some of the advantages that explant platform presents when compared with other preclinical platforms, particularly 2D cell lines and cell line derived xenograft models (Powley et al. 2020). Also, the generation and culture of *ex vivo* explants is relatively inexpensive compared with the production and maintenance of mouse models or the isolation and culture of organoids, which often require costly cell culture reagents and matrices for their maintenance (Powley et al. 2020). A concern with the explant platform is that explants are only retained intact for short periods of time, typically for up to 72 h, and extending the integrity of explants for longer periods needs further research, possibly involving the development of scaffolds or perfused channels to prolong the 3D architecture of the original tumours (Powley et al. 2020).

1.1.1.3 *In vivo* xenograft models

In vivo models overcome some of the limitations presented above for organoids, such as the lack of native microenvironment (e.g., ECM composition, growth factor gradients) or the lack of interactions with immune cells, and consequently, the inability to model immune responses (Langhans 2018). Immunodeficient mice capable of being engrafted with human cells and tissue have become increasingly important to create xenograft models (Walsh et al. 2017). Depending on the material implanted into the immunodeficient mouse, different models can be generated;

- Cell line-derived xenografts (CDXs) are generated by implanting immortalised tumour cell lines into an immunodeficient mouse. These were initially reported to provide a more faithful representation of the tissue microenvironment than monolayer cultures, since they have blood vessels and experience nutrient deprivation or hypoxia. However, these cell lines propagated *in vivo*, are derived from cancer cells that have adapted to

growth outside a natural microenvironment, resulting in genetic changes that are distinct from the genetic stress imposed in tumours in patients (Tentler et al. 2012).

- Organoid-derived xenografts (ODXs) can be generated by injecting cultured organoids (e.g. colorectal cancer organoids) into an immunodeficient mouse (Zhao et al. 2019).
- Patient derived xenografts (PDXs) consist of the implantation of tissue or cells from a patient's tumour into an immunodeficient mouse, providing a more faithful representation of the individual's tumour. Since PDXs are passaged without *in vitro* culture steps, PDX models allow the propagation and expansion of patient tumours for subsequent 2D screening assays without significant genetic transformation of tumour cells over multiple generations. Most PDXs are grown under the skin, however, in some PDX models, tumour cells grow in physiologically-relevant tumour microenvironment (TME) that mimic the oxygen, nutrient, and hormone levels that are found in patient's primary tumour site (Jung et al. 2018). It is worth mentioning that even with the best models, the orthotopic site may be in the wrong physical location, e.g. not near a lymph node. Also, the complexity of human TME is not recapitulated in immunodeficient mice. For example, tumour-promoting cells within the TME, such as stromal cells and vascular cells are often replaced by mouse components, which may behave differently than human cells and may not be modulated by drugs that specifically target human cells (Hirenallur-Shanthappa et al. 2017). PDXs are more predictive for clinical outcome compared to other systems (Xu et al. 2018), but the financial aspect cannot be ignored. PDX models need a substantial budget because the immunodeficient mice are expensive and maintaining those mice in a clean environment also implies a high cost, since it takes long time before tumours are engrafted and began to grow in PDX models (Murayama & Gotoh 2019). Also, PDX models are not amenable to large-scale drug sensitivity studies due to the high cost and low throughput capacity.

Of note, patient-derived xenograft organoids (PDXOs) *ex vivo* derived from PDXs bring the added benefits of speed and scalability inherent to organoid systems which are ideal for high-throughput, large-scale screening and simultaneous testing of multiple therapeutic strategies, such as combination therapy (Nelson et al. 2020).

In summary, cellular models, including *in vitro* 2D and 3D cultures, and *in vivo* xenograft models, have been successfully developed as an alternative to biochemical assays, due to their ability to detect more biologically relevant characteristics of compounds in living organisms. Furthermore, Table 1.1 summarises the advantages and limitations of these human model

systems. The statement ‘all models are wrong, but some are useful’ credited to the statistician George Box (Box 1979), is very true in the study of cellular systems in drug discovery. Every model has distinct advantages and disadvantages, and the more widely each model is used, the better it is understood.

Table 1.1 Advantages and limitations of the different human model systems

	System	Advantages	Limitations
In vitro **2D**	Cell line	Easy to grow Indefinite growth Enables high-throughput Inexpensive	Lack of heterogeneity No microenvironment and vasculature Very low predictive value
	Primary cells	Maintain heterogeneity Enables high-throughput Inexpensive	Limited lifespan Difficulties with isolation No microenvironment and vasculature
In vitro **3D**	Spheroids	Easy to grow/ propagated for long time Enables high-throughput Includes microenvironment that mimics ECM Relatively inexpensive	Lack heterogeneity Lack of vasculature
	Organoids	Retains heterogeneity Propagated for long time Enables high-throughput Includes microenvironment that mimics ECM Relatively inexpensive	Lack of vasculature Variability across batches (viability, size, shape)
	PDXO	Retains heterogeneity Relatively easy and fast to establish Includes microenvironment that mimics ECM Enables high throughput Relatively inexpensive	Lack of vasculature
Ex vivo **3D**	Explants	Retains heterogeneity Includes microenvironment and stromal components Relatively inexpensive	Limited lifespan Low throughput Lack of vasculature
In vivo **xenograft models**	CDX	Includes microenvironment and vasculature Take short time to be established	Lack of heterogeneity Expensive / labour intensive Low throughput Differences in microenvironments between mouse and human
	ODX	Includes microenvironment and vasculature Retains heterogeneity	Expensive / labour intensive Low throughput Differences in microenvironments between mouse and human Take long time to be established
	PDX	High predictive power Includes microenvironment and vasculature Retains heterogeneity	Expensive / labour intensive Low throughput Differences in microenvironments between mouse and human Take long time to be established

1.2 Colorectal cancer organoids for pre-clinical studies

1.2.1 Anatomy and function of the intestine

The mammalian gastrointestinal tract is comprised of the small and large intestine. The small intestine begins at the pyloric sphincter of the stomach and is divided into the duodenum, jejunum and ileum. This tube-like structure is composed of a range of cell types, which facilitate some key roles including enzymatic digestion and absorption of nutrients. The large intestine extends from the caecum, through the ascending colon, transverse colon, descending colon, sigmoid colon, to the rectum, which opens to the anus. The main function of the large intestine is to maintain fluid and electrolyte balance by absorption of water from food material. It is also the main site for degradation of complex carbohydrates and nutrients by the gut microbiota (Badder 2017a).

The gastrointestinal epithelium represents one of the organs with the fastest cellular turnover, with a daily loss of 10 epithelial cells in humans (Tan & Barker 2014). The epithelium of the small intestine arranges itself into finger-like projections known as villi (Figure 1.4), which reach into the lumen of the intestine and serve to absorb nutrients. At the base of these villi are the crypts of Lieberkühn ('crypts', epithelial pockets or invaginations) that constitute instructive niches for small reserves of multipotent cells (Tan & Barker 2014). Stem cells at the crypts give rise to transit-amplifying (TA) cells, which in turn undergo many cycles of rapid proliferation and progressively commit to one of several differentiated lineages as they migrate upwards along the crypt-villus axis (Tan & Barker 2014). Two predominant specialized epithelial lineages emerge, the absorptive and secretory cells. Absorptive enterocytes secrete enzymes and assimilate nutrients, while secretory cells include hormone-secreting enteroendocrine cells, mucous-secreting goblet cells and prostanoid-secreting Tuft cells (Tan & Barker 2014). Goblet cells, identified through their expression of Mucin 2, provide lubrication to soften the impact of mechanical stress from peristalsis of food through the gut. Paneth cells, which help to maintain intestinal stem cell reserves by secreting Wnt, and also have antimicrobial functions, are found in the crypts (Tan & Barker 2014). After 3-5 days, migrating epithelial cells reach the villus tip, where they undergo apoptosis before being lost into the intestinal lumen (Tan & Barker 2014). Paneth cells escape this rapid ascension to certain death, and migrate downwards toward the crypt base where they remain 6-8 weeks before being replaced by local progenitor populations (Tan & Barker 2014).

In contrast to the small intestine, the epithelial lining of the colon does not contain absorptive villi nor Paneth cells (Figure 1.4). This makes it much flatter on the luminal side and reflects its role in stool compaction rather than food absorption (Tan & Barker 2014). The need of efficiently expel stool its reflected by the presence of many more mucous secreting goblet cells in the colon. The stem cells of the colon are located at the base of the crypt and are capable of differentiating into multiple epithelial lineages including enterocytes, endocrine and goblet cells (Tan & Barker 2014). As cells migrate from the base of the crypt towards the lumen of the colon, they undergo differentiation until they are shed into the lumen at the apex of the crypt.

Wnt signalling is an essential factor in normal intestinal function, especially for the maintenance and self-renewal of epithelial stem cells located at the base of the crypts and it is described in the next section.

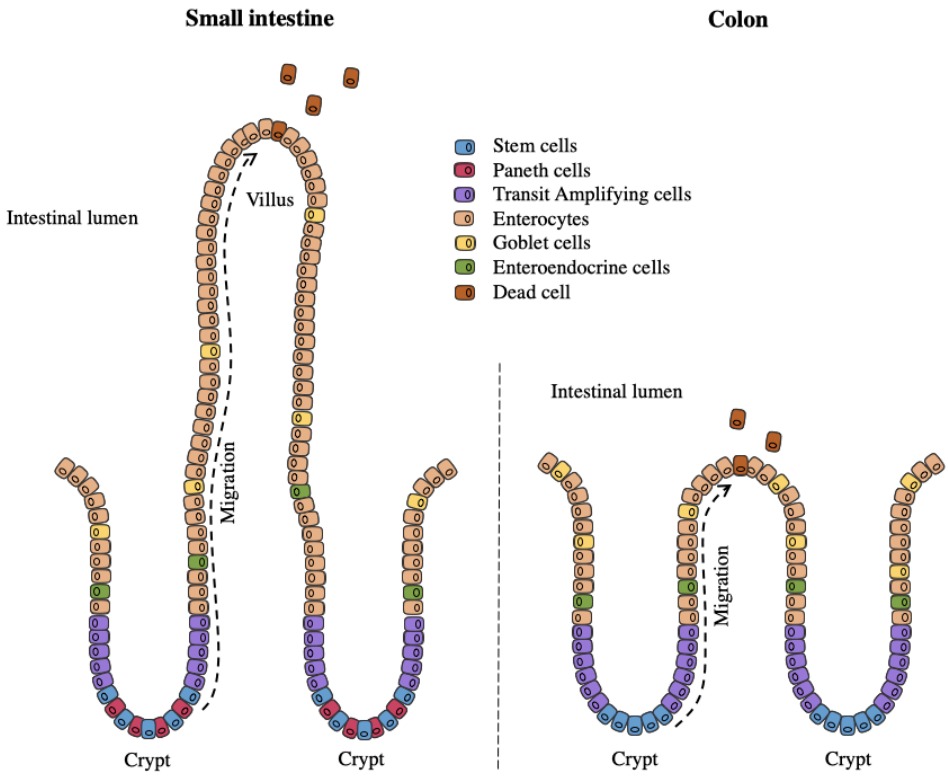

Figure 1.4 Schematic diagram of the small intestine and colon

The small intestine epithelium is organised into crypts and villi. Stem cells located at the bottom of the crypt give raise to immature progenitor cells which terminally differentiate as they migrate up the villus, before being shed into the lumen, which the exception of Paneth cells which migrate downwards and occupy the base of the crypt. The colon is only made up of crypts. The base of the colonic crypts is composed of stem cells which are able to self-renew and differentiate into various lineages whilst migrating to the tip of the crypt where they undergo apoptosis before being discard into the lumen. Figure adapted from (Tan & Barker 2014).

1.2.1.1 Wnt signalling pathway

The canonical (β-catenin dependent) Wnt signalling pathway plays a major role during mammalian development, mediating effects on an array of target genes involved in proliferation, cell adhesion and migration (Flanagan et al. 2018). Furthermore, almost all colorectal cancers demonstrate hyperactivation of this pathway, which in many cases is believed to be the initiating and driving event (Schatoff et al. 2017).

In the absence of WNT ligands (Figure 1.5A), the canonical Wnt signalling pathway remains in a 'off-state' whereby a multi-protein destruction complex composed of the tumour suppressor proteins axis inhibitor (AXIN) and Adenomatous Polyposis Coli (APC), glycogen synthase kinase-3 (GSK3) and serine/threonine kinase-1 (CK1), targets β-catenin for degradation by ubiquitination and proteasomal degradation (Novellasdemunt et al. 2015). Conversely, in the presence of WNT ligands (Figure 1.5B), the destruction complex is inhibited following the binding of WNT ligand to the receptor Frizzled and its co-receptor lipoprotein receptor-related protein 5/6 (LRP5/6). The cytoplasmic tail of LRP is phosphorylated, which leads to the recruitment of AXIN and Dishevelled (DVL) to the activated receptor at the cell membrane and prevents the formation of the β-catenin destruction complex (Spit et al. 2018). Consequently, this allows β-catenin to accumulate in the cytoplasm and its subsequent nuclear translocation. In the nucleus, β-catenin displaces the repressor Groucho from T cell factor (TCF)/lymphoid enhancer-binding factor (LEF) transcription factors (Merenda et al. 2020). β-catenin/TCF/LEF, form an active transcriptional complex, leading to the expression of WNT target genes (Merenda et al. 2020).

Binding of R-spondin to the receptor LGR5 can further potentiate Wnt signalling activation and it is essential for the growth of wild type intestinal crypts *in vitro*. The LGR5/R-spondin complex acts by neutralising the WNT target genes, *Rnf43* and *Znrf3*, two transmembrane E3 ligases that remove WNT receptors from the stem cell surface. Therefore, in the absence of R-spondin, activation of the Wnt signalling pathway results in expression of RNF43 and ZNRF3, which ubiquitinate and degrade the WNT receptor Frizzled. This negative feedback loop functionally limits Wnt signalling and reduces proliferation in the intestine. However, in the presence of R-spondin, the complex LGR5/R-spondin stabilises the WNT receptor by binding with RNF43 and ZNRF3, potentiating the activation of the Wnt signalling and increasing the number of intestinal stem cells (Sato et al. 2009; de Lau et al. 2014; Yan et al. 2017).

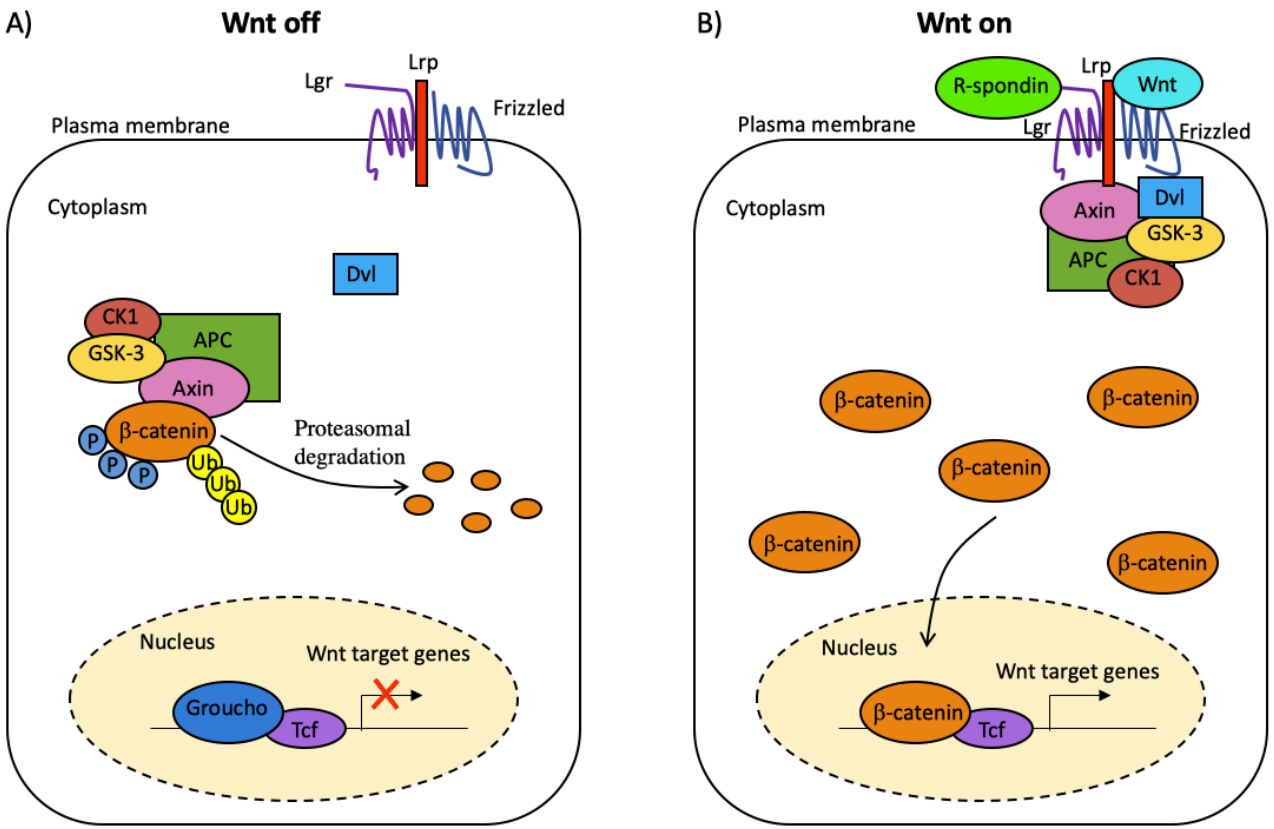

Figure 1.5 Schematic of the canonical Wnt signalling pathway

A. In cells not exposed to WNT ligands (Wnt off), β-catenin is phosphorylated by the destruction complex composed of AXIN, APC, GSK-3 and CK1, and targeted for degradation by the proteasome. TCF transcription factors are complexed with transcriptional inhibitors such as TLE/Groucho, and targeted genes are not transcribed. **B.** In cells exposed to WNT ligands (Wnt on), WNT binding causes disassociation of the complex in a Dishevelled dependent manner, allowing the nuclear translocation of β-catenin to activate transcription of WNT target genes. Figure adapted from (de Lau et al. 2014).

1.2.2 Colorectal cancer

Colorectal cancer (CRC) is the fourth leading cause of cancer-related mortality worldwide and results from the progressive accumulation of multiple genetic and epigenetic aberrations within cells (Nguyen & Duong 2018). The high rate of cell division required to facilitate the rapid turnover of cells within the intestinal crypts provide a potential source of DNA replication errors, making oncogenic transformations more likely (Ashley 2013). Furthermore, colorectal tissue is directly exposed to carcinogens from ingested food, and thus provide multiple factors for carcinogenic occurrences to take place (Santarelli et al. 2008). Approximately 65% of CRC cases are sporadic with no family history or apparent genetic predisposition and are attributed to external factors, such as diet, smoking and increased alcohol consumption. The remaining cases are familial, namely through familial adenomatous polyposis (FAP), a hereditary condition which leads to the development of polyps with potential to form benign lesions and adenocarcinomas, possibly interacting with environmental factors (Nguyen & Duong 2018; Bodmer et al. 1987).

The development of CRC has been established as a multi-step process, whereby mutations are acquired and accumulated, driving tumour progression from a dysplastic epithelium, to benign adenoma and adenocarcinoma, which then has the potential to metastasise into other tissues (Testa et al. 2018). The first genetic model of CRC progression was proposed in 1990 in a study by Fearon and Vogelstein, where they carried out a comprehensive analysis of histopathological and genetic data in late stage tumours compared to early stage tumours to understand the mutations that initiate and play a role in CRC development (Fearon & Vogelstein 1990). They proposed that although the mutations often occur in a preferred sequence, it is the total accumulation of mutations rather than the order in which they accumulate that is responsible for the biological properties of a tumour. The model describes mutations in *Apc* gene as the initiating mutation of CRC, followed by subsequent mutations in Kirsten rat sarcoma viral oncogene homologue (*Kras*), allelic loss of the 18q locus, and mutations in *p53* which contribute to development of malignant disease.

Mutational inactivation of the tumour suppressor *Apc* is well established to be the initiating event in most sporadic and familial CRCs. Disruption of *Apc* drives activation of the Wnt signalling pathway and therefore, the transcription of downstream signals, primarily involved in enhanced cell proliferation. The result consists of disruption of epithelial differentiation and stem cell homeostasis (Tan & Barker 2014). The 2012 report from The Cancer Genome Atlas

(TCGA) consortium estimated that up to 92% of sporadic CRCs contained at least one alteration in a known WNT regulator (The Cancer Genome Atlas Network 2012; Schatoff et al. 2017). In addition, epigenetic silencing of WNT inhibitors by DNA hypermethylation has also been suggested as another common mechanism to activate the Wnt pathway, including the extracellular WNT inhibitors SFRP1-5, WIF1, DKK1 and DKK3, as well as the destruction complex proteins APC and AXIN2 (Novellasdemunt et al. 2015). The high mutation rate of Wnt pathway components observed in human CRCs underpins the growing interest in developing therapeutic agents against Wnt signalling pathway. 3D models offer a valuable tool to preclinically test the therapeutic efficacy of Wnt targeted therapies because organoids present a unique 3D architecture and heterotypic cell-cell interactions that resemble more closely the original tumour than the currently used 2D cell lines.

1.2.3 Colorectal cancer organoids

Colorectal cancer 2D cell lines have been routinely used for drug discovery (Thakuri 2016). However, they do not have sufficient predictive power due to a number of reasons. Firstly, the monolayer culture of cell lines does not represent the tumour environment in which oxygen and nutrients gradients have an effect on cells metabolic profile (Antoni et al. 2015). Furthermore, cell-cell interactions are lost in most of the CRC cell lines and the heterogeneous nature of CRC is also compromised in such cultures. As 2D cell lines only represent a subtype of cells, a large number of cell lines is necessary to capture the genetic diversity of a single tumour. Wilding *et al*. (2014) showed that cetuximab (a monoclonal antibody against epidermal growth factor receptor (EGFR)) response in a panel of 64 CRC cell lines resulted in a power of 95%, but this dropped to 70% if performed on a panel of 30 CRC lines and just 20% for a panel of 7 CRC cell lines (Wilding & Bodmer 2014).

Efforts to establish more clinically representative CRC models *in vivo* have moved the development of CRC organoids forward. For example, in 2011, Sato *et al*. (2011) published the first protocol that allows robust and long-term organoid culture of primary human epithelial cells isolated from colon, as well as colorectal adenoma and adenocarcinoma tissue from patient biopsies (Sato et al. 2011). For normal primary human colon cell culture, the epithelial cells are embedded within Matrigel which supports growth within a 3D matrix, and its laminin-rich nature mimics the microenvironment of the crypt base *in vivo*. In addition, the system requires the provision of culture medium including growth factors supplements designed to

support intestinal crypt growth and maintain the intestinal stem cell population. First, Noggin (a bone morphogenetic protein (BMP) inhibitor) is added to the medium as BMP signalling has been shown to inhibit intestinal stem cell self-renewal (Young & Reed 2016). Second, EGF is another key constituent of the culture medium associated to intestinal proliferation (Sato et al. 2011). Third, R-spondin is added to the medium when growing organoids from normal or non-Wnt-activated intestinal epithelium. As explained before, R-spondin enhances Wnt signalling within the intestinal stem cell population through the interaction with Lgr receptors, such as the intestinal stem cell marker Lgr5 (Sato et al. 2009; de Lau et al. 2014; Yan et al. 2017). Fourth, for colon crypt culture, Wnt ligand is a required factor to maintain Lgr5-positive cells, because Paneth cells (absent in colon crypts) are the only source of Wnt in culture (Sato & Clevers 2013). Furthermore, the Rho-kinase inhibitor Y-27632 is required for culturing single cells, as it has been shown to inhibit anoikis in isolated embryonic stem cells (Ashley et al. 2014). This method generates cystic structures with a highly polarised epithelium, maintaining the crypt region with stem cells and a conserved migration of the differentiated cells (enterocytes, endocrine and goblet cells) along a crypt-lumen axis (Figure 1.6). The basal side of the cells is oriented toward the surrounding Matrigel and the apical side toward the central lumen. In contrast, primary organoids cultured from human CRC biopsies typically grow as irregular compact structures rather than as simple cystic structures (Sato et al. 2011) and they often grow more successfully in the absence of niche factors, dependent on the mutational background of the samples and which signalling pathways are activated (Young & Reed 2016). As Wnt signalling is aberrantly activated in most human CRC, organoids derived from tumour epithelium readily proliferates independent of Wnt and R-spondin (Ohta & Sato 2014). Noggin is required to maintain Lgr5 expression but is not required for expansion of CRC organoids (Sato et al. 2011). EGF was dispensable in most CRC organoids, while some CRC organoids decelerated their proliferation after withdrawal of EGF (Sato et al. 2011).

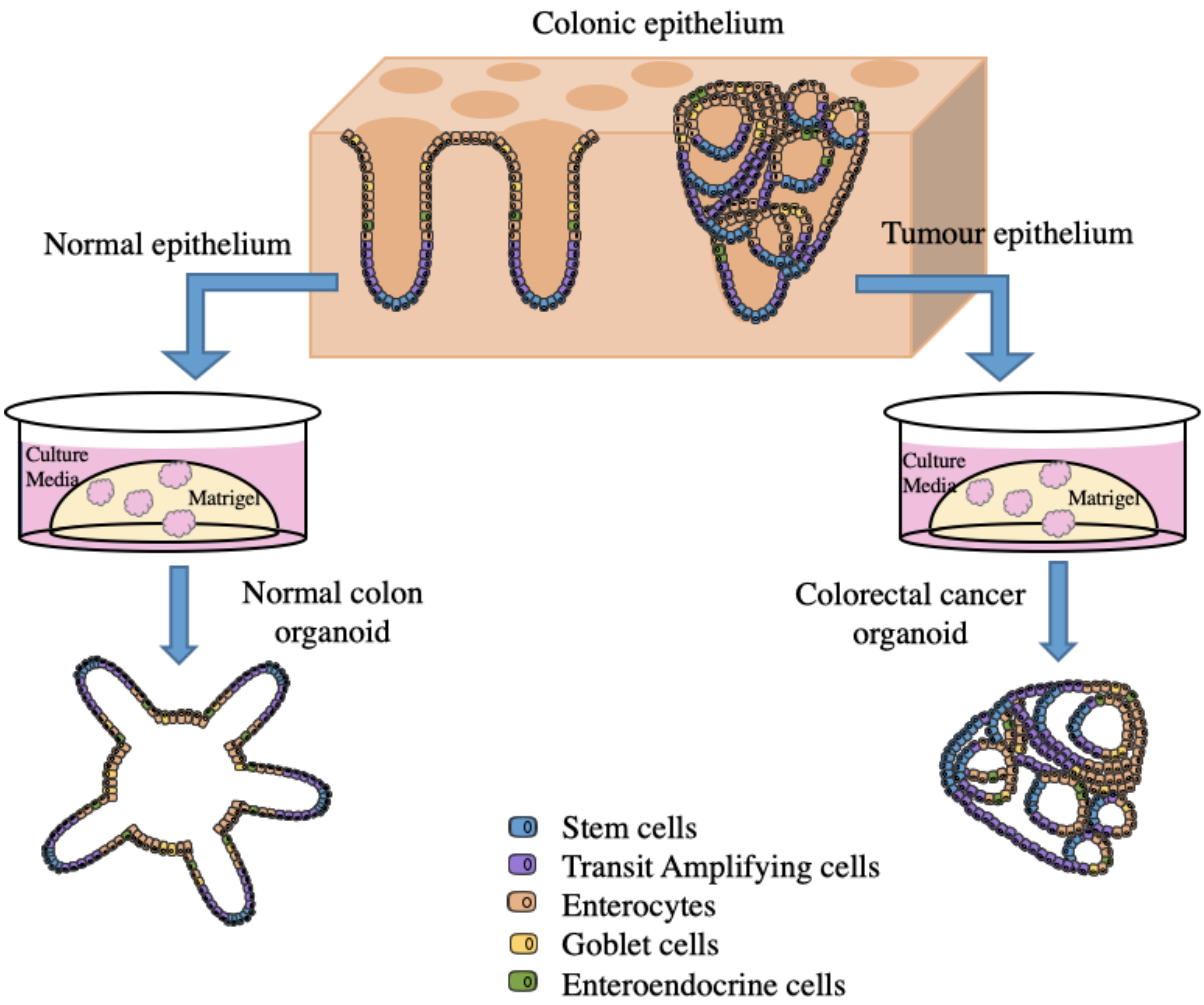

Figure 1.6 Primary organoid culture of normal and tumour CRC epithelium

The normal colon epithelium presents a crypt structure with stem cells at the base of the crypt, and differentiated cells which migrate to the tip of the crypt. On the other side, tumour morphology presents a disorganised structure that can be characterised by mucinous type, large size, polypoid growth, among others. Normal intestinal epithelial and colorectal cells are isolated from the intestine and cultured in Matrigel surrounded with culture media supplemented with growth factors. Normal epithelium forms organoids resembling the intestinal crypts, whereas tumour epithelium develop dysplastic organoid structures. Figure adapted from (Ohta & Sato 2014).

1.3 *In vivo* tumour microenvironment

The normal tissue-specific microenvironment consists of both tissue-specific cell types and tissue-resident cell types, such as immune, mesenchymal and endothelial cells. The microenvironment provides both the biochemical signals and structural constraints that are ultimately required to dictate the cellular behaviours appropriate for the tissue in question (Oliver et al. 2018). Also, normal tissue relies on the body's circulatory system to supply individual cells with nutrients and oxygen for their survival, thus making vascularisation a vital prerequisite for successful tissue regeneration (Rijal & Li 2018; Rademakers et al. 2019). In contrast, solid tumours are highly disorganised versions of normal organs populated with numerous cell types including endothelial cells, such as blood vessels, stromal fibroblasts, immune cells and malignant cancer cells (Lyssiotis & Kimmelman 2017). 3D architecture of tumour growth *in vivo* results in the generation of a variety of physical and chemical gradients contributing to zonation and phenotypic heterogeneity within the tumour. Rapidly growing tumour cells outgrow their blood supply resulting in mass transport limitations which influences intratumoral metabolic heterogeneity. For example, while nutrient and oxygen access is proportional to vascular access, efficient waste removal in inversely proportional (Lyssiotis & Kimmelman 2017). Oxygen and nutrients access in tumours fluctuate temporally and regionally, which generates ischemic, hypoxic and necrotic areas in the central core of the tumour. Tumour cells can adapt to this stressful environment by inducing angiogenesis and altering metabolic strategies, thus ensuring survival and proliferation (Wek & Staschke 2010). The TME is responsible for different stages of the cell cycle of tumour cells that differ in their gene expression profiles, stress response and signal transduction depending on their position within the tumour. Firstly, highly proliferating cells are located at the external layer of tumours with easier access to oxygen and nutrients as they are close to blood vessels. Secondly, live cells that are not actively dividing, named quiescent cells, located in the middle layer, present a slower cell metabolism as the distance from the tumour periphery increases. Finally, cell necrosis at the core of the tumour is the result of oxygen depletion, nutrient shortage and metabolic waste accumulation at the centre of the tumour (Lazzari et al. 2017).

As a result of this heterogeneity, the tumour includes cells harbouring distinct molecular signatures with different levels of sensitivity of treatment. Heterogeneity provides the fuel for drug resistance, therefore an accurate assessment of tumour heterogeneity is essential for the development of effective therapies (Dagogo-Jack & Shaw 2017).

1.3.1 Hypoxia signalling pathway

It is of crucial importance to understand how cells can adapt to changes in levels of oxygen. Interestingly, the Nobel Prize 2019 in Medicine was awarded to William G. Kaelin Jr, Sir Peter J. Ratcliffe and Gregg L. Semenza for their discoveries of how cells sense and adapt to oxygen availability.

The hypoxia signalling pathway is activated in response to low oxygen tension and it is a fundamental feature of physiological processes as well as pathophysiological conditions such as cancer and ischemic diseases (Cavadas et al. 2015). This system is composed of an oxygen-regulated α-subunit Hypoxia-inducible transcription factor 1 (HIF1α) and a constitutively expressed β-subunit (HIF1β) (Shen & Li 2017a). HIF1α is mainly regulated by protein degradation, it is unstable in well-oxygenated tissues owing to ubiquitin-mediated degradation, but rapidly becomes stable in hypoxic conditions. Under normoxia (normal oxygen supply), HIF1α is subjected to oxygen-dependent hydroxylation by three prolyl hydroxylase domain proteins (PHD1, PHD2 and PHD3) on two prolines residues (Pro 402 and 564 in human HIF1α) in the oxygen-dependent degradation (ODD) domain (Shen & Li 2017a). The prolyl-hydroxylated HIF1α is targeted for proteasomal degradation by the tumour suppressor protein von Hippel-Lindau (VHL), an E3 ubiquitin-protein ligase. HIF1α is also regulated in an oxygen-dependent manner by factor inhibiting HIF1 (FIH). In this case, FIH mediates the hydroxylation of an asparagine residue (Asn 803 in human HIF1α) in the C-terminal trans-activation domain, which prevent the binding of HIF1α with transcriptional coactivators P300 and CREB-binding protein (CBP) (Shen & Li 2017a). Under hypoxia, hydroxylation and proteasomal degradation of HIF1α are impaired due to the lack of sufficient oxygen. Stabilised HIF1α translocates into the nucleus, heterodimerises with HIF1β, and the complex HIF1α-HIF1β binds to hypoxic responsive elements (HREs) within the promoter regions of target genes (Figure 1.7) (Shen & Li 2017a; Denko 2008; Chen & Lou 2017).

Multiple oxygen-independent mechanisms can also lead to HIF1α stabilisation. Importantly, growth factor signalling results in stabilised HIF1α due to the activation of mammalian target of rapamycin (mTOR) and subsequent increase in the rate of HIF1α translation (Dengler et al. 2014). Additionally, various metabolites, such as fumarate and succinate, inhibit PHDs often by deregulating their enzymatic activity or outcompeting them for necessary cofactors, including iron and ascorbate (Dengler et al. 2014). Nutrient conditions can also regulate HIF1α

stabilisation independently to oxygen, such as lactate and pyruvate accumulation (Dengler et al. 2014).

There are over 70 known direct HIF1α and HIF1β target genes that function in numerous aspects of both normal pathology and disease processes (Dengler et al. 2014). The most well-characterised targets are involved in regulation of oxygen supply and utilisation via angiogenesis (Dengler et al. 2014). To coordinate the most effective use of oxygen, HIF activates genes that shift energy production from oxidative phosphorylation to glycolysis. The genes encoding all glycolytic enzymes are directly upregulated by HIF. HIF also regulates targets that increase the distribution of oxygen supply such as erythropoietin (*EPO*), vascular endothelial growth factor (*VEGF*) and its receptors vascular endothelial growth factor receptor 1 (*FLT1*) and vascular endothelial growth factor receptor 2 (*FLK1*), as well as endothelin 1 (E*DN1*) and angiopoietin (*ANGPT*). In addition to pathways involved in oxygen homeostasis, HIF targets are also involved in stemness and self-renewal (e.g. octamer-binding transcription factor (*OCT4*)), proliferation, epithelial to mesenchymal transition, metastasis and invasion, redox homeostasis and apoptosis. For example, some studies suggest that many stem cells are also localised in areas with, and benefit from low oxygen, supporting the hypothesis that hypoxia might be important from the undifferentiated phenotype of stem cells (Mathieu et al. 2011). Also, *PHD2* and *PHD3* are HIF target genes, which set up possibly negative feedback loops within the hypoxia signalling pathway (Dengler et al. 2014; Liu et al. 2012; Benita et al. 2009).

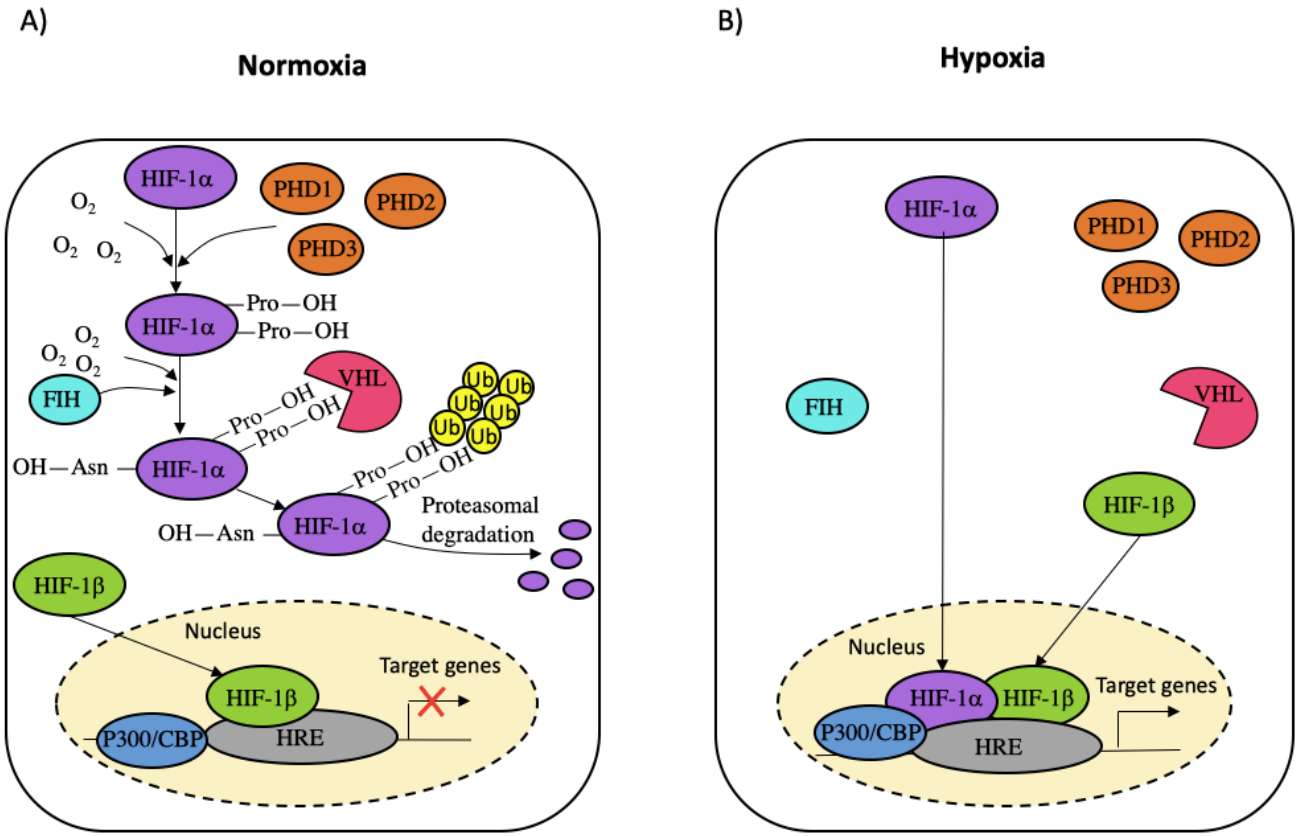

Figure 1.7 Schematic of Hypoxia signalling pathway

A. Under normoxia, HIF1α protein is oxygen-dependent hydroxylated at Pro 402 and 564 by PHD1, PHD2 and PHD3 and subsequently degraded by VHL through the Ubiquitin-Proteasome pathway. Additionally, oxygen-dependent asparaginyl hydroxylation of HIF1α by FIH at Asn 806 impairs its interaction with P300/CBP. **B.** Hypoxia blocks the hydroxylation and proteasomal degradation of HIF1α, leading to its stabilisation and nuclear translocation. HIF1α heterodimerises with HIF1β and activates the transcription of hypoxic responsive elements with the help from additional transcriptional coactivators, such as P300/CBP. Figure adapted from (Vito et al. 2020).

1.3.2 Deregulated metabolic properties in tumour microenvironment

The TME is characterised by deregulated metabolic properties, some of them are the result of a variety of physical and chemical gradients that contribute to zonation and phenotypic heterogeneity within the tumour, as introduced in Section 1.3. Intrinsic features (e.g. genetic programs in cancer cells) and extrinsic characteristics (e.g. oxygen and nutrient availability, pH) contribute to the deregulated metabolic profile of a tumour (Lyssiotis & Kimmelman 2017). This section focuses on the extrinsic variables, such as, oxygen and nutrient diffusional limitation into the tumour, the accumulation of CO_2 and metabolic waste at the tumour core, as well as the acidic microenvironment in that region (Figure 1.8A).

Metabolic activities in normal cells rely primarily on mitochondrial oxidative phosphorylation to generate ATP for cellular growth and maintenance. Cellular respiration consists of three metabolic phases: glycolysis, which is an anaerobic process; and the citric acid cycle and the aforementioned oxidative phosphorylation, which are aerobic processes (Zimmerman et al. 2011). Glycolysis breaks down glucose into pyruvate producing two molecules of ATP per molecule of glucose. Subsequently, pyruvate is shuttled into the mitochondria, where it is transformed into acetyl-CoA (Zimmerman et al. 2011). Finally, during the citric acid cycle, acetyl-CoA is transformed into CO_2 and NADH, which is then used by the oxidative phosphorylation pathway to generate ATP. The theoretical maximum yield of ATP through oxidation of one molecule of glucose in glycolysis, citric acid cycle and oxidative phosphorylation is 38 (2 molecules in glycolysis and 36 molecules in oxidative phosphorylation) (Zimmerman et al. 2011).

In tumours the rate of glucose uptake dramatically increases, which is fermented to produce lactate, even in the presence of oxygen and fully functioning mitochondria. This aerobic glycolysis is known as Warburg effect because it was originally described by Otto Warburg (Weinhouse 1956). However, the understanding of its causes and function remains unclear. Various biological explanations have been hypothesized to explain the function of the Warburg effect. Briefly, the rate of glucose metabolism through aerobic glycolysis is higher such that the production of lactate from glucose occurs 10-100 times faster than the complete oxidation of glucose in the mitochondria. In fact, the amount of ATP synthesised over any given period of time is comparable when either form of glucose metabolism is utilised (Liberti & Locasale 2017). Also, the Warburg effect may present an advantage for cell growth in a multicellular environment. Elevate glucose metabolism decreases the pH in the microenvironment due to

lactate secretion and H^+ ions secreted from cancer cells diffuse into the surrounding environment and alter the tumour stroma interface allowing for enhanced invasiveness (Liberti & Locasale 2017).

When oxygen is not available (hypoxia), cells cannot undergo aerobic respiration, so glycolysis is their only source of ATP. This also explains the higher glycolytic rate in tumour cells, in which oxygen depletion in the core of the tumour has been previously described (Ganapathy-Kanniappan & Geschwind 2013). By contrast, oxygenated tumour cells located in normoxic regions, primarily rely on oxidative metabolism for energy production (Sonveaux et al. 2008; Jiménez-Valerio et al. 2016). Metabolic symbiosis between these two tumour regions has been previously reported and it is described below (Pisarsky et al. 2016; Allen et al. 2016; Jiménez-Valerio et al. 2016; Sonveaux et al. 2008).

To counteract the metabolic heterogeneity, heterocellular metabolite cross-feeding pathways are established to support bioenergetics, biosynthesis and the clearance-reuse of metabolic waste products. For example, cancer cells in hypoxic tumour regions switch on cellular metabolism to anaerobic pathways for ATP production, which occurs through the activation of glucose uptake and glycolysis to produce pyruvate, which is then converted into lactate by lactate dehydrogenase A (LDHA) instead of being oxidised via the citric acid cycle and oxidative phosphorylation (Guillaumond et al. 2013). This creates a lactate gradient that mirrors the oxygen gradient in the tumour (Sonveaux et al. 2008). As shown in Figure 1.8C, this process is supported by well-oxygenated cancer cells which consume lactate discarded by the hypoxic cancer cells to fuel mitochondrial metabolism. Lactate is release from cells via monocarboxylate transporter 4 (MCT4, also known as SLC16A3), whose expression is increased in hypoxic cells. By contrast, the expression of the lactate importer monocarboxylate transporter 1 (MCT1) is increased in normoxic cancer cells with close vicinity to blood vessels. This symbiotic intratumoral metabolism pathway has been detected in pancreatic, colon, breast and renal cancer, showing that it may represent a general phenomenon used across many cancer types (Guillaumond et al. 2013; Sonveaux et al. 2008; Pisarsky et al. 2016; Jiménez-Valerio et al. 2016; Allen et al. 2016; Lyssiotis & Kimmelman 2017). Oxygen-dependent expression of MCT1 allows aerobic cancer cells to efficiently take up lactate and it is the crucial component of the metabolic symbiosis based on lactate exchange in tumours. Soveaux *et al*. (2008) showed that human cancer cells cultured under hypoxic conditions convert glucose to lactate and extrude it, whereas aerobic cancer cells take up lactate via MCT1 and utilise it for oxidative phosphorylation, thereby sparing glucose for glycolytic cells (Sonveaux et al. 2008). When

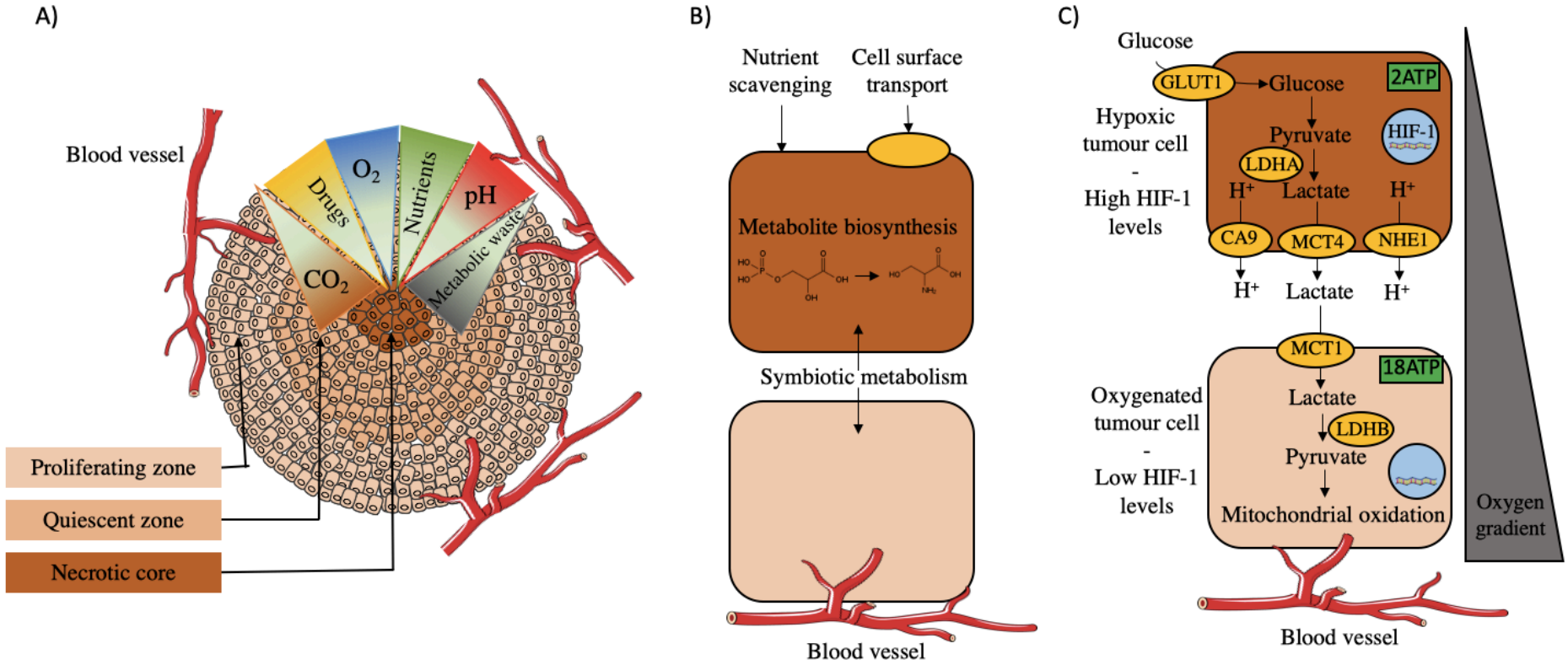

Figure 1.8 Gradients in tumour microenvironment and energy metabolism adaptation

A. Oxygen, nutrient and drug penetration into the tumour is reduced toward the tumour centre due to diffusional limitations. Inversely, carbon dioxide and metabolic waste are accumulated at the tumour core. Acidification in the centre of the tumour is due to lactate accumulation. These gradients generate different zones within the tumour, an external proliferating zone, an intermediate quiescent zone and an internal necrotic core. **B.** Nutrient accessibility to cells within tumours is influenced by upregulation of cell surface transporters, nutrient scavenging, metabolite symbiosis and *de novo* metabolite synthesis. **C.** Energy metabolism is switched under hypoxia conditions and cells activate glycolysis for ATP production. Lactate produced by hypoxic tumour cells is consumed by oxygenated tumour cells to fuel mitochondrial metabolism. HIF1 regulates many genes responsible for this switch. The HIF1 target genes, *GLUT1*, *LDHA*, *CA9*, *MCT4*, *NHE1*, *MCT1* are upregulated under hypoxia conditions and play an essential role for metabolism adaptation.

MCT1 is inhibited, aerobic cancer cells take up glucose rather than lactate, and hypoxic cancer cells die due to glucose deprivation.

This metabolic reprogramming is arranged by HIF1 through the transcriptional activation of key genes encoding metabolic enzymes (see Figure 1.8C), such as: LDHA, which converts pyruvate to lactate, pyruvate dehydrogenase kinase 1 (PDK1), which inactivates the enzyme responsible for conversion of pyruvate to acetyl-CoA, thereby shunting pyruvate away from the mitochondria, and BCL2 Interacting protein 3 (BNIP3), which encodes a member of the BCL2 family that triggers selective mitochondrial autophagy (Semenza 2008). In addition, HIF-1 transactivates GLUT1, which encodes a glucose transporter that increases glucose uptake to compensate for the fact that, compared with oxidative phosphorylation, glycolysis generates approximately 19-fold less ATP per mole of glucose, and HIF also activates the genes encoding the glycolytic enzymes that convert glucose to pyruvate (Semenza 2008). Furthermore, the increased production of lactate by hypoxic cancer cells originates an acidic microenvironment with a pH 5.5-7.2 associated with both increased H^+ production and increased H^+ efflux through the HIF-1 mediated transactivation of carbonic anhydrase IX (CA9), MCT4, which facilitates lactate export, and sodium-hydrogen exchanger 1 (NHE1) (Tredan et al. 2007; Semenza 2008).

Aside from the variation in energy metabolism due to the lack of oxygen availability, nutrient deprivation also affects tumour metabolism. Similar to oxygen, nutrient deprivation is the consequence of the elevated rates of tumour growth and limited blood supply. The TME has been shown to be depleted of the following nutrients: glucose, amino acids and fatty acids (Nazemi & Rainero 2020; Finicle et al. 2018). Thus, processes related to the supply of these nutrients are often upregulated in cancer cells through the different strategies depicted in Figure 1.8B and further presented below.

Glucose availability in the TME is inversely proportional to local utilization. As previously described, cancer cells located in hypoxic tumour regions metabolise glucose through anaerobic glycolysis and this process is supported by well-oxygenated cancer cells that consume the lactate produced by the hypoxic cancer cells. This carbon source sharing strategy is possible due to the increased expression of appropriate intake/release transporters of glucose and lactate in the corresponding cells, that enable cancer cells harvest scarce blood-borne nutrients (glucose), and acquire nutrients (lactate) by scavenging macromolecules from the TME (Figure 1.8C) (Lyssiotis & Kimmelman 2017; Finicle et al. 2018; Nazemi & Rainero 2020).

Furthermore, under amino acid starvation, cancer cells activate alternative mechanisms to improve amino acid availability. High expression of amino acid transporters, such as large neutral amino acids transporter small subunit 1 (LAT1), can facilitate the uptake of amino acids from extracellular milieu and is associated with poor prognosis in some tumours. LAT1 is significantly induced by hypoxia (Kucharzewska et al. 2015; Parks et al. 2017). Also, cancer cells overcome amino acid limitation by scavenging extracellular proteins via a process known micropinocytosis followed by lysosomal degradation and amino acid extraction (Finicle et al. 2018). Moreover, it has been reported that cancer cells can extract amino acids by scavenging of necrotic cell debris to fuel growth and survival (Nazemi & Rainero 2020; Finicle et al. 2018). Finally, the synthesis of amino acids is upregulated in some tumours as a method for tumours to bypass low environmental nutrient accessibility and maintain tumour proliferation (Sullivan & Heiden 2019). For instance, many tumours upregulate the enzymes of the serine synthesis pathway, which converts the glycolytic intermediate 3-phosphoglycerate into serine through a three-step process (Sullivan & Heiden 2019).

Also, cancer cells need lipid and fatty acids to reproduce their membrane and to generate energy. However, the rapid growth and expansion of tumour tissue often leads to a limited supply of lipids. To counteract this limitation, cancer cells adapt their lipid metabolism by increasing *de novo* synthesis of fatty acids, which is observed in many different cancer types, such as breast, liver and prostate (Furuta et al. 2008; Munir et al. 2019). Fatty acid synthase (FASN) expression, regulated by HIF1, has been reported to be increased, decreased, or unaffected in hypoxic cancer cells, depending on the cancer type or the cell line model (Munir et al. 2019; Shen & Li 2017b). Moreover, studies have shown that cancer cells can also acquire exogenous fatty acids by upregulating various fatty acids-uptake mechanisms. Hypoxia increases fatty acid uptake in breast and ovarian cancer by inducing the expression of fatty-acid-binding proteins (FABP3, FABP7 or FABP4), which are involved in the uptake and subcellular trafficking of fatty acids (Munir et al. 2019).

In summary, cancer cells are exposed to a metabolically challenging environment with scarce availability of oxygen and nutrients. However, they can adapt to this stressful environment by altering metabolic strategies, thus ensuring survival and proliferation.

1.3.3 Drug resistance associated to tumour microenvironment

The genetic and phenotypic diversity of cells within tumours is a major obstacle for cancer treatment. Also, the 3D structure of solid tumours behaves as a physical barrier that restricts drug penetration increasing its resistance toward different therapeutics (Choi et al. 2013). In most solid tumours, epithelial junction proteins such as E-cadherin and claudins, and ECM proteins, such as, collagen, elastin, fibronectin and laminin create a physical barrier that prevent intratumoral drug penetration and direct contact between drugs and their target receptor on malignant cells (Choi et al. 2013). In order to enhance the intratumoral diffusion, some studies suggest the transient degradation or downregulation of ECM proteins using injection of ECM-degrading enzymes into the tumour. For instance, the intratumoral injection of relaxin, a protease that decreases the synthesis of collagens, increases drug penetration (Brown et al. 2003; Cernaro et al. 2013; Choi et al. 2013). Another approach to overcome physical barriers in tumours is the use of the epithelial junction openers. Wang *et al*. (2010) have created a recombinant protein, called JO-1, that contains the minimal structure domains from Adenovirus 3 (Ad3) that target the desmosomal junction protein desmoglein 2 (DSG2) and is able to efficiently open the epithelial junctions in polarised epithelial cancer cells *in vitro* and *in vivo*, in mouse models with epithelial tumours (Wang & Li, et al. 2011; Choi et al. 2013).

Furthermore, the characteristic hypoxia of the TME, is one of the key factors that cause the drug resistance to cancer cells for chemotherapy. Chemotherapeutic compounds, such as doxorubicin, 5-fluorouracil, cisplatin and irinotecan, that need oxygen to induce an effective anticancer effect through the formation of reactive oxygen species (ROS) that damage cell's membrane and DNA, loss their efficiency due to the reduced oxygen diffusion (Nunes et al. 2018). To surpass the chemoresistance resulting from the hypoxic environment found in solid tumours, hypoxia-activated prodrugs (HAPS) have been explored. These type of drugs suffer a chemical reduction and become active when they are exposed to hypoxic environments, having no effect in cells with normal oxygen levels (Nunes et al. 2018). Recently, Zhang *et al*. (2019) have developed a new drug carrier with oxygen generation function upon light irradiation that reacts with doxorubicin to produce ROS in hypoxic microenvironments for better therapy efficiency (Zhang et al. 2019; Nunes et al. 2018).

On the other side, the extracellular acidosis, as a result of high glycolytic flux, has an impact on drug efficiency by affecting their cellular uptake. Non-invasive measurements have shown that extracellular pH ranges from 6.5 to 6.9 while intracellular pH remains neutral to alkaline

creating an acid-outside pH gradient typically not observed in normal tissue (Wojtkowiak et al. 2011). In particular, weakly basic drugs with a dissociation constant of 7.5-9.5 (e.g. doxorubicin, mitoxantrone, vincristine among others) are protonated in acidic microenvironments. As a result, the cellular uptake of these drugs is reduced because charged drugs are less effective in transposing cellular membranes. This phenomenon is termed "ion trapping" (Nunes et al. 2018; Wojtkowiak et al. 2011).

1.3.4 3D tumour organoids more closely mimic the natural tumour microenvironment

2D conventional cell cultures cannot mimic sufficiently the complexity of *in vivo* 3D cell-tissue organisation due to the uniform rich oxygenation and nutrition provided to all cells and the lack of tissue–specific architecture, cell-cell and cell-matrix interactions (Edmondson et al. 2014a). However, 3D cell culture systems provide more favourable conditions for tissue physiology, anatomy and structure which are close to *in vivo* situations. Spheroids and organoids structure better reproduce the cellular heterogeneity and microenvironment of the tumour (Lazzari et al. 2017; Edmondson et al. 2014a; Imamura et al. 2015; Saglam-Metiner et al. 2019; Jin et al. 2018).

There are three main approaches for *in vitro* study of hypoxia conditions. The first is by physically creating a hypoxic environment within a multi-gas incubator. The second is by oxygen deprivation using chemicals in cell culture media, such as cobalt salts and deferoxamine mesylate (Qiu et al. 2017). Third is the use of 3D culture systems, such as spheroids and organoids, that mimic better the microenvironment conditions of the tumours. During spheroids growth, a gradient of oxygen is stablished as demonstrated in several studies that measured the oxygen tension or content in spheroids using O_2-sensitive microelectrodes or fibre-optic oxygen sensors (Grimes et al. 2014; Mueller-Klieser & Sutherland 1982; Mueller-Klieser 1984). The oxygen gradient in spheroids is due to the high proliferation of cells in the outer region of the spheroid resulting in a higher consumption of oxygen by these cells. Also, the oxygen diffusion distance increases with the spheroid growth and consequently the oxygen availability is reduced toward the spheroid centre (Nunes et al. 2018). Large spheroids (400-500 μm diameter) present an internal layered cell distribution analogous to that observed in solid tumours (Figure 1.8). Similar to the situation *in vivo*, tumour spheroids are exposed to nutrient, oxygen, pH and growth factors gradients which generate necrotic, hypoxic, quiescent and proliferative zones from the inner spheroid core to the surface (Stadler et al.

2015; Lazzari et al. 2017). Furthermore, pH gradients detected in solid tumours are also present in HCT116 colon cancer spheroids resulting in a proportional decrease of doxorubicin uptake with the spheroid depth (Swietach et al. 2012). One step forward, consist of the use of organoid cultures to mimic both hypoxic conditions and *in vivo* intratumoral heterogeneity (Saglam-Metiner et al. 2019; Qiu et al. 2017). Hubert *et al*. (2016) observed hypoxia gradients of human glioblastomas across organoids using antibody detection of CA9 (a hypoxia marker). Gliobastoma organoids displayed regional heterogeneity with a rapidly dividing outer region detected with the denser expression of SOX2 for pluripotency due to the highest exposure to oxygen, nutrients and media growth factors. Then, the expression of the hypoxia marker CA9 highly correlated with the spatial reduction of SOX2 expression and recapitulates the hypoxic gradients found in tumours (Hubert et al. 2016). Okkelman *et al*. (2019) found that oxygen heterogeneity in intestinal organoids has functional meaning. Crypt regions had higher oxygenation levels, reflecting their higher reliance on glycolysis, than more actively respiring villi regions (Okkelman et al. 2019). Cruz-Gil *et al*. (2019) showed that murine CRC organoid presented increased glycolysis compared to wild-type organoids, by measuring the levels of L-lactate, the end product of glycolysis (Cruz-Gil et al. 2018). Similar to spheroids, ineffective drug penetration has also been observed in tumour organoids using chemotherapeutic compounds (Roscigno et al. 2019). Karolak *et al*. (2019) used a three-dimensional, agent-based, lattice-free computational model to generate a library of multicellular tumour organoids and indicated that limitations in drug penetration is not based solely on organoid size, but also on other tumour features, such as morphology or cellular packing density (Karolak et al. 2019). Recent advances in the organ-on-a-chip technology has enabled the generation of hypoxia conditions on microfluidic cell culture systems (Busek et al. 2016). For instance, Zhang *et al*. (2015) used the SUM159 mesenchymal triple-negative breast cancer cell line on two dimensional microfluidic platforms to demonstrate increased production of lactate under hypoxic conditions (Zhang et al. 2015).

1.4 Organoid size separation

The TME is characterised by oxygen, nutrients and waste metabolites gradients due to the diffusional limitations, that depend in part on the tumour size (Gerlee & Anderson 2009). Therefore, during the planning phase of a specific drug testing, it may be essential to control the size of the organoids accordingly to the mechanism of action of the drug. Also, a more size-

homogeneous organoid population may respond more reproducibly to downstream assays which allows to obtain more reliable conclusions in drug testing. Furthermore, spheroid and organoid size has been object of investigation of previous studies and these are described below.

Daster *et al*. (2017) generated CRC spheroids of different sizes to poduce *in vitro* models that recapitulate the different areas of an *in vivo* tumour generated by oxygenation gradients and differential access to nutrients. They identified three multicellular tumour spheroid (MCTS) stages, corresponding to defined spheroid sizes. Firstly, proliferating and normoxic cells were found in MCTS cultured for 6-7 days with a diameter below 200 μm. Secondly, proliferative zones at the surface and hypoxic zones in the core were identified in MCTS cultured for 9-10 days with a diameter between 300 and 350 μm. Finally, hypoxia plus necrosis was detected in MCTS cultured for 14-15 days with a diameter greater than 500 μm. Also, they showed that MCTS including both hypoxic and necrotic areas most closely mimic gene expression profile of *in vivo* tumours. Furthermore, resistance to 5-FU was higher in the largest MCTS compared to the smaller ones suggesting that sensitivity to 5-FU is associated to the presence of proliferating cells in early stage MCTS. In conclusion, they pointed out the importance of the development of models including hypoxic areas to allow the identification of new drug resistance mechanisms (Daster et al. 2017).

Similarly, Wu *et al*. (2014) built a transient diffusion-reaction model to calculate the effective diffusivity of oxygen within embryonic stem cell aggregates. They found that hypoxia (4-5% oxygen) was negligible in embryonic stem cell aggregates with a smaller radius than 100 μm, but become significant for aggregates larger than 300 μm due to oxygen, nutrients, and metabolic by-product diffusional limitations (Wu et al. 2014).

Moreover, Tirier *et al*. (2019) isolated small (20-40 μm) CRC spheroids from big (70-100 μm) ones by filtering with standard 100 μm, 70 μm, 40 μm and 20 μm cell strainers and they showed that the small-phenotype is enriched for secretory intestinal differentiation markers and the big-phenotype is characterised by the expression of genes involved in intestinal stem/progenitor cell maintenance at the apex and the formation of cell-cell junctions (Tirier et al. 2019).

Arora *et al*. (2017) sorted spheroids using an automated micropipette aspiration and release system in order to increase the efficiency of intestinal organoid formation and make organoid platform tractable for large-scale studies and commercial applications. It is worth mentioning that the "spheroid" term used by Arora described an intermediate stage of organoid development, since they classified the hindgut spheroids as an intermediate step between

endoderm and mature intestinal organoids. They have identified morphological features that distinguish pre-organoids (spheroids that mature into organoids) from spheroids. More specifically, sorting spheroids with a diameter greater than 75 μm and spheroids with an inner mesenchyme cell mass increase efficiency of the maturation into an intestinal organoid by a 3.8 fold over unsorted spheroids. Their system has a sorting speed of 1 spheroid per minute and is based on three major units. First, an image processing and analysis unit that takes as input a series of real-time images from the microscope and analyses them for spheroid of interest. Second, a three-axis positioning unit that moves a micropipette into place. Third, a spheroid harvesting unit that takes up a single spheroid and dispenses it into a tube (Arora et al. 2017).

Moreover, Jung *et al*. (2019) and Lim *et al*. (2018) used microfluidic devices to produce lung cancer organoids, and glioma and breast spheroids in a size controllable manner, respectively. They claim that when the diameter of the spheroids/organoids is nonhomogeneous, the diffusion distance of the drug differs for each spheroid/organoid, resulting in various drug responses. To enhance the reproducibility of drug response tests, standardising the size and uniformity of spheroids/organoids is crucial to ideally reproduce the efficacy of drugs. Jung *et al*. (2018) designed a microfluidic device containing 29 microwells with a 750 μm depth and 500 μm width to produce lung cancer organoids with a diameter range of 120-180 μm after 3 days of culture under perfusion (Jung et al. 2019). Lim *et al*. (2018) used pillars that have barrier function to obtain glioma spheroids with a diameter ranged from 175 to 225 μm after 3 days of culture in a microfluidic pillar array (Lim et al. 2018).

All these findings show that organoid size is a key parameter in multicellular structures due to diffusional limitations and need to be taken into account during organoid production for drug discovery applications to increase the reproducibility of drug sensitivity assays.

1.4.1 Cell size separation technologies

The separation of cells from heterogeneous samples is important in a wide range of fields in medicine, biotechnology and biology; and cell separation methods can be classified as either chemical or physical (Radisic et al. 2006). Chemical methods are based on affinity and comprise capture based on surface charge and adhesion on affinity solid matrix (beads, plates, fibres), and antibody binding to label and select for specific target cell types (e.g. fluorescent-activated cell sorting-FACS and magnetic-activated cell sorting-MACS) (Dainiak et al. 2007).

These techniques are characterised by the high degree of resolution and purity of the samples collected but can be limited by the lack of specific chemistry that uniquely select for the target cell types, as well as the high sample processing cost. On the other hand, physical separation techniques are based on the size, density and shape of cells and include filtration, sedimentation and density gradient centrifugation. These methods are commonly used for the bulk recovery of heterogeneous samples prior to isolation of specific cell subtypes by affinity fractionation techniques (Gossett et al. 2010). In this work, we suggest an organoid size-based separation to ensure the quality requirements for supplying organoids to pharmaceutical companies to perform reproducible drug sensitivity studies without the need of labelling or chemical modifications.

Microfiltration is the most well-known method for separating cells according to their size. This technique is based on passing the cell suspension through a membrane with a specific pore size. Microfiltration devices can be classified depending on the direction of the flow: dead-end or cross-flow filters (Coulson & Richardson 2002). In the case of dead-end, the flow is perpendicular to the filter plane, whereas in the cross-flow filtration, the flow is parallel to the filter plane. Normally, dead-end filtration is more efficient for capturing large particles, but limited by clogging of larger cells and debris (Dalili et al. 2019). Furthermore, the increase in solid concentration close to the membrane surface, an effect known as concentration polarisation phenomena, is less severe in microfiltration when compared to ultrafiltration (Marshall 2018). On the other hand, cross-flow filtration attempts to reduce clogging and concentration polarisation through parallel fluid flow tangent to the filter surface, thus washing away large particles (Dalili et al. 2019).

Gravity sedimentation separates cells according to their size and density. Larger and denser cells sediment faster than smaller and less dense cells. However, the majority of cells do not have major differences in density but do vary considerably in their size. This means that density has little effect when cells are suspended in a low density medium and cells are separated mainly on the basis of size differences (Burdon et al. 1988). The sedimentation velocity of a spherical cell falling through a fluid under the influence of the gravitational force, from Stokes law is outlined in Equation 1.1 (Coulson & Richardson 2002).

$$u_0 = \frac{(\rho_p - \rho_f) g {d_p}^2}{18\mu} \qquad \text{Equation 1.1}$$

where: u_0 is the terminal falling velocity, d_p is the particle diameter, ρ_p is the particle density, ρ_f is the fluid density, μ is the fluid viscosity, and g is the acceleration due to gravity (9.8 m/s^2).

Centrifugation accelerates the separation process by introducing centripetal force many times greater than gravity, and the rate of sedimentation becomes dependent on the size and density of the cells. This technique is widely used for blood cell fractionation, and it was originally described by (Pertoft et al. 1978). This method utilises both zonal (separation by size) and isopycnic (separation by density) techniques, and blood cell types (erythrocytes, granulocytes, lymphocytes and monocytes) can be resolved on preformed gradients of Percoll (Pertoft et al. 1978).

Moreover, during the last decade advances in microfluidics enabled the realization of miniaturised devices offering similar capabilities to conventional methods but with the advantage of reducing equipment size, eliminating potentially biohazardous aerosols, which are generated in FACS, and simplifying the complex protocols associated with cell sorting. These microchip devices are still in the proof-of-concept stage with some limitations, such as the low throughput, due to the single-channel design, to be overcome (Shields et al. 2015).

An alternative particle separation technique widely used in the chemical engineering industry but not introduced in the biotechnology field, is fluidised bed (FB) technology, further described in the next section.

1.5 Fluidised bed technology

A fluidised bed is formed when a fluid passes vertically up through a bed of solids, which is transformed into a fluid-like state through the contact with the fluid (Coulson & Richardson 2002). The most conventional FB systems consist on a cylindrical column, although it may also be rectangular, with a calming or homogenizing section at the bottom of the column, located upstream of the distributor (Figure 1.9A). The function of both is to generate a radially uniform liquid velocity distribution, thus eliminating or at least reducing the presence of channelling, which is the non-uniform distribution of liquid across the column cross-section (Coulson & Richardson 2002). The fluid can be a gas or a liquid, therefore the system is known as gas-solid or liquid-solid fluidisation, respectively (Coulson & Richardson 2002). This project is focused on liquid-solid fluidisation to address the separation of different size organoids.

Fluidisation imparts many important advantages to the system, such as excellent particle mixing and high mass and heat transfer owing to the continuous movement of particles and fluid, which makes it a powerful technology in many industrial applications; from physical processes, such as cooling-heating, drying, adsorption-desorption, coating and granulation, to heterogeneous catalytic gas phase reactions and non-catalytic gas-solid reactions.

1.5.1 Principles of liquid-solid fluidisation

The fluidising medium enters the bed through the bottom and for sufficiently low superficial velocities, the liquid passes through the voids between the particles and the bed remains in a packed bed stage because the drag force of the particles is low. However, as the superficial velocity increases, the drag force on the particle increases and becomes equal to their apparent weight, that is the actual weight less the buoyancy force (Figure 1.9B). The particles become rearranged thus offering less resistance to the flow of liquid and the bed starts to expand with a corresponding increase of voidage (ε). This occurs at a particular superficial velocity, known as minimum fluidisation velocity (u_{mf}), in which the pressure drop of the bed equals the weight of the particles and the bed becomes completely suspended (Bello et al. 2016). This process continues with an increase in superficial velocity, with the total frictional force remaining equal to the weight of the particles, until the bed has acquired its loosest stable form of packing. If the superficial velocity is then increased further, the individual particles separate from one another and become freely supported in the fluid. At this point the bed is described as fluidised (Figure 1.9A) and the drag force drops as the superficial fluid velocity declines. Further increase in superficial velocity causes the particles to separate still further from one another, although the pressure difference remains approximately equal to the weight per unit area of the bed (Coulson & Richardson 2002; Yang 2003; McCabe et al. 1993; Perry & Green 2008). During liquid fluidisation, the bed maintains a uniform character as the superficial velocity is increased, and this type of fluidisation is known as particulate fluidisation characterised by a homogeneous random motion of the particles. At very high rates of liquid flow, the drag force can exceed the net gravitational forces on individual particles. In this regime, particles are carried through the container and must be reintroduced externally.

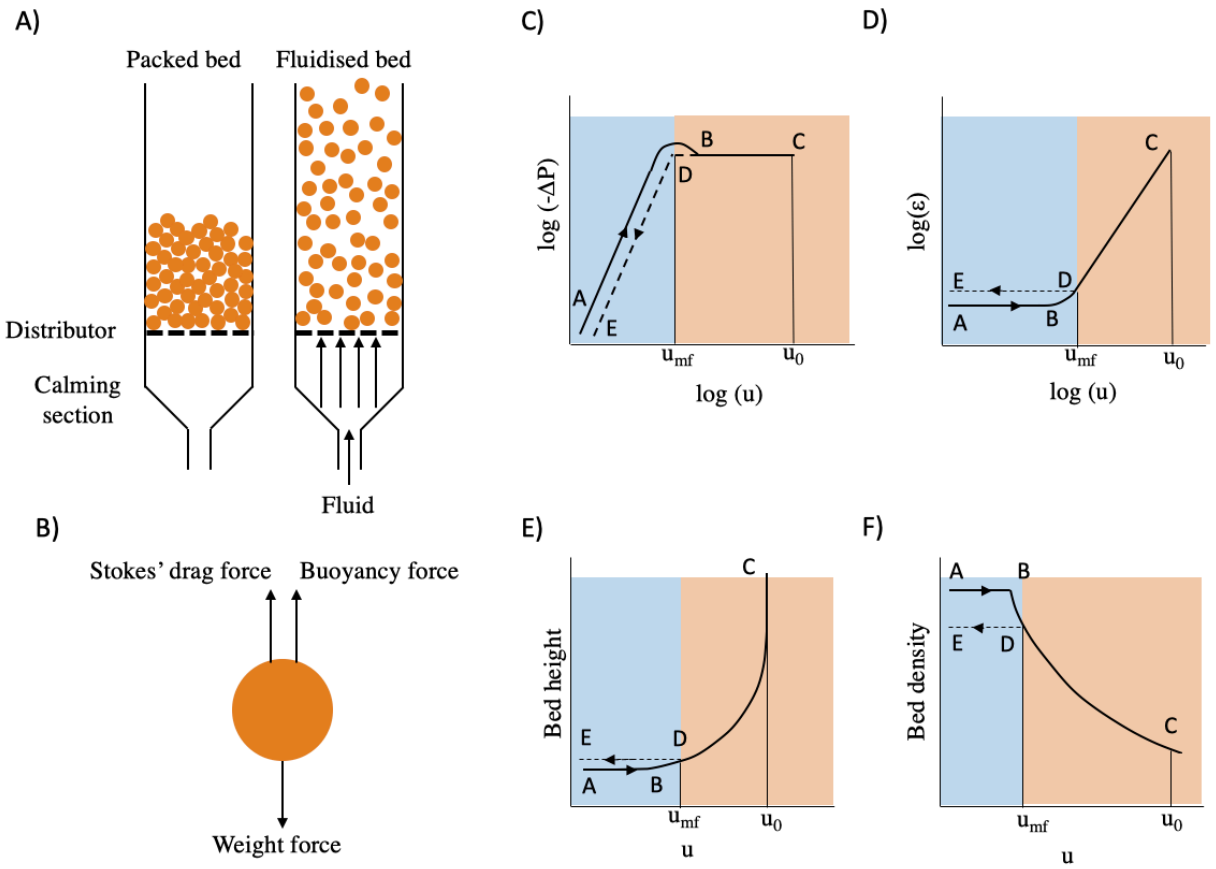

Figure 1.9 Principle of fluidisation and hydrodynamic representation

A. Schematics of a packed bed and fluidised bed. When there is no fluid going upwards the bed of particles remains in a packed state. However, when a fluid passes upwards through the bed of particles, the solids fluidise and the mixture fluid/particles behaves as a fluid. **B.** Balance of forces acting on a fluidised particle. Drag and buoyancy forces act upwards and gravity multiply by the particle's mass produces the downwards weight force. **C.** Pressure drop as a function for fluid superficial velocity for monodispersed particles. **D.** Bed voidage as a function of fluid superficial velocity. **E.** Bed height as a function of fluid superficial velocity. **F.** Fluid-solid bulk density as a function of fluid superficial velocity. Blue and orange colours in **C. D. E. F.** correspond to the packed and fluidised state, respectively (Yang 2003)

1.5.1.1 Hydrodynamic representation

At low fluid velocities, the packed bed of particles is characterised by a specific voidage value and a linear relation exists between the pressure drop and flow rate as described by Carman-Kozeny equation shown in Equation 1.2 (development of Carman-Kozeny equation in Appendix A) (Coulson & Richardson 2002):

$$u_c = \frac{1}{180} \frac{\varepsilon^3}{(1-\varepsilon)^2} \frac{-\Delta P \, {d_p}^2}{\mu l} \qquad \text{Equation 1.2}$$

where: u_c is the average velocity of flow of the fluid, ε is the fraction of the volume of the bed not occupied by solid material and is termed the fractional voidage, voidage or porosity, -ΔP is the pressure drop across the bed, d_p is the particle diameter, μ is the viscosity of the fluid, and l is the height of the bed.

If the pressure drop is plotted against superficial velocity, as shown in Figure 1.9C, a linear relation is obtained up to the point where expansion of the bed starts to take place. Then the slope of the curve gradually diminishes as the bed expands and its porosity increases. This first stage corresponds to a packed bed (AB). As the superficial velocity is further increased, the pressure drop passes through a maximum value because the frictional forces between the particles have to be overcome before bed rearrangement can take place. Then the pressure drop falls slightly and attains an approximately constant value that is independent of the fluid superficial velocity (BC). If the fluid superficial velocity is reduced again, the bed contracts until reaches the condition where the particles are just resting on one another (D). The porosity then has the maximum stable value which can occur for a packed bed of the particles. The superficial velocity at point D is the minimum fluidisation velocity u_{mf}. If the superficial velocity is further decreased, the structure of the bed then remains unaffected provided that the bed is not subjected to vibration. The pressure drop (DE) across this reformed packed bed at any fluid superficial velocity is less than that before fluidisation. In an ideal fluidised bed, pressure drop corresponding DBC is equal to the buoyant weight of particles per unit area. In practice, it may deviate appreciably from this value as a result of channelling and the effect of particle-wall friction (Coulson & Richardson 2002; Yang 2003). Plots corresponding to Figure 1.9C of bed ε, bed height (l) and bed density as a function of superficial velocity, are shown in Figures 1.9D, E and F. For a total mass M of particles, the volumetric particle concentration in

either a packed or a fluidised bed is determined by Equation 1.3:

$$1 - \varepsilon = \frac{M}{\rho_p A l} \qquad \text{Equation 1.3}$$

where: ε is the voidage, M is the total mass of particles, ρ_p is the particle density, A is the cross-sectional area of the column and l is the bed height. Therefore, for a fluidised bed, the product of bed height and particle concentration is constant and can be obtained from Equation 1.4:

$$l(1 - \varepsilon) = \frac{M}{\rho_p A} = constant \qquad \text{Equation 1.4}$$

Thus as l increases, ε increases accordingly, as show in Figure 1.9D and Figure 1.9E. The minimum fluidisation voidage, ε_{mf}, is typically about 0.4 for monosize smooth spheres in the absence of significant wall effect ($d_p/D_c \leq 0.01$, where: $d_p$is the particle diameter and D_c is the column diameter) but varies considerably with the geometry. Also, the value of the fluidised bed suspension density (ρ_B) in Figure 1.9F is given by the following equation:

$$\rho_B = \rho_p(1 - \varepsilon) + \rho_f \varepsilon \qquad \text{Equation 1.5}$$

where: $\rho_B$is the bed density, $\rho_p$is the particle density, ε is the voidage and $\rho_f$is the fluid density.

1.5.1.2 Minimum fluidisation velocity and terminal falling velocity

As described previously, the minimum fluidisation velocity is the lowest fluid velocity at which the bed starts to fluidise. It can be calculated theoretically using characteristics parameters like particle density, fluid density, fluid viscosity, minimum fluidisation voidage, bed height, among others. But the best method of calculating u_{mf} is experimentally determined by a plot of superficial fluid velocity versus pressure drop in the bed (Figure 1.9C) (Coulson & Richardson 2002).

Fluidisation range occurs between u_{mf} and terminal falling velocity (u_0), which is reached when the downward force of gravity is equal to the sum of the particle buoyancy and drag force (Figure 1.9B). At this velocity the particles are carried out of the column.

When a particle falls in vacuum, it attains constant acceleration and velocity increases indefinitely irrespective of its size and density. This behaviour is quite different in a medium, like air or water, where the resistance increases with the velocity until equilibrium between gravitational and fluid resistance is achieved at a critical velocity called terminal falling velocity. Under viscous or laminar flow, Tripathy *et al*. (2015) has shown that u_0 for fine particles of size less than 100 μm can be expressed as Equation 1.1 (Tripathy et al. 2015).

Any particle settling in a medium, depending on its surroundings may undergo free or hindered settling. When individual particles fall freely in a medium without being obstructed by other particles in the near vicinity, it is termed as free settling. In free settling, the particle velocity is controlled by gravity, drag and dominated friction creates medium resistance (Coulson & Richardson 2002).

However, when the interaction with other particles is appreciable, the process is known as hindered settling. This phenomenon is exhibited only when particle concentrations exceed 20% by volume of total mixture and the application of this concept on hydraulic classification has been considered to be vital. The hindered settling velocity may be considerably less than the free settling velocity due to various factors: a decrease in the open cross section for the upward flow of the fluid, which results in an increased fluid velocity and increased apparent viscosity (Jain 2014). For suspensions that have very low particle concentrations (<0.02-1% v/v), Stokes' law is applicable but it does not hold true when the particle-particle interactions increase. For multi-particle suspensions, the Richardson and Zaki equation (Equation 1.6) represents the most popular empirical hindered settling model to accommodate the increased resistance to settling with increased solids concentrations (Johnson et al. 2016).

$$\frac{u}{u_0} = k\left(1 - \emptyset_p\right)^n \qquad \text{Equation 1.6}$$

where: u is the hindered settling velocity, u_0 is the free settling velocity, $\emptyset_p$ is the particle volume fraction, k is a dimensionless multiplier in the range $0.8 < k \leq 1$, and n is the model exponent typically found in the range of 2-5.

It is worth noting that particles start to fluidise (u_{mf}) before reaching the force equilibrium (u_0). Since the fluid density is lower than the particle density, the bed density is smaller than particle density at any voidage value, as shown in Equation 1.5. Therefore, when considering a bed of particles instead of than a single particle, less drag force and consequently less fluid velocity, is necessary to reach the force equilibrium.

1.5.2 Fluidised bed applications

Fluidised beds present numerous advantages, such as intensive solid mixing and high rate of heat and mass transfer between the solids and the fluid, which allow this technology to be extensively used in chemical engineering applications. Mainly three applications have been described: fluidised bed for solids separation (further discussed in Section 1.5.3), fluidised bed reactors for multiphase chemical reactions and fluidised bed bioreactors (FBBs) for cell culture.

FBBs consist of a bed of biological particles that is suspended using high liquid or gas flow rates that allow the cells to be fluidised. FBBs were originally developed for wastewater treatment (WWT) in 1980's and nowadays this application has many large-scale plants (Nelson et al. 2017; Özkaya et al. 2019). Furthermore, considerable interest in immobilised cells has been directed toward their use in FBB, in which the cells can be immobilised by entrapment (within support particles) or by biofilm growth (onto support surface). Bacteria (Gholizadeh et al. 2016), yeast (Gabardo et al. 2012; Gabardo et al. 2014; Gabardo et al. 2015; Sarrouh & da Silva 2008) and microalgae (Mohd-Sahib et al. 2017) fermentations in FBB have been described for the production of several bulk chemicals, such as ethanol, xylitol and lipids. Moreover, FBBs have been used in tissue engineering to overcome limitations of stirred tanks, hollow fibre bioreactors or the channelling that occurs with packed bed bioreactors by fluidising encapsulated cells, reducing cell damage by shear stress and providing sufficient rates of mass transfer between the media and the cells. Jurkat cells and primary human T lymphocytes encapsulated in sodium cellulose sulfate-poly(diallydimethyl) ammonium chloride polyelectrolyte capsules can be expanded in a FBB with higher cell densities than previously reported spinner cultivations (Kaiser et al. 2014; Kaiser et al. 2018). Also, Nikravesh *et al*. (2017) demonstrated the application of a FBB for the cultivation of endocrine pancreatic beta-cells within alginate capsules (Nikravesh et al. 2017). Numerous authors have proposed several geometries and conditions for a FB bioartificial liver hosting alginate/chitosan-encapsulated hepatocytes that can act as a promising therapy for treating patients with acute hepatic failure or other severe liver diseases (Jeffries et al. 2013; Figaro et al. 2017; Lu et al. 2016; Lv et al. 2011; Naghib et al. 2017; Tikunov et al. 2017;Yang et al. 2010; Yu 2014; Selden et al. 2013; Selden et al. 2017; Yang et al. 2013; Zhou et al. 2016).

Less common are the FBB systems in which the cells freely float in the fluid. Prudent *et al*. (2016) designed a small-scale FBB to study the behaviour of red blood cells and their signalling

pathways under various conditions (Prudent et al. 2016). Also, mycelial pellets of *Aspergillus niger* and *Phanerochaete chrysosporium* have been used in FBB for the production of citric acid and manganese peroxidase, respectively (Moreira et al. 1995).

1.5.3 Fluidised bed for particle classification

Classification is a method of segregating the particles of different sizes, densities and shapes into two or more products on the basis of their settling velocities in a medium of separation, which may be liquid or gas. In that application, solids are separated by their different settling velocities and fine particles tend to be elutriated while bigger/heavier particles tend to sink.

The use of a fluidised bed for particle separation is widely used in the mineral and coal industries (Tripathy et al. 2015). Coal is one of the most important fossil fuels globally and the International Energy Agency predicted that the global coal demand will continue to increase until 2040 (Zhou et al. 2018). However, the direct coal utilisation, which is composed of substantial amount of ash-forming mineral matter and moisture, not only reduces the efficiency of power plants but also generates additional particulate materials, sulphur oxides, and emission trace elements that cause important environmental pollution (Zhao et al. 2015; Zhou et al. 2018). Traditional coal cleaning methods are mostly wet processes in which the coal is usually fluidised in water media for gravity classification, although nowadays dry coal beneficiation it is also used for this purpose (Firdaus et al. 2012; He et al. 2016; Lv et al. 2015; Lv et al. 2018). In liquid-solid fluidisation for coal cleaning, the feed slurry enters into the classifier through a feed well and the water is added through the bottom of the column. Since the size and density of the particles are not uniform, the particles are separated according to their mass. In general, the coarser heavier particles form a layer at the bottom of the bed and the finer lighter particles form the top layer, and all the particles are distributed along the bed depending on their density and size (Tripathy et al. 2015). Table 1.2 summarises some of the liquid-solid FB systems described in literature and it shows that FB for particle classification is mainly used for coal and mineral materials.

Furthermore, the Reflux Classifier (RC) deserves a special mention, since most of the liquid-solid FBs for particle separation are based on that technology (as indicated in Table 1.2). The RC was developed by Prof Galvin and his team at the University of Newcastle (Australia) in 2001. This device combines a system of parallel inclined channels above a conventional FB (Nguyentranlam & Galvin 2001). A schematic representation of this system is shown in Figure

1.8A. The inclined channels provide a significant hydraulic advantage over conventional FB, consistent with the well-known "Boycott effect" (Boycott 1920; Ponder 1925). Particulate solids are suspended by an upward flow of liquid from the bottom of the column. When the fluidised suspension flows into the inclined channels the faster settling particles settle onto the upward facing plates, and slide down as concentrated sediment, returning to the zone below, while the slower settling particles remain in the suspension, and hence are carried through the channels to the zone above. The returned sediment is mixed with the rest of the suspension in the fluidised zone below and returned to the inclined channels as a result of the fluidisation (Figure 1.10C). The inclined plates result in a significant increase in the levels of particle segregation based on the projected area of the inclined channels, relative to the vessel area (Nguyentranlam & Galvin 2001; Galvin et al. 2005; Galvin et al. 2010). The Inverted Reflux Classifier (IRC) is a variant of the conventional RC. This system consist of RC placed in an inverted position and the particles are fluidised by adding water from above which helps to wash any entrained dense material from the overhead product (Figure 1.10B) (Li et al. 2014; Kiani et al. 2015).

As detailed above, a lot of research has been done to separate mineral particles using FB systems. However, there are no references found in literature related to the use of FB technology for cell size separation. Putnam *et al*. (2003), for example, examined the use of magnetically stabilised FB to separate erythrocyte subpopulations based on a cell affinity chromatography system (Putnam et al. 2003). However, this project proposes the use of a FB for organoid size-based fractionation as a function of their different settling velocities. The well-established design of the RC could be taken into consideration during the design of a FB for organoid size-based fractionation, as it is the main commercially available FB system for particle classification.

Table 1.2 Liquid-solid fluidised bed systems for particle classification. RC: Reflux Classifier, IRC: Inverted Reflux Classifier

Principle of separation	Material used	System	Particle size	Variables studied	Reference
Density	Coal	RC	150 – 1400 um	Comparison with traditional methods	(Campbell et al. 2015)
			0.5 – 2 mm	Particle size	(Galvin et al. 2010)
			0.075 – 8 mm	Parallel inclined channels	(Galvin et al. 2010)
			0.25 – 2 mm	Two RC in cascading sequence	(Iveson et al. 2014)
			0.25 – 2 mm	Feed flow rate, water velocity	(Kopparthi et al. 2019)
			0.038 – 2 mm	Channel spacing	(Walton et al. 2010)
		FB	0.044 – 2 mm	Numerical study. Particle size distribution	(Wei & Sun 2016)
	Mineral sand	RC	53 – 150 um	Feed solid throughputs (t/(m^{2}h))	(Galvin et al. 2016)
			45 – 500 um	Feed solid throughputs and density. Channel aspect ratio	(Zhou et al. 2006)
	Glass beads, zirconia beads	FB	60 – 500 um	Liquid velocity, particle size and density	(Tatemoto et al. 2005)
	Plastic particles		1.25 – 2.18 mm	Particle size, liquid velocity, thermal modification	(Hu & Calo 2006)
Density and size	Coal	RC	0.25 – 2 mm	Separation performance at full scale	(Galvin et al. 2005)
Size	Glass beds	RC	60 -180 um	CFD study. Parallel inclined plates	(Doroodchi et al. 2005)
			20- 200 um	Parallel inclined plates	(Nguyentranlam & Galvin 2001)
	Sand, glass beads		45 – 500 um	Split fluidisation, underflow rate, solids throughput	(Doroodchi et al. 2006)
	Sand, ilmenite, PVC		175 – 990 um	Parallel inclined plates.	(Laskovski et al. 2006)
	Silica sand		425 – 880 um	Particle motion, water velocity, solids inventory	(Li et al. 2018)
	Cenospheres, fly ash	IRC	1 - 200 um	Feed pulp density	(Kiani et al. 2015)
	Cenospheres, silica		5 – 90 um	Lab-scale, pilot-scale. Feed concentration	(Li et al. 2014)
	Coal	FB	0.038 – 2 mm	Simulation and experimental study. Distributor configuration	(Maharaj et al. 2007)
	Coal, quartz sand		0.375 – 2 mm	Particle density and size, water velocity, initial bed height	(Sha et al. 2011)
	Glass beads		1 – 4 mm	Feed entry location	(Reddy & Sai 2018)
	Quartz, iron ore		100 – 1000 um	Particle misplacement	(Tripathy et al. 2017)

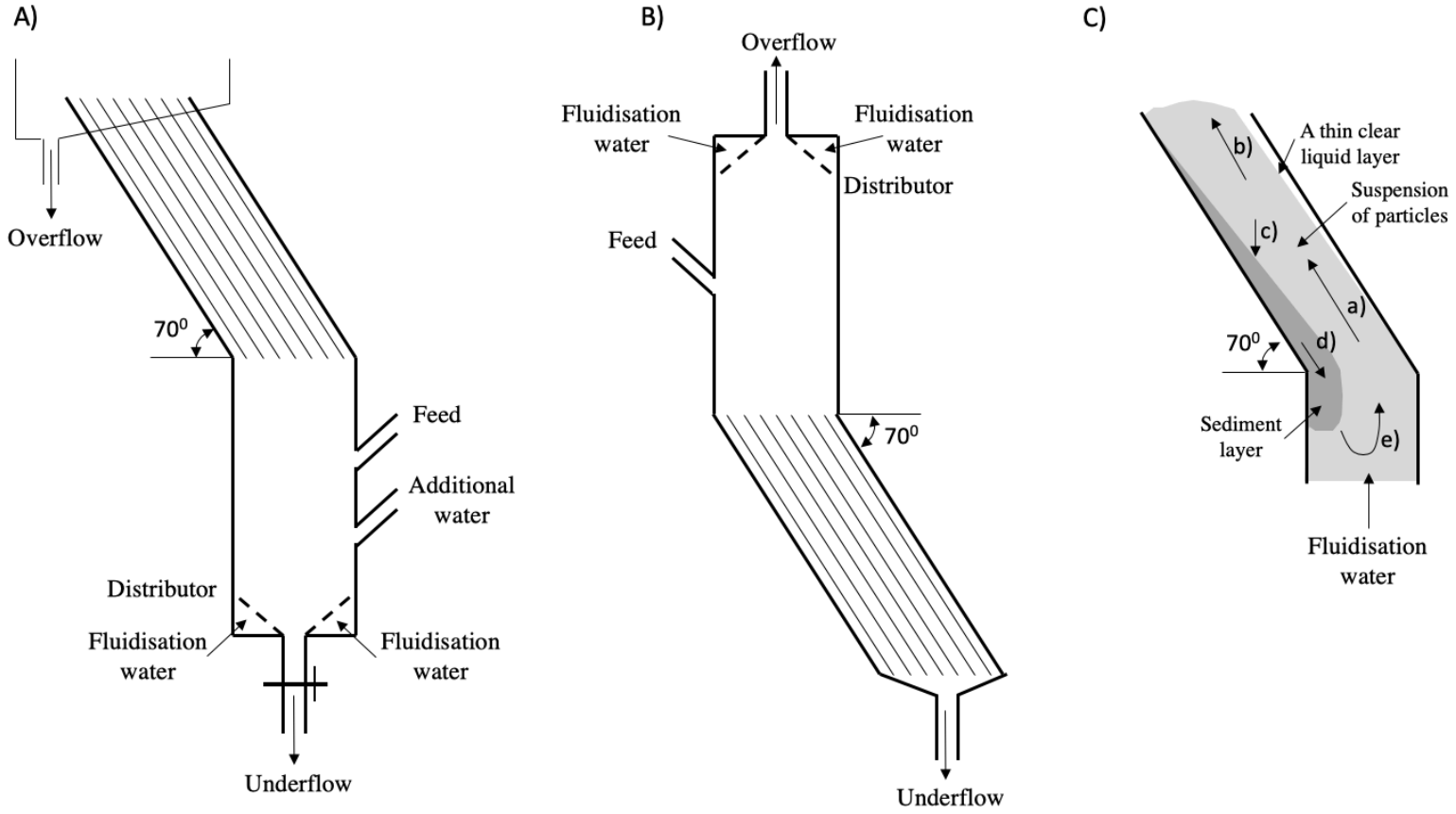

Figure 1.10 Reflux classifier configuration

A. Schematic diagram of the Reflux Classifier (adapted from(Tripathy et al. 2015)). **B.** Schematic diagram of the Inverted Reflux Classifier (adapted from (Li et al. 2014)). **C.** Flow conditions within an inclined channel between two parallel plates: a) Suspension of particles entering the channel, b) particles passing through the channel to the zone above, c) Particles segregating from the suspension, settling onto the upward facing inclined surface of the channel and forming a sediment layer, d) particles in the sediment sliding down rapidly from the inclined channel to the zone below, e) remixing of the returned sediment by fluidisation into the suspension (adapted from (Nguyentranlam & Galvin 2004)).

1.6 Hypothesis and aims

Organoids are more representative of the tumour of origin that traditional 2D cultures. However, the use of organoid for drug discovery is challenged due to drug response variability associated with organoid size heterogeneity. Differences in size leads to limitation in nutrients, oxygen and drug diffusion that results in various drug responses (Jung et al. 2019; Lim et al. 2018). In order to enhance the reproducibility of drug response screenings, an organoid size-based fractionation was proposed in this work to obtain a more uniform organoid population. Organoid fractionation by size has not previously been described and in the present study, a fluidised bed is designed for this purpose. Furthermore, organoid size heterogeneity was investigated in relation to transcriptome differences within the organoid population.

The primary objective of the project was to develop a novel biophysical technique based on a fluidized bed for size-based organoid fractionation to increase drug assays reproducibility and reduce batch-to-batch variability of large-scale organoid production. The evolution of the design and the hydrodynamic characterisation of the system are described in Chapter 3. Furthermore, the separation performance using the designed fluidised bed was assessed and compared with a membrane organoid filtration and these results are shown in Chapter 4. This chapter also includes the evaluation of whether drug response variability is reduced when drug treatment is performed with organoids that present a uniform size.

Following on from this, the second objective was the utilization of size-based fractionated organoids to investigate the differences in gene expression of different size organoids and to determine whether organoid size should be selected accordingly to the mechanism of action of the drug during the planning phase of a drug testing using organoids. The results from this are shown in Chapter 5.

2. Materials and methods

2.1 Culture of colorectal cancer organoids

The human colorectal cancer organoid line used in this work (Iso50) was generated by Dr. Luned Badder from samples provided by the Wales Cancer Bank (WCB, University Hospital of Wales) with informed ethical consent and anonymised, and later retained in the Dale lab and commercialised by Cellesce Ltd. Further details regarding ethical aspects can be found in (Badder et al. 2019). Dr. Luned Badder generated the Iso50 CRC organoids from fragments of carcinoma isolated from the rectum of a 75 years old male with poor tumour differentiation (Badder 2017a). This organoid line presents mutations in *APC, TP53*, *KRAS*, *SMAD4* and *SMAD2*.

All organoid work was performed within a Class II laminar flow biohood and with an aspirator unless otherwise specified. Incubators were humidified and were set to 37^0C and 5% CO_2.

All reagents are specified as (supplier, catalogue number).

2.1.1 Media preparation: 3+ and 6+

3+ basal medium was prepared with Advanced DMEM F12 (Thermo Fisher Scientific, 11550446), GlutaMax 100X (Thermo Fisher Scientific, 35050-038), HEPES 1 M (Thermo Fisher Scientific, 15630-056) and Penicillin/Streptomycin 10000 U/mL (Thermo Fisher Scientific, 15140122). The concentration of each component is specified in Table 2.1.

6+ organoid culture medium consists of 3+ medium supplemented with B27 Supplement 50X (Thermo Fisher Scientific, 17504044), N-2 Supplement 100 X (Thermo Fisher Scientific, 17502048) and N-acetylcysteine (Sigma, A9165). N-acetylcysteine aliquots were sterilised with a syringe 0.22 μm filter (Thermo Fisher Scientific, 15206869). The concentration of each component is specified in Table 2.1. 6+ medium can be stored for up to 1 week in the fridge.

Table 2.1 Components required for 3+ and 6+ media preparation

Component	3+ Medium	6+ Medium
Advanced DMEM F12 (1X)	1X	1X
GlutaMAX (100X)	1X	1X
HEPES (1M)	10mM	10mM
Penicillin/Streptomycin (100X)	1X	1X
B27 (50X)	-	1X
N-2 (100X)	-	1X
N-acetylcysteine	-	1.25M

2.1.2 Routine organoid culture for maintenance

Cryovials of organoids stored at -80^{0}C were thawed rapidly in a 37^{0}C water bath and the content was added to a 15 mL tube. Freezing media was washed away by centrifugation at 100g, 5 min and the pellet of organoids was resuspended in the required volume of ice cold Matrigel. Typically, one vial contained enough organoids to plate four droplets of 50 µL of Matrigel each one. 50 µL droplets of Matrigel were then seeded onto pre-warmed 6-well plates, approximately 6-7 droplets per well. 6-well plate was incubated at 37^{0}C to allow full polymerisation during 10 min and then 2 mL of 6+ medium supplemented with Y-27632 dihydrochloride (ROCK inhibitor) (Tocris, 1254) at 10 µM was added to each well. This medium was replaced every 2-3 days, removing the ROCK inhibitor after initial seeding. ROCK inhibitor was previously implicated in improving cell survival (Ashley et al. 2014).
Organoids were passaged by trituration (physically sheared), at a split ratio between 1:4-1:6 approximately every 4-6 days, or as required. Culture medium was removed from wells and replaced with basal medium. Organoids-Matrigel-medium mixture was lifted from wells and introduced in a 15 mL tube for centrifugation (200g, 5 min). Supernatant was removed, leaving approximately 0.5-1 mL of medium. Organoids were triturated using a P200 pipette tip and washed in basal medium to remove residual Matrigel by centrifugation (200g, 5 min). Supernatant was removed and the triturated organoids were resuspended in the desired volume (considering a split ratio between 1:4-1:6) of ice cold Growth Factor Reduced (GFR) BD Matrigel basement membrane matrix, without Phenol Red (Corning, 356231). 50 µL droplets of Matrigel were then seeded onto pre-warmed 6-well plates (Thermo Fisher Scientific,

11825275), approximately 6-7 droplets per well. The 6-well plate was incubated at 37^{0}C for 10 min to allow full polymerisation and then, 2 mL of pre-warmed 6+ medium was added to each well. This medium was replaced every 2-3 days.

2.1.3 Passaging organoids to single cells

Before an experiment of organoid size separation, organoids were digested into a single cell suspension to increase the homogeneity of the final organoid population. Culture medium was removed from wells and these were washed with Phosphate-buffered saline (PBS) (Thermo Fisher Scientific, 11503387). 1 mL of TrypLE Express Enzyme 1X (Thermo Fisher Scientific, 12604013) was added to each well and organoid-Matrigel mixture was disrupted with a P200 pipette tip. The plate was incubated at 37^{0}C during 5 min. The content was triturated again until a single cell suspension was achieved. To inhibit TrypLE activity, 1 mL of 10% Foetal Bovine Serum (FBS) (Thermo Fisher Scientific, 10270-106) in DMEM F12 (Thermo Fisher Sientific, 11039047) was added to the well. Trypsinised organoids were recovered by centrifugation (300g, 5 min). To ensure a single cell suspension, the mixture was gently passed through a 40 μm filter (Greiner Bio-One, 542040) to remove aggregates and the filtered cells were washed several times with 3+medium. The number of live cells within the suspension was measured with LUNA-FL fluorescence cell counter (Logos Biosystems, L20001) as detailed in Section 2.2.1. Single cells were resuspended in the desired volume of ice cold Matrigel to obtain a concentration of 400 cell/μL of Matrigel. 50 μL droplets of Matrigel were then seeded onto pre-warmed 6-well plates, approximately 6-7 droplets per well. 6-well plate was incubated at 37^{0}C to allow full polymerisation during 10 min and then 2 mL of 6+ medium supplemented with Y-27632 dihydrochloride (ROCK inhibitor) at 10 μM was added to each well. This medium was replaced every 2-3 days, removing the ROCK inhibitor after initial seeding.

2.1.4 Organoid expansion in bioreactor (CXP1)

For large-scale organoid expansion, the patented bioreactor technology developed by Cellesce Ltd. (www.cellesce.com) was used and here it is referred as CXP1 (Ellis et al. 2018).

2.1.4.1 CXP1 seeding

First, a single cell suspension was generated as described in Section 2.1.3. The number of cells was counted using the LUNA-FL fluorescence cell counter (see Section 2.2.1) and the volume required to provide $3x10^6$ cells was centrifuged (300g, 5 min). The supernatant was aspirated, and the cells were resuspended in 0.9 mL of ice cold 6+ medium. Then, 5.1 mL of ice cold Matrigel was added to the suspension, gently mixed and transferred to a 10 cm tissue culture polystyrene dish (Thermo Fisher Scientific, 10075371). The dish was incubated at 37^0C for 2 hours and then 15 mL of 6+ media supplemented with ROCK inhibitor 10 μM was added on top of the Matrigel layer. The dish was maintained in the incubator at 37^0C for 24 hours.

2.1.4.2 CXP1 assembly and flow

CXP1 technology includes a bioreactor that utilises flow of nutrient-rich media to enhance oxygen delivery to the organoids and facilitates the removal of waste product. Organoids were seeded as single cells on a thin layer of Matrigel and media is pumped across the top of the Matrigel through an inlet pipe, flowing across the bioreactor. The media is then pumped out of the bioreactor through the outlet pipe (Ellis et al. 2018). On day 1 of culture, CXP1 components were sterilised by autoclaving (glassware) or soaking in 70% ethanol (plastic and tubing), and rinsing in sterile PBS. The clean components (media reservoir, waste reservoir, pump tubing, plate lid with connectors) were assembled in a sterile Class II cabinet as shown in Figure 2.1. The media reservoir was filled with 6+ medium at a volume of 16 mL per day remaining of culture. The original lid of the seeded CXP1 dish was replaced with the CXP1 connected lid and the dish was sealed with Parafilm (Thermo Fisher Scientific, 11762644). The inlet and outlet tubing were connected to the pump (205 series Watson Marlow) and it was operated at 0.6 mL/h. The complete CXP1 system was returned to the incubator for the required culture time.

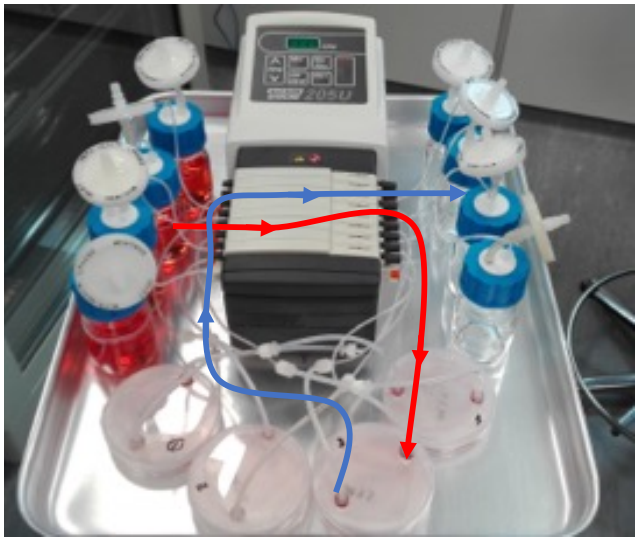

Figure 2.1 Fully assembled CXP1. Four CXP1s were run in parallel

Red arrow indicates the inlet flow direction of 6+ medium from the media reservoir into the dish. Blue arrow indicates the outlet flow direction of medium from the dish into the waste reservoir.

2.1.4.3 CXP1 harvesting

After 5 days of CXP1 culture of Iso50 CRC organoids, the system was removed from the incubator and disconnected. The CXP1 components were removed for cleaning and 10 mL of cold Cell Recovery Solution (Corning, 354253) was added on top of the Matrigel layer and gently mixed. The mixture was incubated on ice for 30 min with periodic agitation to dissolve the Matrigel. After this time, the mixture was diluted up to 15 mL with DMEM F12 and centrifuged at 200g for 5 min to pellet the organoids. Finally, the pellet of organoids was resuspended in 10 mL of DMEM F12.

2.1.5 Freezing of colorectal cancer organoids

For organoid freezing, CRC organoids were cultured as described in Section 2.1.2 for 3 days. Wells were washed with DMEM F12 and the organoid-Matrigel-medium mixture was centrifuged at 200g, 5 min. The pellet of organoids was resuspended in the required volume of Recovery Cell Culture Freezing Medium (Thermo Fisher Scientific, 12648010) to freeze the amount of organoids present in 2 droplets of 50 µl of Matrigel using 200 µL of freezing medium or to freeze 100000 organoids in 200 µL of freezing medium after a CXP1 expansion. 200 µL aliquots of these suspensions were transferred to labelled cryovials (Thermo Fisher Scientific,

10504591), which were frozen in Corning CoolCell FT container (Corning, 432006) to -80^{0}C for 24 hours. After this time, the vials were transferred to freezer boxes and maintained at -80^{0}C.

2.2 General organoid analysis techniques

2.2.1 Cell counting and cell viability assays

The number of single cells in suspension was counted by staining 18 µL of the cell suspension with 2 µL of a dual Acridine Orange/Propidium Iodide (AO/PI) live/dead cell stain (Logos Biosystems, F23001), Then, 10 µL of stained cells was loaded into a PhotonSlide (Logos Biosystems, L12005) and subsequently counted with an automated LUNA-FL fluorescence cell counter (Logos Biosystems, L20001). Total cell concentration, live cell concentration, dead cell concentration, viability and average cell size were annotated.

2.2.2 Organoid viability

Organoids plated in Matrigel or in suspension were stained with Hoechst 0.01 mg/mL (Sigma Aldrich, 33258) and Propidium Iodide 0.01 mg/mL (Sigma Aldrich, P4864) and incubated in the dark for 30 min at room temperature. Hoechst stains all cells and Propidium Iodide is not membrane-permeable staining only dead cells. Organoids were then transferred to a black 96-well plate (Thermo Fisher Scientific, 10530753) and images were acquired using wide-field setting of a Cell Insight CX7, at 4X magnification, and analysed with CellProfiler.

2.2.2.1 Hoechst and Propidium Iodide staining analysis with CellProfiler

Organoid diameter and number of dead cells per organoid was determined using the free and open source CellProfiler software (http://www.cellprofiler.org). A pipeline was set up consisting of the following modules. Images acquired with Cell Insight CX7 were first pre-processed using the 'ColoToGray' module to convert an image with multiple colour channels to two grayscale images corresponding to the Hoechst stain and the Propidium Iodide stain. Then, organoids were then identified automatically using 'IdentifyPrimaryObjects' module with Hoechst images and threshold was set globally through the Otsu (two classes) method.

Subsequently, object clumping was distinguished by 'shape' and object separation was performed by 'shape', as well. Similarly, dead cells were identified automatically using 'IdentifyPrimaryObjects' module with Propidium iodide images and threshold was set globally through the Otsu (two classes) method. After that, object clumping was distinguished by 'intensity' as well as object separation. Then, 'RelateObjects' module was used to associate child objects (dead cells) with parent objects (organoids). Afterwards, to visualise organoid and dead cell identification, outlines of organoids and dead cells were overlaid on pre-processed images with 'OverlayOutlines' and 'SaveImages' modules. Finally, the number of dead cells per organoid and organoid diameter was finally calculated for each organoid with 'MeasureObjectSizeShape' module and exported to a spreadsheet with 'ExportToSpreadsheet' module.

2.2.3 Morphological analysis

Organoid diameter was determined by microscopic analysis. For that, representative images were taken routinely using a Leica DM IL or Olympus CKX53 inverted contrasting microscopes with a Moticam 2000 or GXCAM HiChrome-Met cameras attached, respectively. Images were quantified with CellProfiler for measuring organoid diameter using 'IdentifyPrimaryObjects' module for organoid and single cells identification and subsequently the 'MeasureObjectSizeShape' module for organoid diameter measurement.

2.2.3.1 Hoechst and Phalloidin staining

For morphological analysis, organoids in a 384-well plate were stained with OcellO 2X fix and stain solution composed of Phalloidin-Tetramethylrhodamine B isothiocyanate 0.1 μM (Sigma Aldrich, P1951), Hoechst 1μg/mL (Sigma Aldrich, 33258) and Triton X-100 0.2% (Sigma Aldrich, 93443). Hoechst is a nuclear stain whereas Phalloidin is an actin stain that enables lumen visualisation. Fixation and staining took place overnight at room temperature, whilst organoids within the well were placed on a rocker. Each well was then topped up with PBS and the plate was sealed. Plates were imaged with the confocal Opera Phenix High Content Screening microscope (PerkinElmer) at 40X magnification. Image z-stacks were collected with 50 image stacks taken at 3 μm step per well. Images were analysed with Harmony software to measure organoids diameter and count the number of cells per organoid.

2.2.3.2 Multisizer 3 Coulter Counter analysis

Organoid number and size were measured using a Multisizer 3 (MS3) Coulter Counter (Beckman Coulter, BR-10052B) with a 400 μm aperture. MS3 cuvettes (Meritics, ME0200) were filled with 20 mL of MS3 Buffer, which consist of a mixture 6:4 Isoton II (Beckman Coulter, 8448011):Glycerol (Thermo Fisher Scientific, 11453297). 100 μL of sample was added to the cuvette, mixed by inversion and the measurement was run. Blank measurements were performed with 100 μL of medium and subtracted from the organoid sample measurement.

Number-based particle size distribution was plotted and volume-based particle size distribution was calculated assuming that particles are spheres.

The most widely used averaging procedure for evaluating the mean value of particle diameter in a mixture is the surface-volume diameter, also known as Sauter mean diameter (Kowalczuk & Drzymala 2016). It is defined as the diameter of a sphere having the same external-surface-area-to-volume ratio as the particle and it was calculated with Equation 2.1 using the data obtained with MS3 Coulter Counter.

$$d_{sauter} = \frac{\sum_{i=1}^{n} N_i d_i^3}{\sum_{i=1}^{n} N_i d_i^2} \qquad \text{Equation 2.1}$$

where: N is the number of particles with diameter d.

2.3 Quantitative Reverse Transcription Polymerase Chain Reaction (qRT-PCR)

qRT-PCR was used to quantify relative expression levels of genes within organoids. For qRT-PCR experiments, organoids were plated as single cells as described in Section 2.1.3 and cultured for 3, 5 and 8 days. Three biological replicates (N = 3) were used for all qRT-PCR experiments, as well as three technical replicates (n = 3).

2.3.1 RNA extraction

Culture medium was removed and the droplets of Matrigel with organoids were transferred into a 1.5 mL centrifuge tube using PBS. Organoids were recovered by centrifugation (300g, 5 min) and the pellet was vigorously resuspended in 0.5 mL of cold TRIzol Reagent (Thermo Fisher Scientific, 15596026) and stored at -80^{0}C.

Samples were thawed and incubated at room temperature for 5 min. Then, 150 µL of pure chloroform (Sigma Aldrich, 288306) was added to each sample and vigorously shaken by hand before being incubated at room temperature for 2 min. The samples were then centrifuged at 10000g for 15 min at 4^{0}C to separate the aqueous phase from the organic phase. The aqueous transparent upper phase was transferred in a new tube and equal volume of 70% ethanol, prepared from ethanol absolute (VWR, 20821), was added and mixed to precipitate the RNA. The RNeasy Mini Kit (Qiagen, 74034) was then used to isolate and purify the RNA. The RNA containing solution was added to RNeasy mini spin columns (previously stored at 4^{0}C) and centrifuged at 10000g for 30 sec and the flow through was discarded. The RNA in the column was consecutively washed by adding 700 µL RW1 buffer, centrifuged at 10000g 30 sec and the flow through was discarded. Then, 500 µL of RPE buffer containing ethanol was added to the column and centrifuged at 10000g for 30 sec, the flow through was discarded. Afterwards, 500 µL of 80% ethanol, prepared from ethanol absolute, was added to the column, centrifuged at 10000g 2 min and the flow through was discarded. To dry completely the membrane, a new collection tube was placed and the column was centrifuged at 10000g for 5 min with the lid open. The RNA was eluted by adding 17 µL of Nuclease-free water (Thermo Fisher Scientific, AM9937), pre-warmed to 55^{0}C, directly to the centre of the membrane. After 1 min to let the water diffuse through the membrane, the column was centrifuged at 10000g for 1 min. The

RNA was finally quantified in a 1 μL sample using a NanoDrop 1000 Spectrophotometer (Thermo Fisher Scientific, ND-1000) and RNA quality was assessed based on the ratio of absorbance at 260 nm and 280 nm and results are shown in Appendix C. Samples with a 260/280 ratio below 1.8 were discarded for the qRT-PCR experiment.

2.3.2 Reverse Transcription reaction

cDNA was synthesised from 300 ng of RNA using iScript cDNA Synthesis Kit (Bio-Rad, 1708890). First, the required volume of the eluted RNA was pipetted into strip tubes (Sarstedt, 72.991.002) to get 300 ng of RNA. Then, a mastermix was prepared by mixing 4 μL of 5x iScript reaction mix and 1 μL of iScript reverse transcriptase enzyme. The iScript reaction mix contains a blend of oligo(dT) and random hexamer primers and the iScript is a modified Moloney murine leukemia virus (MMLV) reverse transcriptase. Afterwards, 5 μL of the Master Mix was added to each sample. Reverse transcription was carried out in a DNA Engine Peltier thermocycler (Bio Rad) under the following conditions: 25^0C for 5 min, 42^0C for 30 min, 85^0C for 5 min and finally the sample was hold at 4^0C. After completion of cDNA synthesis, 60 μL of Nuclease-free water was added to each sample to dilute the cDNA (1:4).

2.3.3 Design of real-time qRT-PCR primers

Primers sets for qRT-PCR reactions were designed across exon boundaries to avoid amplification of contaminating genomic DNA and designed to ensure a resulting product between 75 and 200 bp in size. The PrimerBank website (https://pga.mgh.harvard.edu/primerbank/) was used to select a pair of primers specific for each gene. Then, the In-Silico PCR tool from Genome Browser (https://genome.ucsc.edu/cgi-bin/hgPcr) and Primer-Blast tool from NCBI (https://www.ncbi.nlm.nih.gov/tools/primer-blast/) were used to predict the sequence and size of products that would result from a PCR using the primers selected by PrimerBank. Pair of primers were synthesised by Sigma Aldrich. Primer sequences used in this work can be found in Table 2.2.

Table 2.2 Outline of primer sequences used for qRT-PCR

Gene	Forward Primer Sequence	Reverse Primer Sequence	Product size (bp)
LGR5	GAGTTACGTCTTGCGGGAAAC	TGGGTACGTGTCTTAGCTGATTA	112
SOX9	AGCGAACGCACATCAAGAC	CTGTAGGCGATCTGTTGGGG	85
OLFM4	ACCTTTCCCGTGGACAGAGT	TGGACATATTCCCTCACTTTGGA	98
CD44	CTGCAGGTATGGGTTCATAG	ATATGTGTCATACTGGGAGGTG	124
OCT4	GGAGAAGCTGGAGCAAAACC	TGGCTGAATACCTTCCC AAA	165
LYZ	CCGCTACTGGTGTAATGATGG	CATCAGCGATGTTATCTTGCAG	92
MUC2	GCCAGCTCATCAAGGACAG	GCAGGCATCGTAGTAGTGCTG	74
ALPI	CCAGAAGGTCGCCAAGAAC	CAGAGCCAGGTATGGGAAGC	151
KRT20	TTGAAGAGCTGCGAAGTCAG	GAAGTCCTCAGCAGCCAGTT	95
HIF1α	ATCCATGTGACCATGAGGAAATG	TCGGCTAGTTAGGGTACACTTC	125
GLUT1	TCTGGCATCAACGCTGTCTTC	CGATACCGGAGCCAATGGT	94
MKI67	GCCTGCTCGACCCTACAGA	GCTTGTCAACTGCGGTTGC	127
PCNA	GCGTGAACCTCACCAGTATGT	TCTTCGGCCCTTAGTGTAATGAT	76
MCM2	CCGTGACCTTCCACCATTTGA	GGTAGTCCCTTTCCATGCCAT	116
ITGA6	ATGCACGCGGATCGAGTTT	TTCCTGCTTCGTATTAACATGCT	160
CLDN1	CCTCCTGGGAGTGATAGCAAT	GGCAACTAAAATAGCCAGACCT	145
ACTB	AAATCTGGCACCACACCTTC	AGAGGCGT ACAGGGATAGCA	185
GAPDH	TGAAGGTCGGAGTCAACGGA	CCATTGATGACAAGCTTCCCG	148

2.3.4 Gene expression analysis

All qRT-PCR reactions were carried out using MicroAmp optical 384-well reaction plates (Applied Biosystems, 4309849), on a QuantStudio 7 Flex Real-Time PCR system (Thermo Fisher Scientific), using the SensiFAST SYBR Hi-ROX kit (Bioline, BIO-92020) for detection and measurement of relative mRNA abundance. Each reaction was performed in triplicate, with three biological replicates. Typically, the housekeeping genes *ACTB* (β-actin) and *GAPDH* were simultaneously run during each experiment as reference genes.

A primer mastermix composed of 5μL SensiFAST SYBR Hi-ROX, 0.1μL Nuclease-free water and 0.4 μL of primer Forward + Reverse mix was prepared for each primer. Primer Forward + Reverse mix was previously prepared by mixing forward primer and reverse primer to get a final concentration of 10 μM. Then, a cDNA mastermix was prepared by mixing 0.5 μL of

cDNA synthesized (see Section 2.3.2) with 4 μL of Nuclease-free water. Finally, 5.5 μL of primer mastermix was loaded per well into a thin wall 384-well PCR plate and 4.5 μL of cDNA mastermix was subsequently added. Plates were sealed using optically clear sealing film (Applied Biosystems, 4311971), centrifuged and run using the following cycling conditions: 95^0C for 2 min, followed by 40 cycles of 95^0C denaturation for 5 sec and 60^0C annealing for 30 sec. To determine whether a single product had been amplified, a melt curve was run after cycling from 60^0C to 95^0C with a 0.05 ^{0}C/s increment. The melting curve analysis allows to eliminate the possibility of primer contamination or unspecific products.

QuantStudio Real-Time PCR software automatically recorded data and individual threshold cycle (C_T) values per well. The C_T value corresponds to the PCR cycle number at which the fluorescence generated within the reaction crosses the fluorescence threshold, a fluorescent signal significantly above the background fluorescence. The data was examined prior to analysis to ensure amplification of one fluorescent product. Differences between target gene expression between each sample was assessed by comparing the changed in the number of cycles required for the fluorescent product to reach exponential phase, i.e. the higher the abundance of target gene, the lower the number of cycles required for the level of fluorescence to reach the same point in the exponential phase. Analysis was performed on the average of triplicate C_T values, normalised by subtraction of the average of the triplicates of the two housekeeping gene C_T values, generating a ΔC_T value. The $\Delta\Delta C_T$ method, whereby the average of the ΔC_T values of the control condition (D3 sample, i.e. organoids cultured for 3 days) is subtracted from the average of the ΔC_T values of the D5 and D8 conditions (organoids cultured for 5 and 8 days, respectively), was used to generate a $\Delta\Delta C_T$ value. This value was used by the Equation 2.2 to calculate the fold change in expression relative to control (Boretto et al. 2017; Kourkoumpetis et al. 2018).

$$Fold\ change\ in\ expression\ relative\ to\ control\ (D3) = 2^{-\Delta\Delta C_T} \qquad \text{Equation 2.2}$$

2.3.5 Real-time qRT-PCR primer test

Three aspects were assessed to determine that the designed primers were amplifying only one product. For that, a positive organoid sample for the gene of interest was necessary.

First, mRNA was isolated from the organoid samples (see Section 2.3.1). Then, cDNA was synthesised by reverse transcription reaction (see Section 2.3.2). Next, qRT-PCR reactions

were performed (see Section 2.3.4) using the following dilutions of the previously synthesised cDNA: 1:1000, 1:100, 1:10 and non-diluted cDNA. C_T values were plotted vs. the logarithm of the cDNA concentration and primers were considered valid when R-square value of the linear regression was above 0.9. Next, melting curves were assessed and primers were considered valid when a single peak was obtained. The number of qRT-PCR amplified products was also visualised by gel electrophoresis (Section 2.3.6). Results of primer test are shown in Appendix B (*ALPI* and *MUC2* were discarded).

2.3.6 Agarose gel electrophoresis

Agarose gel electrophoresis was used to separate DNA fragments from PCR to visualise them. 2% agarose gel was made by dissolving agarose (Sigma Aldrich, A9414) in 1X Tris base, acid acetic and EDTA (TAE) buffer, prepared from TAE buffer 50X (Thermo Fisher Scientific, B49), and heated in a microwave until boiling. Once boiling, the gel solution was quickly cooled under a running tap and 5 μL of Safe View (NBS Biologicals, NBS-SV) was added per 100 μL of gel solution. The gel was then poured into clean moulds (Bio-Rad) and combs were placed to create wells. Once set, the gel was placed into gel electrophoresis tanks (Sub-Cell GT cell (Bio-Rad)), with their moulds to prevent slippage and covered with 1X TAE buffer. Gel loading dye 6x (Promega, G190A) was added to each qRT-PCR product sample, mixed by pipetting and added to individual well. A molecular weight marker 100 bp (New England Biolabs, N3231S) was added to one well to ensure correct PCR product size. The gel was run at 160 V for approximately 15-20 min using a PowerPac 200 (Bio-Rad). Following this, PCR products were visualised using a transilluminator and images were captured using a Pulnix TM-6EX camera (Jai). Theoretical PCR product sizes are outlined in Table 2.2.

2.4 RNA sequencing

RNA-sequencing (RNA-seq) was used to study organoids transcriptome. Three biological replicates were considered in all RNA-seq experiments.

2.4.1 RNA extraction - RNA quantity and quality.

See Section 2.3.1 for the RNA extraction protocol from organoid samples. The RNA elution was performed by two steps of 15 µL of Nuclease-free water, pre-warmed at 55^0C, directly to the centre of the membrane.

Concentration of RNA samples was assessed by Qubit RNA BR Assay Kit (Thermo Fisher Scientific, Q10211), which is a fluorescence-based quantification kit for samples with a RNA concentration in the range 0.1 µg/mL to 5 µg/mL. For that, the Qubit working solution was prepared by diluting the Qubit RNA BR Reagent 1:200 in Qubit RNA BR Buffer. This assay requires 2 standards and they were prepared individually by mixing 10 µL of each standard with 190 µL of Qubit working solution. Then, 2 µL of each individual sample was mixed with 198 µL of Qubit working solution. Samples and standards were vortexed 2-3 sec and incubated at room temperature for 2 min. Qubit 3.0 Fluorometer (Thermo Fisher Scientific, Q33216) was used to read the fluorescence of the standards first for the instrument calibration, followed by the samples. Samples with a RNA concentration below 10 ng/mL were discarded.

TapeStation 2200 RNA ScreenTape (Agilent) was used to assess RNA integrity. The TapeStation is an automated electrophoresis system for RNA sample quality control that provides the quality assessment with the RNA Integrity Number equivalent (RIN^e), which evaluates total RNA degradation (RIN^e values from 1 to 10, whereby highest quality RNA is assigned with a RIN^e value of 10). RNA samples were prepared by mixing 1 µL of RNA sample with 5 µL of RNA ScreenTape Sample Buffer (Agilent, 5067-5577). Also, 1 µl of RNA ScreenTape Ladder (Agilent, 5067-5578) was mixed with 5 µL of RNA ScreenTape Sample Buffer. Samples and ladder were spin down and vortexed at 2000 rpm for 1 min. For samples and ladder denaturation, tubes were heated at 72^0C for 3 min and consecutively placed on ice for 2 min. Finally, samples and ladder were loaded into a RNA ScreenTape (Agilent, 5067-5576) and introduced in the 2200 TapeStation instrument for electrophoresis. The results

obtained with the TapeStation 2200 RNA ScreenTape are shown in Appendix C and samples with RIN^{e} value below 8 were discarded.

2.4.2 Library preparation

The library preparation was performed by the Genome Research Hub at Cardiff University by Angela Marchbank. For that, Illumina TruSeq Stranded mRNA kit (Illumina, 20020594) was used as per manufacturer's instructions with 390 ng of mRNA. The mechanism of action of TrueSeq Stranded mRNA is based on the purification of the poly-A containing mRNA molecules using oligo-dT magnetic beads for the subsequent first strand cDNA synthesis using reverse transcriptase and random primers. Afterwards, second strand cDNA was synthesised using DNA polymerase I and RNase H, followed by adapter ligation to prepare the ds cDNA for hybridization onto a flow cell.

2.4.3 RNA sequencing

The sequencing was carried out at the Genome Research Hub at Cardiff University by Angela Marchbank. RNA libraries were added to High Output flow cells (Illumina, FC-404-1005) and sequencing was performed on Illumina NextSeq 500 (Illumina, SY-415-1001) to generate single-end reads of 75bp in length. Two runs of 1x75 bp were necessary to ensure all samples have the same number of reads (30 million reads per sample).

2.4.4 Bioinformatics analysis of RNA sequencing data

First, single-end reads were demultiplexed into FastQ files, which allows to determine which sequences came from which samples after they had all been sequenced together with the help of barcodes. Then, FastQ reads were trimmed with Trimmomatic 0.35 software to remove residual Illumina adapter sequences and bases with Phred scores below 15, which corresponds to a base calling accuracy of 97%. The STAR software was used to index the human GRCh38 reference genome and generate a Fasta file. This software was used to map trimmed reads to the reference Fasta index generated previously. Duplicates on the generated BAM files were marked and removed with Picard software. Next, the 'featureCounts' software was used to generate the raw number of read-counts per gene with the GRCh38.89 Ensembl gene build

GTF. Counts per million (CPM) and fragments per kilobase of transcript per million mapped reads (FPKM) were calculated for each gene. Trimming, mapping and CPM and FPKM normalizations were performed by Dr Sumukh Deshpande from the College of Biomedical and Life Sciences Core Bioinformatics and Statistics Team at Cardiff University.

The gene expression analysis was performed with R following the Bioconductor DESeq2 analysis guide. First, the dataset was pre-filtered to remove genes with no counts or very low number of counts because they were considered as not expressed and discarded from the analysis. Genes with less than 5-15 raw counts are usually considered as non-expressed. However, by probability long genes are expected to generate more reads than short genes, therefore non-expressed long genes might not be adequately removed using this criterion and to be able to compare the expression levels across different genes the FPKM need to be considered, which reflects the abundance of each gene normalised based on the gene length. Genes with a FPKM value lower than 0.2-1 are usually considered as non-expressed. Following Bioconductor recommendations, genes with an average of raw counts below 10 and an average of FPKM below 0.5 were removed from the dataset analysed in this work.

Then, the differential expression analysis was performed with the filtered dataset considering if the samples were paired or not using the function DESeq of R, with default 0.1 false discovery rate (FDR). Samples of size-fractionated organoids that derived from the same pull of organoids were considered paired samples. DESeq corrected for multiple hypothesis testing via the Benjamini-Hochberg procedure (Benjamini & Hochberg 1995). For each gene an 'adjusted p-value' was calculated to enable the expected false discovery rate to be used to control for differential expression.

Hierarchical clustering of samples was performed by calculating the sample-to-sample Euclidean distances on the regularised-logarithm transformation data (further explained below), using the function 'dist' in R. Results from hierarchical clustering were represented in binary colour coding heatmaps that grouped together samples with lower sample-to-sample distance, i.e. samples with higher similarity.

Also, principal component analysis (PCA) was performed to identify strong patterns in a complex biological dataset using the 'plotPCA' function of R on the regularised-logarithm transformation data (further explained below). In this type of analysis, the information of a multivariate dataset is reduced into a few variables called principal components (PCs) that capture the variance in the original samples. Most of the variation in the dataset is usually explained by the first two of these PCs (PC1 and PC2), and therefore two-dimensional

representations of PC1 and PC2 are used to visualise the similarity between samples in this type of analysis.

For Euclidean distance and PCA analyses, the data was previously transformed using the regularised-logarithm transformation (rlog function) to stabilise the variance across the mean. This allows to remove the dependence of the variance on the mean, particularly the high variance of the logarithm of count data when the mean is low.

MA-plots were generated to evaluate the distribution of the estimated coefficients in the model. This plots are a helpful tool to identify artefacts and to detect intensity-dependent patterns in the log ratios. On the y-axis, the "M" stands for "minus" – subtraction of log values is equivalent to the log of the ratio – and on the x-axis, the "A" stands for "average". Each gene is represented with a dot and red dots show the differently expressed genes (p-value below 0.1) and black dots show the non-differently expressed genes (p-value above 0.1). Before making the MA-plot, the function lfcShrink was used to shrink the log2 fold changes (LFC) for the comparison of samples using the apeglm shrinking method. The apeglm method for shrinking coefficients is good for shrinking the noisy LFC estimates of reads with low counts or with high coefficient of variation in one or a subset of the conditions (Zhu et al. 2019).

The Broad Institute online tool Morpheus was used to perform a hierarchical clustering to generate a heatmap considering the genes that were significantly differentially express (adj-pvalue below 0.01). The hierarchical clustering was performed applying one minus Pearson correlation clustering method. Also, differentially express genes were assessed for pathway enrichment analysis using Ingenuity Pathway Analysis (IPA) and AmiGO online software to determine whether the sets of genes identified were associated with particular cellular functions. Finally, AmiGO results were visualised using the online tool REVIGO, which from a list of Gene Ontology (GO) terms summarises them by removing redundant GO terms. The remaining terms were visualised as a treemap plot in which a single cluster of genes was represented by each rectangle. Rectangles were then joined into smaller rectangles representing sub-branches. Sizes of the rectangles were proportional to the p-value.

2.5 End-point viability measurement for drug assays

Following Cellesce drug assays protocol, organoids were plated from single cells (see Section 2.1.3) and after 5 days of culture organoids were harvested and frozen. Thawed organoids were then used for drug assays. Three biological replicates were made for all drug assay experiments.

2.5.1 Organoid plating

Vials of organoids were thawed rapidly in a 37^{0}C water bath, and freezing medium was removed by addition of 12 mL of pre-warmed DMEM F12 medium and centrifugation at 100g for 5 min. Organoid pellet was resuspended in 10 mL of Advanced DMEM F12. The number of organoids required for the drug assay was calculated taking into account that each well contained approximately 200 organoids. The volume of organoid suspension necessary to ensure the required number of organoids was centrifuged 100g for 5 min and the pellet of organoids was resuspended in the appropriate volume of ice cold Matrigel.
For end-point viability readings using CellTiter-Glo 3D, organoids were seeded in white, clear bottom 96-well plate (10 µL droplets of Matrigel containing organoids). For end-point morphological analysis, organoids were seeded in black, clear bottom 384-well plate (12 µL droplets of Matrigel containing organoids). 96 and 384-well plates were incubated at 37^{0}C to allow full polymerisation during 10 min and then 50 µL (for the 96-well plate) or 25 µl (for the 384-well plate) of 6+ medium supplemented with ROCK inhibitor at 10 µM was added to each well. Organoids were then left to grow for 48 h before treatment with compounds.

2.5.2 Drug treatments

All compounds stocks were prepared according to manufacturer's instructions typically dissolved in 100% dimethyl sulfoxide (DMSO) (Sigma Aldrich, D8414). Compounds were diluted in 6+medium from stocks, in a 9 point, two-fold dilution series between ranges detailed in Table 2.3. Old media was removed from 96 and 384-well plates by spraying a folded piece of paper tissue with 70% ethanol, then inside the hood the plates were tipped upside down onto the tissue paper, gently tapping to encourage the media to leave the wells. For 96-well plate containing organoids, 5 µl of 10X compound solution was mixed with 45 µL of 6+medium and added to the well. For 384-well plate containing organoids, 25 µL of 2X compound solution was mixed with 25 µL of 6+medium and added to the well. Organoids were exposed to compounds for 5 days before final analysis without medium replacement.

Table 2.3 Compounds and concentrations used in organoids drug assays

Compound	Supplier (catalogue number)	Dilution range (nM)	Fold dilution
LGK974	MedChem Express (HY-17545)	50000 - 200	2
5-Fluorouracil	Tocris (3257)	20000 - 80	2
Trametinib	MedChem Express (HY-10999)	25 - 0.10	2

2.5.3 Cell Titer Glo 3D ATP measurement

After 5 days of compound treatment, organoid viability was measured using an end-point CellTiter-Glo 3D assay in 96-well plates. Each well containing 50 µL of growth medium was treated with 50 µL CellTiter-Glo 3D reagent (Promega, G9683). 50 µL of medium and 50 µL reagent were also added to three wells of the 96-well plate to serve as a control (blank values). Next, plates were shaken vigorously for 5 min to initiate cell lysis and ATP extraction, followed by 25 min slow agitation on a shaker. Luminescence was recorded using BMG FLUOstar plate reader (BMG Labtech, 415-101-AFL). Blank values were subtracted from samples of interest to account for background signal.

2.6 Organoid size fractionation

OcellO B. V. (a biotech company offering Contract Research Organisation (CRO) services for the drug discovery industry) previously indicated that 40-85 µm was an ideal starting size for organoids seeded/treated in their drug treatment assays, and thus the target organoid size range chosen in this work is 40-85 µm.

2.6.1 Fractionation with PluriStrainers

Organoids were cultured from single cells as described in Section 2.1.3. After 5 days of culture, medium was removed and wells were washed with PBS. Then, 1 mL of cold Cell Recovery Solution was added per well and gently mixed. The mixture was incubated on ice for 30 min with periodic agitation to dissolve the Matrigel. The mixture was transferred into a tube and labelled as non-fractionated organoid suspension. 100 µl samples were taken for sizing in MS3 Coulter Counter and imaging (see Section 2.2.3). The non-fractionated organoid suspension

was filtered through an 85 μm PluriStrainer (Cambridge Biosciences, 43-50085-03), previously pre-wet with a 10 mg/mL BSA (Thermo Fisher Scientific, 12827172) solution. The non-fractionated organoid suspension tube was rinsed with DMEM F12 to obtain any remaining organoids and passed through the same 85 μm PluriStrainer. The 85 μm PluriStrainer was flipped over on top of a new 50 mL tube and the filter was rinsed with 10 mL of DMEM F12 to recover organoids larger than 85 μm. The fraction of organoids smaller than 85 μm was filtered through a 40 μm PluriStrainer (Cambridge Biosciences, 43-40040-03), previously pre-wet with a 10 mg/mL BSA solution. The organoid suspension tube was rinsed with DMEM F12 medium and passed through the same 40 μm PluriStrainer. The filtered suspension contained the organoids smaller than 40 μm. To recover the fraction of organoids between 40 μm and 85 μm, the 40 μm PluriStrainer was flipped over on top of a new 50 mL tube and the filter was rinsed with 10 mL of DMEM F12. At the end of the process, three different organoid fractions were obtained: Fraction < 40 μm, Fraction 40-85 μm and Fraction >85 μm.

2.6.2 Fractionation with fluidised bed

2.6.2.1 Fluidised bed assembly

A custom-made glass column (Soham Scientific) was used for organoid size fractionation. Various column setups were designed in this work and the schematics of each setup are shown in Figure 2.2.

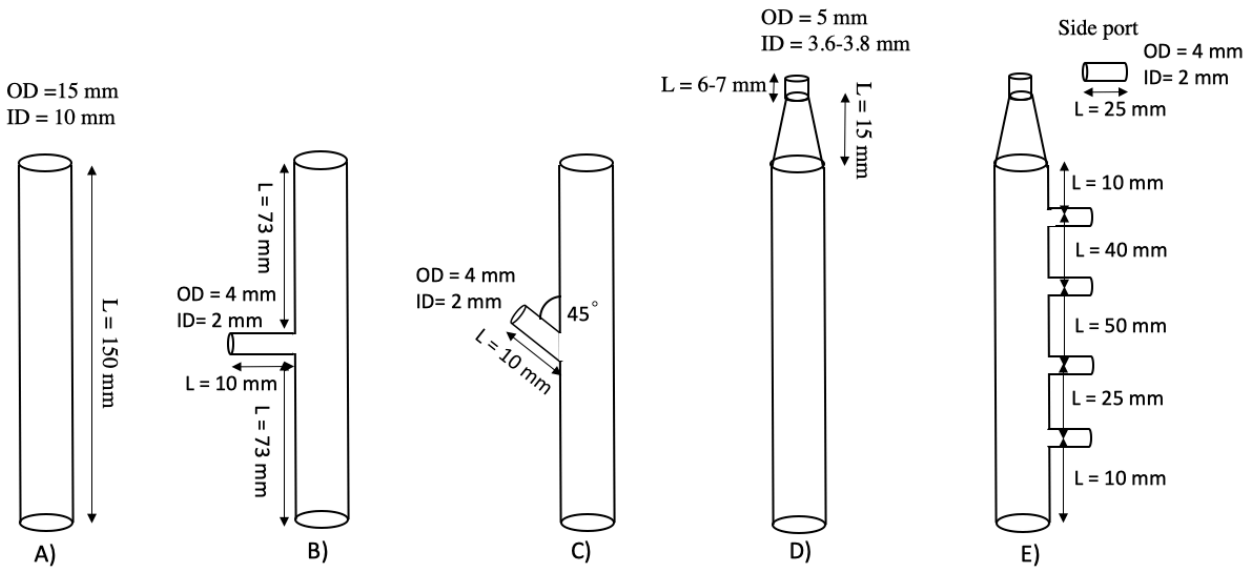

Figure 2.2 Schematic diagram of the different FB setups used in this work

All columns were supplied by Soham Scientific and they were open ended glass columns with borosilicate fired ends. **A.** Initial setup consisted of a simple column. **B.** Horizontal side port was added for organoid loading. **C.** Inclined side port was tested to reduce organoid sedimentation in the side port. **D.** Conical exit at the top of the column was added. **E.** Sampling ports were added at different heights of the column.

Schematic diagram of the final design is specified in Figure 2.3. Column was pre-treated with SigmaCote (Sigma Aldrich, SL2) to reduce cell attachment to the walls. Column, bottom end-piece, media reservoir (Thermo Fisher Scientific) with attached HEPA filter (SLS, FIL5220), dip plastic tubing, and glass beads 0.5 mm diameter (Sigma Aldrich, Z250465-1PAK) were sterilised by autoclaving. Nylon membranes with 10 μm pore size (Sigma Aldrich, NY1002500), PVC pump tubing (Watson Marlow, 980.0142.000), and silicone tubing (Cole-Parmer, 96410-16) were sterilised by soaking in 70% ethanol and rinsing in sterile PBS. The clean components were assembled in a sterile Class II cabinet as shown in Figure 2.3. A Nylon membrane with 10 μm pore size was cut and fit at the bottom of the end-piece. The column was connected to the end-piece and 1 g of glass beads was added from the top of the column, the bed of beads resting on the membrane. These glass beads distributed the flow homogeneously, as demonstrated in this work (see Section 3.2.2.3). The media reservoir was filled with 6+ medium and connected to the pump tubing and the end-piece of the column. Media was pumped with a Watson Marlow 200 Series peristaltic pump (Watson Marlow) using a tubing cassette (Watson Marlow, DEA0081A).

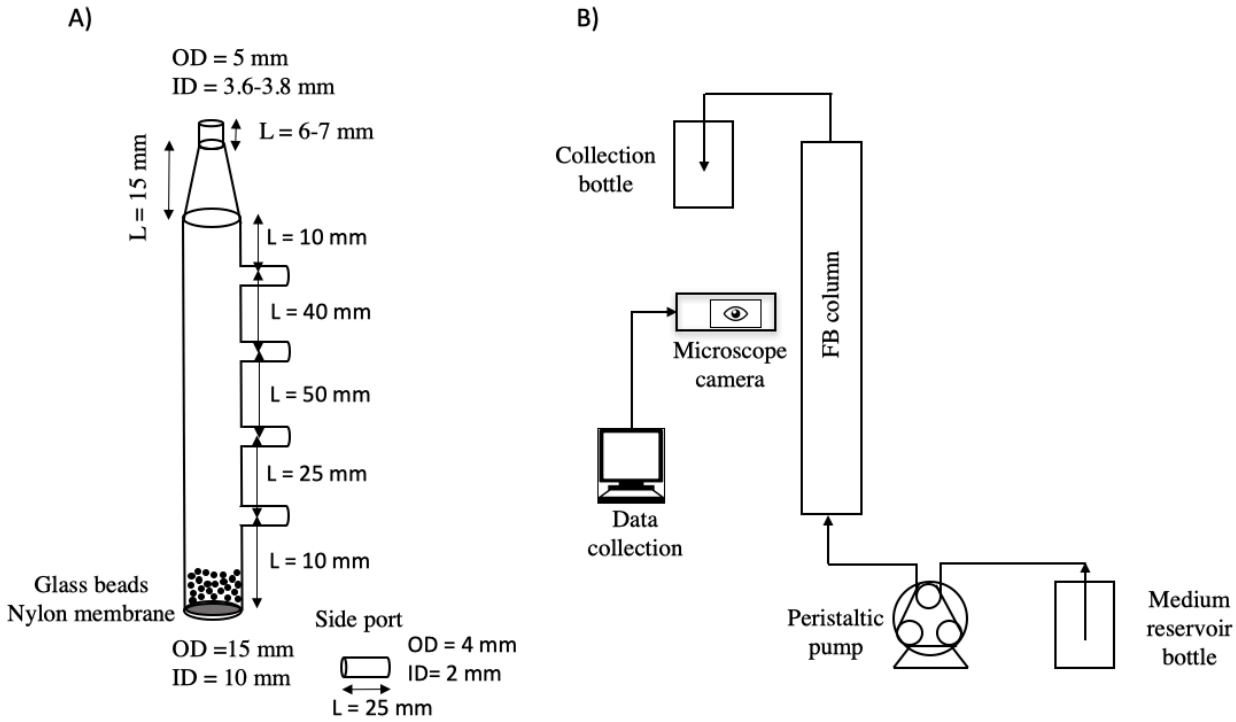

Figure 2.3 Schematic diagram of the final design of the Fluidised Bed for organoid separation

A. Column dimensions. Glass beads of 0.5 mm diameter have distributor function. OD refers to outside diameter. ID refers to interior diameter. **B.** Experimental set-up of a Fluidised Bed for organoids separation.

2.6.2.2 Organoid loading

Organoids were cultured from single cells as described in Section 2.1.3. After 5 days of culture, medium was removed and wells were washed with PBS. Then, 1 mL of cold Cell Recovery Solution was added per well and gently mixed. The mixture was incubated on ice for 30 min with periodic agitation to dissolve the Matrigel. The mixture was transferred into a tube and labelled as non-fractionated organoid suspension. 100 µl samples were taken for sizing in MS3 Coulter Counter and imaging (see Section 2.2.3). The non-fractionated organoid suspension was loaded into the column through the top using a 10 mL syringe (SLS, SYR1040) and a 27G needle (Thermo Fisher Scientific, 10204444). Then, the column exit was connected to a silicone tubing that collect the fluidisation output into a 15 mL falcon tube. The fractionation was run at different flowrates by changing the revolutions per minute (RPM) of the pump. Once the collection tube was full, it was changed for a new one. Images and videos of organoid fluidisation were taken using a microscope camera (Veho, VMS-004) and a light source.

2.6.2.3 Organoid harvesting

Aside from organoids collected in the tubes, organoids in the column were also harvested. For that, the pump was switched off and the content of the column was transferred into a 50 mL falcon tube. 100 µL samples were taken for sizing in MS3 Coulter Counter and imaging (see Section 2.2.3). Also, organoid viability was assessed after the fractionation by LUNA-FL fluorescence cell counter (see Section 2.2.1).

2.6.3 Separation performance indicators

Based on MS3 Coulter Counter data and microscope image quantification results, the composition of the Initial mixture and separated fractions was calculated as the number of particles of a specific size range divided by the total number of particles of the fraction (Equation 2.3). 'Chosen fraction' consist either of Initial mixture or the suspension outlet streams, i.e. for PluriStrainer filtration: Fraction < 40 µm, Fraction 40-85 µm and Fraction > 85 µm, and for FB separation: Top fraction and Column fraction.

$$Composition_i\% = \frac{[No.\ particles_i]_{chosen\ fraction}}{[Total\ No.particles]_{chosen\ fraction}} \cdot 100 \qquad \text{Equation 2.3}$$

where *i* corresponds to the particle size ranges.

In order to assess the separation performance of the system under investigation, different indexes were considered in this work, such as purity, recovery, enrichment and separation efficiency. Purity (P) corresponds to the composition formula for the target size range (Equation 2.4).

$$Purity_{target}\% = \frac{[No.\ particles_{target}]_{chosen\ fraction}}{[Total\ No.particles]_{chosen\ fraction}} \cdot 100 \qquad \text{Equation 2.4}$$

Recovery is defined as the number of particles of a size range in a separated fraction divided by the number of particles of the same size range in the Initial mixture (Equation 2.5).

$$Recovery_i\% = \frac{[No.particles_i]_{chosen\ fraction}}{[No.particles_i]_{Initial\ mixture}} \cdot 100 \qquad \text{Equation 2.5}$$

where *i* corresponds to the different particle size ranges.

Enrichment (E) entails dividing the ratio of the target particle number to non-target particle number in a specific fraction of outlets divided by the ratio of the target particle number to non-target particle number in the Initial mixture (Equation 2.6).

$$Enrichment = \frac{[No.particles_{target}{:}No.particles_{non-target}]_{chosen\ fraction}}{[No.particles_{target}{:}No.particles_{non-target}]_{Initial\ mixture}} \qquad \text{Equation 2.6}$$

Separation efficiency (SE) is defined as the number of particles of a specific size range in a separated fraction divided by the total number of particles recovered of the same size range (Equation 2.7).

$$Separation\ efficiency\ \% = \frac{[No.particles_i]_{chosen\ fraction}}{[No.particles_i]_{all\ fractions}} \cdot 100 \qquad \text{Equation 2.7}$$

where *i* corresponds to the particle size ranges.

2.7 Hydrodynamic characterisation of a fluidised bed containing organoids

Hydrodynamic characterisation of a fluidised bed containing human CRC organoids was performed by experimentally determining minimum fluidisation velocity and terminal falling velocity of the system. Three biological replicates were performed for the determination of both parameters.

Table 2.4 summarises physical properties of Iso50 CRC organoids and 6+ medium, required for theoretical calculation of minimum fluidisation velocity and terminal falling velocity.

Table 2.4 Physical properties of Iso50 CRC organoids and 6+ medium

Property	Value	Source
Iso50 CRC organoids density	1132 kg/m^3	CRC organoid density assumed equal to large intestine density reported by (Erdmann & Gos 1990; Mcintosh & Anderson 2010)
6+ medium density	1023.44 kg/m^3	Experimentally determined
6+ medium viscosity	0.001011 Pa·s	Assumed equal to DMEM +Glutamax viscosity reported by (Hinderliter et al. 2010)

2.7.1 Minimum fluidisation velocity (u_{mf})

See Section 1.5.1.2 for u_{mf} definition. $u_{mf}$was experimentally determined by measuring pressure drop and bed height while decreasing the superficial fluid velocity. Instead of fluidisation-defluidisation experiment, only defluidisation was carried out to avoid organoid aggregation when starting from a packed bed. Organoids were first cultured from single cells as detailed in Section 2.1.3.

2.7.1.1 Pressure drop measurements

Pressure drop across the bed of organoids was measured at different superficial velocities using a Scanivalve Digital Sensor Array (Evolution, DSA3217). Two plastic T junctions were connected to the tubing connected to the column, one before the column inlet and other after the column outlet. One tubing was connected from each of the two T junctions to two ports of the pressure sensor. Before running the experiment with CRC organoids, 6+ medium was passed through an empty column to get the background pressure drop (ΔP_B) due to the distributor: polytetrafluoroethylene (PTFE) frit 50 μm (Kinesis, 006FR-10-50) and Nylon membrane 10 μm. Then, the measurements were performed with 1 million CRC organoids to get the pressure drop of the whole system (ΔP_W). The total pressure drop due to the bed of organoids (ΔP), was calculated by subtracting ΔP_B from ΔP_W. Sampling frequency was 0.5 Hz and 150 points were taken for each fluid velocity, which were averaged subsequently.

Superficial velocities tested are detailed in Table 2.5. ΔP data was plotted against superficial velocity and u_{mf} was considered the intersection of the pressure drop line for packed bed with the horizontal line for fully fluidised bed.

Table 2.5 Superficial velocities (u) tested for u_{mf} determination in a column of 10 mm inner diameter

RPM (min^{-1})	Q (mL/min)	u (m/s)	RPM (min^{-1})	Q (mL/min)	u (m/s)	RPM (min^{-1})	Q (mL/min)	u (m/s)
15	1.105	2.35E-04	8	0.580	1.23E-04	1	0.054	1.15E-05
14	1.030	2.19E-04	7	0.505	1.07E-04	0.9	0.047	9.91E-06
13	0.955	2.03E-04	6	0.430	9.12E-05	0.8	0.039	8.32E-06
12	0.880	1.87E-04	5	0.355	7.52E-05	0.7	0.032	6.72E-06
11	0.805	1.71E-04	4	0.280	5.93E-05	0.6	0.024	5.13E-06
10	0.723	1.55E-04	3	0.204	4.34E-05	0.5	0.017	3.54E-06
9	0.655	1.39E-04	2	0.129	2.74E-05	0	0.000	0.00

2.7.1.2 Bed height measurements

During the experimental procedure detailed in Section 2.7.1.1, bed heights were measured by taking pictures of the bed of organoids at every superficial velocity, using a microscope camera (Veho, VMS-004), a light source and a millimetre scale attached to the column. Images were then manually analysed in ImageJ software by measuring the distance from the bottom to the top of the bed of organoids. Bed height was plotted versus fluid velocity and u_{mf} was considered the intersection of the horizontal line that define packed bed and the fully fluidised line.

2.7.2 Terminal falling velocity (u_0)

CRC organoids cultured from single cells (see Section 2.1.3) were loaded into the column from the top and their free settling motion was recorded with a microscope camera (Veho, VMS-004). Microscope camera was placed 2 cm above the distributor to avoid recording the deceleration of particles when reaching the bottom of the column and 11 cm below the top of the column to allow organoids to accelerate and reach their u_0. A millimetre scale was attached

to the wall of the column and the time needed by the organoids to cover a 5 mm distance was measured. The fall of 50 organoids was analysed for each experiment and data was averaged.

2.7.3 Flow distribution

Trypan blue (Logos Biosystems, T13001) was used to visualise the flow distribution inside the column. A pulse of 2 μL of trypan blue was injected in the continuous upwards flow of PBS, using a T connection upstream of the column inlet. PBS was chosen, instead of 6+ medium, for the flow distribution experiments to ensure a high contrast between the blue dye and the colourless PBS. After injection, pictures of the column were taken every 5 seconds and the pattern of flow distribution of the dye inside the column was analysed.

2.7.4 Particle velocity and particle trajectory (PIVlab)

Organoid velocity and particle trajectories inside the FB were analysed with PIVlab, a particle image velocimetry software developed in Matlab environment by Thielicke *et al*. (Thielicke & Stamhuis 2014). First, image video sequences were loaded into the software and the section of interest was selected for individual frame. Then, images were processed by Wiener2 denoise filtering and analysed by direct cross correlation (DCC) algorithm. Images were calibrated and heat maps were generated by plotting the velocity magnitude and the vector direction.

2.8 Statistical analysis

Unless stated otherwise, experiments were performed using biological and technical triplicates. Raw data obtained was analysed using Microsoft Excel for Mac to calculate means, standard deviation and coefficient of variation. Means and standard deviations were used for graphical representation of the data using GraphPad for Mac software.

2.8.1 Generation of drug dose response curves

Data analysis was performed using GraphPad software by applying a nonlinear regression (curve fit) and the equation log (inhibitor) vs. normalised response (variable slope) for dose –

response curve generation. Half maximal inhibitory concentration (IC_{50}) values were obtained from GraphPad after fitting the model.

2.8.2 PCR data analysis

A Student unpaired t-test was used to determine significant differences between two data sets and one-way analysis of variance (ANOVA), with Tukey test post-hoc analysis was used for comparison between three or more independent samples. Statistically significant differences were determined when p-values were less than or equal to (≤) 0.05 (* indicates $p \leq 0.05$, ** indicates $p \leq 0.01$, *** indicates $p \leq 0.001$).

2.8.3 Minimum fluidisation velocity statistical analysis

Mean and standard deviation of the pressure drop readings of the bed of organoids were calculated using Equation 2.8.

$$\Delta P_W - \Delta P_B = \left(\mu_{\Delta P_W} - \mu_{\Delta P_B}\right) \pm \sqrt{s_{\Delta P_W}^2 + s_{\Delta P_B}^2} \qquad \text{Equation 2.8}$$

where: $\mu_{\Delta P_W}$is the mean of the pressure drop of the whole system, $\mu_{\Delta P_B}$is the mean of the pressure drop of the background, $s_{\Delta P_W}$ is the standard deviation of the pressure drop of the whole system and $s_{\Delta P_B}$ is the standard deviation of the pressure drop of the background.
Standard deviations (s) of the pressure drop of the three biological replicates was calculated using Equation 2.9.

$$s = \sqrt{\frac{(n_1-1)s_1^2+(n_2-1)s_2^2+(n_3-1)s_3^2+n_1(\mu_1-\mu)^2+n_2(\mu_2-\mu)^2+n_3(\mu_3-\mu)^2}{n_1+n_2+n_3-1}} \qquad \text{Equation 2.9}$$

where: n_1, n_2, n_3 are the sample size of biological replicates 1, 2 and 3, respetively, s_1, s_2, s_3 are the standard deviation of biological replicates 1, 2 and 3, respectively, μ_1, μ_2, μ_3 are the mean of biological replicates 1, 2 and 3, respectively and μ is the mean of the pressure drop of the three biological replicates.

3. Fluidised bed design for organoid separation

3.1 Introduction

So far, several authors have described FB designs for coal and mineral sand size-based separation (see Table 1.2 for references), however, no previous research has investigated cell size separation using a FB. Here, an organoid size-based separation using a FB is proposed to reduce batch-to-batch variability and increase drug assays reproducibility.

When fluidising particles in a FB, it is necessary to determine what range of flowrates allow fluidisation (u_{mf}) and also, what flowrates will begin to carry the particles out of the top of the column (u_0). Organoid suspension is characterised by being a multi-component system and particle size distribution (PSD) has a strong effect on the hydrodynamic parameters (u_{mf} and u_0) of a FB (Geldart 1972; Gauthier 1999; Jiliang et al. 2013; Rasteh et al. 2018). Geldart *et al*. (1972) noted that fluidisation characteristics are independent of an average diameter, especially for systems with the same average diameter but different PSD (Geldart 1972). Similarly, Gauthier *et al*. (1999) performed an experiment with four different PSD cases: narrow-cut, Gaussian-type, binary mixture and flat (wide), but all of them with the same Sauter mean diameter. They found that Gaussian-type and narrow-cut PSDs hardly segregate and have the same u_{mf}, which means that u_{mf} from Gaussian-type PSDs can be estimated from classical correlations proposed for uniform-sized particles. On the other hand, binary mixtures and flat PSDs always segregate and have a very different hydrodynamic behaviour from narrow-cut PSDs, although similar to each other (Gauthier 1999). For ideal mono-component systems, in which all particles have the same size and density, fluidisation of the whole bed occurs at a certain fluid velocity, as described in Section 1.5.1.2. However, for multi-component systems, in which particles present a variety of sizes and/or densities, fluidisation is achieved in a range of fluidisation velocities. U_{mf} of multi-component beds is more complicated to be determined due to particle segregation leading to an already fluidised part of the bed on the top, while the lower part might still be in the packed bed stage. Two characteristic velocities are needed to describe the fluidisation of multi-component systems, corresponding to the incipient fluidisation of the most fluidisable particles (u_{if}) and the complete fluidisation of the whole set of particles in the mixture (u_{cf}) (Figure 3.1) (Gauthier 1999).

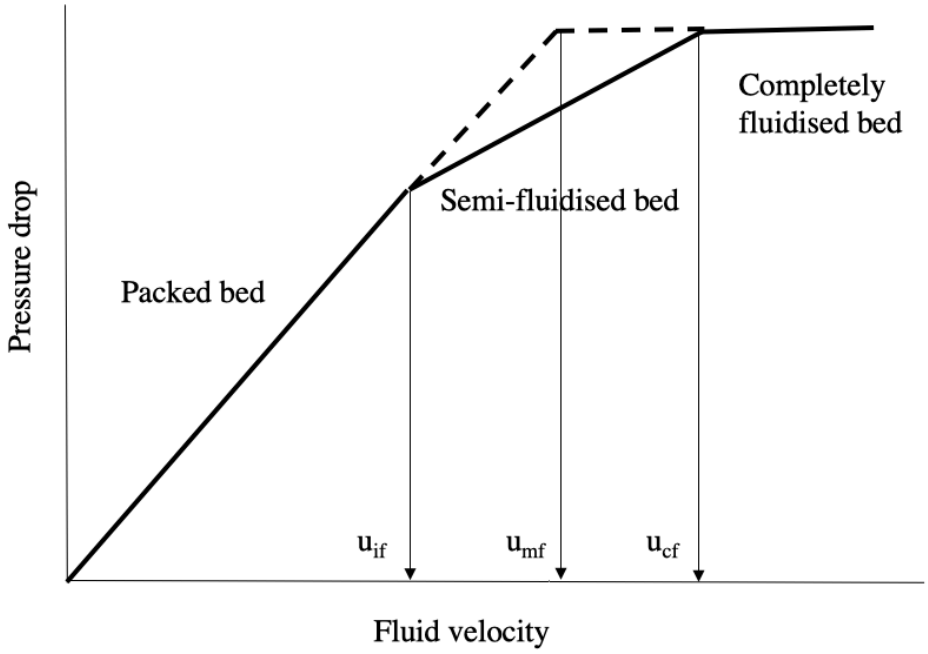

Figure 3.1 Pressure drop vs. fluid velocity for a mono-component system (dashed line) and for a multi-component system (solid line)

For mono-component systems, pressure drop increases linearly with fluid velocity during the packed bed stage. When the u_{mf} is reached particles start to fluidise and the pressure drop of the system keeps constant while increasing fluid velocity. For multi-component systems, pressure drop increases linearly with fluid velocity until the u_{if} is reached. At this velocity, the smaller/lighter particles start to fluidise while the larger/heavier particles are settled at the bottom of the bed. During this particle rearrangement, pressure drop increases with fluid velocity but with a lower slope. Once the u_{cf} is reached, the whole bed of particles is fluidised and pressure drop is maintained constant with the increase of fluid velocity. (Gauthier 1999)

Apart from experimental determination of u_{mf} and u_0, several theoretic, semi-empirical and empirical correlations have been described to predict these values. The most widely accepted equations for u_{mf} prediction are the Ergun equation (Equation 3.1) and Carman-Kozeny equation (Equation 3.2), which are semi-empirical correlations that depend on coefficients obtained from experimental data. Simplifications of Ergun equation were then proposed by Wen-Yu (Equation 3.4), Lucas (Equation 3.5) and Foscolo (Equation 3.7), among others. The Stokes' law (Equation 3.8) allows u_0 prediction by balancing drag, buoyancy and gravity forces that act on a spherical particle falling through a viscous fluid. Also, empirical correlations that rely on fitted parameters have been developed by several authors for u_0 calculation. The correlations used in this study are presented in Table 3.1 for u_{mf} and Table 3.2 for u_0.

Table 3.1 Minimum fluidisation velocity correlations and applicability claims. Dimensionless numbers used in these equations are specified in Table 3.3

Correlation	Equation	Applicability claims	Reference	Equation number
Ergun	$\frac{1.75}{{\varepsilon_{mf}}^3} {Re_{mf}}^2 + \frac{150(1-\varepsilon_{mf})}{{\varepsilon_{mf}}^3} Re_{mf} = \frac{d_p^3 \rho_f (\rho_s - \rho_f)}{{\mu_f}^2} g$	Re_{mf}>15, packed beds	(Coulson & Richardson 2002)	Equation 3.1
Carman-Kozeny	$u_{mf} = \frac{d_p^2 (\rho_s - \rho_f) g}{180 \mu_f} \frac{{\varepsilon_{mf}}^3}{(1-\varepsilon_{mf})}$	Re_{mf}<15, spheres	(Coulson & Richardson 2002)	Equation 3.2
Richardson-Zaki	$u_{mf} = u_0 {\varepsilon_{mf}}^n$ $Re < 0.2 \quad n = 4.65 + 19.5 \frac{d_p}{D}$ $0.2 < Re < 1 \quad n = \left(4.35 + 17.5 \frac{d_p}{D}\right) Re^{-0.03}$ $1 < Re < 200 \quad n = \left(4.45 + 18 \frac{d_p}{D}\right) Re^{-0.1}$ $200 < Re < 500 \quad n = 4.45\, Re^{-0.1}$ $Re > 500 \quad n = 2.39$	N depends on Reynolds number Spherical particles	(Richardson & Zaki 1997)	Equation 3.3
Wen-Yu	$Re_{mf} = [33.7^2 + 0.0408\, Ar]^{1/2} - 33.7$	10^{-2}<Re_t<10^4	(Coulson & Richardson 2002)	Equation 3.4
Lucas	$Re_{mf} = [29.5^2 + 0.0357\, Ar]^{1/2} - 29.5$	Round particles	(Lucas et al. 1986)	Equation 3.5
Rowe	$u_{mf} = \frac{0.00081(\rho_p - \rho_f) g d_p^2}{\mu_f}$	Water flow through a regular array of spheres. Equation derived from Stokes law	(Rowe & Nienow 1975)	Equation 3.6
Foscolo	$Re_{mf} = \left[25.74^2 + \frac{{\varepsilon_{mf}}^{4.8}}{0.336} Ar\right]^{1/2} - 25.74$	Spheres	(Foscolo et al. 1983)	Equation 3.7

Table 3.2 Terminal falling velocity correlations and applicability claims. Dimensionless numbers used in these equations are specified in Table 3.3

Correlation	Equation	Applicability claims	Reference	Equation number
Stokes	$u_0 = \frac{1}{18}\frac{(\rho_s - \rho_f)gd_p^2}{\mu_f}$	Spheres with 10^{-4}<Re<0.2	(Coulson & Richardson 2002)	Equation 3.8
Zigrang	$u_* = \frac{\left[\left(14.51 + 1.83{d_*}^{3/2}\right)^{1/2} - 3.81\right]^2}{d_*}$	Spheres, solid-liquid systems	(Zigrang & Sylvester 1981)	Equation 3.9
Turton	$u_* = \left[\left(\frac{18}{d_*^2}\right)^{0.824} + \left(\frac{0.321}{d_*}\right)^{0.412}\right]^{-1.214}$	Sphere	(Turton & Clark 1987)	Equation 3.10
Hartman	$\log(Re_t) = -1.2738 + 1.04185\log(Ar) - 0.060409(\log(Ar))^2 + 0.0020226(\log(Ar))^3$	0.01<Re_t<16000	(Hartman et al. 1994)	Equation 3.11
Khan & Richardson	$u_* = \frac{\left(2.33{d_*}^{0.054} - 1.53{d_*}^{-0.048}\right)^{13.3}}{d_*}$	Spheres with 0.1<Ar<10^{10}	(Khan & Richardson 1989)	Equation 3.12

Table 3.3 Dimensionless numbers used in equations presented in Table 3.1 and Table 3.2

Dimensionless number	Equation	Reference	Equation number
Reynolds number	$Re = \frac{\rho_f\, u\, d_p}{\mu_f}$	(Coulson & Richardson 1999)	Equation 3.13
Reynolds number at minimum fluidisation	$Re_{mf} = \frac{\rho_f\, u_{mf}\, d_p}{\mu_f}$	(Coulson & Richardson 2002)	Equation 3.14
Reynolds number at terminal falling velocity	$Re_t = \frac{\rho_f\, u_0\, d_p}{\mu_f}$	(Coulson & Richardson 2002)	Equation 3.15
Archimedes number	$Ar = \frac{{d_p}^3\, g\, \rho_f\left(\rho_s - \rho_f\right)}{{\mu_f}^2}$	(Coulson & Richardson 1999)	Equation 3.16
Dimensionless terminal velocity	$u_* = u_0\left[\frac{{\rho_f}^2}{g\mu_f\left(\rho_s - \rho_f\right)}\right]^{1/3}$	(Turton & Clark 1987)	Equation 3.17
Dimensionless particle diameter	$d_* = d_p\left[\frac{g\,\rho_f\left(\rho_s - \rho_f\right)}{{\mu_f}^2}\right]^{1/3}$	(Turton & Clark 1987)	Equation 3.18

In summary, a FB is proposed for the size-based separation of organoids in order to reduce batch-to-batch variability and increase the reproducibility of drug sensitivity assays. This chapter focuses on the design aspects, as well as the hydrodynamic characterisation of the system.

The key aims for this chapter were:

(i) To determine experimentally the minimum fluidisation and terminal falling velocities of Iso50 CRC organoids and to compare experimental values with correlations found in literature.

(ii) To design a fluidised bed for organoid size-based separation and optimise the operating conditions, including organoid loading strategy, distributor material and design, as well as the reduction of organoid aggregation.

(iii) To validate the designed FB for size-based separation using polystyrene beads with similar physical properties to Iso50 CRC organoids and to calculate the separation performance indicators.

3.2 Results and Discussion

3.2.1 Hydrodynamic characterisation of a fluidised bed containing CRC organoids

3.2.1.1 Minimum fluidisation velocity of CRC organoids

As a starting point for the design of a fluidised bed for organoid size-based separation, it was necessary to experimentally determine u_{mf} for Iso50 CRC organoids. From the different CRC organoid lines available in Dale lab, Iso50 CRC was the organoid line used for this work because it was the most well characterised in terms of growth kinetic, plating efficiency and organoid viability when the project was started. Iso50 CRC organoids were expanded in the CXP1 bioreactor from single cells, and harvested after 5 days of culture. The time of culture was optimised to harvest the major volume of organoids with a size range between 40 μm and 85 μm (see Section 5.2.1). Organoid size was assessed with MS3 Coulter Counter and the PSDs obtained are shown in Figures 3.2A and 3.2B for number-based and volume-based PSD, respectively. As seen in Figure 3.2A, 68% of the particles have a diameter below 20 μm which indicates the large amount of single cells present in the organoid solution recovered from CXP1. This could be explained due to the low organoid formation efficiency (3%) of Iso50

CRC organoids (Badder 2017b). On the other hand, a volume-based distribution (equivalent to mass distribution for constant density) fitted with a Gaussian distribution overlapped in the plot and showed a wider distribution (Figure 3.2B). Organoids with a dimeter between 40-100 μm represented around 75% of the total weight of organoids (Figure 3.2.C). Similarly, Goto-Silva *et al*. (2019) showed that the size distribution of brain organoids grown on a shaker for 30 days resembled a Gaussian fit (Goto-Silva et al. 2019). The Sauter mean diameter (Equation 2.1) of organoids cultured for 5 days was 55.59 ± 0.63 μm (expressed as average ± standard deviation).

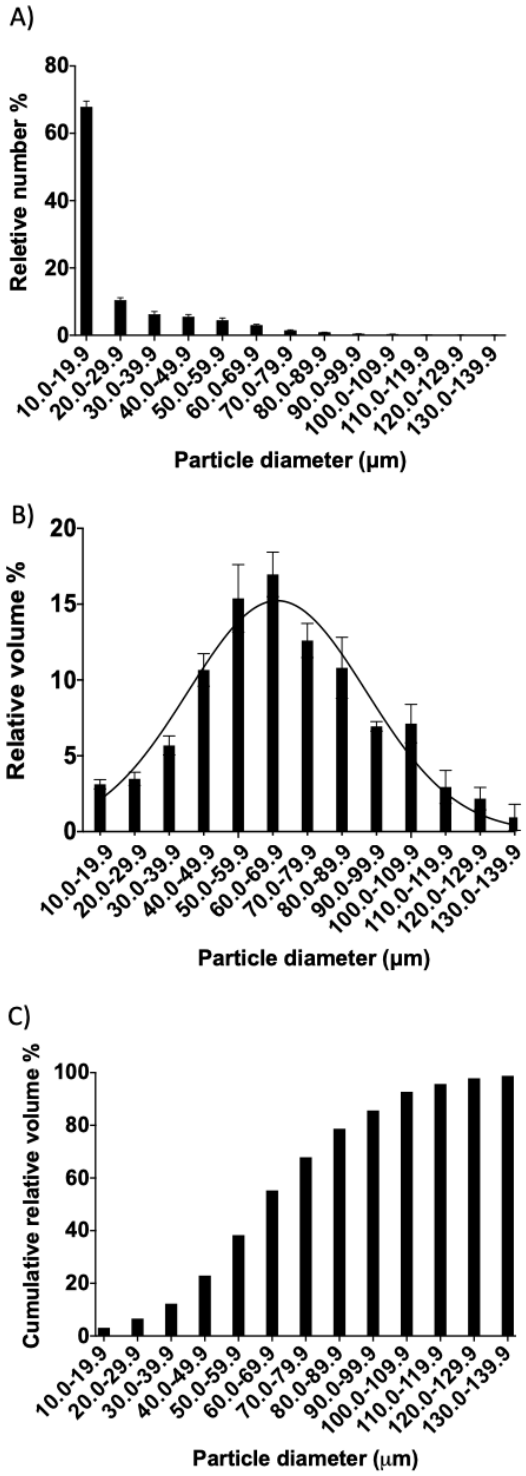

Figure 3.2 Particle size distribution of Iso50 CRC organoids harvested after 5 days of culture in CXP1 measured with MS3 Coulter Counter

A. Number-based particle size distribution. **B.** Volume-based particle size distribution with Gaussian distribution fitting (R^2=0.9013). **C.** Cumulative volume-based particle size distribution. Error bars represent standard deviation, n=3, N=3.

To measure u_{mf}, one million Iso50 CRC organoids were loaded into the column and pressure drop and bed height measurements were taken during a de-fluidisation experiment to avoid organoid aggregation when starting from a packed bed. Before organoid loading, pressure drop of the background (ΔP_B) was measured with media for each superficial velocity. As seen in Figure 3.3A, pressure drop increased while increasing fluid velocity and the pressure drop associated to the background presented a linear relation with the fluid velocity and lower values than the pressure drop of the whole system (ΔP_W). Figure 3.3B shows the pressure drop of the bed of organoids after subtracting ΔP_B from ΔP_W and three zones were identified, corresponding to packed, semi-fluidised and fluidised bed. With the increase of superficial velocity of the liquid, the pressure drop increased linearly in packed bed until u_{if}. U_{if} corresponded to 7.50 x 10^{-5} m/s and at that point, single cells and small organoids started to fluidise. After passing u_{if}, the slope of the curve had a slight variation, but with the general trend of increase while the liquid velocity increased. This stage presented a spatial rearrangement of organoids with different sizes; single cells and small organoid began to fluidise while larger organoids remained in the packed bed giving rise to a semi-fluidised bed. Pressure drop increased with superficial velocity until u_{cf}, which corresponded to 1.40 x 10^{-4} m/s. Upon rearrangement, pressure drop decreased slightly and approached almost a constant level where all organoids were fluidised. U_{mf} is defined as the intersection of the pressure drop line for the packed bed and the horizontal line for the fully fluidised bed, which corresponded to a u_{mf} value of 7.90 x 10^{-5} m/s for Iso50 CRC organoids cultured for 5 days.

Bed heights during de-fluidisation experiment were measured with a microscope camera as explained in Section 2.7.1.2 to determine u_{mf} with an alternative method. This was based on visual observation of the bed expansion using a millimetre scale attached to the column. Then, ImageJ was used for offline analysis to obtain the height of the bed of organoids as a function of the superficial velocity. As reported by do Nascimiento *et al*. (2016), a constant height was expected while the organoids were on the packed bed state, followed by a linear increase once the organoids reached their u_{mf} (do Nascimento et al. 2016). Figure 3.3C shows the normalised bed height $(H-H_0)/H_0$, where H_0 is the final bed height (at u = 0 m/s), versus superficial velocity. Organoid bed height was not constant at low superficial velocities, in fact it increased almost 25 times from 3.54 x 10^{-6} m/s to 7.50 x 10^{-5} m/s, which meant that a packed state was not reached. This was not in agreement with the pressure drop data reported above in which a clear change of slope was detected at 7.50 x 10^{-5} and 1.40 x 10^{-4} m/s. Bed height measurements with

ImageJ were prone to error because of researcher's judgment, while pressure drop measurements relied on the accuracy and precision of the sensor.

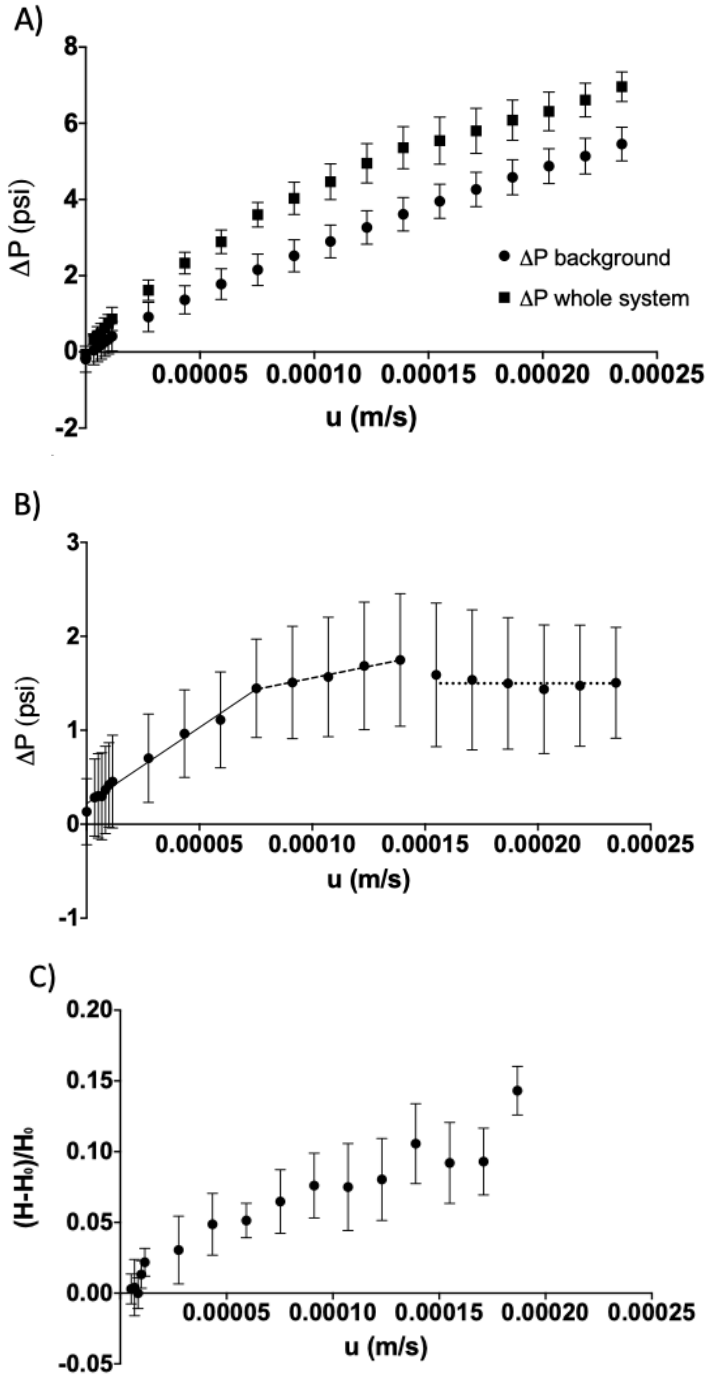

Figure 3.3 Minimum fluidisation velocity determination of one million Iso50 CRC organoids cultured for 5 days in CXP1 with a de-fluidisation experiment

A. Pressure drop vs. superficial velocity for a column without organoids (background, ΔP_B) and with Iso50 CRC organoids (whole system, ΔP_W). **B.** Pressure drop vs. superficial velocity of the bed of organoids calculated as: ΔP_W- ΔP_B. **C.** Normalised bed height vs. superficial velocity for Iso50 CRC organoids. Error bars represent standard deviation, for A and B: n=150, N=3; for C: n=3, N =2. Standard deviation in B was calculated with Equation 2.8 and Equation 2.9.

In order to predict u_{mf} many empirical and semi-empirical correlations have been proposed to estimate the u_{mf} of a particles in a FB. Table 3.4 shows the predicted values obtained for some correlations considering the physical properties of Iso50 CRC organoids and 6+ medium described in Table 2.4. Furthermore, it was considered a ε_{mf} of 0.4 and particle diameter of 10 μm for single cells, 55.59 μm for Sauter mean diameter (experimentally determined) and 140 μm for large organoids. Also, these predicted values were compared with experimental u_{mf} (7.90 x 10^{-5} m/s) and the ratios Experimental u_{mf}/Predicted u_{mf} are presented in Table 3.4. Experimental u_{mf} was around 36 times greater than the predicted u_{mf} values for particles with a diameter equal to the Sauter mean diameter of the organoid suspension. On the other hand, experimental u_{mf} was closer to predicted u_{mf} values of larger organoids (140 μm). This could mean that the correlations used are not a suitable model for the organoid system or, as observed during the experiments, organoids aggregated inside the FB forming larger particles and the velocity required to fluidise these organoid clumps was higher than the predicted u_{mf} for single organoids. Additionally, particle diameter has a significant influence in u_{mf} correlations (to the power of 2 or 3), so that small deviations between the theoretical and experimental diameter could affect notably the predicted values.

Table 3.4 Predicted values of u_{mf} for Iso 50 CRC organoids and Experimental u_{mf}/Predicted u_{mf}ratio

Equations used for this correlations are presented in Table 3.1. Particle diameter of 10 μm, 55.59 μm and 140 μm were considered for single cells, Sauter mean diameter and large organoids, respectively. Organoid density was assumed 1132 kg/m^3, fluid density and viscosity 1023.44 kg/m^3 and 0.001011 Pa·s, respectively and ε_{mf} was considered 0.4. Applicability claims are specified in Table 3.1 for each correlation.

	Predicted u_{mf} (m/s)			**Exp u_{mf} / Pred u_{mf}ratio**			
Correlation	**Single cells**	**Sauter mean diameter**	**Large organoids**	**Single cells**	**Sauter mean diameter**	**Large organoids**	**Applicability**
Ergun	7.48 x 10^{-8}	2.31 x 10^{-6}	1.47 x 10^{-5}	1055.71	34.16	5.39	No
Carman-Kozeny	6.24 x 10^{-8}	1.93 x 10^{-6}	1.22 x 10^{-5}	1266.85	41.00	6.46	Yes
Richardson-Zaki	8.10 x 10^{-8}	2.31 x 10^{-6}	1.26 x 10^{-5}	974.85	34.22	6.27	Yes
Wen-Yu	6.37 x 10^{-8}	1.97 x 10^{-6}	1.25 x 10^{-5}	1240.17	40.13	6.33	Yes
Lucas	6.37 x 10^{-8}	1.97 x 10^{-6}	1.25 x 10^{-5}	1240.70	40.15	6.33	Yes
Rowe	8.52 x 10^{-8}	2.63 x 10^{-6}	1.67 x 10^{-5}	926.82	29.99	4.73	Yes
Foscolo	7.48 x 10^{-8}	2.31 x 10^{-6}	1.47 x 10^{-5}	1055.78	34.16	5.39	Yes

3.2.1.2 Terminal falling velocity

Terminal falling velocity was a crucial parameter for the design of a FB for organoid size-based fractionation because organoids were elutriated from the top of the column once they reached their u_0. As shown in Equations 3.8-3.12, u_0 depends on particle diameter and particle density, fluid density and fluid viscosity, however, particle diameter had the major impact on organoids size-based separation assuming that the other parameters remained constant in the system (organoid density, fluid density and fluid viscosity values considered are summarised in Table 2.4). U_0 of different size organoids was measured by recording their free settling motion with a microscope video camera. Iso50 CRC organoids were cultured for different times (4, 5, 6, 7 and 8 days) in order to get a wide range of organoid sizes with Sauter mean diameters of 54.00 ± 2.98 μm, 58.96 ± 3.48 μm, 61.36 ± 3.33 μm, 66.70 ± 1.50 μm and 71.79 ± 4.21 μm, respectively. Figure 3.4 shows the relationship between u_0 and Sauter mean diameter for experimental values obtained with Iso50 CRC organoids and also for some correlations that can be applied under the specific experimental conditions. U_0 showed a quadratic dependence with organoid diameter for both, experimental and predicted values, but with a higher quadratic coefficient in the first case. U_0 of small organoids agreed with predicted values, however at larger organoid diameters, experimental u_0 increased more sharply than calculated u_0. At larger organoid diameters, wall effects could contribute to deviations on predicted u_0, however, this phenomenon has an opposite effect. Confining walls reduce the settling velocities by exerting a retardation on particles due to the upward flow of the liquid displaced by particles moving downwards and the narrower the gap between the walls and the particle, the more pronounced is the effect. On the other hand, organoid density was assumed constant for different organoid sizes, however Iso50 CRC organoids did not present a solid homogeneous structure and they were characterised by a hollow branching lumen containing mucous and cellular debris that could affect organoid density (Williamson et al. 2018). Dead cells could present different density from live cells due to loss of osmotic control or total lysis (Luby et al. 2017). It is well-known that dead cells and cell debris can be removed from cell suspension by centrifugation and supernatant removal due to their lower density compared to viable cells, e.g. purification of hepatocytes (Meng et al. 2010), however, other authors have reported opposite results. Lamina propia mononuclear cells from the colon were purified with Percoll gradients and dead cells lay at the bottom indicating a larger density compared to live cells (Weigmann et al. 2007). Altogether, accumulation of dead cells in organoid lumen could

contribute to organoid density variations with organoid size. Also, larger organoids might present higher amounts of intestinal mucous secreted by Goblet cells that could interfere with the organoid density, since mucous membrane present a higher density than large intestine (Park et al. 2018). Measuring single-cell or single-organoid densities is challenging due to the limitations to determine mass and volume at the level of a single cell or single organoid. Furthermore, no references about organoid densities have been found in the literature. Experimental u_0 values were used to calculate organoid densities applying Stokes equation (Equation 3.8) and the results are shown in Figure 3.5 . Calculated organoid densities ranged from 1100 kg/m^3 for 54 µm organoids to 1170 kg/m^3 for 72 µm organoids, with the reported value for large intestine density, 1132 kg/m^3 (Erdmann & Gos 1990; Mcintosh & Anderson 2010) therefore in this range. These variations on organoid density could be associated to the different proportion of live/dead cells or the ratio cells/lumen of different size organoids.

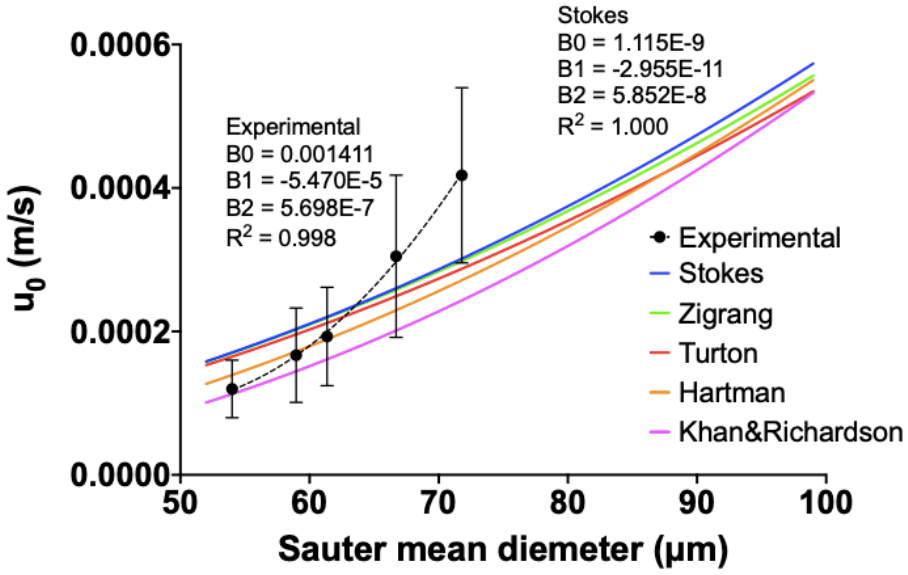

Figure 3.4 Terminal falling velocity of different size Iso50 CRC organoids.

Experimental u_0 values (represented as black dots) were measured by recording organoids free settling motion with a microscope video camera. Different size organoids were obtained by culturing them for 4, 5, 6, 7 and 8 days which corresponds to Sauter mean diameters of 54.00 ± 2.98 µm, 58.96 ± 3.48 µm, 61.36 ± 3.33 µm, 66.70 ± 1.50 µm and 71.79 ± 4.21 µm, respectively. The black dashed line corresponds to the quadratic regression ($Y=B0+B1\cdot X+B2\cdot X^2$) for the experimental u_0 values and the coefficients and goodness of that regression are specified. Coloured solid lines correspond to the correlations indicated on the legend, whose equations are summarised in Table 3.2 and the coefficients for the Stokes equation are indicated ($Y=B0+B1\cdot X+B2\cdot X^2$). Error bars represent standard deviation, n=50, N=3.

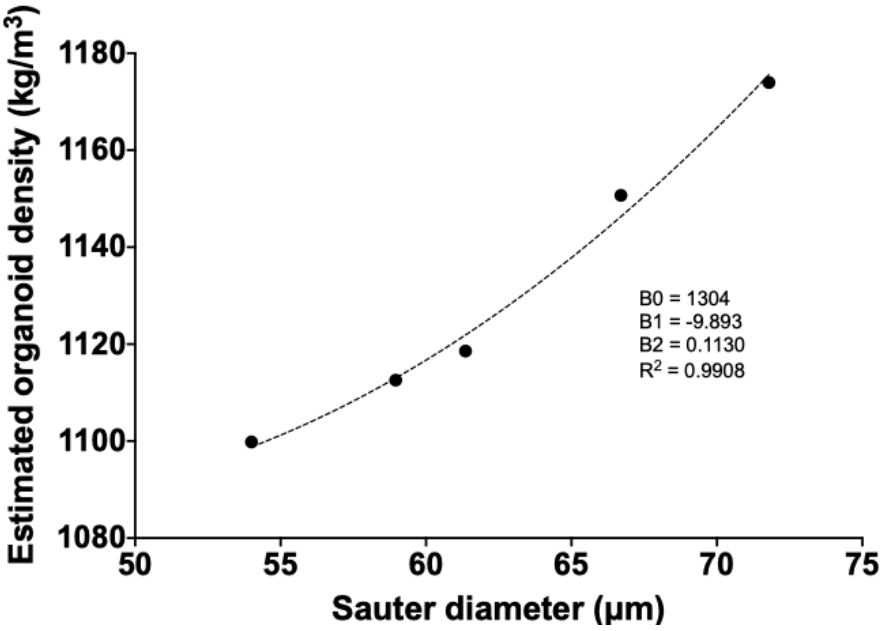

Figure 3.5 Estimated organoid density vs. Sauter mean diameter

Experimental u_0 was used to calculate organoid density using Stokes equation (Equation 3.8). Black dashed line corresponds to the quadratic regression ($Y=B0+B1 \cdot X+B2 \cdot X^2$) for the calculated organoid density and the coefficients and goodness of the fit are specified.

In summary, the hydrodynamic parameters of Iso50 CRC organoids were determined experimentally, obtaining u_{mf}= 7.90 x 10^{-5} m/s and u_0=1.67 x 10^{-4} m/s for organoids cultured during 5 days. These results were of utmost importance for the design of a FB for organoid size-based separation to determine the range of flowrates that allow fluidisation, as well as, the range of velocities that carry the particles out of the top of the column. The following section describes the process of design of a FB for organoid size-based separation.

3.2.2 Fluidised bed design for organoid separation

Once u_{mf} and u_0 were experimentally determined, the design of a FB bed for organoids size-based separation was focused on several influential parameters, such as the liquid velocity, column shape, distributor design and loading method. In this study, the target size range was selected based on the recommended organoid size by OcellO B. V., a biotech company offering CRO services for the drug discovery industry (www.ocello.nl). They have indicated that 40-85 µm diameter is the ideal size range of organoids seeded/treated in their drug treatment assays. This information was given from a verbal communication from Ocello based on their commercial experience as to the optimal size range required to allow growth and cellular

responses in the presence of drugs while overcoming issues with low plating efficiency for single cells. Taking into account the target size range and the PSD of organoids recovered after 5 days of culture (Figure 3.2A), it was clear that the important point was to remove the large amount of single cells present in the organoid solution, as around 70% of the particles were smaller than 20 μm. Detailed below is the design process of a FB for organoid size-based separation considering column shape, operating conditions and limitations of the process, such as organoid aggregation.

3.2.2.1 Organoid aggregation

The simplest setup was chosen as the starting point for the design of a FB for organoid size-based separation, as described in Figure 2.2A. This consisted of a glass column with 0.01 m diameter and 0.15 m height. A peristaltic pump introduced the fluidising medium (6+ medium) at the desired flowrate through a 10 μm pore size PTFE frit, located at the bottom of the column. The PTFE frit had two functions: to prevent organoid loss through the inlet tubing and to distribute evenly the flow inside the column. Iso50 CRC organoids harvested after 5 days of culture were recovered from Matrigel with Cell Recovery Solution and washed with DMEM F12. Then, organoids were loaded into the column from the top and 6+medium was pumped into the column at 0.4 mL/min (8.49×10^{-5} m/s) from the bottom. As seen in Figure 3.6, organoids formed a big aggregate at the bottom of the column, so the fluid velocity was increased gradually to accomplish organoid fluidisation. At 2.97×10^{-4} m/s was clearly seen that organoids fluidised as a big aggregate containing all the organoids of the bed instead of single organoid fluidisation. Also, when the clump of organoids was lifted away from the bottom of the column, air bubbles were detected at the top surface of the PTFE frit. Organoid aggregation was expected to have a significant impact on the hydrodynamic behaviour. Due to the larger diameter of the aggregate compared to a single organoid, a higher fluid velocity was needed to fluidise the aggregate than a single organoid. This agreed with published data that described bed de-fluidisation when particle clumping occurs during fluidisation, as well as the requirement of higher fluidisation velocities to break up the clumps of particles (Ng &Tan 2006).

Recently, a few studies have identified brain organoid clumping as an issue associated with the organoid contact with one another over an extended period of time (Bergmann et al. 2018; Ao et al. 2020). Keeping them under rotation throughout the cultivation to maintain them in

suspension has been proposed as a solution to prevent brain organoids from merging (Bergmann et al. 2018). Moreover, Ao *et al*. (2020) have developed a microfluidic device that incorporates a physical size restriction to avoid random brain organoid merging (Ao et al. 2020). Although, references to CRC organoid clumping were not found in the scientific literature, this work showed aggregation of Iso50 CRC organoids when introduced into a FB column (Figure 3.6). It was expected that organoid fluidisation was limited due to their aggregation, and therefore this issue needed to be solved in order to achieve an organoid size-based separation. For that, organoid aggregation was assessed considering biological, physicochemical and mechanical implications on the process.

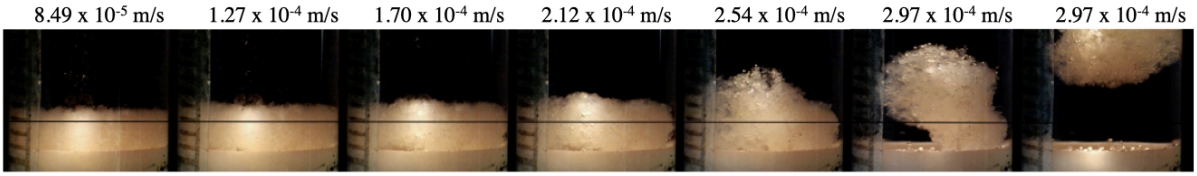

Figure 3.6 Iso50 organoid aggregation at the bottom of the FB column

Iso50 CRC organoids recovered from Matrigel after 5 days of culture were loaded into the FB column. 6+ medium was introduced through the bottom of the column with a peristaltic pump and the fluid velocities are indicated on top of each image. Representative images of the organoid aggregation at the bottom of the FB column are shown for 3 biological replicates. Millimetre scale was attached to the column and a horizontal black line helped to visualise the increase of bed height.

3.2.2.1.1 Biological implications

Tight, adherens and gap junctions connect adjacent intestinal epithelial cells laterally and seal them to act as a permselective barrier preventing the entry of harmful molecules and microbes while still allowing the selective passage of dietary nutrients, ions and water (Pearce et al. 2018). Cells forming an organoid are held together through cell-to-cell interactions along their lateral surface (Fatehullah et al. 2013). For instance, cadherins, an adherens junction protein, bind to the actin microfilaments of the cytoskeleton of the cell to maintain epithelial integrity and organisation (Zhang 2005). Cadherins are calcium-dependent adhesion molecules, thus the divalent cation chelating agent EDTA (2 mM) was added to the medium to bind the calcium present in Advanced DMEM F12 ($CaCl_2$ 1.05 mM), which is a well-established disaggregation technique (Freshney 2010). Removal of Ca^{2+} could reduce cell-cell adhesion, however, EDTA failed in preventing the aggregation of Iso50 CRC organoids based on microscope video

camera recordings (Figure 3.7A). This suggested that the mechanism by which Iso50 CRC organoids clumped together was not based on cadherins junctions between organoids.

On the other hand, organoid clumping could occur due to environmental stress (e.g. centrifugation steps for washing with DMEM F12 after the Cell Recovery Solution treatment) that accelerates cell death rate within the sample, resulting in the release of free DNA and cellular debris from dying cells that clump neighbouring cells together (Reichard & Asosingh 2018). DNase I (0.05 mg/mL) plus $MgCl_2$ (10 mM) was added to the medium to minimise the presence of free-floating DNA fragments. This reduced partially the aggregation but not completely (Figure 3.7B), which could indicate that free-floating DNA was not the only mechanism involved in organoid aggregation and further research was required to prevent the clumping.

Also, the presence of traces of Matrigel in the organoid suspension could contribute on enhancing organoid aggregation because organoids could stick to Matrigel. Therefore, three washing steps with DMEM F12 + 10% FBS (200g, 5 min) after treatment with Cell Recovery Solution were included in the protocol to avoid the presence of Matrigel in the final organoid suspension.

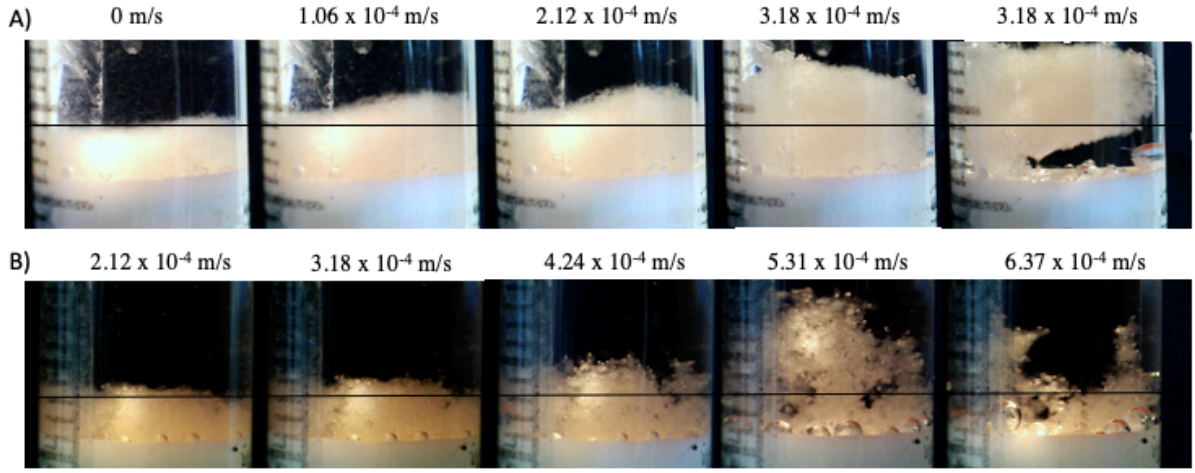

Figure 3.7 Iso50 CRC organoid aggregation during fluidisation

To reduce organoids aggregation at the bottom of the FB column during fluidisation, the fluidising media was supplemented with EDTA (2 mM) in **A.** and DNase I (0.05 mg/mL) plus $MgCl_2$ (10 mM) in **B.** The supplemented fluidising media was introduced through the bottom of the column with a peristaltic pump and the fluid velocities are indicated on top of each image. Representative images of 2 biological replicates (N = 2) for each treatment show that these treatments failed in preventing organoid aggregation at the bottom of the FB column. Millimetre scale was attached to the column and a horizontal black line helped to visualise the increase of bed height.

3.2.2.1.2 Physicochemical interactions

Adding dispersing agents was thought of as a possible solution to avoid organoid aggregation. Dextran sulphate (DS), Pluronic F-68 (PF-68) and Anti Clumping Agent (ACA) from Gibco were tested at different concentrations and different exposure times to reduce organoid aggregation. None of these agents have previously been used with organoids but they have been applied to mammalian cell cultures to avoid their aggregation. DS, a highly sulphated polyanion, has been successfully applied to mitigate CHO cells aggregation and to maintain single cell suspension of BTI-TN5B1-4 insect cells (Dee et al. 1997). This polymer increases the electrostatic repulsion and reduces the cell aggregation. Moreover, it was reported that DS treatment decreased the expression of the cell-cell adhesion factor, cadherin-11, which prevented cell adhesion (Takagi 2005). PF-68 is a non-ionic surfactant, commonly used as shear protectant in animal and insect cell cultures, that reduces cell hydrophobicity. This accounts for the decreased cell-to-cell interactions and as a consequence fewer cellular aggregates were observed in PF-68-supplemented mammalian cell cultures (Tharmalingam et al. 2008). ACA from Gibco is an animal origin-free, with a chemically defined formulation that has been used with CHO cells to alleviate the aggregation problem (Pan 2018).

Iso50 CRC organoids cultured for 5 days were recovered from Matrigel and treated in a 6-well plate with DS (10 μg/mL, 100 μg/mL and 1000 μg/mL), PF-68 (10 μg/mL, 100 μg/mL and 1000 μg/mL) and ACA (1:1000, 1:500 and 1:100) during different times (10, 30, 60 and 120 min) under agitation with a rocker at 300 rpm. Figure 3.8 shows the organoid suspension for the highest concentration of each dispersing agent at different exposure times. Also, a control (Blank) was included in which no dispersing agent was added. Relevant differences were not detected between treated and non-treated organoids. Furthermore, it was found that the dispersing agents tested did not dissociate the cells of an organoid producing a single cell suspension. Organoid aggregation increased over time as clearly seen after 120 min of treatment and the use of dispersing agents to avoid organoid aggregation was discarded. Thus, the organoid aggregation cause seemed to be different from the physicochemical interactions aimed to be tackled with theses dispersing agents, i.e. electrostatic interaction in the case of DS and hydrophobic interaction for PF-68.

Another physicochemical interaction that could promote cell clumping is the van der Waals interaction, which is an ubiquitous attractive force between all molecules, and thereby might contribute to cell adhesion (Leckband & Israelachvili 2001; Kendall et al. 2011). However, van

der Waals force has a short-range of action and although it becomes very significant for nanoparticles fluidisation, where aggregation is commonly observed, it can be neglected at the micrometre-scale of an organoid (Hakim et al. 2005; Dee et al. 1997).

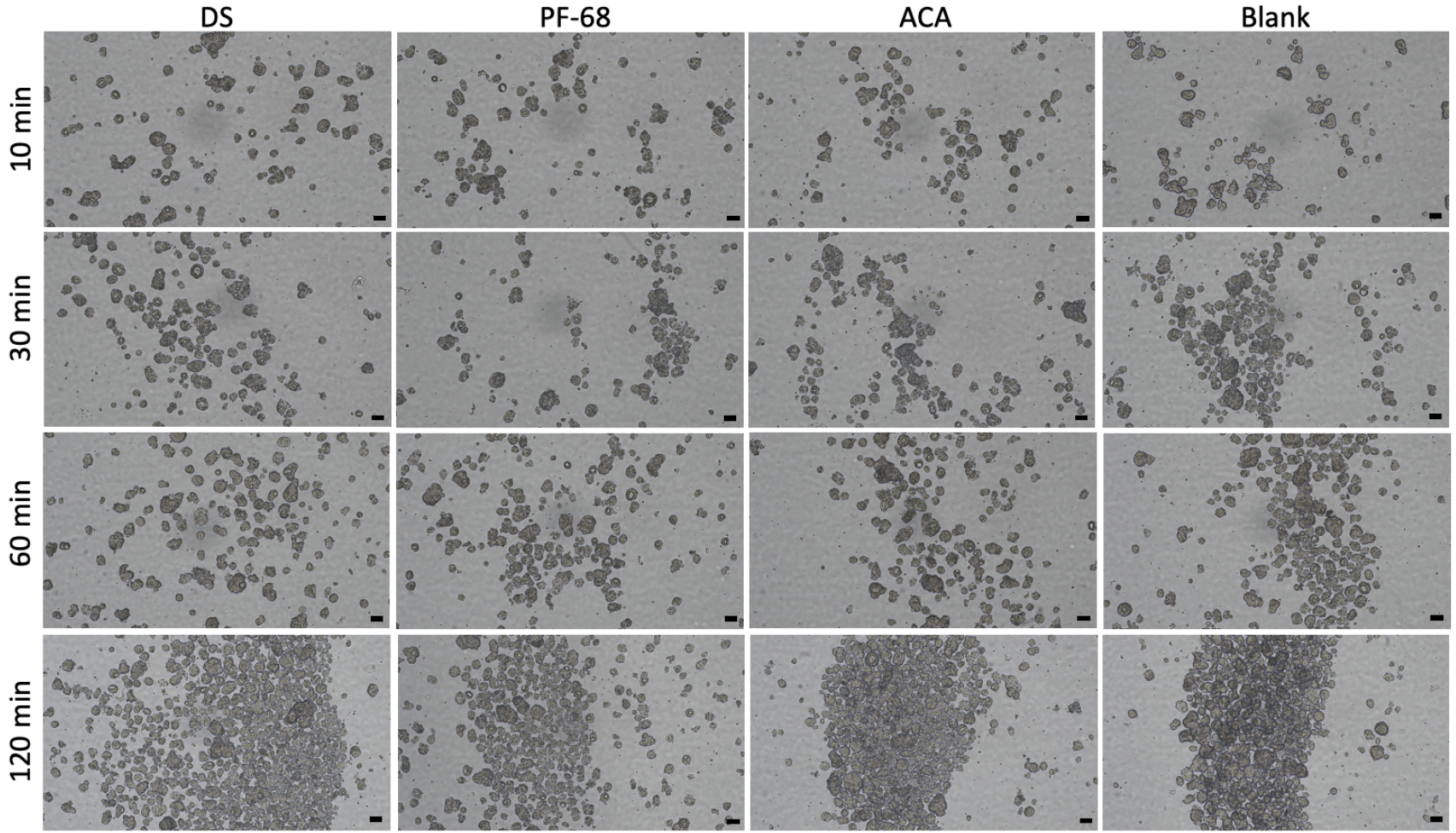

Figure 3.8 Organoid treatment with dispersing agent to avoid organoid aggregation

Iso50 CRC organoids were cultured for 5 days, harvested from Matrigel and treated in a 6-well plate with DS (1 mg/mL), PF-68 (1mg/mL) and ACA (1/100) during different exposure times (10, 30, 60 and 120 min) under agitation with a rocker (300 rpm). Blank corresponds to a control in which no dispersing agent was added. Representative images of 2 biological replicates (N = 2) are shown. Scale bars correspond to 100 μm.

3.2.2.1.3 Mechanical features

A mechanical approach to solving the problem of organoid aggregation was suggested based on the bioreactor design for brain organoid culture. Qian *et al*. (2018) designed a bioreactor for culturing brain organoids in suspension using a spin shaft and adjusting the spinning speed to the minimal speed required to lift the organoids in constant suspension without damaging them (90 rpm for 3.5-4 mL culture volume) (Qian et al. 2018). Similarly, Bergmann *et al*. (2018) cultured brain organoids under rotation to avoid organoid merging (Bergmann et al. 2018). Constant suspension prevents organoid aggregation, therefore, here we suggest maintaining organoid in suspension and load them continuously into the FB column through a side port (Figure 2.2B), similar to the particles loading system in the Reflux Classifier (Doroodchi et al. 2006; Galvin & Dickinson 2013). Organoid solution was kept in a bottle and a magnetic stirrer bar at 300 rpm was used to maintain organoids in a homogeneous suspension. Then, a peristaltic pump was used to transfer the organoid solution from the feed bottle into the FB column through a side port as shown in Figure 3.9.

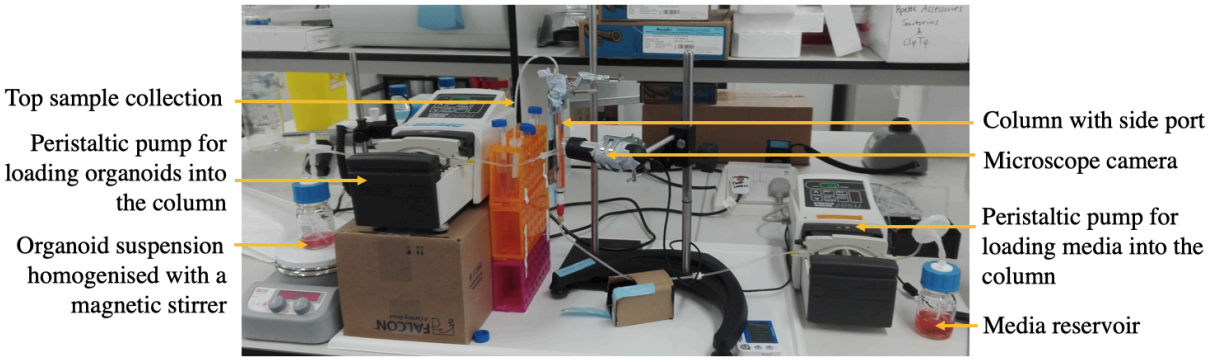

Figure 3.9 Fluidised bed set up with two peristaltic pumps for organoid and 6+medium continuous loading

To reduce organoid aggregation, CRC organoids were maintained in suspension using a magnetic stirrer (300 rpm) and continuously loaded into the column through a side port with a peristaltic pump. Also, 6+ medium was pumped into the FB through the bottom of the column.

As shown in Figure 3.10, organoid aggregation was mostly reduced with continuous agitation using a magnetic stirrer inside the feed bottle. Agitation velocity was optimised to lift organoids and avoid organoid breakage. This result agreed with the only references to organoid aggregation in the literature and the approach suggested by them to solve that limitation (Qian et al. 2018; Bergmann et al. 2018).

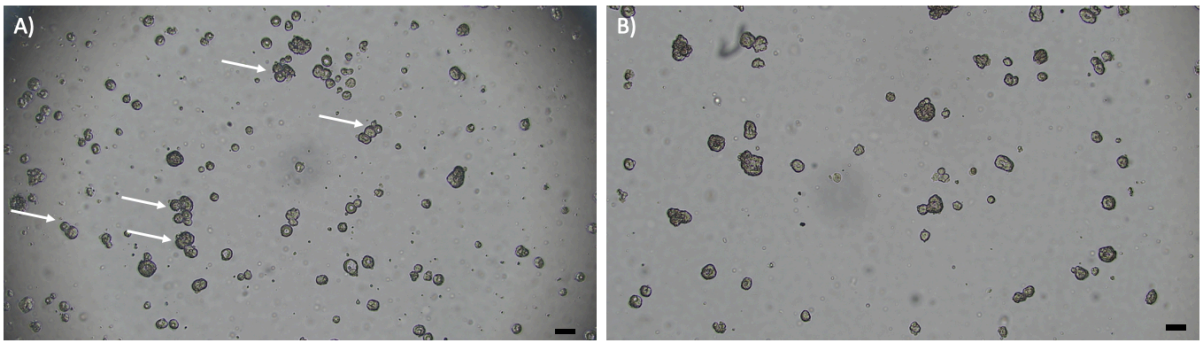

Figure 3.10 Organoid aggregation is reduced with magnetic stirring

A. Organoid suspension under static conditions. White arrows point to organoid aggregates. **B.** Organoid suspension under agitation with a magnetic stirrer at 300 rpm. Representative images from 5 biological replicates are shown (N = 5). Scale bars correspond to 100 μm.

In summary, organoid aggregation was identified as a major limitation for the design of a FB for organoid size-based separation. Biological, physicochemical and mechanical aspects affecting the system were studied and the preferred solution to reduce organoid aggregation was to maintain organoids in suspension with a magnetic bar stirrer and use a peristaltic pump to load them into the FB column. Nevertheless, further studies should include a design of experiments to optimise the methods described above aiming at minimising the aggregate formation using microscopic analysis and PSD as responses. Moreover, it would be required to perform an investigation of how organoid viability is affected by the different strategies described previously, although a negative impact would not be expected because the concentrations tested of EDTA, DNase I, DS, PF-68 and ACA have been previously applied to mammalian cell cultures and viability issues have not been reported (Jing et al. 2014; Tharmalingam et al. 2008).

3.2.2.2 Organoid loading strategy

As detailed in Section 3.2.2.1, maintaining organoids in suspension with a magnetic stirrer reduced organoid aggregation. Accordingly, organoids needed to be loaded into the column through a side port using a peristaltic pump (schematic of the setup in Figure 2.2B). Organoid loading velocity can be easily controlled but shear stress generated by the pump could damage the organoids. Based on Equation 3.19, shear stress is proportional to flowrate and inversely proportional to the tubing diameter to the power of 3 (Coulson & Richardson 1999). For that reason, these two parameters were studied during organoid pumping.

$$\dot{\gamma} = \frac{4Q}{\pi r^3}$$ Equation 3.19

where: $\dot{\gamma}$ is the mechanical shear rate generated by the fluid, Q is the volumetric flowrate and r is the radius of the tubing.

Figure 3.11 shows microscope pictures of Iso50 CRC organoids pumped by a peristaltic pump at different flowrates and using different tubing diameters. Fewer and smaller organoids were pumped with the larger tubing diameter and lower flowrate. Based on visual inspection of microscope pictures in Figure 3.11, organoid morphology was not affected at higher flowrates when using the smaller tubing diameter, in contrast to what Equation 3.19 predicted.

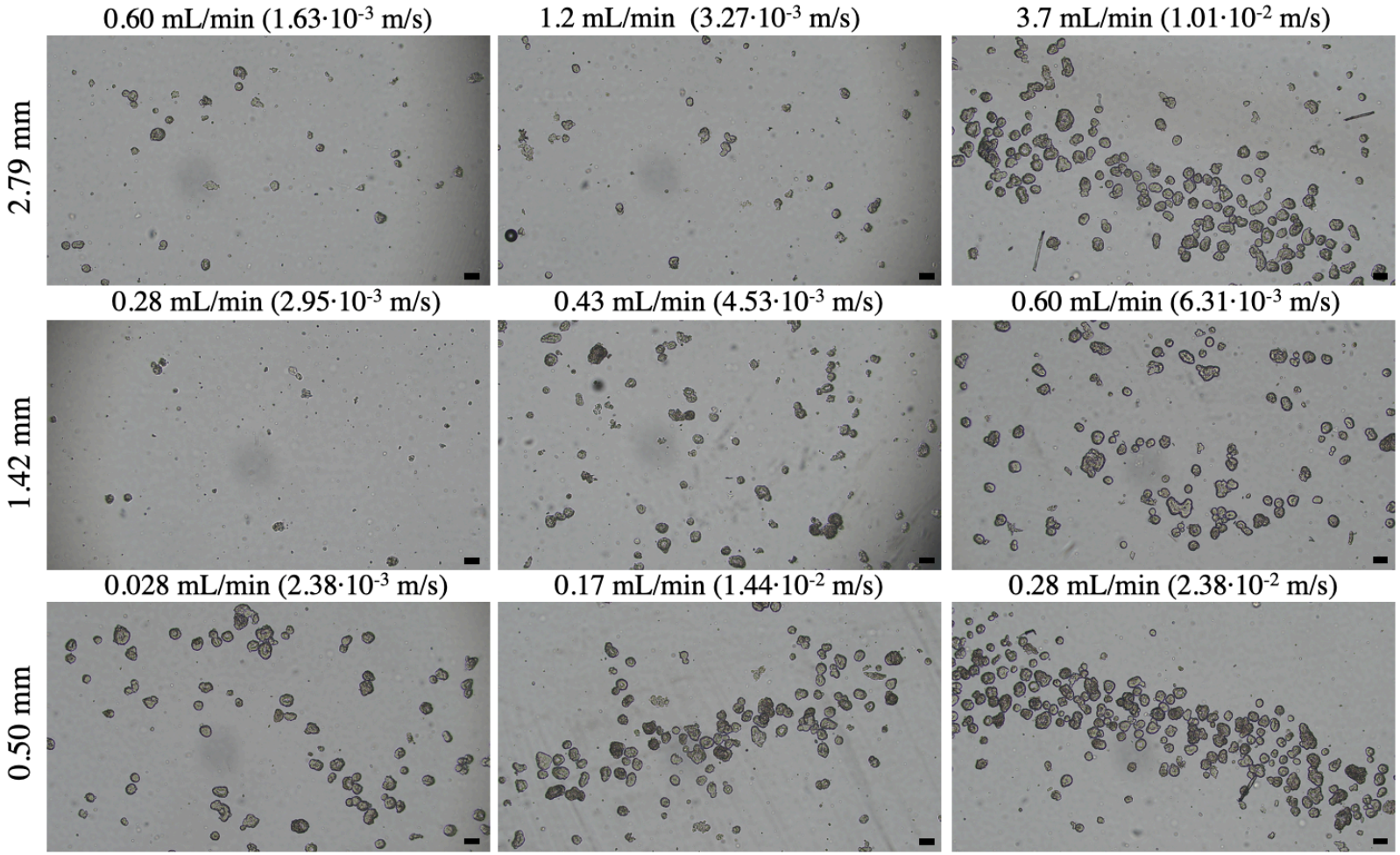

Figure 3.11 Representative images of Iso50 CRC organoid pumped out with a peristaltic pump at different flowrates and using different tubing diameters

Organoids were maintained in suspension under agitation with a magnetic bar (300 rpm) and pumped out with a Watson Marlow 200 Series peristaltic pump. Purple-white (diameter of 2.79 mm), yellow-yellow (diameter of 1.42 mm) and orange-yellow (diameter of 0.50 mm) were the Watson Marlow tubing tested. Flowrates and fluid velocity tested are indicated on top of each microscope image. Representative images from 2 biological replicates are shown (N = 2). Scale bars correspond to 100 µm.

The variations observed in Figure 3.11 could be correlated with the minimum flow velocity required to suspend particles in a horizontal pipe, in this case the horizontal tubing. This velocity can be calculated with the Durand and Condolios equation (Equation 3.20) (Perry & Green 2008) and the theoretical values obtained for each tubing diameter are summarised in Table 3.5.

$$u_m = F_L \left[2g\left(\frac{\rho_s - \rho_l}{\rho_l}\right)\right]^{1/2} D^{1/2} \qquad \text{Equation 3.20}$$

where: u_m is the minimum flow velocity required to suspend particles in horizontal pipe flow, F_L is the Durand velocity factor (influenced by particle size and concentration), g is the acceleration due to gravity, ρ_s is the solid density, ρ_l is the fluid density and D is the tubing diameter.

Schiller and Herbich proposed Equation 3.21 for the calculation of the Durand factor (Azamathulla & Ahmad 2013).

$$F_L = (1.3C_v^{0.125})\left(1 - exp(-6.9 \cdot d_{50})\right) \qquad \text{Equation 3.21}$$

where: C_v is the volumetric concentration in percent and d_{50} is the particle size at which 50% of the solids are finer (mm).

Comparing u_m values in Table 3.5 and fluid velocities used in Figure 3.11 can be noted that in most of the cases, the fluid velocity used experimentally was below the critical value, which means that organoids were settling inside the tubing. Medium and high velocities for the smaller tubing diameter (0.50 mm diameter) were higher than the corresponding theoretical u_m and this agreed with the large amount of organoids pumped out.

Table 3.5 Minimum flow velocity required to suspend particles in horizontal pipe flow

Velocity calculated with Durand and Condolios equation (Equation 3.20 and Equation 3.21) for different tubing diameters. Considering solid density 1132 kg/m^3, fluid density 1023.44 kg/m^3, C_v 0.11% and d_{50} 0.05896 mm.

Tubing diameter (mm)	u_m (m/s)
2.79	0.025
1.42	0.018
0.50	0.011

From here on, organoids were loaded into the FB column at 0.17 mL/min with a peristaltic pump using a tubing diameter of 0.50 mm. The tubing was connected to the column through a side port located halfway up from the bottom of it and organoid sedimentation was detected at this point, as shown in Figure 3.12A-B. This could be due to the slight increase in tubing diameter in the connection point, since the peristaltic pump tubing diameter was 0.50 mm and side port diameter was 2 mm. In order to reduce organoid sedimentation in the side port, the loading velocity could be increased or the side port diameter reduced. The former could increase shear stress suffered by organoids and the latter was not feasible for the glassblowing company. Based on the Reflux Classifier design, an inclined side port was tested to increase fluid velocity at the entrance of the column (Doroodchi et al. 2006; Galvin & Dickinson 2013). The average velocity of a fluid in a horizontal pipe on laminar regime can be described with Hagen-Poiseuille equation (Equation 3.22). For non-horizontal pipes an adjustment needs to be done to consider the angle of inclination and Equation 3.22 is transformed into Equation 3.23 (Coulson & Richardson 1999).

$$u_{average} = \frac{\Delta P D^2}{32 \mu l} \qquad \text{Equation 3.22}$$

$$u_{average} = \frac{(\Delta P - \rho_f g l \, sin\theta_p) D^2}{32 \mu l} \qquad \text{Equation 3.23}$$

where: ΔP is the pressure drop across the pipe, D is the diameter of the pipe, μ is the fluid viscosity, l is the length of the pipe, g is the acceleration due to gravity, ρ_f is the fluid density and θ_p is the angle of inclination of the pipe.

For downhill flow, $\theta_p < 0$, $\sin \theta_p < 0$, and therefore the average velocity of a fluid in an inclined pipe is higher than the average velocity of the fluid in a horizontal pipe.

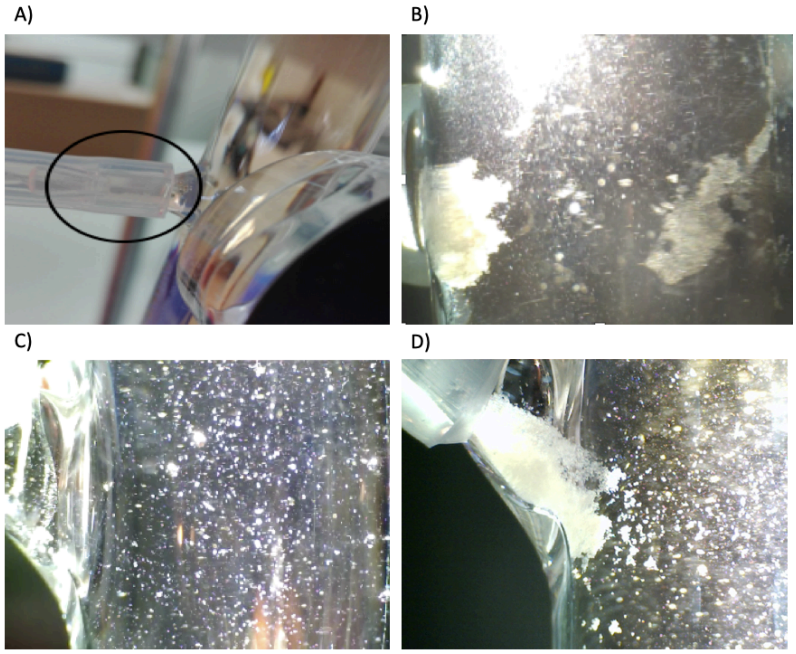

Figure 3.12 Horizontal and inclined side port for organoid loading into the FB column

A side port (OD = 4 mm, ID = 2 mm and length = 10 mm) located halfway up from the bottom of the column was used to load the organoid suspension into the FB column. **A.** and **B.** correspond to a horizontal side port. **C.** and **D.** correspond to organoid loading through a 45° inclined side port without organoid aggregation (**C.**) and with organoid aggregation (**D.**).

A 45° inlet port was tested to increase the loading velocity and therefore, reduce organoid sedimentation in the side port (see schematics of the design in Figure 2.2C). Organoid sedimentation was not detected in the inclined side port in most of the cases (Figure 3.12C), however, this could not be always reproduced, as shown in Figure 3.12D, in which a clump of organoids was formed in the inclined side port. Therefore, a reproducible organoid loading through an inclined side port was not achieved. Furthermore, the high loading velocity required to avoid organoid sedimentation in the tubing notably affected the flow pattern inside the column, especially near the loading area. Particle velocity and particle trajectories near the inlet were analysed with PIVlab, a particle image velocimetry software (see Section 2.7.4). Organoids entered into the column at high velocity and this disrupted the uniform flow coming up from the distributor, as shown in Figure 3.13. Part of the organoids were carried upwards, while others were sent downwards and "S" shape particle trajectories were detected below the loading area. Thus, the flow inside the column was not homogeneously distributed during organoid loading and this hindered organoid size-based separation.

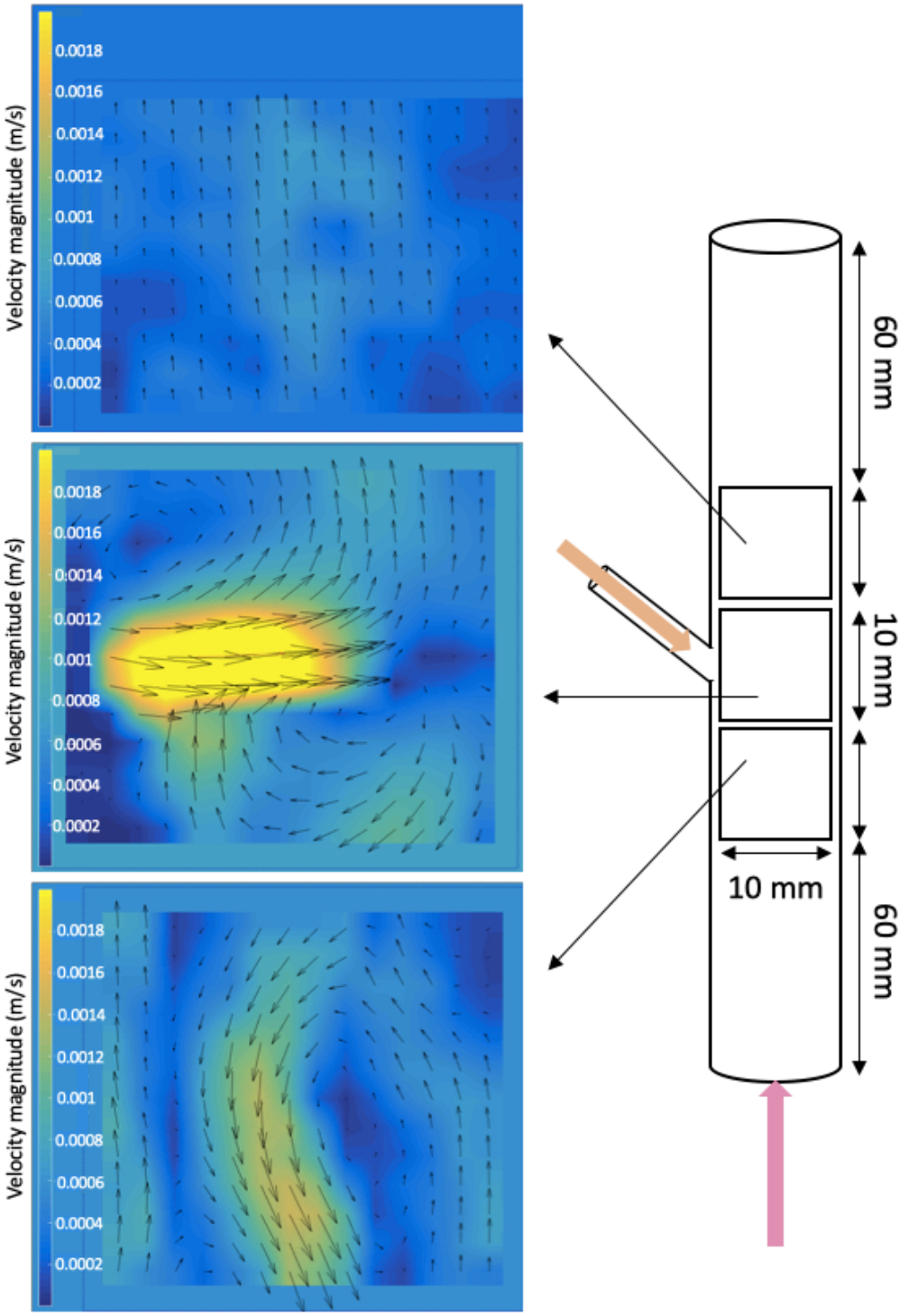

Figure 3.13 Organoid velocity and organoid trajectories near the loading area

Organoids were loaded into the FB column through an inclined side port using a peristaltic pump (1.44 x 10^{-2} m/s in 0.5 mm tubing diameter). Fluidising 6+ medium was pumped into the column at 8.49 x 10^{-5} m/s. Organoids loading and subsequent fluidisation was recorded using a microscope video camera. Images were analysed with PIVlab tool for Matlab and vector plots of the particle velocity field were obtained for the inlet area and the zones just below and just above, indicated on the diagram. Warmer colour indicates higher velocities as shown by the colour scale. Orange arrow indicates the direction of organoid loading and pink arrow indicates the direction of 6+ medium entrance.

Summarising, organoid stirring and continuous organoid loading into a FB column through a side port using a peristaltic pump was suggested as a solution to avoid organoid aggregation. Tubing diameter and peristaltic pump velocity were optimised to avoid organoid settling inside the tubing. However, organoid aggregation was detected in the side port of the column because there was a slight increase in the cross-sectional area. Then, an inclined inlet was tested to enhance the entrance of organoids into the FB. However, the high velocity required to load the organoids without sedimentation in the tubing affected the upwards flow of fluidising media. This prevented the upwards flow from achieving a uniform velocity profile necessary to reach a particle size-based separation.

The steps of organoid centrifugation prior to fluidisation, with the purpose of removing Cell Recovery Solution, could be the cause of their aggregation in the previous described set ups. Thus, a different strategy was suggested to reduce organoid handling during sample preparation prior to FB and consequent aggregation. Therefore, organoids were recovered from Matrigel with Cell Recovery Solution (30 min, on ice) and the organoid suspension was introduced directly into the column to avoid any centrifugation step that could contribute to organoid clumping (Figure 3.14). Then, Cell Recovery Solution was washed out during fluidisation with the upwards flow of 6+ medium. Considering that the column volume was around 12 mL and the fluidisation flowrate was 0.4 mL/min (8.49×10^{-5} m/s), during the first 30 min of fluidisation Cell Recovery Solution was replaced by 6+ medium. This approach reduced considerably the aggregation of organoids and enabled the loading of a single-organoid suspension into the FB column, as appreciated in Figure 3.14A. It is worth noting that by removing the centrifugation steps prior to fluidisation, the dead cells present in the organoid suspension were not eliminated from it, and therefore they were introduced in the subsequent fluidisation. This could be appreciated in the higher number of dead cells in panel A than in panel B of Figure 3.14. However, dead cells could easily be removed by fluidisation due to their lower size when compared to organoids. Moreover, the viability of the organoid suspension after 60 min in Cell Recovery Solution was assessed by dissociating the organoids into single cells with TrypLE Express Enzyme treatment (Section 2.1.3) and measuring cell viability with Luna-FL fluorescence cell counter (Section 2.2.1). The average cell viability, considering technical duplicates (n = 2) of three biological replicates (N = 3), was 89.1 ± 4.5% (average ± standard deviation). This result indicated that organoid viability was not negatively affected after 60 min in suspension with Cell Recovery Solution.

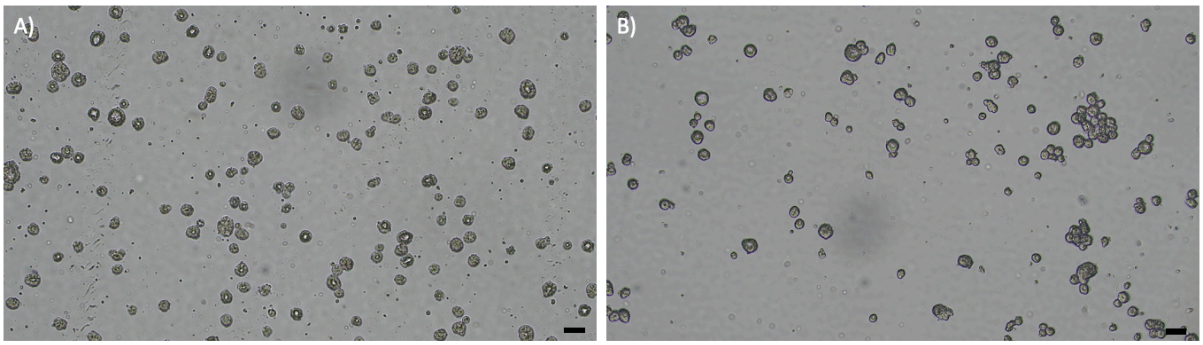

Figure 3.14 Centrifugation steps to wash out Cell Recovery Solution contribute to organoid aggregation

Iso50 CRC organoids were cultured for 5 days and recovered from Matrigel using Cell Recovery Solution (30 min, on ice). **A.** Organoid aggregation was minimum after Cell Recovery Solution treatment. **B.** Organoid aggregation was clearly detected when Cell Recovery Solution was washed out with three centrifugation steps with DMEM F12 + 10% FBS (200g, 5 min). Representative images of three biological replicates (N = 3), scale bars correspond to 100 μm.

3.2.2.3 Distributor material and design

The fluid that enters through the bottom of the FB column must be evenly distributed, thus, it is usually necessary to provide a distributor. A PTFE frit of 10 μm pore size was used in the first tests of organoid separation to distribute homogeneously the flow and to maintain single cells inside the column. However, air bubbles were trapped at the top surface of the frit (Figure 3.6 and Figure 3.7) that could interfere with flow distribution and organoid fluidisation. Then, PTFE frit was soaked overnight in ethanol 70% and washed out in PBS and 6+medium to overcome the hydrophobicity of this material. Nevertheless, this procedure was not enough to get a wettable frit and air bubbles at the surface of the frit could interfere in the fluidisation by pushing the bed of organoids upwards. But even more important, cell surface hydrophobicity is responsible of cell adhesion to air bubbles which can promote organoid clumping and cell damage during bubble rupture (Ma et al. 2004). Based on Meng *et al*. (2006), air bubbles entrapped in microfluidics devices is a common issue even if the system does not involve a gas phase. Bubbles are commonly trapped accidentally in liquid microchannels during charging up or generated undesirably by heating, electrolysis or cavitations. The bubble-capture mechanism is based on the multiphase fluidic system's tendency to minimise its total surface energy. When a bubble is allowed to move around, it will tend to find and stay on a surface that the total system energy is minimised. The total system energy can be calculated from surface free

energy, whose components can be found in Young's equation contact angle (Equation3.24) (Meng et al. 2006).

$$\gamma_{lv}\, cos\theta = \gamma_{sv} - \gamma_{sl} \qquad \text{Equation 3.24}$$

where: γ_{lv}, γ_{sv} and γ_{sl} are the surface free energies of liquid-vapor, solid-vapor and solid-liquid interfaces, respectively and θ is the contact angle of liquid on the solid surface.
The total surface energy ($E_{surface}$) of the system can be defined as:

$$E_{surface} = \sum A\gamma = A_{lv}\gamma_{lv} + A_{sv}\gamma_{sv} + A_{sl}\gamma_{sl} \qquad \text{Equation 3.25}$$

where: A_{lv} , A_{sv} and A_{sl} are the surface areas of liquid-vapor, solid-vapor and solid-liquid interfaces, respectively (Meng et al. 2006).
Bubbles are attached where $E_{surface}$ is minimised. To understand the bubble-capture process, it is assumed that, the liquid-vapor surface is kept constant when a floating bubble attaches to a hydrophilic or hydrophobic flat surface. The attaching process can be viewed as substituting a solid-liquid interface with a solid-vapor interface of the same ΔA, and Equation 3.25 can be written as Equation 3.26:

$$\Delta E_{surface} = \Delta A(\gamma_{sv} - \gamma_{sl}) \qquad \text{Equation 3.26}$$

- On a hydrophilic surface, θ is smaller than 90° (Figure 3.15), so cos $\theta > 0$, $\gamma_{sv} > \gamma_{sl}$ and $\Delta E_{surface}$ is positive, which means that the formation of a solid-vapor interface increases the system energy. This is not favourable, so the bubble tends to detach from the hydrophilic surface.
- On a hydrophobic surface, θ is larger than 90° (Figure 3.15), so cos $\theta < 0$, $\gamma_{sv} < \gamma_{sl}$ and $\Delta E_{surface}$ is negative, which means that the formation of a solid-vapor interface decreases the system energy. This is favourable, so the bubble tends to attach to the hydrophobic surface.

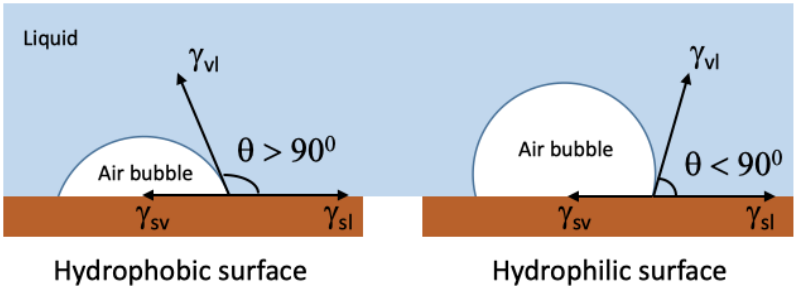

Figure 3.15 Contact angle of air bubble on hydrophobic and hydrophilic surfaces

On a hydrophobic surface, an air bubble tends to spread and the contact angle is greater than 90°. However, on a hydrophilic surface, an air bubble tends to bead up and the contact angle is less than 90°. Figure adapted from (Meng et al. 2006).

PTFE is a hydrophobic material and this is why the PTFE frit may capture air bubbles on its surface. On the other hand, a hydrophilic distributor (e.g. nylon, stainless steel or glass) could favour air bubbles detachment. Nylon frits were not commercially available but a nylon membrane of 10 μm pore size was tested at the bottom of the column to maintain organoids inside the column and to distribute evenly the flow. Air bubbles were not detected anymore when a nylon membrane was used as a distributor but concerns about non uniformities in flow distribution arose due to unusual trends of organoid motion inside the column. Organoids were going upwards on the left hand side of the column and downwards on the right hand side of the column. For that, flow distribution inside the column was studied with a pulse of a blue dye introduced in the upwards flow of PBS just before entering into the FB column. PBS (colourless) was used as upward medium instead of 6+ medium (pink colour) to ensure a high contrast between the blue dye and the colourless PBS, while both solutions are water-based with similar densities and viscosities. Figure 3.16A shows that flow was not evenly distributed across the nylon membrane and channelling was detected with the blue dye. This nylon membrane was designed for filtration applications, however, PTFE frits were designed for flow distribution. For this reason, a PTFE frit was placed at the bottom of the column to distribute homogeneously the flow and on top of it a nylon membrane was added to avoid the presence of air bubbles in contact with organoids. Figure 3.16B shows that the flow distribution provided by this design was not uniformly distributed as well. A calming section packed with beads preceding the distributor is a usual procedure in FB applications, the function of it is to equalise the liquid flow as much as is feasible before it reaches the distributor. Kalaga *et al*. (2014) used a calming section of 0.1 m height, packed with glass beads for making the velocity profile flat before it reached the liquid distributor. They used a perforated plate and a stainless steel mesh

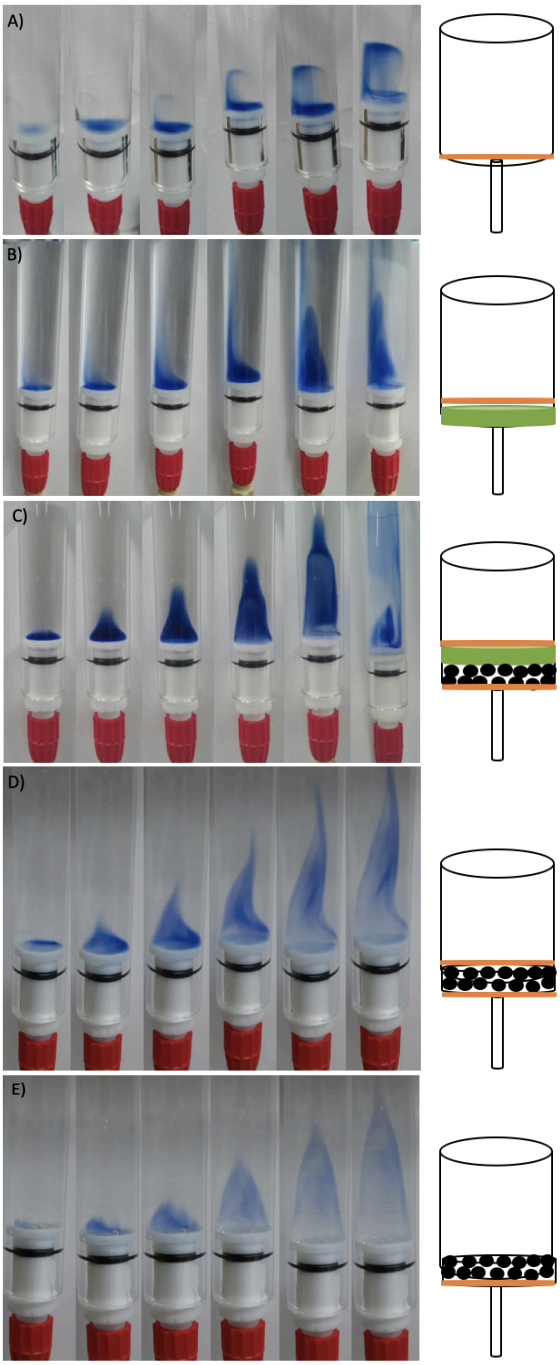

Figure 3.16 Flow distribution provided by different distributor designs

A pulse of 2 µL of Trypan Blue was introduced in the continuous upwards flow of PBS (5 rpm = 8.49 x 10^{-5} m/s) provided by a peristaltic pump. In the schematics distributor designs the orange line represents the nylon membrane of 10 µm pore size, green rectangle represents the PTFE frit of 50 µm pore size and the black circle represents the glass beads of 0.5 mm diameter. Different distributor designs were tested: **A.** Nylon membrane 10 µm pore size. **B.** From bottom to top (FBTT): PTFE frit 50 µm pore size plus a nylon membrane of 10 µm pore size. **C.** FBTT: nylon membrane of 10 µm pore size plus 1 g of glass beads plus PTFE frit 50 µm pore size plus nylon membrane of 10 µm pore size. The column was rotated in the last image to appreciate clearly the channelling. **D.** FBTT: nylon membrane of 10 µm pore size plus 1 g of glass beads plus nylon membrane of 10 µm pore size. **E.** FBTT: nylon membrane of 10 µm pore size plus 1 g of glass beads.

with smaller pore size attached to the distributor at the bottom of the column to ensure no loss of the solid particles (Kalaga et al. 2014). Similarly, Asif *et al*. (1991) setup had a calming section that consist of a Plexiglas column of 12.7 cm diameter and 25 cm length, packed with 3 mm glass beads and they placed a low pressure drop wire mesh on top of the distributor to prevent the backflow of solids when the column was shut down (Asif 1991; Asif 1992). Here, a calming section containing 1 g of glass beads of 0.5 mm diameter was placed before the PTFE frit and the nylon membrane on top. Also, it was necessary to add a nylon membrane below the beads to avoid their loss through the inlet tubing. As shown in Figure 3.16C, the flow was not evenly distributed and it was decided to remove the PTFE frit from the design and test a calming section containing 1 g of glass beads of 0.5 mm diameter between two nylon membranes. Figure 3.16D shows the flow distribution obtained with the detailed setup, and the performance was improved but some channelling was detected. A similar design but changing the order of the calming section components was suggested by Khan *et al*. (2017). They used a wire mesh at the bottom and on top of it, a flow calming section of 50 mm height packed with 12 mm diameter steel balls (much heavier than the particles to be fluidised) (Khan et al. 2017). Following this design, a nylon membrane was placed at the bottom of the distribution area and on top of it 1 g of glass beads of 0.5 mm diameter were added. During fluidisation organoids were in contact with glass beads but the low fluid velocities required to fluidise organoids were not enough to fluidise the glass beads that remained in the distributor area. Figure 3.16E shows that the flow was evenly distributed with the typical parabolic velocity profile associated with laminar flow in which the fluid velocity is maximum along the cross-sectional centre of the column and it decreases near the walls due to the increase of shear stress. This velocity profile was confirmed when organoid fluidisation was analysed with PIVlab tool near the distributor area, as shown in Figure 3.17A and Figure 3.17B. Furthermore, this leads to convective circulation pattern of the particles in which organoids were rising up at the centre of the column and falling down near the walls as shown in Figure 3.17C, which has been previously described by other authors (Asif 1992; Yang 2003). It is worth noting that the range of velocities obtained with PIVlab (Figure 3.17B) were slightly higher than the experimental fluid velocity (8.49×10^{-5} m/s) provided by the peristaltic pump which could be a slight deviation in PIVlab image calibration.

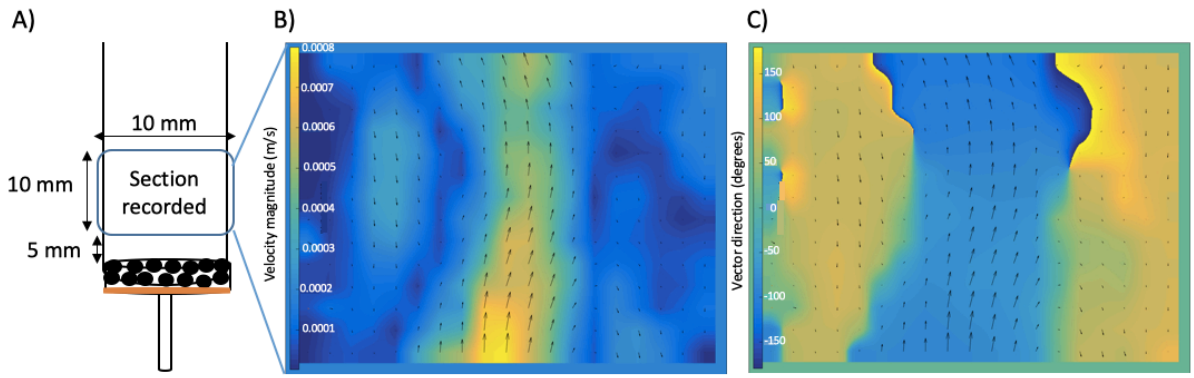

Figure 3.17 Organoid velocity and organoid direction near the distributor composed of a nylon membrane of 10 µm pore size and 1 g of glass beads of 0.5 mm diameter

A. Organoids were fluidised at 8.49 x 10^{-5} m/s and their movement was recorded using a microscope video camera (column section recorded = 10 mm width x 10 mm height, height from the glass beads = 5 mm). Images were analysed with PIVlab tool for Matlab and vector of particle velocity field (**B.**) and vector direction (**C.**) were obtained for the bottom part of the column. **B.** Warmer colour indicates higher velocities as shown by the colour scale. This figure demonstrates that the highest particle velocities (approx. 8 x 10^{-4} m/s) occur in the centre of the column and lower velocities (approx. 9 x 10^{-5} m/s) near the walls. **C.** Warm colour corresponds to a downwards flow and cold colour corresponds to an upwards flow. Organoids move upwards in the centre of the column and downwards near the wall.

This experiment was performed in triplicate and confirmed that a calming section with a 10 µm pore size nylon membrane and on top of it 1 g of 0.5 mm diameter glass beads provided a more uniform flow distribution than other tested setups, which is a requirement for a size-based separation FB.

3.2.2.4 Other aspects of the FB column design

Additional elements were considered during the design of a FB for organoid size-based separation, including the organoid exit through the top of the column, the addition of sampling ports and the siliconization of the column walls.

The top connector (bottom right image of Figure 3.18A) used in the FB column had a small hole (1 mm diameter) through which the organoids had to exit the column. Organoid accumulation was detected at the upper part of the column due to the sharp reduction in cross sectional area, i.e. from 10 mm column diameter to 1 mm exit diameter. Figure 3.18C and 3.18E show the organoid velocity field and the organoid direction at the top of the column, respectively. Organoids reduced their velocity and changed their direction when they collided

with the top connector and moved downwards. In order to avoid the flow recirculation and facilitate organoids elutriation, a progressive reduction of column diameter was tested, as described in Figure 2.2D. This conical exit enabled the smooth elution of organoids, as shown in Figures 3.18D and 3.18F. Organoids direction was not affected by this change in the design and no recirculation was detected on the upper part of the column when a conical exit was tested.

Additionally, to monitor organoid separation during fluidisation it was necessary to determine the size of the organoids along the column. The microscope video camera used to record organoid movements inside the column did not have enough resolution to measure organoids size, therefore sampling ports were added at different heights of the column as shown in Figure 2.2E. Silcoset 151 adhesive was used to seal the ports (Figure 3.20) and a syringe was used for sampling at different column heights during fluidisation. Figure 3.19 shows representative images of organoids sampled through the sampling ports during fluidisation. As expected, bottom samples contained larger organoids than top samples, which confirmed the gradient of organoid sizes along the column.

Furthermore, to reduce organoid adhesion to the column walls, glass columns were treated overnight with Sigmacote prior to organoid loading. This siliconized coating left behind a hydrophobic layer inhibiting organoid attachment on the glass. This treatment was used in the rest of the experiments.

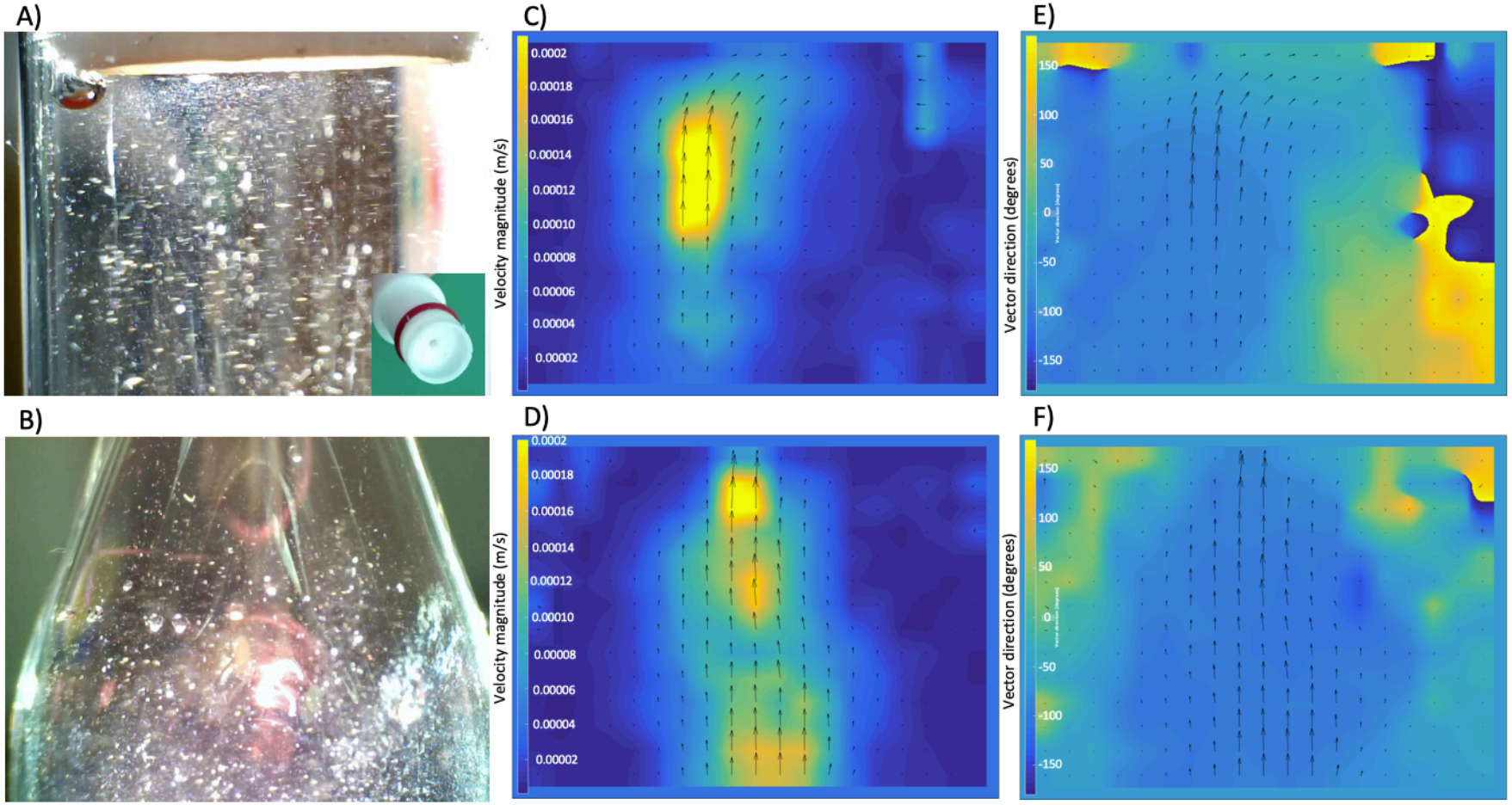

Figure 3.18 Organoid elutriation through the top of the column

A. and **B.** pictures of the upper part of the column with top connector and conical exit, respectively. Inset of **A.** corresponds to a picture of the top connector. Organoid elutriation was recorded with a microscope video camera and images were analysed with PIVlab tool for Matlab. **C.** and **D.** plots of vector of particle velocity field for top connector and conical exit, respectively. Warmer colour indicates higher velocities as shown by the colour scale. **E.** and **F.** velocity vector direction for top connector and conical exit, respectively. Warm colour corresponds to a downwards flow and cold colour corresponds to an upwards flow.

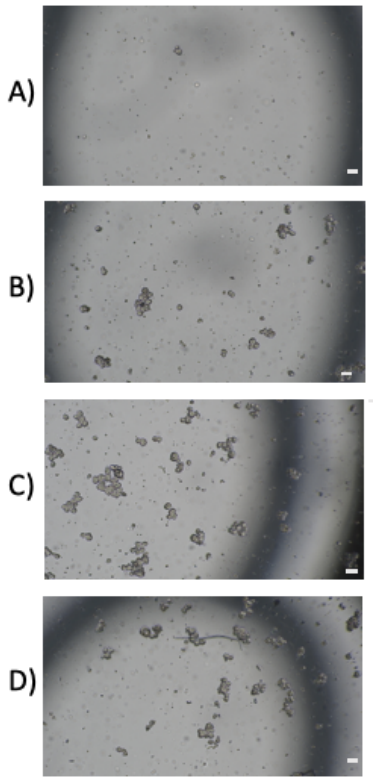

Figure 3.19 Sampling ports to monitor organoid separation during fluidisation

Representative images of Iso50 CRC organoids sampled through the four sampling ports during fluidisation (8.49 x 10^{-5} m/s). Sampling ports from top to bottom port correspond to A, B, C and D. Scale bars correspond to 100 μm.

Finally, the FB design for organoid size-based separation consisted of a glass column treated overnight with Sigmacote with the dimensions specified in Table 3.6 and a picture is shown in Figure 3.20.

Table 3.6 Dimensions of FB glass column designed for organoid size-based separation

Fluidised bed column dimensions	Size
Open ended glass column ends fired borosilicate	
Length (mm)	150
ID (mm)	10
OD (mm)	15
Volume (mL)	11.78
Conical top	
Length (mm)	22
ID (mm)	3.8
OD (mm)	5
4 Sampling ports	
Length (mm)	10
ID (mm)	2
OD (mm)	4
Distance from the bottom (mm)	25, 50, 100, 140
Calming section	
Nylon membrane pore size (µm)	10
Glass beads diameter (mm)	0.5
Glass beads amount (g)	1

Figure 3.20 FB glass column designed for organoid size-based separation

Column dimensions are specified in Table 3.6. Column is composed of four sampling ports with Silcoset 151, and a conical exit.

3.2.3 Polystyrene beads separation

Polystyrene standard beads with similar physical properties to organoids were used to validate the designed FB. Standard beads of 20 µm and 60 µm diameter and 1050 kg/m^3 density were chosen as equivalent to small and large organoids, respectively. Both standards were mixed to prepare an initial mixture with a similar PSD as the organoid suspension recovered after 5 days of culture. Based on Figure 3.2A, 80% of the organoids had a diameter below 40 µm that were represented with the 20 µm beads and 20% of the organoids had a diameter larger than 40 µm that were represented with the 60 µm beads. For that, a total of 5 x 10^5 beads were loaded into the designed FB (specifications in Table 3.6), consisting of 4 x 10^5 beads of 20 µm diameter

and 1 x 10^5 beads of 60 μm diameter (Figure 3.21A). Polystyrene beads were fluidised at 8.49 x 10^{-5} m/s during 1 h and beads elutriated from the top were collected in a tube. As shown in Figure 3.21B and 3.21C, the two standards were separated based on size as the Top fraction contained the 20 μm beads and the Column fraction contained mostly the 60 μm beads. Furthermore, the PSDs of the initial mixture and the final Column and Top fractions were obtained with MS3 Coulter Counter. Figure 3.21D shows that the 20 μm standard contained two peaks, a high narrow peak at 20 μm and a smaller one at 27 μm. On the other hand, the 60 μm standard corresponded to a wider peak with a range of beads between 60 μm and 70 μm diameter. The PSD of the Top fraction obtained by fluidisation shows that only the 20 μm polystyrene beads were elutriated as its PSD contained peaks at 20 μm and 27 μm but no peaks were detected at a higher particle size (Figure 3.21D). Instead, the PSD for the Column fraction shows a major peak in the 60-70 μm range and a smaller one at 20 μm, which indicated that this fraction contained mostly 60 μm beads but some 20 μm beads remained in the column after 1 h of fluidisation. Only particles between 20-30 and 60-70 μm were considered for composition, purity, recovery, enrichment and separation efficiency calculations as the standards only contained beads of these sizes. Composition of the initial mixture and final fractions are shown in Figure 3.21E. As expected, the initial mixture contained 79.7±0.4% of particles in the range 20-30 μm and 20.3±0.4% of particles in the 60-70 μm range. Clearly, 20 μm beads were more concentrated in Top fraction relative to Initial mixture and 60 μm beads were also more concentrated in Column fraction compared to Initial mixture. Furthermore, beads recovery was also studied based on the MS3 Coulter Counter data and the results obtained are shown in Figure 3.21F. Almost all the 20 μm beads loaded into the column were recovered after the fluidisation (84.6±3.4% in the Top fraction and 9.3±1.1% in the Column fraction) and around 86% of the 60 μm beads present in the initial mixture were recovered after the fluidisation (14.7±5.8% in the Top fraction and 71.7±4.9% in the Column fraction). The purity (P), enrichment (E) and separation efficiency (SE) are reported in Table 3.7. Small beads (20-30 μm) were enriched by a factor of 7.1 times in the Top fraction with a high purity (95.8%) and large beads (60-70 μm) were also enriched by 7.8 times in the Column fraction but with a lower purity (66.2%). This means that some 20 μm beads remained in the Column after 1 h of fluidisation. It is possible that a longer fluidisation experiment could reduce the amount of small beads inside the column and increase the purity of the Column fraction. The designed FB showed a good separation efficiency, as 90.1% of the total collected small beads were

collected in the Top fraction and 83.6% of the total collected large beads were collected in the Column fraction.

Overall, these results validated the designed FB with the dimensions specified in Table 3.6, and the operating conditions (1 h fluidisation at fluidisation velocity = 8.49 x 10^{-5} m/s) for the size-based separation of particles with similar physical properties to Iso50 CRC organoids cultured for 5 days. High bead recovery, enrichment and separation efficiency were achieved, and fraction purity was acceptable. The next step was to test the designed FB for organoid size-based separation, which is described in Chapter 4.

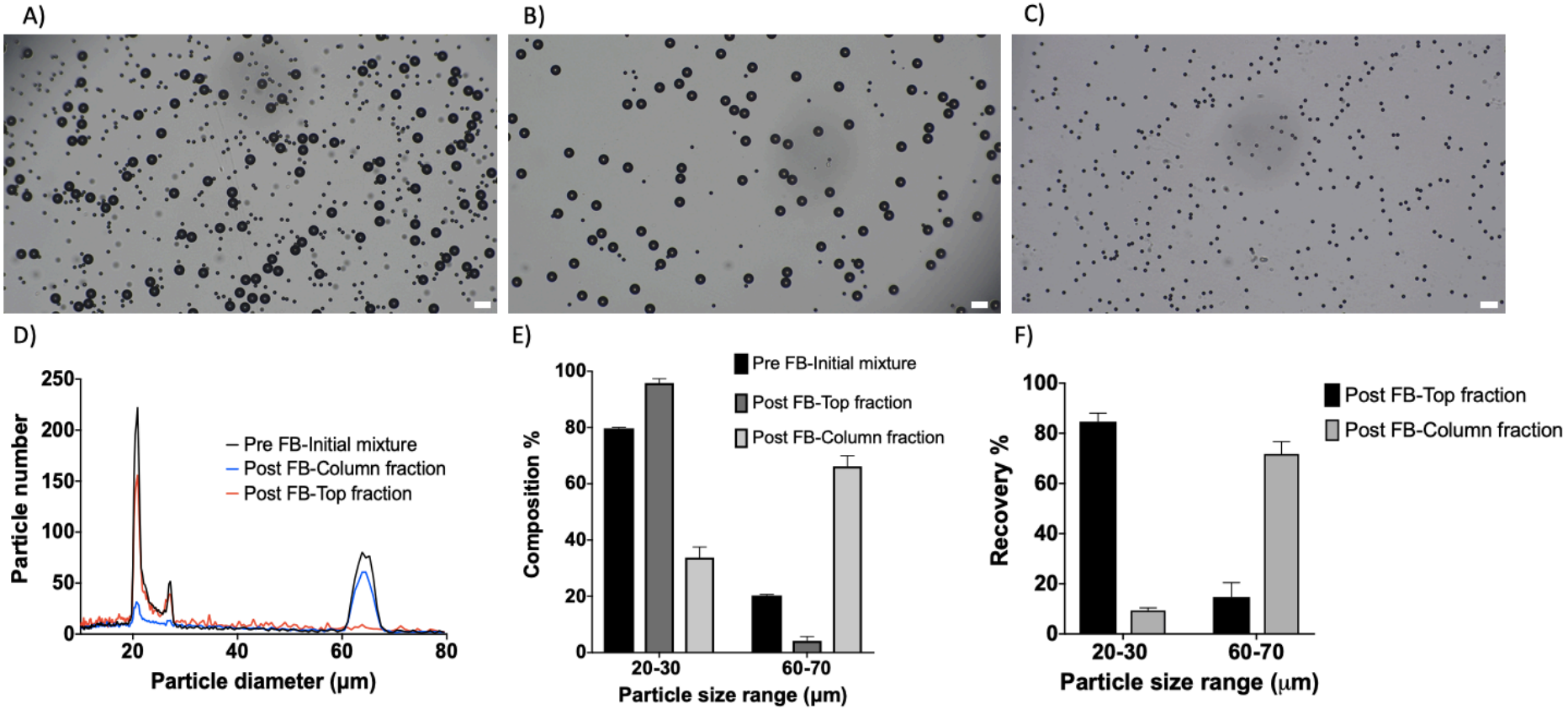

Figure 3.21 Validation of the designed FB with polystyrene standard beads of 20 µm and 60 µm.

Polystyrene standard beads of 20 µm and 60 µm diameters and 1050 kg/m^3 density were used as equivalent to small and large organoids, respectively. 400,000 of 20 µm beads and 100,000 of 60 µm beads were mixed with 6+ medium and introduced in the designed FB column (specifications in Table 3.6). Beads were fluidised at 8.49 x 10^{-5} m/s during 1 h and the elutriated particles were collected in a tube. Initial mixture, and Top and Column fractions obtained after fluidisation were imaged with the microscope (**A**, **B** and **C**, respectively) and PSDs were obtained with MS3 Coulter Counter (**D**). Considering as noise all particles outside the size range 20-30 µm and 60-70 µm, composition (**E**) and recovery (**F**) were calculated for the different fractions with Equation 2.3 and Equation 2.5, respectively. Scale bars represent 100 µm. Error bars represent standard deviation (n=3, N=3).

Table 3.7 Polystyrene beads separation performance using the designed FB

Data is presented as average±standard deviation with n=3, N=3.

Index	20-30 μm in Top fraction	60-70 μm in Column fraction
P (%)	95.8±1.5	66.2±3.8
E	7.1±3.6	7.8±1.3
SE (%)	90.1±1.0	83.6±5.0

3.3 Summary

In this chapter, the design of a FB for organoid size-based separation was explored. From the experiments outlined in this chapter it has been concluded:

i) Minimum fluidisation velocity of Iso50 CRC organoids grown for 5 days is 7.90 x 10^{-5} m/s.

ii) Terminal falling velocity presents a quadratic dependence with organoid size and it takes the value of 1.67 x 10^{-4} m/s for Iso50 CRC organoids cultured for 5 days.

iii) Fluidised bed design for organoid size-based separation has been described based on the fundamentals of physics, chemistry and biology. Organoid aggregation, loading strategy and distributor design have been identified as key aspects of the design process.

iv) The designed FB and operating conditions have been validated with polystyrene standard beads with similar physical properties to Iso50 CRC organoids. Acceptable purity (96% in Top fraction and 66% in Column fraction) and high recovery, i.e. 94% of the 20 μm loaded beads and 86% of the 60 μm loaded beads, were achieved.

This chapter has shown for the first time the hydrodynamic characterisation of a FB containing organoids, which provided essential information for the design of a FB for organoid size-based separation. The minimum fluidisation velocity of Iso50 CRC organoids determined here is used in the following chapter to study the size-based separation of organoids by fluidisation. Similarly, the calculated values of terminal falling velocities of various size Iso50 CRC organoids were necessary to select the range of velocities that carry the organoids of a specific

diameter out of the top of the column for their fractionation. Furthermore, the detailed study presented in this chapter concluded with a FB design and setup conditions that distribute uniformly the flow inside the column and reduce organoid aggregation, which are essential requirements for organoid size-based separation. This design has been validated with polystyrene standard beads with similar physical properties to Iso50 CRC organoids and the next chapter quantifies the separation capability of the designed FB with Iso50 CRC organoids. These findings contribute to the understanding of the main challenges that the organoid manufacturing field might experience in future processes (e.g. organoid aggregation, hydrodynamic characterisation and flow distribution).

4. Organoids size separation and drug response variability

4.1 Introduction

The three-dimensional architecture of tumour microenvironments is characterised by oxygen, nutrients and waste metabolites gradients that can be mimicked in organoid cultures, as presented in Section 1.3.4 (Qiu et al. 2017; Saglam-Metiner et al. 2019; Hubert et al. 2016; Okkelman et al. 2019; Cruz-Gil et al. 2018; Roscigno et al. 2019; Karolak et al. 2019; Zhang et al. 2015). These gradients are the result of diffusional limitations and depend on tumour or organoid size (Karolak et al. 2019). Therefore, organoid size may play and important role during drug testing depending on the mechanism of action of the drug. In relation to that, it has been described that in most solid tumours, epithelial junction proteins, such as, E-cadherin and claudins, and ECM proteins, such as, collagen, elastin, fibronectin and laminin create a physical barrier that prevent intratumoral drug penetration and direct contact between drugs and their target receptor on malignant cells (Choi et al. 2013). Similar to solid tumours, limitation of drug diffusion has also been observed in tumour organoids using chemotherapeutic compounds (Roscigno et al. 2019; Karolak et al. 2019), which could result in the apparent ineffectiveness of drugs caused by the restriction of compounds penetration. Furthermore, hypoxia, detected in spheroids and stem cell aggregates larger than 300 μm (Daster 2017; Wu et al. 2014), is considered one of the main reasons of drug resistance of therapeutic compounds, e.g. doxorubicin, 5-fluorouracil, cisplatin and irinotecan, that need oxygen to induce an effective anticancer effect (Nunes et al. 2018). Moreover, doxorubicin uptake decreased with spheroid depth in HCT116 colon cancer spheroids due to the extracellular acidosis associated to the core of spheroids. Weakly basic drugs, such as doxorubicin, are protonated in acidic environments and charged drugs are less effective in transposing cellular membranes (Swietach et al. 2012). All these evidences suggested that organoid size might need to be controlled during drug testing since diffusional limitations and tumour microenvironment were considered important factors behind drug resistance of cancer cells for chemotherapy. This chapter focuses on the effect of organoid size in the drug response variability.

Organoid and spheroid size has been object of study of various authors (see Section 1.4) identifying the aggregate size in which hypoxia is detected, more specifically, the lack of oxygen was appreciated in spheroids and stem cell aggregates larger than 300 μm (Daster et al. 2017; Wu et al. 2014). Also, differences on the transcriptome of different size CRC

spheroids (20-40 μm vs. 70-100 μm) have been previously studied (Tirier et al. 2019). Moreover, other authors claimed there was a need to produce organoids in a size controllable manner to standardise spheroid/organoid uniformity to enhance the reproducibility of drug response tests (Arora et al. 2017; Jung et al. 2019; Lim et al. 2018; Yu et al. 2019).

Yu *et al*. (2019) identified the lack of standardised organoids as an important limitation of the current organoid technology and claimed that limited uniformity and reproducibility difficult organoid use for toxicity screening or high-throughput testing. This suggests that consistencies in size, shape and cell number per organoids might facilitate the normalising of the pharmacokinetics profiles of drug candidates and therefore, drug responses might be quantified more accurately. Based on this limitation of current organoid models, in this chapter we suggest for the first time a size-based separation of organoids to obtain a more homogeneous organoid population that may respond more reproducibly to downstream assays. OcellO B. V. have indicated that 40-85 μm diameter is the ideal size range of organoids seeded/treated in their drug treatments assays (personal communication, September 20, 2016) and thus the same organoid size range was selected as target diameter range in this work. In this thesis, the main focus was placed in removal of the large amount of single cells recovered after organoid expansion.

In this chapter, first, an already established method for cell size separation - dead end membrane filtration - is described for organoid fractionation and separation ability is evaluated based on separation metrics defined in Section 2.6.3. Then, the FB column designed in Section 3.2.2 was tested for organoid fractionation and separation capability was compared with membrane filtration results. Finally, drug response variability using fractionated and non-fractionated organoids was studied with known CRC targeting compounds that Cellesce Ltd uses for validation of their organoid expansions, i.e. 5-Fluorouracil (5-FU), LGK974 and Trametinib. 5-FU is the most widely used treatment regime for CRC and is thought to function by inhibiting thymidylate synthase. Therefore, DNA and RNA synthesis is disrupted leading to the initiation of apoptosis and cell death (Gill et al. 2003). LGK974 is a porcupine inhibitor that inhibits Wnt ligand secretion and results in reduced Wnt signalling, which causes cell cycle arrest and induces apoptosis in CRC cell lines (Bagheri et al. 2019). Trametinib is a MEK1/2 inhibitor that inhibits RAS signalling through mitogen-activated protein kinase (MAPK) cascade suppression (Dai et al. 2019).

In summary, this chapter focuses on the assessment of the size-based fractionation of organoids using the designed FB, and the comparison of the obtained separation metrics with a well-

established method for cell separation, such as filtration. Also, it is hypothesised that drug response reproducibility is enhanced when a homogeneous in size organoid population is treated with known CRC targeting compounds, and this chapter evaluates whether this assumption is true.

The key aims for this chapter were:

i) To fractionate Iso50 CRC organoids with 40 and 85 μm PluriStrainers (PSs) and to assess the separation ability through the separation metrics.

ii) To fractionate Iso50 CRC organoids with a FB and compare the separation performance with PS separation.

iii) To evaluate whether drug response differs between fractionated and non-fractionated Iso50 CRC organoids.

iv) To determine whether drug response variability is reduced when drug treatment is performed with organoids that present a uniform size.

4.2 Results and Discussion

4.2.1 Iso50 CRC organoid size separation with PluriStrainers

The size-based separation of Iso50 CRC organoids was first assessed through a dead end filtration using PluriStrainers, which have been used in literature as a sieving device for organoids (Przepiorski et al. 2018; Mazzucchelli et al. 2019). For this purpose, Iso50 CRC organoids grown for 5 days were recovered from Matrigel with Cell Recovery Solution (30 min treatment on ice) and the resulting suspension is shown in Figure 4.1A. PSD of Initial mixture of organoids was obtained from the quantification of microscope pictures (Figure 4.1E) and it was also measured with MS3 Coulter Counter (Figure 4.1F) and an organoid suspension containing 5 x 10^5 particles was fractionated using PSs of 40 μm and 85 μm pore size, as detailed in Section 2.6.1. Three different fractions were obtained: Fraction < 40 μm (Figure 4.1B), Fraction 40-85 μm (Figure 4.1C) and Fraction > 85 μm (Figure 4.1D), and their PSDs were analysed with MS3 Coulter Counter data and microscope image quantification.

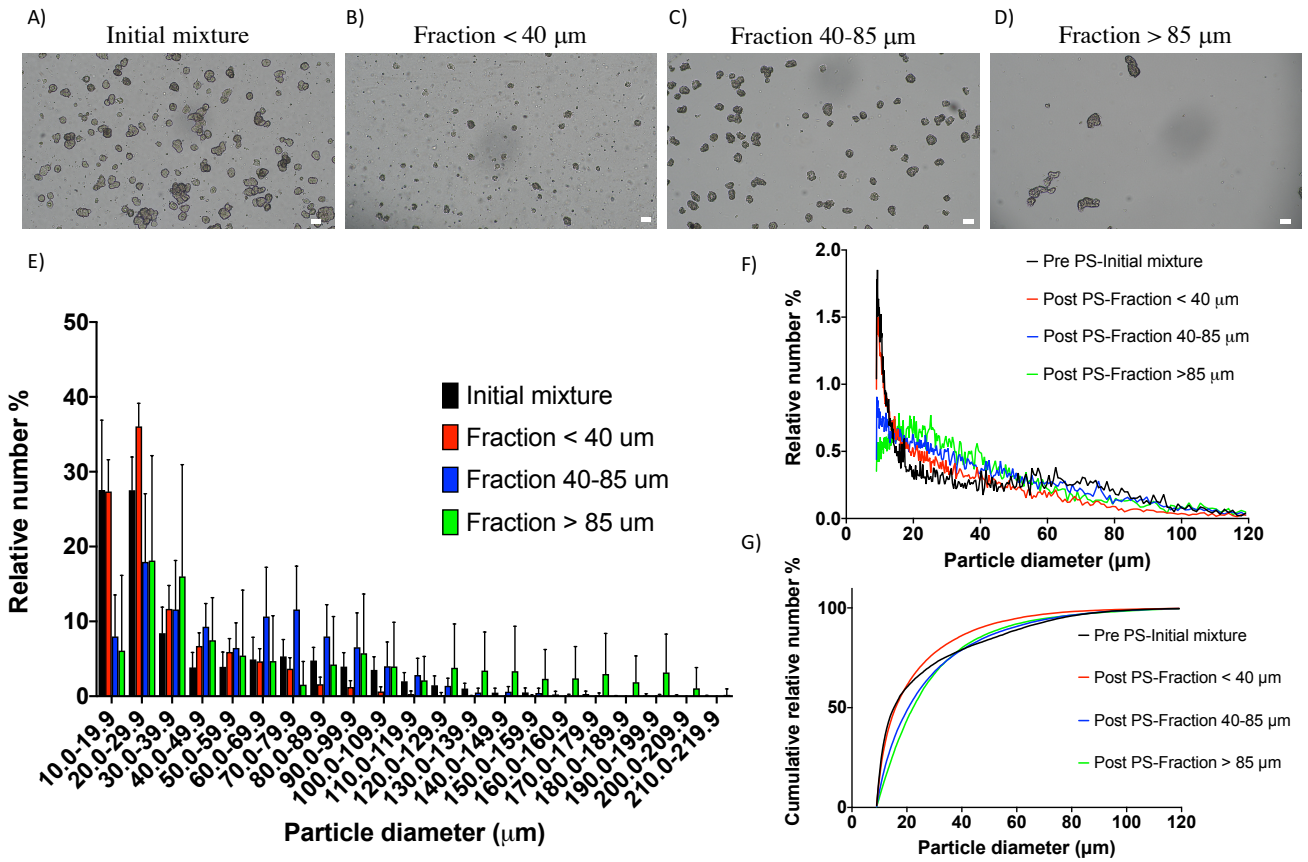

Figure 4.1 Iso50 CRC organoid size based separation with PluriStrainers of 40 µm and 85 µm

A. Microscope picture of the Initial organoid mixture recovered from Matrigel after 5 days of culture. Microscope pictures of the three fractions obtained after filtration with 40 µm and 85 µm PS, corresponding to **B.** Fraction <40 µm, **C.** Fraction 40-85 µm and **D.** Fraction >85 µm. **E.** Number-based PSD obtained from the image quantification of panels A-D with CellProfiler. **F.** Number-based PSD of the Initial mixture, Fraction <40 µm, Fraction 40-85 µm and Fraction >85 µm, obtained from MS3 Coulter Counter data. **G.** Cumulative number-based PSD of the Initial mixture, Fraction <40 µm, Fraction 40-85 µm and Fraction >85 µm, obtained from MS3 Coulter Counter data. **E.**, **F.** and G data corresponds to average of N=4. Error bars in **E.** represent standard deviation. Scale bars correspond to 100 µm.

Microscope pictures in Figures 4.1B-D show clear organoid size differences between the three fractions. As expected, Fraction < 40 μm contained cell debris, single cells and small organoids, Fraction 40-85 μm included a homogeneous organoid-sized population and Fraction > 85 μm retained bigger organoids and aggregates. Moreover, these results were confirmed with the microscope image quantification using CellProfiler software (Figure 4.1E) in which three different PSDs were obtained for each resulting fraction. Despite clear size differences detected in the microscope images (Figure 4.1B-D), and in their quantification (Figure 4.1E), these were not seen when the MS3 Coulter Counter data was analysed (Figure 4.1F). Figure 4.1F shows that Initial mixture and Fraction <40 μm presented a high amount of 10 μm particles, corresponding to single cells but PSDs of Fraction 40-85 μm and Fraction > 85 μm did not show peaks at 40-85 μm and > 85 μm range, respectively. However, it is important to note that the amount of single cells was reduced considerably in the target fraction (Fraction 40-85 μm) compared to the Initial mixture, which was required due to the large amount of single cells recovered after organoid expansion. Furthermore, Figure 4.1G shows the cumulative number-based PSD of the suspensions before and after separation based on the results obtained from MS3 Coulter Counter analysis. Although the differences between curves were small, it can be noted that Fraction < 40 μm contained the smallest particles. Also, MS3 Coulter Counter data was used to calculate Sauter mean diameter and the values obtained were 63.70±5.55 μm for Initial mixture, 56.71±4.30 μm for Fraction < 40 μm, 62.87±1.82 μm for Fraction 40-85 μm and 61.74±4.04 μm for Fraction >85 μm indicating that PSDs of Initial mixture, Fraction 40-85 μm and Fraction >85 μm were similar and Fraction < 40 μm contained smaller particles than the other samples (Figure 4.1F).

Composition of the Initial mixture and resulting fractions obtained after filtration was calculated with MS3 Coulter Counter data and it is shown in Figure 4.2A. As reported before, almost 80% of the particles of the Initial mixture had a diameter below 40 μm which corresponded mainly to single cells and this was the main group of particles to be removed. However, after filtration, composition of the separated suspensions was largely unchanged. Particles < 40 μm were slightly more concentrated in Fraction < 40 μm compared to Initial mixture but based on these results, PSs were ineffective at concentrating 40-85 μm particles in the corresponding fraction.

Furthermore, based on MS3 Coulter Counter data, more particles were recovered after filtration than the number of particles present in the Initial mixture, as shown in Figure 4.2B. After

filtration, the recovery of particles < 40 μm was 203% (130.2±11.7% in Fraction < 40 μm, 52.1±6.6% in Fraction 40-85 μm and 21.0±4.0% in Fraction > 85 μm). Similar results were obtained for 40-85 μm particles with a 155% recovery (82.3±10.8% in Fraction < 40 μm, 53.1±6.5% in Fraction 40-85 μm and 19.5±3.2% in Fraction > 85 μm) and for particles > 85 μm with a 110% recovery (48.0±3.5% in Fraction < 40 μm, 45.8±8.0% in Fraction 40-85 μm and 16.7±0.5% in Fraction > 85 μm). All in all, the amount of particles recovered was much larger than the initial number of particles in the inlet. Possible explanation for this observation could be that organoids were broken during the filtration process generating smaller particles that were not present in Initial mixture. Also, organoids breakup during the analysis in MS3 Coulter Counter when passing through the small orifice (400 μm aperture) or channels present in the equipment could increase the number of particles detected by the counter. Organoids are deformable particles that could be broken due to shear suffered in the PS or in the analysis device generating more particles than the initially number of particles loaded in the system. This could explain the large number of particles < 40 μm recovered after filtration, but remained unclear the large recoveries of particles > 40 μm. Moreover, representative images of the PSs captured after filtration (Figure 4.2C-D), show some organoids being trapped in both filters, thus confirming that all organoids were not retrieved and recoveries should have been below 100%. Furthermore, recovery results showed that lots of particles were collected in a size-fraction that did not agree with the actual particle size, e.g. 82.3% of the 40-85 μm particles present in the Initial mixture were recovered in Fraction < 40 μm instead than in Fraction 40-85 μm. This did not agree with the microscope picture of the separated fractions (Figure 4.1B-D), in which a few small organoids were detected in Fraction < 40 μm and organoids were mainly found in Fraction 40-85 μm. Particle overcounting with MS3 Coulter Counter could justify the different results obtained with microscope images and MS3 Coulter Counter, although a blank was previously performed with medium and subtracted from the organoid sample measurement.

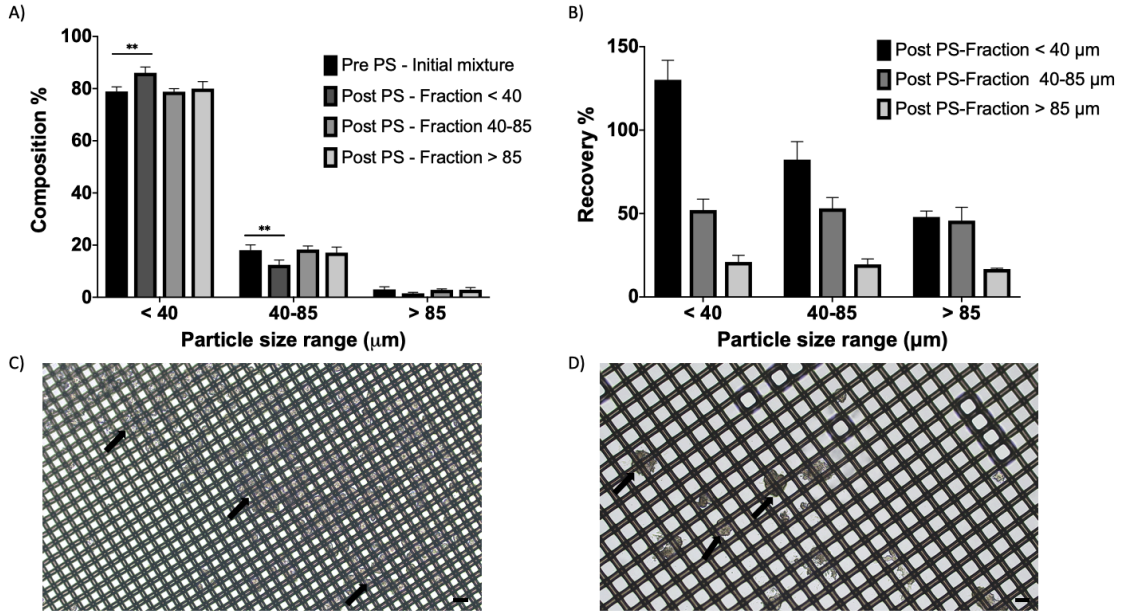

Figure 4.2 Iso50 CRC organoids separation performance using PluriStrainers of 40 µm and 85 µm

A. Organoid composition, calculated with Equation 2.3, for Initial mixture and the resulting fractions obtained after filtration with PS, i.e. Fraction < 40 µm, Fraction 40-85 µm and Fraction > 85 µm. **B.** Organoid recovery, calculated with Equation 2.5, in the resulting fractions obtained after filtration with PS, i.e. Fraction < 40 µm, Fraction 40-85 µm and Fraction > 85 µm. Error bars represent standard deviation (n=3, N=4). **C.** Representative image of 40 µm PS mesh after filtration. **D.** Representative image of 85 µm PS mesh after filtration. Black arrows point to some of the organoids entrapped in the mesh. Scale bars correspond to 100 µm.

Organoids purity, enrichment and separation efficiency with PS filtration are displayed in Table 4.1 based on the quantification of microscope images and MS3 Coulter Counter data. Different results were obtained for both quantification methods. According to microscope image quantification, there was some enrichment of particles < 40 µm in Fraction < 40 µm (E = 1.8), which presented a purity of 75.1%. Moreover, higher enrichment was obtained for particles 40-85 µm (E = 3.1) and particles >85 µm (E = 4.0) in the corresponding fractions, although the purity was not high (46.0% for Fraction 40-85 µm and 35.6% for Fraction >85 µm). Similarly, separation efficiencies of particles <40 µm, particles 40-85 µm and particles > 85 µm in the respective fractions were calculated to be 50.1%, 49.5% and 64.5%, respectively, which indicated that half of the available small, medium and large organoids were not captured in the appropriate fraction. On the other side, separation metrics obtained from MS3 Coulter Counter data showed that there was some enrichment of particles < 40 µm in Fraction < 40 µm, as E=1.7, and a good purity was attained (86.1%). However, target organoids (40-85 µm) were not enriched in the Fraction 40-85 µm and presented a low purity (13.8%) due to the large

amount of small particles present in that fraction. Based on MS3 Coulter Counter data, PS did not show a good separation efficiency, as only 64.1% of the total collected < 40 μm particles were found in Fraction < 40 μm, and just 34.3% of the collected 40-85 μm particles were isolated in Fraction 40-85 μm. The comparison between the separation metrics results obtained from both quantifications showed that a better separation performance was achieved based on the quantification of microscope images. This methodology required less manual handling than MS3 Coulter Counter, which could lead to more reliable results, however, further investigation is needed to understand the differences obtained between both quantifications.

Table 4.1 Iso50 CRC organoids separation performance using PluriStrainers of 40 μm and 85 μm

Purity (P%), Enrichment (E) and Separation efficiency (SE%) were calculated with Equation 2.4, Equation 2.6 and Equation 2.7, respectively. Data is presented as average±standard deviation with n=3, N=4.

Based on	Index	<40 μm in F <40 μm	40-85 μm in F 40-85 μm	>85 μm in F >85 μm
Microscope image quantification	P (%)	75.1±3.1	46.0±14.4	35.6±13.0
	E	1.8±0.2	3.1±1.2	4.0±1.4
	SE (%)	50.1±5.3	49.5±7.5	64.5±11.0
MS3 Coulter Counter data	P (%)	86.1±2.2	13.8±1.4	2.9±0.8
	E	1.7±0.3	1.0±0.1	0.9±0.1
	SE (%)	64.1±3.3	34.3±1.8	15.0±1.1

Organoid viability in the resulting Fraction <40 μm, Fraction 40-85 μm and Fraction >85 μm was measured by digesting the organoid suspension in each fraction into single cells using TrypLE (see Section 2.1.3 for methods) and staining them with Acridine Orange and Propidium Iodide for cell viability assessment with LUNA-FL fluorescence cell counter (see Section 2.2.1 for methods). The results showed a 87.7±3.6%, 83.7±1.7% and 86.7±10.1% of viable cells in Fraction <40 μm, Fraction 40-85 μm and Fraction >85 μm, respectively, expressed as average ± standard deviation of n=2 and N=4. These results revealed that organoid viability was not affected by filtration with PS since the three fractions showed a high percentage of viable cells.

Overall, microscope pictures of separated fractions suggested that organoids were separated by size using PSs, which was confirmed with microscope image quantification and the calculated separation performance indicators, and Fraction 40-85 μm contained a homogeneous organoid size population. In contrast to these results, PSD and separation metrics calculated with MS3

Coulter Counter data showed a slight reduction of single cells in Fraction 40-85 μm compared to Initial mixture and purity, enrichment and separation efficiency of this fraction were low. These discrepancies between microscope pictures and their quantification, and the quantitative results obtained with MS3 Coulter Counter could be caused by an overcounting of the number of particles with MS3 Coulter Counter. Also, small orifices and microchannels of this device could cause organoid breakup during counting and sizing which results in a larger number of particles detected by the analyser. This effect was not noted during polystyrene beads analysis (Section 3.2.3), as these are rigid particles that were not broken during the sizing process. However, cells are deformable particles that could be broken when passing through small orifices or microchannels present in the counter. In agreement with that, it has been described that cell viability may be compromised by the hydrodynamic shear stress and the impact force generated in microfluidic channels (Lee et al. 2018). Therefore, to maximise cell viability, a low flow rate is typically used to infuse or withdraw cells into microfluidic channels, but this may result in cell settling at the bottom of the cell reservoir, causing variations in the cell composition (Lee et al. 2018). It would have been interesting to know the flow rate used by MS3 Coulter Counter to infuse the cell sample, in order to determine whether organoid settling and/or organoid breakup were occurring or not during the counting and sizing measurements with MS3 Coulter Counter. On the other side, some authors have used MS3 Coulter Counter for spheroids counting and sizing and no problems related to spheroids breakup have been reported (Brophy et al. 2008; Arendt et al. 2014; Keller et al. 2012; Bao et al. 2016). No differences in terms of resistance to shear between organoids and spheroids have been described in literature, therefore further research would be necessary to understand the mismatch between the microscopy and the MS3 Coulter Counter results when using Iso50 CRC organoids.

The separation performance of Iso50 CRC organoids using PSs could not be directly compared with other filtration studies because, although PSs have been used in literature as a mere sieving device for organoids (Przepiorski et al. 2018; Mazzucchelli et al. 2019), there has been no detailed investigation of organoid sorting with filters. On the other hand, spheroid size-based fractionation has been previously described by Freyer *et al*. (1987) and it could be considered as a reference point. The authors reported the development of a flow cytometric procedure for viably sorting intact, unstained spheroids on the basis of light-scattering measurements, in order to obtain uniformly-sized populations with diameters in the range of 50-100 μm. They achieved a separation efficiency of 90% for spheroids, which represented a much greater

performance than the separation efficiencies obtained with PSs in this work (Freyer et al. 1987). Flow cytometry is a single cell sorting method that provides an accurate sorting but the complexity of the system and the low throughput capacity of this technique could restrict its use in processing the large amount of organoids generated in a bioreactor. However, filtration is a bulk cell sorting method that can process large cell populations in a short duration of time, but the low separation efficiency obtained in this work needed to be improved to include this fractionation step in the organoid production workflow. An alternative method for size-based separation was suggested, and the designed FB (see specifications in Table 3.6) was tested for organoid fluidisation with the purpose to improve the separation metrics and the results obtained are presented in the section below.

4.2.2 Iso50 CRC organoids size separation with Fluidised Bed

Iso50 CRC organoids cultured for 5 days were recovered from Matrigel with Cell Recovery Solution and the resulting suspension is shown in Figure 4.3A. Moreover, the PSD of the Initial mixture was calculated based on microscope image analysis and MS3 Coulter Counter data and the results are shown in Figure 4.3D and Figure 4.3E, respectively. Organoid suspension containing 5 x 10^5 particles was loaded into the designed FB (specification in Table 3.6) through the top, and organoids were fluidised at 8.49 x 10^{-5} m/s during 1 h with 6+ medium as fluidising medium. Samples elutriated from the top were collected in a tube and at the end of the fluidisation the content of the column was recovered for further analysis. Microscope pictures of the resulting fractions are shown in Figure 4.3B for Top fraction and Figure 4.3C for Column fraction. As expected, Top fraction contained mainly single cells and a few small organoids, which meant that the fluidisation velocity was high enough for single cells fluidisation but not for bigger organoid elutriation. In agreement with that, most of the organoids were kept inside the Column but single cells were also detected in that fraction based on microscope pictures. Also, organoid aggregation was detected in Column fraction, possibly due to the long-time (1 h) of contact between organoids when settled at the bottom of the column. This agreed with a few recent studies that have identified brain organoid merging as an issue associated with the organoid contact with one another over an extended period of time (Bergmann et al. 2018; Ao et al. 2020).

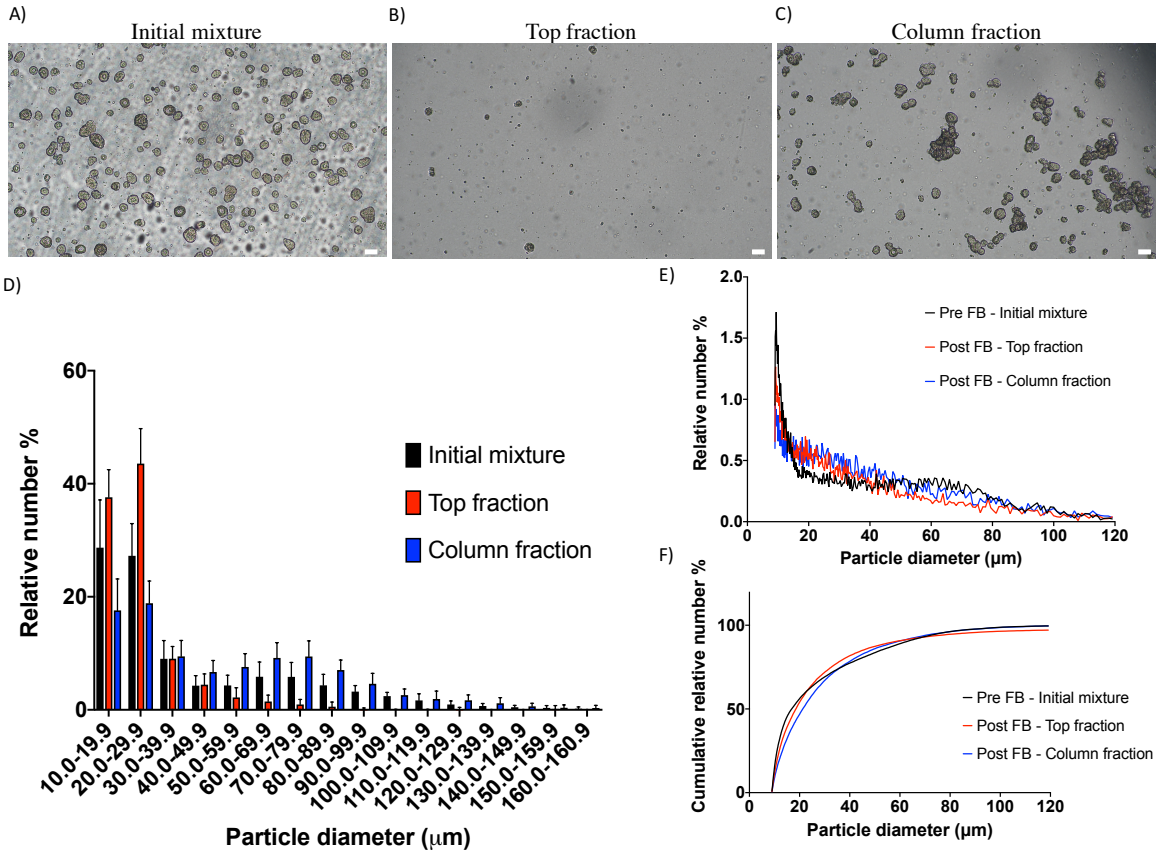

Figure 4.3 Iso50 CRC organoids size-based separation with FB

A. Microscope picture of the Initial organoid mixture recovered from Matrigel after 5 days of culture. Microscope pictures of the two fractions obtained after fluidisation with the designed FB, **B.** corresponds to Top fraction and **C.** corresponds to Column fraction. **D.** Number-based PSD obtained from the image quantification of panels A-C with CellProfiler. **E.** Number-based PSD of the Initial mixture, Top fraction and Column fraction, obtained from MS3 Coulter Counter data. **E.** Cumulative number-based PSD of the Initial mixture, Top fraction and Column fraction, obtained from MS3 Coulter Counter data. **D.**, **E.** and **F.** data corresponds to average of N=3. Error bars in **D.** represent standard deviation. Scale bars correspond to 100 μm.

Microscope images from the resulting fractions were quantified using CellProfiler and the PSDs obtained are shown in Figure 4.3D. PSD of the Top fraction shows that 80% of the particles had a diameter below 30 μm and PSD of the Column fraction presents a peak between 60-80 μm, which confirmed the effectiveness of organoid fluidisation for their size-based separation. Number based-PSDs of the resulting fractions were also measured with MS3 Coulter Counter data and the results are shown in Figure 4.3E, along with number-based PSD of the Initial mixture. The starting suspension contained a large number of 10 μm particles, corresponding to single cells, that were reduced in Column fraction after fluidisation. However, Column fraction did not show a peak at a higher size range based on MS3 Coulter Counter data. Figure 4.3F shows the cumulative number-based PSD of the suspensions before and after separation, and no significant differences were observed between them. Also, MS3 Coulter Counter data was used to calculate Sauter mean diameter of the different samples and the values obtained were 67.07±2.77 μm for Initial mixture, 61.08±2.28 μm for Top fraction and 63.71±0.22 μm for Column fraction. This also showed the close resemblance between samples before and after fluidisation when MS3 Coulter Counter results were analysed.

The composition of the Initial mixture, Top fraction and Column fraction were calculated with MS3 Coulter Counter data and results are shown in Figure 4.4A. As previously shown, the composition of the Initial mixture corresponded to almost 80% of particles with a diameter < 40 μm and 20% of particles with a diameter in the range 40-85 μm. The composition of the resulting fractions obtained after fluidisation was very similar to the composition of the Initial mixture, which indicated a low separation ability of the FB. Particles < 40 μm were slightly concentrated in Top fraction compared to Initial mixture, however, the percentage of particles 40-85 μm in Column fraction remained constant. Moreover, only 3% of the particles in Initial mixture had a diameter > 85 μm, because day of culture was previously optimised to maximise the volume of organoids in the range of 40-85 μm diameter (see Section 5.2.1 for further information regarding Iso50 CRC organoids growth kinetics), and this concentration remained equal inside the column after fluidisation. However, due to organoid aggregation in Column fraction observed in microscope pictures (Figure 4.3C), concentration of particles > 85 μm in the column was expected to be higher. This could suggest that organoid counting and sizing with MS3 Coulter Counter were affected by the small diameter of the aperture and microchannels present in the device (Figure 4.5).

Furthermore, organoid recovery after fluidisation is shown in Figure 4.4B. Similar to PS filtration, organoid recovery was over 100%, which indicated that more particles were

recovered in Top fraction and Column fraction than the number of particles loaded in the FB. The recovery of particles < 40 μm was 151% (88.9±4.0% in Top fraction and 62.6±4.5% in Column fraction), 117% for particles 40-85 μm (59.7±6.9% in Top fraction and 57.7±4.3% in Column fraction) and 131% for particles > 85 μm (68.5±14.0% in Top fraction and 62.6±6.3% in Column fraction). This could indicate that the fluidisation process or the counting process with MS3 Coulter Counter broke some organoids generating smaller particles in the system (Figure 4.5), however, recovery of bigger particles was also greater than 100%. This might be explained by overestimation of organoid counting with MS3 Coulter Counter due to background noise (Figure 4.5).

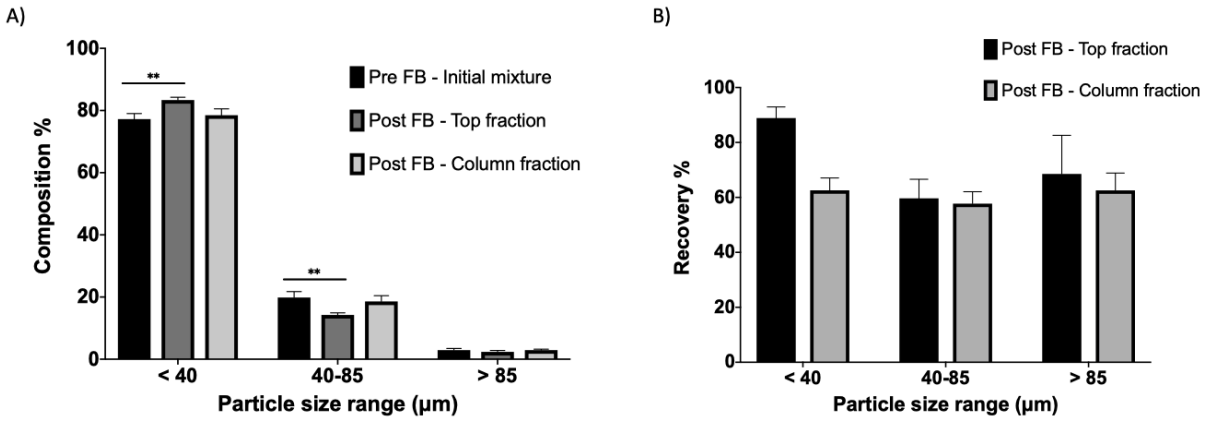

Figure 4.4 Iso50 CRC organoids separation performance using the designed FB

Iso50 CRC organoids were cultured for 5 days from single cells and fractionated using the designed FB. **A.** Organoid composition, calculated with Equation 2.3, for Initial mixture and the resulting fractions obtained after fluidisation, i.e. Top fraction and Column fraction. **B.** Organoid recovery, calculated with Equation 2.5, in the resulting fractions obtained after fluidisation, i.e. Top fraction and Column fraction. Error bars represent standard deviation (n=3, N=3).

Purity, enrichment and separation efficiency based on microscope image quantification and MS3 Coulter Counter data obtained for organoid fluidisation are summarised in Table 4.2. According to image-based quantification, a high enrichment of particles < 40 μm in Top fraction (E = 5.6) was obtained with a high purity (90.1%). Particles 40-85 μm and particles > 85 μm were also enriched in Column fraction, but at a lower extent, E = 2.2 and E = 1.5 for particles 40-85 μm and particles > 85 μm, respectively, with a 39.9% purity for particles 40-85 μm and 14.2% purity for particles > 85 μm. Moreover, the fluidisation achieved a high separation efficiency for particles 40-85 μm (SE = 81.3%) and particles > 85 μm (96.7%) in

the Column fraction, which indicated that almost all particles > 40 μm were captured in the Column fraction. The good separation performance indicators obtained from the quantification of microscope images of the Initial mixture and Top and Column fractions differed from the results obtained from MS3 Coulter Counter data, which are shown below. Based on MS3 Coulter Counter results, there was some enrichment of particles < 40 μm in Top fraction (E = 1.5), which presented a purity of 83.4%. Particles 40-85 μm and particles > 85 μm were not enriched in Column fraction and purities obtained in that fraction were very low due to the high number of small particles inside the Column after fluidisation. Moreover, the designed FB did not show a good organoid separation efficiency, as only 58.7% of the total collected < 40 μm particles were found in Top fraction. Similarly, separation efficiencies of large organoids in Column fraction were calculated to be 49.3% and 48.2% for particles 40-85 μm and particles > 85 μm, respectively, implying that half of the available large organoids were not captured in the Column fraction, thus being recovered in Top fraction. These results did not agree with microscope pictures of Top fraction, wherein practically not a large organoid was observed. Overcounting of particles with MS3 Coulter Counter could be a possible explanation for that discrepancy between microscope pictures and their quantification, and MS3 Coulter Counter results, although a blank measurement was always previously performed with medium and subtracted from the organoid sample measurement. More specifically, a different blank was used for each suspension: Initial mixture blank consisted of Cell Recovery Solution, Column fraction blank was 6+ medium and Top fraction blank consisted of a mixture 1:1 of Cell Recovery Solution and 6+ medium because during 1 h of fluidisation, column was washed with two column volumes, corresponding to one column volume of Cell Recovery Solution in which organoids were initially suspended and one column volume of the fluidising medium, which was 6+ medium.

Table 4.2 Iso50 CRC organoids separation performance using the designed FB.

Purity (P%), Enrichment (E) and Separation efficiency (SE%) were calculated with Equation 2.4, Equation 2.6 and Equation 2.7, respectively. Data is presented as average±standard deviation with n=3, N=3.

Based on	Index	<40 μm in Top fraction	40-85 μm in Column fraction	>85 μm in Column fraction
Microscope image quantification	P (%)	90.1±3.7	39.9±1.4	14.2±3.7
	E	5.6±1.8	2.2±0.7	1.5±0.5
	SE (%)	66.2±2.1	81.3±5.0	96.7±3.1
MS3 Coulter Counter data	P (%)	83.4±0.9	18.6±1.8	2.9±0.3
	E	1.5±0.2	0.9±0.1	1.0±0.1
	SE (%)	58.7±2.6	49.3±2.4	48.2±4.1

Organoid viability in the resulting Top and Column fractions was measured by digesting the organoid suspension in each fraction into single cells using TrypLE (see Section 2.1.3 for methods) and staining them with Acridine Orange and Propidium Iodide for cell viability assessment with LUNA-FL fluorescence cell counter (see Section 2.2.1 for methods). The results showed a 94.1±4.2% and 81.6±6.6% of viable cells in Top and Column fraction, respectively, expressed as average ± standard deviation of n=2 and N=3. The lower viability obtained in the Column fraction when compared to the Top fraction might be explained due to the presence of larger organoids that could present necrotic cores. Despite this, the percentage of viable cells in Top and Column fractions was high, which indicated that fluidisation did not have a negative impact on organoid viability.

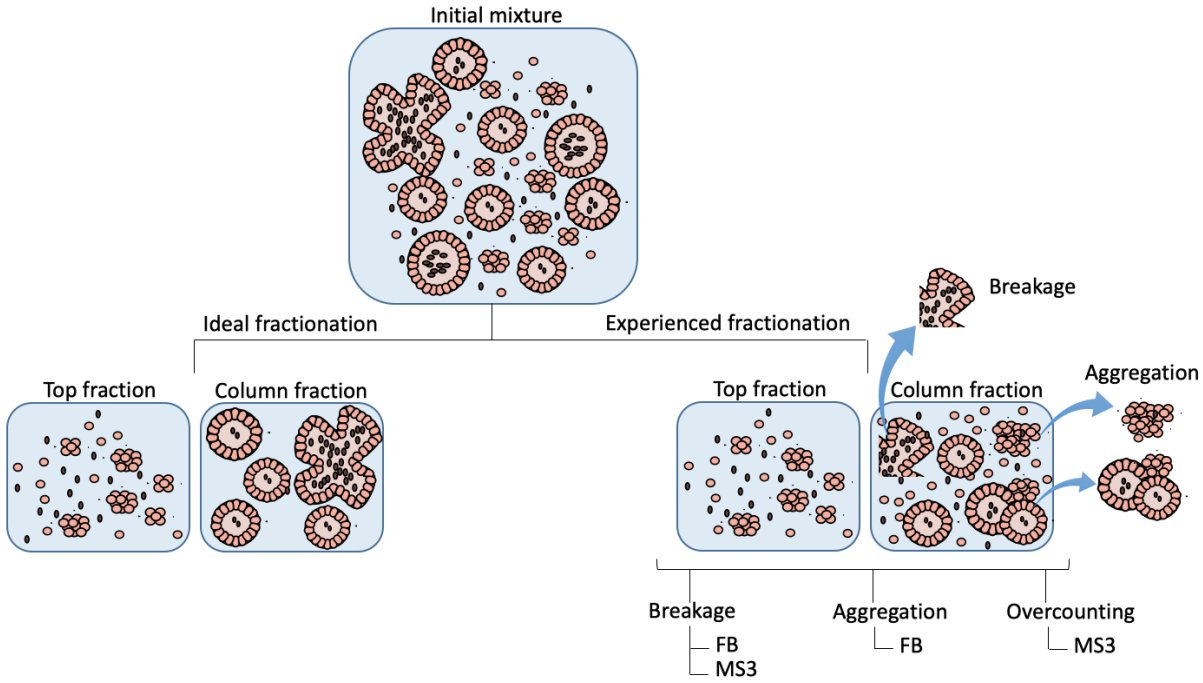

Figure 4.5. Schematics of organoid fractionation in a FB – Ideal fractionation vs. Experienced fractionation

Organoid fractionation in the designed FB is represented in this diagram. An ideal fractionation would separate single cells and small organoids (Top fraction) from medium size and large organoids (Column fraction). However, the experienced fractionation presented a Column fraction with some organoids broken and some aggregated, apart from a large amount of single cells. Furthermore, counting and sizing with MS3 Coulter Counter could induce organoid breakup and/or particle overcounting, which could explain the discrepancy between microscope pictures and MS3 Coulter Counter results.

In summary, fluidisation of an organoid suspension obtained after 5 days of culture removed single cells that were elutriated from the top. However, 1 h of fluidisation was not enough for complete elimination of them, since single cells were also found in Column fraction images. Maybe longer fluidisation could further reduce the amount of single cells inside the column. In addition, microscope pictures of the column content revealed organoid aggregation, which could be associated with the contact of organoids forming the bed inside the column. As observed previously with PSs separation, results obtained with microscope pictures and MS3 Coulter Counter data differed in organoid separation capacity. Quantification of microscope pictures showed a better separation performance than the results obtained with MS3 Coulter Counter. Sizing and counting with MS3 Coulter Counter involved extra handling and sample processing, that could affect organoid integrity, although this device is recommended for cell analysis and no issues have been reported for spheroids counting (Brophy et al. 2008; Arendt et al. 2014; Keller et al. 2012; Bao et al. 2016).

This is the first time that a FB has been applied for organoid size-based separation, and the use of FB technology for cell size separation has not been reported in literature to our knowledge. Furthermore, cells could be considered as non-rigid particles and although gel beads made of, e.g. alginate, agar or k-carrageenan, have been widely used in FBB for cells or enzymes immobilisation (van Zessen et al. 2005), there is little work on size-based separation of non-rigid particles. Indeed, FB technology has not been described for that purpose. Moreover, size-based separation of non-rigid bodies has been achieved in rotating drums for deformable rubber particles (Kuo et al. 2006), and in deterministic lateral displacement (DLD) arrays (Salafi et al. 2019). In this regard, Tottori *et al*. (2020) proposed a microfluidic DLD device to separate MCF-7 cells, which are used as a model of circulating tumour cells (CTCs), from whole blood cells, since they are smaller than MCF-7 cells. The authors achieved a recovery and purity of the MCF-7 cells collected of 99.0% and 17.9%, respectively (Tottori & Nisisako 2020). Also, CTC clusters (2-100 cells) were separated from blood cells using a microfluidic DLD device that resulted in 99% recovery of CTC clusters, cell viabilities over 87% and the most important, the device caused minimal cluster disruption because the relative ratios of clusters and single cells remained relatively unchanged after operation (purity values not reported) (Au et al. 2017). Taking into account that a different separation mechanism is applied in FB and DLD technologies, the results obtained in this work were compared with these published data. On the one hand, the purity reported by Tottori *et al*. (2020) (17.9%) was similar to the purity of Iso50 CRC organoids with a diameter between 40-85 μm obtained in the Column fraction with MS3 Coulter Counter results (18.6%, Table 4.2), although a higher purity was obtained based on the microscope image quantification (39.9%, Table 4.2). On the other hand, high recoveries were achieved in all studies, although the values obtained for Iso50 CRC organoid were over 100% (Figure 4.4B). As discussed previously in this section and depicted in Figure 4.5, this could indicate an overcounting of particles with MS3 Coulter Counter and/or the breakage of some organoids during fluidisation or during the counting process with MS3 Coulter Counter (Figure 4.5). In relation to that, the most valuable achievement by Au *et al*. (2017), when compared to organoid fluidisation, corresponded to the minimal shedding of single cells or disruption of clusters into smaller cluster fragments, which indicated minimal cluster dissociation. For that reason, it would be interesting to test a DLD device for organoid size-based separation in the future, to study whether an improvement of the separation metrics could be achieved.

In the following section, the two techniques considered in this work for Iso50 CRC organoid separation, i.e. PSs and FB, are compared and pros and cons for each technique are described.

4.2.3 Comparison of organoid size-based separation by PS and FB

This work aimed to separate organoids based on size in order to increase drug assay reproducibility. A standard sizing technique, as filtration with PSs of 40 μm and 85 μm pore size, was first tested to generate defined organoid subpopulations. Subsequently, organoid fluidisation was also assessed as a new approach for organoid size-based separation using a custom-built column. Both techniques are compared below, not only in terms of quantitative results obtained with microscope pictures and MS3 Coulter Counter, but also in terms of operation mode, cost, time, flexibility, scalability, and improvement capacity.

Image analysis of samples pre and post separation (Figures 4.1A-E for PS filtration and Figures 4.3A-D for fluidisation), showed differences between the techniques. Filtration with PSs produced three fractions. Fluidisation, which in principle might have been able to isolate organoids of any size, in practise was able to generate two fractions. The fraction corresponding to particles elutriated through the top of the column primarily comprised single cells and very small cell clusters, while particles that remained in the column were organoids. Microscope pictures and their quantification revealed that the two techniques were able to generate fractions with particles of different sizes, including a fraction with mainly single cells and some small organoids, and a fraction with mostly organoids.

The main difference between the two techniques came from the particle size range within the target fraction. PSs generated the Fraction 40-85 μm including organoids of consistent size and very low content of single cells. However, the Column fraction obtained after fluidisation contained all sized organoids and a higher number of single cells. Furthermore, microscope pictures showed evident organoid aggregation in the column content. Therefore, based on microscope pictures, both approaches provided a size separation of the particles present in the organoid suspension, but PSs seemed to be a better option for the removal of single cells and larger organoids.

Second, results obtained with MS3 Coulter Counter data showed large similarity between both techniques, although discrepancies with microscope pictures. Based on MS3 Coulter Counter results, organoid composition remained unchanged after the separation process, regardless of the approach. Organoid recoveries were surprisingly over 100% for both techniques, although

much higher amount of particles were recovered after filtration process compared to fluidisation. The largest difference was found in recovery of particles <40 μm, with a recovery value of 203% for filtration versus 155% for fluidisation. This could indicate that organoid integrity might be more affected when passing through the membranes than during fluidisation. Furthermore, based on MS3 Coulter Counter results, no significant differences were found in purity and enrichment values obtained for both techniques but higher separation efficiency of 40-85 μm particles was achieved with fluidisation. Thus, MS3 Coulter Counter data showed very similar results between the two approaches, but fluidisation offered a slight better separation efficiency of target size particles.

Third, organoid viability of the resulting fractions showed high percentage of viable cells in Fraction <40 μm, Fraction 40-85 μm and Fraction >85 μm, as well as, Top and Column fractions.

Since the separation principle is different for each technique, the operation procedure was not the same for both methods. Next, operational aspects are compared assuming the same volume of sample processed (10 mL organoid suspension) as in this work. In terms of consumables required, two single-use PSs (40 μm and 85 μm) were used for filtration, and a peristaltic pump and a custom-made glass column were needed for fluidisation. The higher cost of the column and the pump, compared to PSs, could be depreciated over time as the column could be reused after sterilisation. Furthermore, same volume of 6+ medium (25-30 mL) was used for both approaches in this study. Regarding operation time, filtration with PS was a quicker procedure (around 30 min) when compared with fluidisation (around 2 h, including column assembly), although these times could vary depending on the sample volume. Here, due to the low sample volume (10 mL organoid suspension), a batch mode was employed for both technologies. However, for larger volumes FB could be a better option, as it could offer the possibility to work in continuous mode and PSs might experience clogging problems. This correlates with process scalability, while FB column dimensions could be easily increased, PSs present a small surface area and other formats (e.g. membrane stack disc filters) are required for filtration of larger volume samples. Moreover, the ease of each process was evaluated, and filtration with PSs was considered a much simpler procedure compared to fluidisation. Furthermore, PSs provide more flexibility regarding the target size range, due to the large variety of membrane pore sizes offered. By contrast, target size range could be more laborious to change in FB, because this requires previous studies to adjust the fluidisation velocity to the specific organoid diameter range. Summarising the operational aspects, filtration with PSs can be considered a

quick, flexible and easy process suitable for organoid size-based separation of small volume samples, as in this work. However, PSs could present clogging problems when processing larger volumes or highly concentrated samples. Thus, continuous operation and easier scalability of FB could benefit organoid size-based separation of larger samples.

It is worth mentioning that FB design for organoid separation has higher capacity for improvement than PSs whose design is already defined. FB design proposed in this work could evolve to more efficient set-ups with further studies. For example, continuous operation of a FB might require the addition of a bottom exit to provide a continuous source of the larger organoid fraction. On the other side, a gradual increase of fluidisation velocity could enable the progressive elutriation of different sized organoids.

Below, Table 4.3 summarises the different aspects assessed in this Section and it can be concluded that PS might present more advantages than FB for an organoid size-based separation but the current FB design has more chance of being improved and adapted to large-scale processes and commercial applications.

Table 4.3 Comparison of PSs and FB performance for an organoid size-based separation

Aspect	PS	FB
Removal of single cells based on microscope pictures quantification	Good	Medium
Separation metrics results	Poor	Poor
Organoid viability	Good	Good
Consumables/cost	Low	Medium
Operation time	Low	High
Operation mode	Batch	Batch/Continuous
Scalability	Poor	Good
Ease of the process	Good	Medium
Flexibility target size range	Good	Low
Improvement capacity	Low	High

4.2.4 Drug assay variability with fractionated Iso50 CRC organoids

The use of organoid/spheroids for drug discovery is challenged due to drug response variability associated with organoid/spheroid size heterogeneity. Differences in size leads to limitation in

nutrients, oxygen and drug diffusion that results in various drug responses (Jung et al. 2019; Lim et al. 2018). In order to enhance the reproducibility of drug response tests, an organoid size-based fractionation was proposed in this work and this section evaluates whether drug response differs between fractionated and non-fractionated population of Iso50 CRC organoids. The chosen technique to perform the size separation was filtration with PSs of 40 μm and 85 μm, rather than fluidisation, due to the better results obtained with filtration regarding the removal of single cells based on the microscope pictures quantification. Iso50 CRC organoids grown for 5 days were harvested and recovered from Matrigel. Organoid suspension was fractionated with PSs of 40 μm and 85 μm as described in Section 2.6.1 and the resulting fractions were frozen (-80°C) following Cellesce Ltd workflow. As a control, non-fractionated organoids were also frozen (-80°C). Organoids were thawed and seeded in Matrigel (200 organoids per well) and incubated at 37°C during 48h for organoid recovery. Then, organoids were treated with known colorectal cancer targeting compounds, following the same procedure as Cellesce Ltd in their organoid expansion validations. First, viability of fractionated organoids after the process of freeze-thaw was tested and results obtained are shown below.

4.2.4.1 Fractionated organoid viability after freeze-thaw process

Viability of fractionated organoids after the process of freeze-thaw was tested to determine whether this process could affect organoid viability. For that, live/dead staining with Hoechst (all cell stain) and Propidium Iodide (dead cell stain) was applied to fractionated and non-fractionated organoids that have undergone the process of freeze-thaw and plating for 48 h. As a control, fractionated and non-fractionated organoids recovered after 5 days of culture were also stained with Hoechst and Propidium Iodide (without going through the process of freeze-thaw). Figure 4.6A shows that organoid size-based separation with PSs did not affect organoid viability, since organoids did not contain more dead cells in the post separation fractions. Hoechst and Propidium Iodide staining analysis was performed with CellProfiler to calculate the average number of dead cells per organoid and the results obtained were: 1.7±0.4 for Non-fractionated organoids and 0.8±0.2, 1.0±0.1 and 3.8±0.3 for Fraction < 40 μm, Fraction 40-85 μm and Fraction >85 μm, respectively, as shown in Figure 4.6D. The larger number of dead cells per organoid in Fraction > 85 μm could be explained due to diffusional limitations of nutrients or oxygen in larger organoids. Furthermore, clear size differences were detected

between the three resulting fractions and the amount of organoids in Fraction 40-85 μm was higher than the number of organoids in the other fractions. On the other side, freeze-thaw process produced an increase in the number of dead cell in both fractionated and non-fractionated organoid suspensions, as shown in Figure 4.6B, which indicated that cell death was associated with the cryopreservation process, rather than fractionation process. Cell stress suffered during freeze-thaw process could be associated with mechanical membrane damage caused by intracellular ice formation and dehydration that increased cell damage (Wolfe & Bryant 1999). After thawing, organoids were plated in Matrigel, cultured during 48 h and the live/dead staining after the recovery time is shown in Figure 4.6C. 48 h of recovery time was chosen to follow Cellesce Ltd workflow regarding the time lapse between organoid thawing and plating, and drug treatments. The amount of dead cells was considerably reduced, which probably were removed during washing steps before plating, and organoid viability was deemed to be high enough for fractionated and non-fractionated organoid use in subsequent assays. Number of dead cells per organoid was calculated with Hoechst and Propidium Iodide staining analysis with CellProfiler and a slight increase was obtained compared to the number of dead cells in organoids that did not pass through the freeze-thaw process. Figure 4.6D shows that the average numbers of dead cells per organoids were: 3.4±1.9 for Non-fractionated organoids and 1.1±0.2, 2.4±1.4 and 6.9±2.0 for Fraction< 40 μm, Fraction 40-85 μm and Fraction >85 μm, respectively. As indicated before, the higher number of dead cells obtained for Fraction > 85 μm could be related with the increase of organoid diameter and thus, diffusional distance for nutrients and oxygen. In contrast, the content of dead cells in organoids recovered in Fraction 40-85 μm was low relative to the total number of cells per organoid (11-76 cells per organoid of 40-85 μm size, see Section 5.2.2) and therefore unlikely to influence overall fraction viability, since entirely dead organoids were rarely observed. Furthermore, viability of organoids thawed from Fraction 40-85 μm was also proved due to the increase of organoid diameter (measured with CellProfiler) after being plated for 48 h compared with their diameter just after the fractionation (Figure 4.6E).

In summary, viable organoids were obtained after the fractionation step and the subsequent freeze-thaw process. Furthermore, the low number of dead cells per organoid in Fraction 40-85 μm after 48 h of culture post-thawing was unlikely to affect the overall fraction viability. This study including the fractionation step, supplemented the previous freeze-thaw protocol optimised in the Dale lab to improve Iso50 CRC organoid recovery from freezing conditions (Badder 2017a).

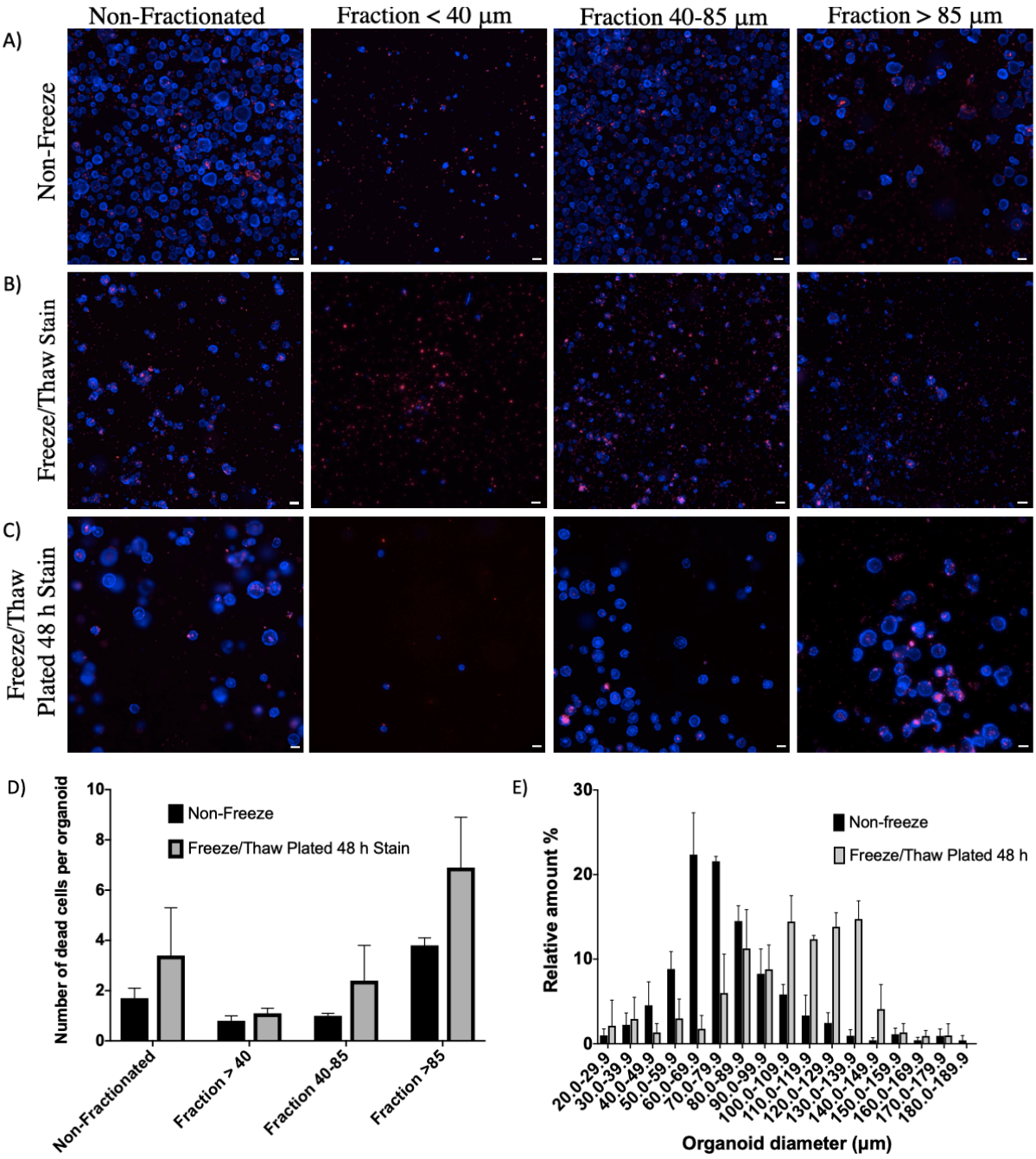

Figure 4.6 Assessment of fractionated and non-fractionated organoid viability after freeze-thaw process

Representative images of live/dead stain with Hoechst (blue, all cell stain) and Propidium Iodide (red, dead cell stain) of fractionated and non-fractionated organoids after the separation process (**A.**), after the freeze-thaw process (**B.**) and after the freeze-thaw process, plating in Matrigel and culture for 48 h (**C.**). Scale bars correspond to 100 µm. **D.** Quantification of number of dead cells per organoid using CellProfiler software. **E.** Organoid size distribution of Fraction 40-85 µm before freezing and after passing through the process of freeze-thaw and plating for 48h. Organoid diameter was calculated by Hoechst staining analysing with CellProfiler. Error bars represent standard deviation (n=3, N=1).

4.2.4.2 Drug treatment assays with fractionated organoids

After 48 h of recovery, fractionated and non-fractionated Iso50 CRC organoids were treated with LGK974, 5-FU and Trametinib and each drug was applied in a 9 point, two-fold titration. These drugs were chosen because they are known CRC targeting compounds that Cellesce Ltd uses for validation of their organoid expansions. First, LGK974 is a porcupine inhibitor that reduces Wnt ligand secretion and inhibits the Wnt signalling pathway arresting cell cycle and inducing apoptosis in CRC cell lines (Bagheri et al. 2019). Since Wnt is essential for maintenance and self-renewal of epithelial stem cells (Nusse 2008), it is expected that LGK974 treatment would have a major effect on the growth of organoids with a higher percentage of stem cells, and therefore small and medium-sized organoids. Second, 5-FU is the most widely used treatment regime for CRC and is thought to function by inhibiting thymidylate synthase (Gill et al. 2003). This blocks DNA biosynthesis and consequently, cells contained in any organoid size could be affected by 5-FU. Third, Trametinib is a MEK1/2 inhibitor that inhibits RAS signalling through mitogen-activated protein kinase (MAPK) cascade suppression. Trametinib has a better response in BRAF mutant cancer cells than KRAS mutant cancer cells because Trametinib treatment leads to induction of a feedback loop, via SPRY and DUSP proteins, and reactivation of the MAPK pathway (Luke et al. 2014). RAS mutant, but not BRAF mutant, tumours exhibit a relative abundance of wild-type RAF proteins, thus in RAS mutant tumours, MEK inhibitor-induced feedback mediates activation of wild-type RAF proteins through the formation of CRAF-MEK complexes (Luke et al. 2014). This results in feedback phosphorylation of MEK and an eventual increase in downstream MAPK pathway activation (Luke et al. 2014; Dai et al. 2019). Iso50, the organoid line used in this study, contained mutation in KRAS and therefore an inhibitory impact was not expected when Iso50 organoids were treated with Trametinib. Nevertheless, this compound was included in the study to assess the reproducibility in drug response of fractionated organoids when treated with a non-effective drug. Furthermore, drug response of fractionated organoids was expected to be more reproducible and easier to interpret than the response of non-fractionated ones, since a more homogeneous organoid size population is assumed to present a more uniform cell type composition (Arora et al. 2017; Jung et al. 2019; Yu et al. 2019).

After 5 days of compound treatment, organoids were fixed and stained with Hoechst (blue, DNA) and Phalloidin (red, cytoskeleton) to mark nuclear and f-actin structures, respectively, and all conditions were imaged. A total of three replicate (n = 3) wells were used per condition

with three biological replicates (N = 3). For visual assessment of drug response, representative images of LGK974, 5-FU and Trametinib treatment are shown in Figure 4.7, Figure 4.8 and Figure 4.9, respectively. Iso50 CRC fractionated and non-fractionated organoids responded to the three drugs, since a progressive change in organoid morphology was detected in all fractions from the lowest to the highest drug concentration. Big differences in morphology between fractionated and non-fractionated organoids and between the fractions were not detected at a specific drug concentration. Nevertheless, organoids in Fraction 40-85 μm seemed to present a more uniform morphology, and less cell debris that could generate noise in drug response. Also, in agreement with results shown in Figure 4.6C, Fraction < 40 μm contained less organoids than the other samples since lower number of organoids were seeded after freeze-thaw process. Ideally, for a fair comparison across different size fractions, same total cell number should have been seeded. For LGK974 and 5-FU treatments, organoids suffered an obvious deterioration with the increase in drug concentration, since organoid size was highly reduced at the highest concentrations. Although Iso50 organoids should not respond to Trametinib treatment because this compound leads to induction of a feedback loop in RAS mutant tumours, via SPRY and DUSP proteins, and reactivation of the MAPK pathway, Iso50 CRC organoids treated with this compound seemed to experience a change in organoid shape rather than in organoid size when drug concentration was higher than 1.56 nM. Other factors can activate the MAPK cascade as well, since a KRAS mutation is not the only genetic driver of activated MEK signalling, therefore further investigation is required to determine the mechanism underlying the Trametinib effect in Iso50 CRC organoids.

In order to easily visualise morphological alterations due to compound treatment, Figure 4.10 shows images of organoids after 5 days of treatment with the lowest and the highest concentration of each compound at a higher magnification. First, fractionated and non-fractionated Iso50 CRC organoids were sensitive to LGK974 treatment, since structural integrity was lost at the highest drug concentration. Organoids did not show a single epithelial cell layer anymore and became dense, compact and consisted of apoptotic-like cells, regardless of the size fraction. Also, lumen size was reduced and sometimes speckled satellite cells were observed. Opposite of what was expected, LGK974 induced apoptosis of organoids of any size and the effect was not limited to small organoids in which the relative amount of stem cells might be higher than in larger organoids. For that reason, it would be interesting to determine the cell type composition of different size organoids in future studies. Moreover, the LGK974 concentrations tested in this work were much larger than physiological concentrations reported

in literature (below 50 nM, (Picco et al. 2017; Liu et al. 2013)). Thus, organoid deterioration observed in Figure 4.7 and Figure 4.10 could be as an indication of off-target effects at high LGK974 concentrations. This might explain why the morphological changes were the same in all fractions, regardless of the organoid size, and thus relative stem cell amount. Second, morphology of fractionated and non-fractionated organoids varied similarly when organoids were treated with 5-FU for 5 days. Organoid structures appear to be reduced in size, although maintained the organisational structure of a single epithelial cell layer with central lumen. Third, neither organoid integrity was disturbed with Trametinib treatment, nor did the structures appear to become more compact. However, organoid appearance of both fractionated and non-fractionated samples was altered in terms of morphological type, which differed from the null inhibitory effect expected when Iso50 CRC organoids were treated with Trametinib. Untreated Iso50 CRC organoids presented a mixture of branched and cystic structures but the number of branched structures significantly decreased in response to Trametinib and only cystic morphologies were observed at the highest drug concentration. This observation has previously been reported by Zhan et al. and Betge et al., who showed that Trametinib induced a morphological change of cancer organoids resulting in a cystic phenotype, which is characteristic of the high Wnt activity induced by Trametinib (Zhan et al. 2019; Betge et al. 2019; Boretto et al. 2017; Merenda et al. 2020).

Overall, the descriptive analysis of morphometry showed that both fractionated and non-fractionated organoids responded to LGK974, 5-FU and Trametinib treatment. On the one hand, LGK974 and 5-FU induced cell death, as revealed by organoid deterioration and overall darker appearance. On the other hand, Trametinib induced a cystic reorganisation and organoid numbers did not appear to be largely affected, since Iso50 is a KRAS mutant line and organoid survival was expected. Moreover, it was difficult to assess with these results whether organoid fractionation increased drug response reproducibility, as no obvious differences were found between non-fractionated and Fraction 40-85 μm samples. However, images corresponding to Fraction 40-85 μm showed that this fraction contained less cell debris and single cells, which could be beneficial to reduce drug response variability. Further studies with focus on quantitative morphometric measurements, as the ones reported by (Badder et al. 2019; Sandercock et al. 2015; Borten et al. 2018; Ahonen et al. 2017; Karolak et al. 2019), will need to be undertaken to capture subtle effects of drug-induced phenotypes and assess whether organoid fractionation could generate more reproducible results.

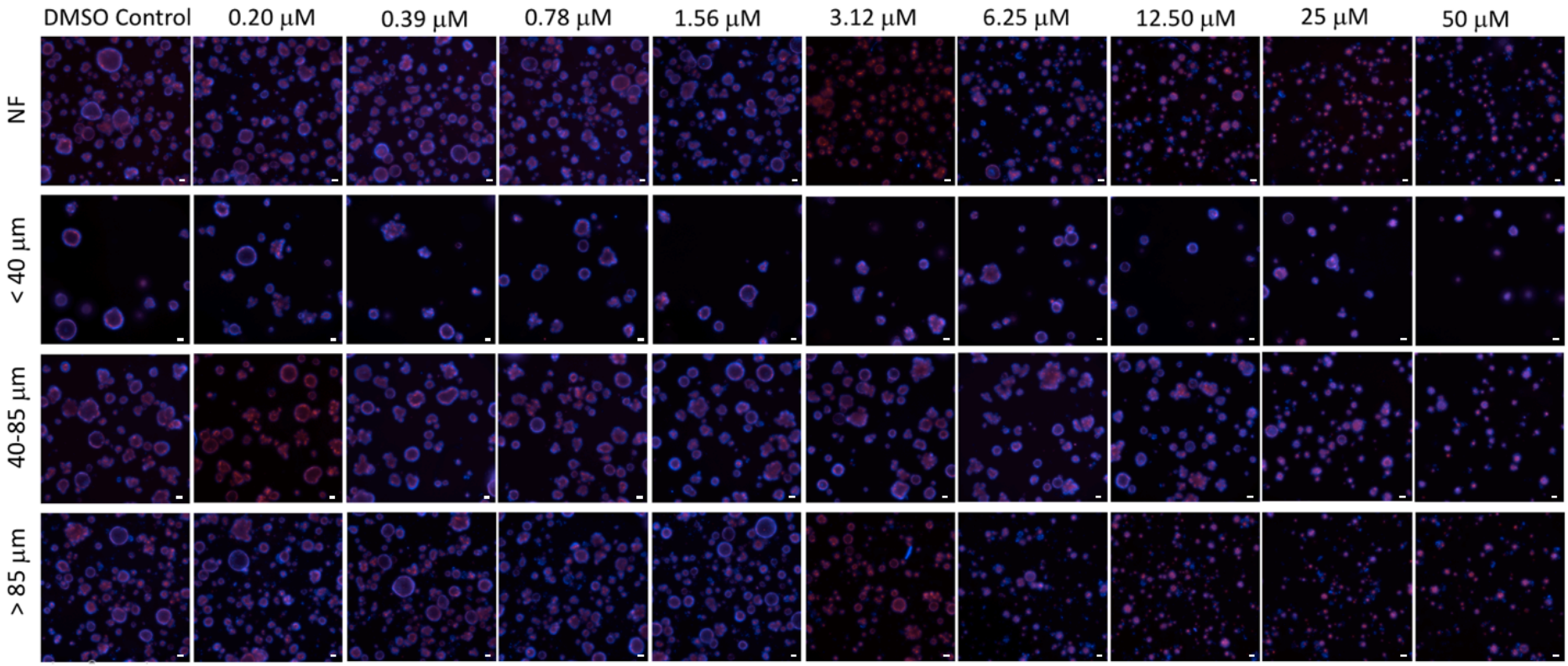

Figure 4.7 Hoechst and Phalloidin staining of fractionated and non-fractionated organoids after LGK974 treatment

Iso50 CRC organoids grown for 5 days were fractionated with PS of 40 µm and 85 µm. Non-fractionated (NF) organoids and organoids present in Fraction <40 µm, Fraction 40-85 µm and Fraction > 85 µm were frozen (-80°C), thawed and plated in Matrigel. After 48 h recovery, organoids were treated with LGK974 in a 9 point, two-fold titration (LGK974 concentrations are specified in the figure). After 5 days of drug treatment, organoids were fixed and stained with Hoechst (blue, DNA stain) and Phalloidin (red, cytoskeleton stain). Representative images of organoids captured following treatment with LGK974 of n=3, N=3 replicates. Scale bars correspond to 100 µm.

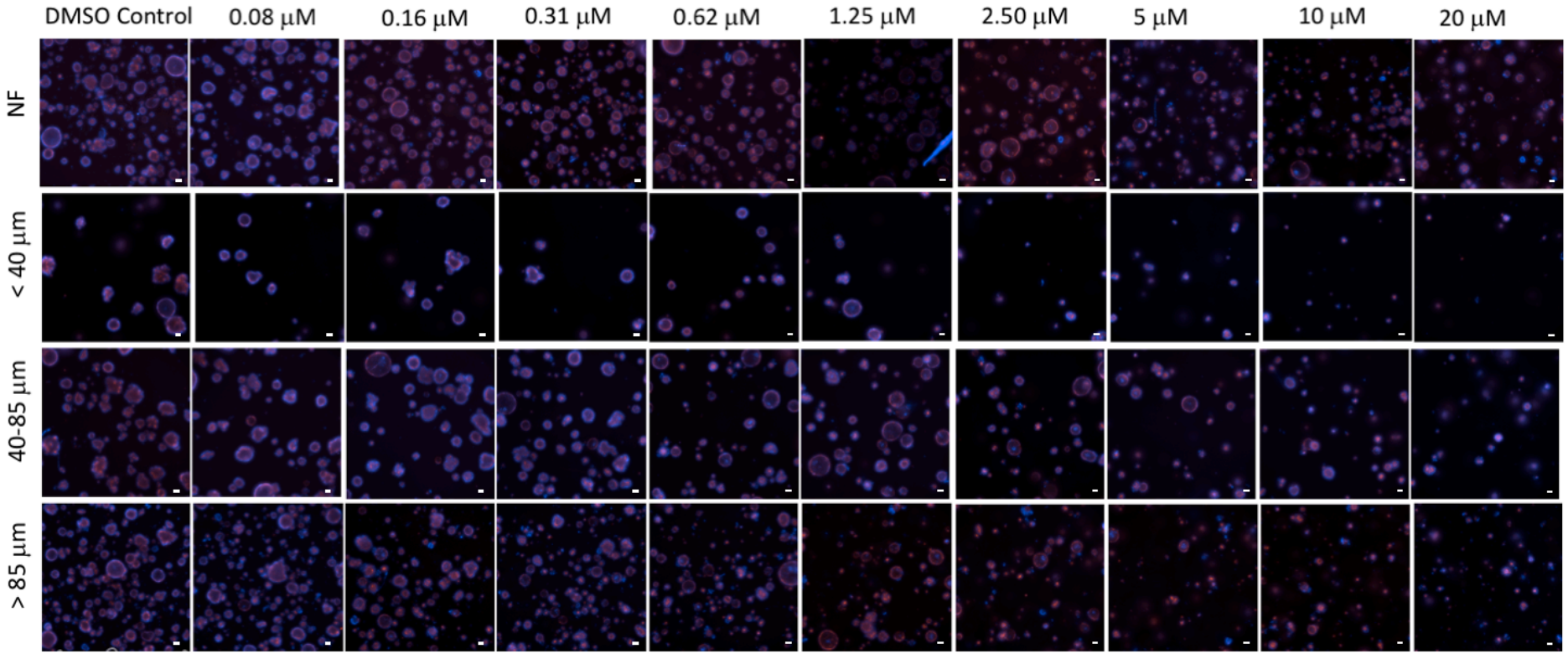

Figure 4.8 Hoechst and Phalloidin staining of fractionated and non-fractionated organoids after 5-FU treatment

Iso50 CRC organoids grown for 5 days were fractionated with PS of 40 µm and 85 µm. Non-fractionated (NF) organoids and organoids present in Fraction <40 µm, Fraction 40-85 µm and Fraction > 85 µm were frozen (-80°C), thawed and plated in Matrigel. After 48 h recovery, organoids were treated with 5-FU in a 9 point, two-fold titration (5-FU concentrations are specified in the figure). After 5 days of drug treatment, organoids were fixed and stained with Hoechst (blue, DNA stain) and Phalloidin (red, cytoskeleton stain). Representative images of organoids captured following treatment with 5-FU of n=3, N=3 replicates. Scale bars correspond to 100 µm.

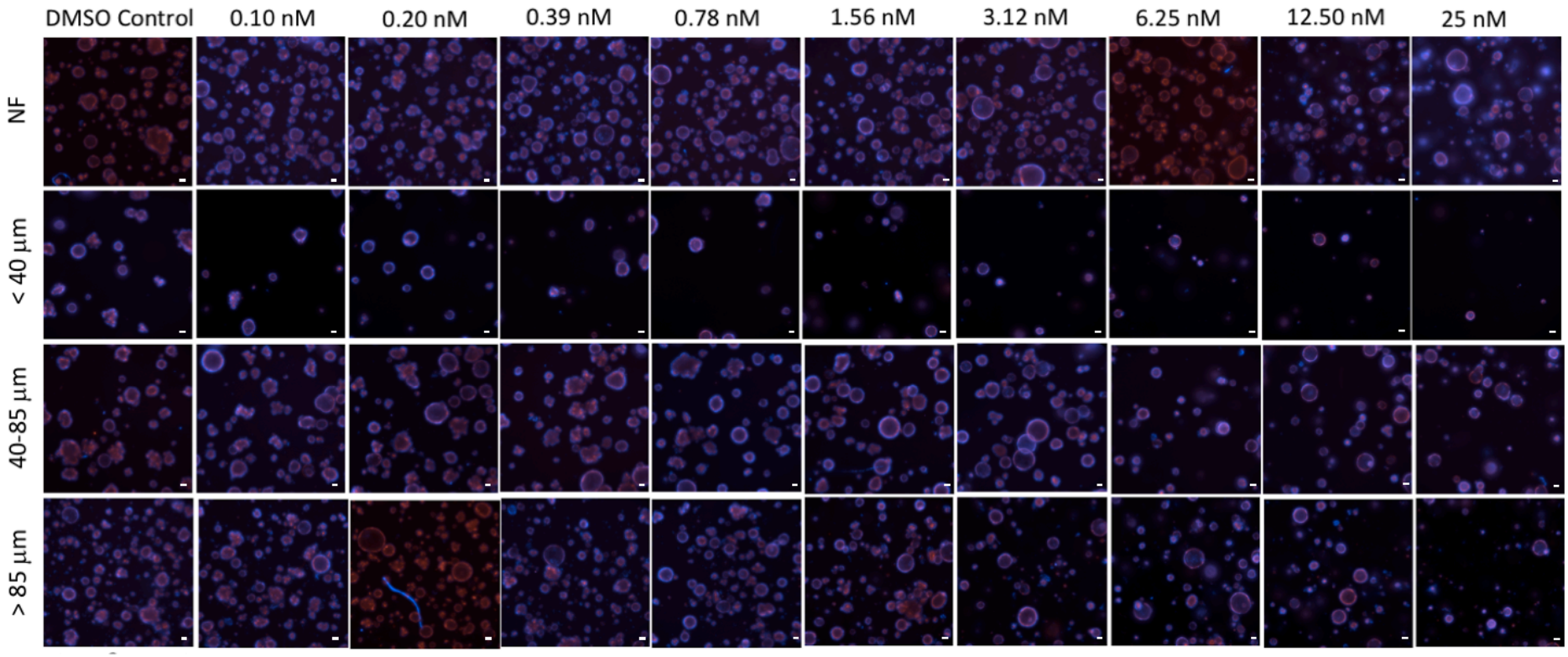

Figure 4.9 Hoechst and Phalloidin staining of fractionated and non-fractionated organoids after Trametinib treatment

Iso50 CRC organoids grown for 5 days were fractionated with PS of 40 µm and 85 µm. Non-fractionated (NF) organoids and organoids present in Fraction <40 µm, Fraction 40-85 µm and Fraction > 85 µm were frozen (-80°C), thawed and plated in Matrigel. After 48 h recovery, organoids were treated with Trametinib in a 9 point, two-fold titration (Trametinib concentrations are specified in the figure). After 5 days of drug treatment, organoids were fixed and stained with Hoechst (blue, DNA stain) and Phalloidin (red, cytoskeleton stain). Representative images of organoids captured following treatment with Trametinib of n=3, N=3 replicates. Scale bars correspond to 100 µm.

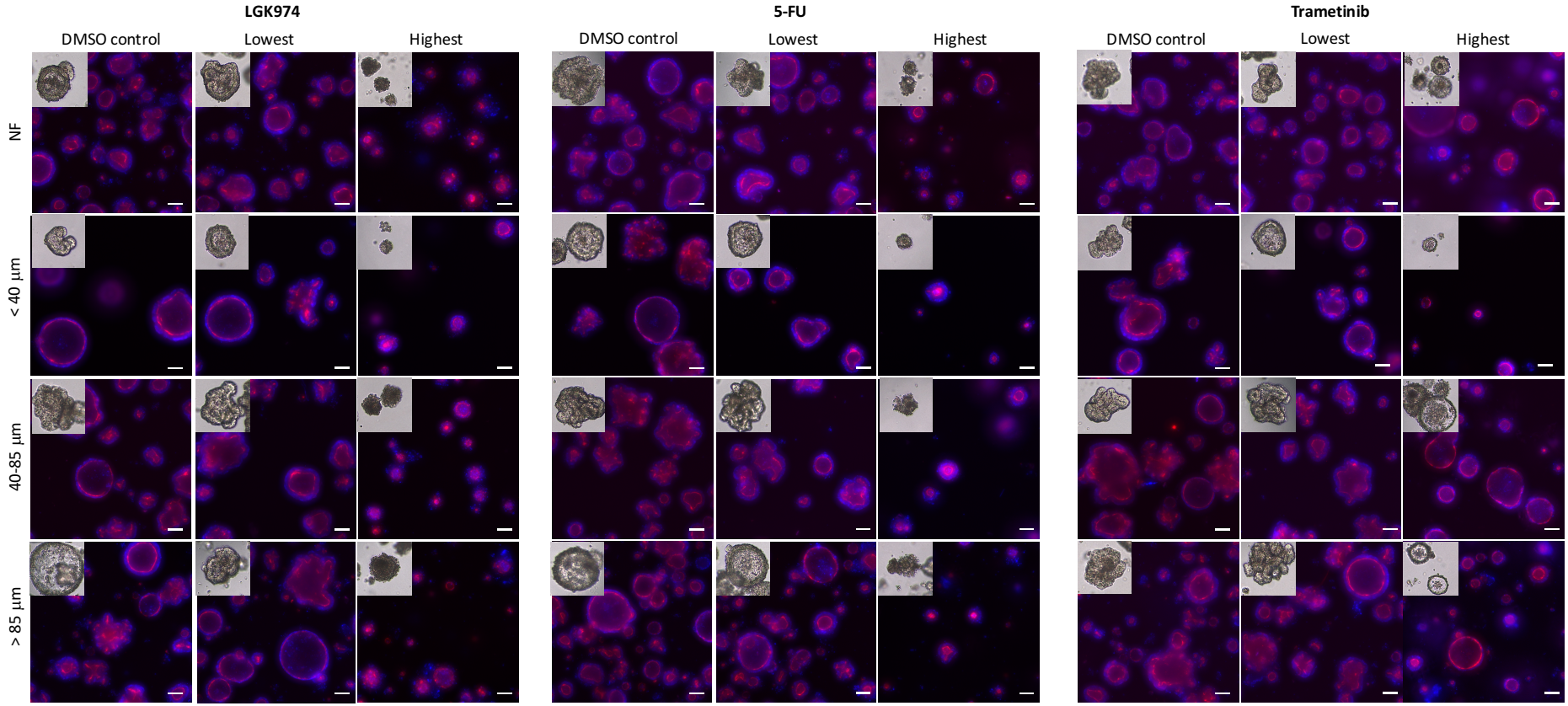

Figure 4.10 Organoid morphological alterations after 5 days treatment with LGK974, 5-FU and Trametinib

Higher magnification of images presented in Figure 4.7, Figure 4.8 and Figure 4.9 for the DMSO control (0.1%) and the lowest and highest concentration of LGK974 (0.20 µM, 50 µM), 5-FU (0.08 µM, 20 µM) and Trametinib (0.10 nM, 25 nM) after 5 days' treatment of fractionated and non-fractionated (NF) Iso50 CRC organoids. Hoechst (blue, DNA) and Phalloidin (red, cytoskeleton). Insets correspond to representative brightfield images of treated organoids. Representative images of organoids captured following treatment with LGK974, 5-FU and Trametinib of n=3, N=3 replicates. Scale bars correspond to 100 µm.

4.2.4.2.1 Reproducibility of dose-response curves of fractionated Iso50 CRC organoids

An ATP-based metabolic activity readout (CellTiter-Glo 3D) endpoint was also used to assess the response of fractionated and non-fractionated organoids to LGK974, 5-FU and Trametinib after 5 days of treatment. Luminescence values obtained were used to quantify ATP levels as an indication of the number of metabolically active cells present. The results, normalised over a DMSO control, were represented as dose-response curves for each compound (Figure 4.11). Visual evaluation of the curves generated for fractionated and non-fractionated organoids suggested that drug response of non-fractionated organoids was similar to response of Fraction 40-85 μm and Fraction > 85 μm, but different from Fraction < 40 μm response. Furthermore, error bars of Fraction < 40 μm were notably larger than error bars of other samples, indicating a lack of reproducibility between individual wells. The reason behind the larger error bars in Fraction < 40 μm, could be the lower amount of organoids plated after the freeze-thaw process in Fraction < 40 μm when compared to other fractions, as shown in Figure 4.7, Figure 4.8 and Figure 4.9. Ideally, same total cell number should have been seeded for a fair comparison between different size fractions.

Surprisingly, Trametinib induced a decrease of ATP levels, although an inhibitory impact was not expected when Iso50 organoids were treated with this MEK1/2 inhibitor, as mentioned before. On the other side, the morphological change from branched to cystic structures observed in organoids treated with this drug (Figure 4.9 and Figure 4.10) might contribute to the reduction in cellular ATP, which is further discussed below.

In the next lines, IC_{50} (half inhibition concentration) values and a statistical analysis of the dose-response curves are presented in order to quantitatively discuss the reproducibility of drug response of fractionated Iso50 CRC organoids.

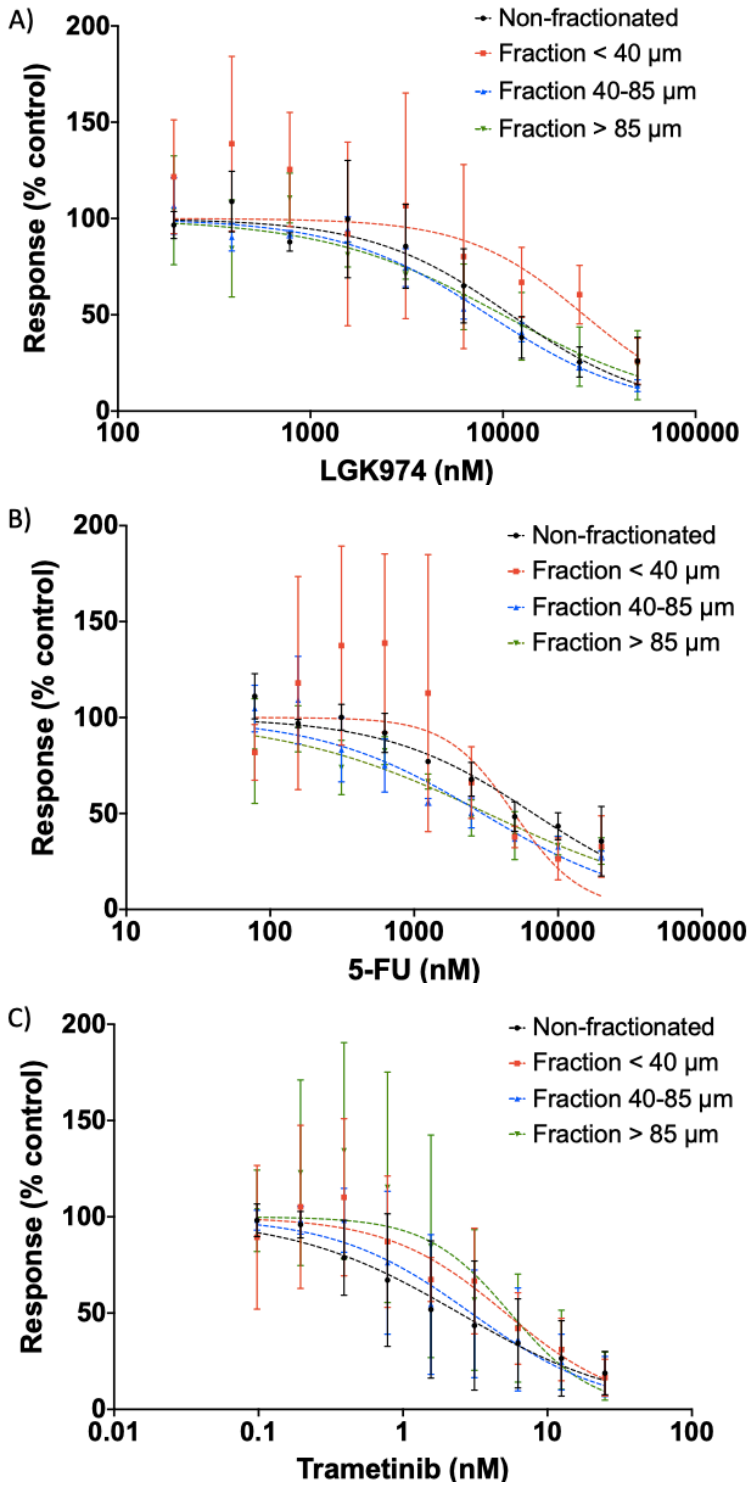

Figure 4.11 Dose-response of fractionated and non-fractionated Iso50 CRC organoids

Iso50 CRC organoids cultured for 5 days were fractionated with PluriStrainers of 40 µm and 85 µm. Non-fractionated organoids and the three resulting fractions were frozen (-80^{0}C). Organoids were thawed and seeded in Matrigel. After 48 h of recovery, a titration of **A.** LGK974 (0.20-50 µM), **B.** 5-FU (0.08-20 µM) and **C.** Trametinib (0.10-25 nM) or DMSO (0.1%) negative control were supplemented with media. Following 5 days of treatment, a CellTiter-Glo 3D assay was performed to quantify relative ATP levels per well (% of relative luminescence over DMSO control). Error bars represent standard deviation (n=3, N=3).

In order to quantify drug response reproducibility, the average IC_{50} values from each curve were obtained from N=3 independent experiments, as listed in Table 4.4 along with standard deviation (s) and coefficient of variation (CV). These results confirmed the higher variability in drug response of organoids present in Fraction < 40 μm for LGK974 and 5-FU treatments, since larger CVs were calculated for this fraction compared to the others. Moreover, IC_{50} values of Fraction 40-85 μm presented a lower degree of variation than for non-fractionated organoids (except for 5-FU treatment, that presented similar CVs), as CV was reduced from 17.36% to 8.82% in LGK974 and from 29.16% to 25.78% in Trametinib. This suggested that drug response variability was reduced when a more homogeneous organoid population was used in drug testing. Assay Validation Guidelines state that CVs should be not greater than 20% to accept a result (Iversen et al. 2012). Thus, IC_{50} values obtained from treatment of Fraction 40-85 μm with LGK974 and 5-FU were trusted. On the other side, CV of Trametinib treatment of Fraction 40-85 μm was 25.78%, which did not pass the 20% criterion. This might be explained by the particular response of Iso50 CRC organoids to this compound, as observed in Figure 4.9 and Figure 4.10. An ATP assay readout may not be the best method to quantify Trametinib effect in Iso50 CRC organoids, as cell death might not be induced in this line. Furthermore, for each compound, statistical comparisons between IC_{50} values were performed using analysis of variance (ANOVA) with Tukey's post-hoc test to correct for multiple comparisons, to determine whether IC_{50} values of fractionated and non-fractionated organoids were statistically different or not. Interestingly, no significant differences, i.e. p-values > 0.05, were found between any of the six possible comparisons in each compound treatment, which indicated that organoid fractionation did not affect the drug response in terms of IC_{50} values but improved the reproducibility of the results. IC_{50} values calculated in this work were in the same range as validation data generated by Cellesce Ltd for Iso50 line with the three compounds (2992 - 4486 nM for LGK974, 2697 - 8034 nM for 5-FU and 2.015 - 5.081 nM for Trametinib). However, it is worth noting that calculated IC_{50} values for LGK974 (Table 4.4), are much larger than reported IC_{50} in literature, values below 50 nM (Picco et al. 2017; Liu et al. 2013). Thus, organoid deterioration (Figure 4.7) and reduction of cellular ATP (Figure 4.11A) could be as an indication of off-target effects at high LGK974 concentrations. Reported IC_{50} values for 5-FU, 2.37±1.86 μM (Linnekamp et al. 2018), agreed with experimental values obtained in this work (Table 4.4), which confirmed the potential inhibitory effect of this compound in Iso50 CRC organoids. Ma *et al*. reported IC_{50} values for Trametinib in various CRC lines and the

average value was 10.32±5.96 nM (Ma et al. 2017), which was consistent with IC_{50} values obtained for fractionated and non-fractionated Iso50 CRC organoids (Table 4.4). On the other side, cellular ATP reduction, and thus cell death was not expected by Trametinib treatment, since Iso50 was a KRAS mutated line and Trametinib could lead the induction of a feedback loop, via SPRY and DUSP proteins, and reactivation of the MAPK pathway (Luke et al. 2014). RAS mutant tumours exhibit a relative abundance of wild-type RAF proteins (Luke et al. 2014), thus Trametinib-induced feedback could mediate the activation of wild-type RAF proteins through the formation of CRAF-MEK complexes. This causes an induction of phosphorylated MEK and phosphorylated ERK and eventual increase in downstream MAPK pathway activation that facilitates multiple cellular processes, such as cell proliferation and survival (Luke et al. 2014; Dai et al. 2019). Nevertheless, the reduction in cellular ATP could be related to the morphology change observed in Figure 4.10 from a mixture of branched and cystic organoids to an only cystic phenotype, due to Wnt signalling activation by Trametinib (Zhan et al. 2019). A cystic organoid might present less specific surface area, and thus less number of cells than a branched organoid, that resulted in lower cellular ATP. The biological meaning of branched-cystic transition requires further investigation.

Table 4.4 IC_{50} values of fractionated and non-fractionated Iso50 CRC organoids, generated from ATP assay, CV corresponds to coefficient of variation, (n=3, N=3)

	IC_{50} LGK974			IC_{50} 5-FU			IC_{50} Trametinib		
	Average (nM)	**s (nM)**	**CV%**	**Average (nM)**	**s (nM)**	**CV%**	**Average (nM)**	**s (nM)**	**CV%**
Non-fractionated	10973.00	1905.00	**17.36**	6750.00	1169.00	**17.32**	2.45	0.72	**29.16**
Fraction < 40 μm	26324.00	10325.00	**39.22**	4944.00	1790.00	**36.21**	5.14	1.55	**30.23**
Fraction 40-85 μm	8382.00	739.50	**8.82**	2972.00	558.50	**18.79**	2.97	0.76	**25.78**
Fraction > 85 μm	9960.00	2163.00	**21.72**	3231.00	685.20	**21.21**	5.52	2.10	**38.03**

In summary, statistical analysis of ATP endpoint viability readouts showed that organoid fractionation did not alter IC_{50} values because the results obtained with Fraction 40-85 μm were not statistically different from IC_{50} values of non-fractionated organoids. Furthermore, although some authors have suggested the enhancement of reproducibility of drug response test with uniform sized organoids (Jung et al. 2019; Yu et al. 2019; Arora et al. 2017), it is the first time that this has been proven. IC_{50} reproducibility was improved in Fraction 40-85 μm, since CV was reduced when comparing degree of variation of non-fractionated organoids and organoids present in Fraction 40-85 μm. This suggested that a more uniform population of organoid sizes during initial seeding generated relatively robust ATP readouts in terms of IC_{50} variation. Further studies should be performed including a larger panel of drugs, other CRC organoid lines and other cancer organoid types to confirm whether the observed increase of reproducibility could be generally accepted.

4.3 Summary

The work described in this chapter has shown the utility of an organoid size-based fractionation to reduce drug response variability. From the experiments outlined in this chapter it can be concluded that:

i) Size separation of Iso50 CRC organoids with PluriStrainers of 40 μm and 85 μm exhibited better outcome than fluidisation with the designed fluidised bed, since microscope pictures of Fraction 40-85 μm showed a homogenous in size organoid population and Column fraction contained larger amount of single cells.

ii) Purity, enrichment and separation efficiency of both approaches showed poor performance.

iii) Discrepancies between microscope pictures quantification results and MS3 Coulter Counter data suggests that counting and sizing with this device might involve extra handling and sample processing, that could affect organoid integrity.

iv) Fractionated organoids respond to known CRC targeting compounds and IC_{50} values calculated for fractionated organoids were statistically equivalent to IC_{50} values of non-fractionated organoids.

v) Importantly, organoid size-based fractionation improved drug response reproducibility, since organoids in Fraction 40-85 μm displayed lower coefficient of variations in IC_{50} values than non-fractionated organoids.

These findings showed the importance of considering organoid size in drug testing in order to reduce the variability of the drug response. Fluidisation for organoid size-based separation has been tested for the first time and although the separation performance of the current FB design is unsatisfactory, there is still room for improvement if this technology would like to be commercially applied. Future directions for improving the FB performance are discussed in Section 6.2, regarding design aspects, operating conditions and the implementation of process analytical tools for the better separation monitoring and performance assessment.

5. Organoid biology as a function of size

5.1 Introduction

Previous chapters have assessed organoid size from a technical point of view and how this parameter affects drug response reproducibility. However, the improved reproducibility that results from size uniformity probably depends on the underlying differences in organoid biology according to organoid size. As described in Section 1.3, organoids resemble 3D architecture and diffusional gradients observed in solid tumours. As such, concentrations of oxygen, nutrients, pH and metabolites vary from the organoid surface to the core and these gradients may be responsible for different stages of the cell cycle and gene expression profiles that depend on cell locations within and between organoids (Saglam-Metiner et al. 2019; Jin et al. 2018). For example, large solid organoids might crudely be regarded as layered structures with rapidly dividing cells in the outer region of the organoid due to the highest exposure to oxygen, nutrients and media growth factors, and a hypoxic environment in the core as a result of oxygen depletion, nutrient shortage and metabolic by-products accumulation (Hubert et al. 2016; Daster et al. 2017). In order to adapt to this stressful environment, cells modify their metabolism to ensure survival and proliferation. For example, cells under hypoxic conditions switch on cellular metabolism to anaerobic pathways for ATP production, such as glycolysis (described more extensively in Section 1.3.2) (Sonveaux et al. 2008; Guillaumond et al. 2013). Furthermore, an increase of organoid size might restrict drug penetration and direct contact between drugs and their target receptors as observed in solid tumours (Roscigno et al. 2019; Karolak et al. 2019). But limitation in drug penetration is not the only drug-assay dependent issue influenced by organoid size, since hypoxia can alter drug resistance and several drugs (e.g. doxorubicin, 5-FU, cisplatin and irinotecan) lose their efficacy in absence of oxygen (Nunes et al. 2018; Zhang et al. 2019). All this suggests that organoid size needs to be taken into account during the planning phase of drug testing and it may be essential to control this parameter accordingly to the mechanism of action of the drug.

Although implications of organoid size on its biology have not been reported yet, Daster *et al.* (2017) assessed gene expression profiles of different size CRC spheroids that recapitulate the different areas of an *in vivo* tumour. They found that spheroids with a diameter below 200 μm contained proliferating and normoxic cells, spheroids with a diameter between 300 and 350 μm presented proliferating zones at the surface and hypoxic zones in the core, and spheroids

with a diameter larger than 500 μm showed hypoxic and necrotic areas. Furthermore, they demonstrated that the largest spheroids most closely mimicked gene expression profile of *in vivo* tumours and presented higher resistance to 5-FU compared to the smaller spheroids (Daster et al. 2017). Similar to hypoxic tumours and hypoxic spheroids becoming more resistant to therapy as they increase their size (West 1989; Daster et al. 2017; Jamieson et al. 2019), organoids may develop increasing resistance as they grow, mimicking closely the characteristics of cancer *in vivo*. Size-dependent drug resistance of spheroids raised the importance of considering organoid size when using organoids in screening assays to mimic the *in vivo* environment.

This chapter evaluated physiological characteristics of Iso50 CRC organoids with different sizes, such as the number of cells per organoid and the increase of organoid size over the culture time span. Then, gene expression profile was assessed through a bulk RNA-seq experiment to elucidate whether transcriptome is altered according to day of culture and organoid size.

In summary, cell biology involving cellular functions within organoids was studied for different size Iso50 CRC organoids and the key aims for this chapter were:

v) To characterise the increase of Iso50 CRC organoid size during cultivation time.
vi) To determine the number of cells per organoid of different size Iso50 CRC organoids.
vii) To assess whether gene expression profile of Iso50 CRC organoids is altered accordingly to organoid size.

5.2 Results and Discussion

5.2.1 Growth kinetics of Iso50 CRC organoids

OcellO B.V. suggested that, 40-85 μm organoid diameter was an ideal size range for seeding of organoids for drug treatment assays. To determine the time of culture to maximise 40-85 μm size Iso50 CRC organoids, they were seeded as single cells and were grown and harvested after 4, 5, 6, 7 and 8 days of culture. Particle size distribution (PSD) and Sauter mean diameter were calculated with MS3 Coulter Counter data and results are shown in Figure 5.1.

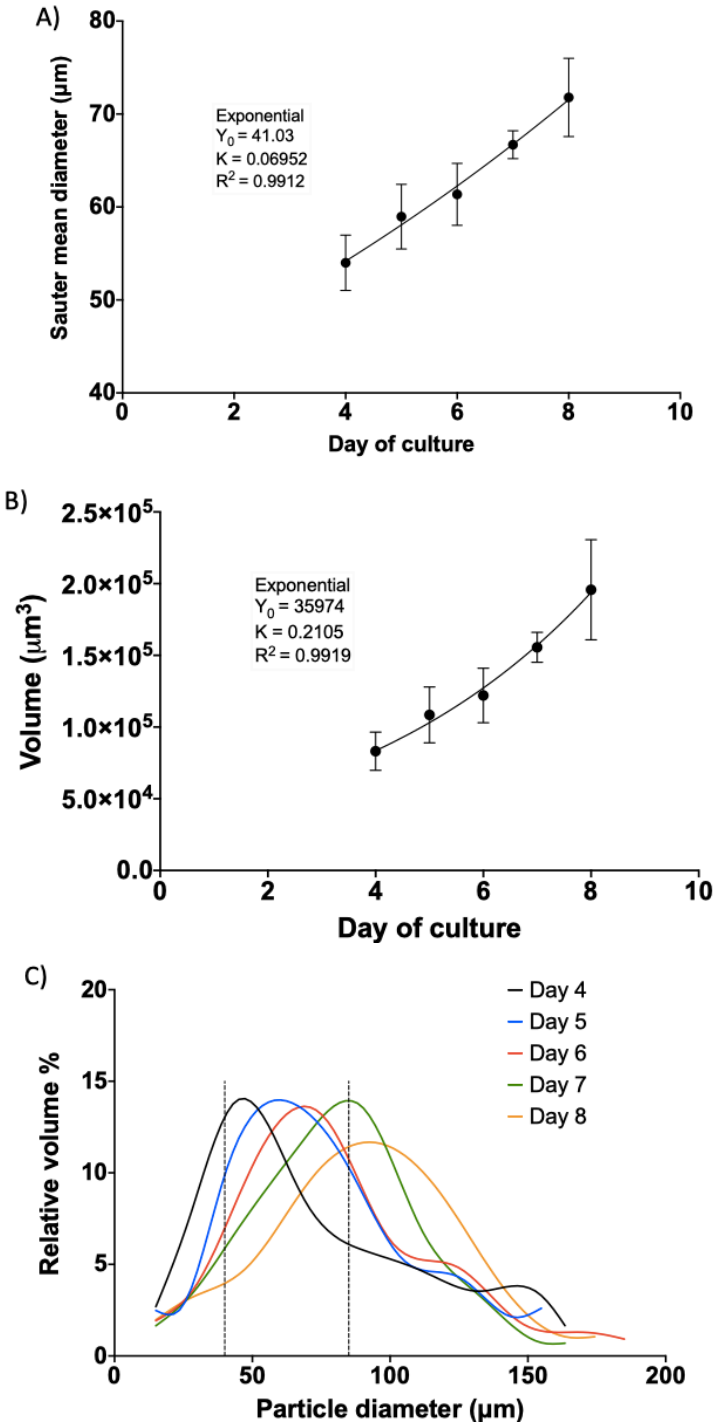

Figure 5.1 Iso50 CRC organoid growth during culture time span

Iso50 CRC organoids were grown and harvested after 4, 5, 6, 7 and 8 days of culture. Each organoid suspension was analysed with MS3 Coulter Counter. **A.** Sauter mean diameter for each organoid suspension was calculated with Equation 2.1 using MS3 Coulter Counter data. The pattern of organoid diameter resembled an exponential curve ($Y_d = Y_0 \exp(Kt)$). **B.** Organoid volume was calculated from Sauter mean diameter values, assuming an organoid as a sphere. Data was fitted to an exponential curve ($Y_V = Y_0 \exp(Kt)$). **A.** and **B.** error bars represent standard deviation (n=3, N=3) **C.** Volume-based PSD of Iso50 CRC organoids grown during different culture times. Dashed vertical lines correspond to particle diameter of 40 µm and 85 µm.

Organoid diameter increased exponentially with the cultivation time, with R squared value of 0.9912, as seen in Figure 5.1A. This trend was theoretically predicted assuming that organoids and single cells were spheres. The volume of an organoid can be calculated on the basis of the single cell volume (Equation 5.1).

$$V_{org} = N_{cell/org} * V_{cell} = N_{cell/org} * 4/3\,\pi(d_{cell}/2)^3 \qquad \text{Equation 5.1}$$

where: V_{org} is the volume of an organoid, $N_{cell/org}$ is the number of cells per organoid, V_{cell} is the volume of a single cell and d_{cell} is the diameter of a single cell.
Also, the volume of an organoid can be calculated with Equation 5.2.

$$V_{org} = 4/3\,\pi\left(d_{org}/2\right)^3 \qquad \text{Equation 5.2}$$

where: d_{org} is the diameter of an organoid.
Then, exponential growth of cell number can be described with Equation 5.3.

$$N_{cell/org} = \exp\,(\alpha * t) \qquad \text{Equation 5.3}$$

where: α is the constant growth rate and t is the cultivation time.
Finally, rearranging Equation 5.1, Equation 5.2 and Equation 5.3, the organoid diameter can be expressed as an exponential function of the cultivation time (Equation 5.4)

$$d_{org} = d_{cell} * \exp\,(\alpha/3 * t) \qquad \text{Equation 5.4}$$

The experimental trend obtained in Figure 5.1A correlated with Equation 5.4, however, the Y_0 term of the fitted equation did not agree with the expected value. Based on Equation 5.4, the Y_0 term corresponded to the diameter of a single cell (d_{cell}) and 41.03 μm is four times larger than the single cell diameter values obtained with Luna-FL fluorescence cell counter. This could be explained due to the fact that organoids present an internal empty lumen, which is not represented in the compact structure assumed with Equation 5.1, and thus experimental organoid diameters were larger than the predicted values.

Furthermore, exponential growth has previously been reported with brain organoids by Goto-Silva *et al*. (2019) and pancreas organoids by Huch *et al*. (2013) (Goto-Silva et al. 2019; Huch et al. 2013). Moreover, further research has been published regarding spheroid growth compared to organoid growth (Wallace 2013; Van Liedekerke et al. 2019; Nirmala et al. 2001). It is well documented in the literature that the early growth phase of most of the spheroids is exponential but then the growth rate decreases as spheroids increase their size (Wallace 2013). This is explained due to the layered structure of spheroids consisting of proliferating, quiescent and necrotic cells which present different growth kinetics. In early stage spheroids, proliferating cells constitute the entire spheroid and they are characterised by an exponential growth. However, for longer cultivation times, inner proliferating cells experience restriction to nutrients access and become quiescent cells which are live cells but not actively dividing. These quiescent cells can return to a proliferating state or experience cell death due to necrosis. Transition from proliferating to quiescent implies a decline of the exponential growth rate characteristic of early stage spheroid cultures (Wallace 2013). Deviations from exponential growth have been observed for mouse colon carcinoma spheroids with diameter larger than 350 μm (after 2 days of culture, starting from initial spheroid diameter of 200 μm) (Van Liedekerke et al. 2019) and human melanoma spheroids with diameters larger than 270-340 μm (Rofstad et al. 1986). Experimental data obtained in this work with Iso50 CRC organoids (organoid diameters below 150 μm, Figure 5.1C) was far from the diameters reported above (>270 μm) and this might explain the exponential growth observed during 8 days of culture. Assuming an organoid as a sphere, organoid volume was calculated from Sauter mean diameters reported in Figure 5.1A, and organoid volume showed an exponential growth during cultivation time (Figure 5.1B). Volume doubling time (VDT), defined as time required to double the volume of organoids, was calculated with Equation 5.5 and a VDT = 3.2 days was obtained for Iso50 CRC organoids. This value was in the same range as published data of different types of organoids, e.g. 53 - 60 h for pancreas organoids (Huch et al. 2013), 3 days - 2 weeks for prostate organoids (Gao et al. 2014), and 12 – 96 h for intestinal organoids (Keysselt et al. 2019).

$$VDT = \frac{\ln 2 * (t_2 - t_1)}{\ln (V_2/V_1)} \qquad \text{Equation 5.5}$$

where: t_2 and t_1 are the final and initial times, respectively, and V_2 and V_1 are the final and initial volumes, respectively.

Furthermore, the longer the cultivation time, the more normally distributed the volume-based PSD of Iso50 CRC organoids was (Figure 5.1C). This pattern has previously been reported with brain organoids (Goto-Silva et al. 2019). Moreover, wider curves and shifted towards higher diameters were observed as time of culture increased. PSDs corresponding to Day 5 and Day 6 presented their peaks of maximum volume of organoids within the range of 40-85 μm. To quantify this observation, relative area under the curve for the target size range (40-85 μm) was analysed and the values obtained were: 39.5%, 50.2%, 47.8%, 43.3% and 32.9% for Day 4, Day 5, Day 6, Day 7 and Day 8, respectively. These results indicated that Day 5 presented the major volume of organoids with a size range between 40 μm and 85 μm, therefore, Iso50 CRC organoids were grown during 5 days when 40-85 μm was the target size range.

5.2.2 Number of cells per organoid

Correlations of organoid diameter and number of cells per organoid have not been published yet. However, this could be a useful parameter to assess drug effects or to control specific ratios of different cell types within the organoid. The number of cells per organoid could even be considered as a new quality attribute for their manufacturing. In order to obtain a wide range of organoid sizes, Iso50 CRC organoids were cultured for 3, 4, 5, 6, 7 and 8 days, and at the end of each culture time span organoids were fixed and stained with Hoechst to detect nuclei. Organoids were imaged with the confocal Opera Phenix High Content Screening microscope at 40X magnification, with 50 image stacks taken at 3 μm step per well. The z-stack images were analysed with Harmony software for organoid 3D reconstruction and to automatically measure organoid diameter and count the number of cells per organoid (Figure 5.2). Automated counting was chosen because it has lower error rate per sample and does not suffer from the subjectivity inherent to manual counting. In order to determine organoid diameter, Harmony software fitted an ellipsoid approximating the shape of each organoid and calculated the ellipsoid longest axis, medium axis and shortest axis lengths. Ellipsoid medium axis length was chosen here to present the results. Moreover, to determine the number of cells per organoid, Harmony software counted nuclear objects stained with Hoechst within the fitted ellipsoid (Figure 5.2B). Figure 5.2A shows that the relationship between number of cells per organoid and organoid size followed a power function, with R squared value of 0.9451. Interestingly, a higher variability in both axes was identified at extended cultivation times, thus indicating a decreased consistency in size as well as cells/organoid ratio after 8 days of culture. A power

function pattern was theoretically predicted assuming that organoids and single cells were spheres. The volume of an organoid can be calculated on the basis of the single cell volume, as indicated in Equation 5.1, as well as, on the basis of the organoid diameter, as represented in Equation 5.2. Furthermore, Equation 5.6 is obtained by combining Equation 5.1 and Equation 5.2.

$$d_{org}{}^{3} = N_{cell/org} * d_{cell}{}^{3} \qquad \text{Equation 5.6}$$

Finally, rearranging the above equation, number of cell per organoid can be expressed as a function of organoid diameter to the power of 3, as expressed in Equation 5.7.

$$N_{cell/org} = \left(1/d_{cell}{}^{3}\right) * d_{org}{}^{3} \qquad \text{Equation 5.7}$$

This theoretical expression approximates to the experimental trend obtained with Iso50 CRC organoids, in which the number of cell per organoid was function of organoid diameter to the power of 2.5 (Figure 5.2A). The exponent deviation might be due to the fact that organoids and single cells are not perfect spheres, and also organoids present a lumen without cells, which was not considered in Equation 5.1. In future work, this could be corrected by measuring the lumen volume through organoid staining with Phalloidin, which is an actin stain that enables lumen visualisation, and subsequently Opera Phenix High Content Screening microscope imaging and lumen volume calculation with Harmony software. Furthermore, the A term (0.0009316) of the fitted equation correlated to $\left(1/d_{cell}{}^{3}\right)$ of Equation 5.7, and thus, the diameter of a single cell corresponded to 10.2 μm, which is a reasonable value based on single cell size results (11.55 ± 0.22 μm) obtained experimentally from the analysis with Luna-FL fluorescence cell counter of single cell suspensions generated from Iso50 CRC organoids. No previous study has investigated the relation between number of cells per organoid and organoid diameter, however, Tirier *et al*. (2019) and Arora *et al*. (2017) determined the relationship between spheroid size and nuclei counts per spheroid. On the one side, Tirier *et al*. (2019) showed a linear relationship between CRC spheroid area and the number of cells per spheroid (Area (μm^2) = 40.85 * #cells + 1706) (Tirier et al. 2019). This trend agreed with the results obtained in this work (see relationship between Area and number cells per Iso50 CRC organoid in Appendix D). On the other side, Arora *et al*. (2017) found a correlation for hindgut spheroids (Arora et al. 2017). They showed that number of cells per spheroid and spheroid diameter

positively correlated (R=0.76) but a specific trend was not defined. Furthermore, reported values (193 ± 117 cells/spheroid corresponded to 68 ± 22 µm spheroid diameter) did not agree with experimental results presented in Figure 5.2A (based on fitted equation, 43 cell per organoid corresponded to 68 µm organoid diameter). The larger number of cells per spheroid compared to cells per organoid could be due to the differences in spheroid and organoid architectures. Organoids have an internal empty lumen, which in Iso50 CRC organoids varied between branched and cystic shapes, however, spheroids consist of a compact mass of cells that could increase the number of nuclei in structures of the same size.

Furthermore, the fitted equation presented in Figure 5.2A was used to determine the target range of number of cells per organoid corresponding to the 40-85 µm target size range, which resulted in 11-76 cells per organoid. This correlation is specific for Iso50 CRC organoids and new correlations are required for other organoid lines due to the specific morphology of each line.

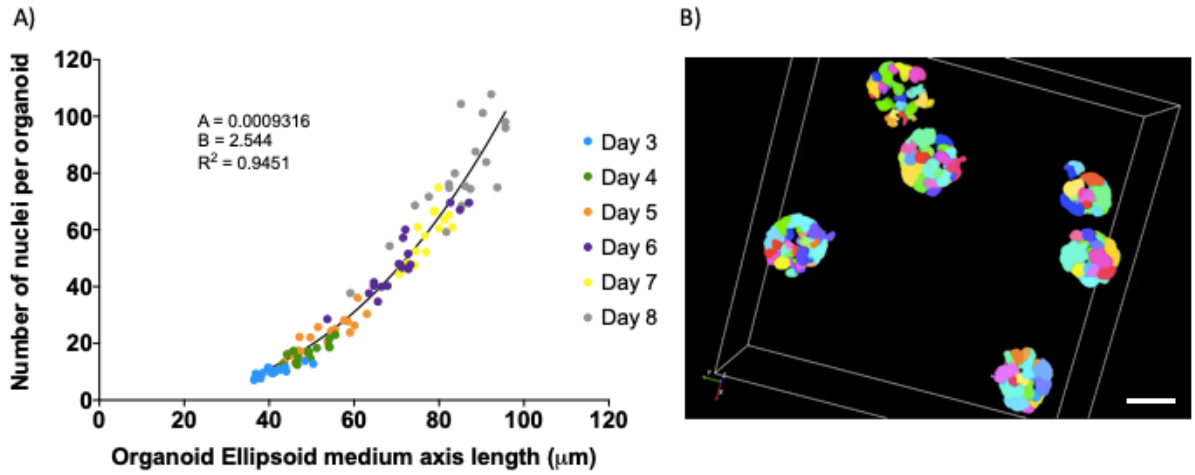

Figure 5.2 Number of cells per organoid

Iso50 CRC organoids cultured during 3, 4, 5, 6, 7, and 8 days of culture were fixed and stained with Hoechst (nuclei stain) at the end of each culture time span. Then, organoids were imaged with Opera Phenix High Content Screening microscope and images were analysed with Harmony software to calculate the average number of cells per organoids and the average ellipsoid medium axis length per well. **A.** A nonlinear regression was applied to the data and the fitted equation was a power function with the expression $Y= AX^B$, where Y is the number of nuclei per organoid and X is the organoid ellipsoid medium axis length. Confidence interval (CI) of the adjusted parameters, for A: 0.0004640 to 0.001815 and for B: 2.391 to 2.703. Each dot represents the average number of nuclei per organoid per well and between 14 and 84 organoids were identified in each well. n=14-84, N=1. **B.** Representative image of the nuclei segmentation using the Harmony software of Iso50 CRC organoids grown for 5 days. Scale bar represents 50 µm.

5.2.3 Gene expression analysis of different size organoids

Gene expression profile of different size Iso50 CRC organoids was analysed by RNA-seq to evaluate whether size heterogeneity was associated with biomolecular changes. To obtain different size organoids two different strategies were considered: a time course experiment and a size-based fractionation experiment. For time course experiment, the gene expression profiles of organoids that had been cultured for 3, 5 and 8 days were compared. The rationale for this experiment was to determine which differences in the gene expression profile between organoids cultured for 3, 5 and 8 days were due to differences in the culture time or due to differences in the organoid size. Aside from size differences, other parameters related to the cultivation time might alter gene expression including changes in biology related to media conditions and organoid time in culture. To avoid these problems, different sized organoids were also generated by filtration with PS of 40 μm and 85 μm and gene expression profile of the three resulting fractions (Fraction < 40, Fraction 40-85 and Fraction > 85) was compared. Size fractionation was performed with Iso50 CRC organoids cultured for 5 and 8 days. Since, Daster *et al*. (2017) identified hypoxia in spheroids larger than 200 μm (Daster et al. 2017), and as shown in Figure 5.1C, 8 days of culture were not enough to generate many large Iso50 CRC organoids from single cells, organoids larger than 200 μm were hand-picked from cultures that had been grown from triturated samples for 5 days. Table 5.1 summarises the different samples included in each RNA-seq experiment. RNA-seq analysis and subsequent qRT-PCR analysis for RNA-seq data validation, were carried out on RNA samples, including three biological replicates per condition.

Table 5.1 Overview of all size-dependent RNA-seq experiments

RNA-seq experiment	Samples	Comments
Time course experiment (Non-fractionated)	Day 3 (D3)	Apart from size, differences could be driven by culture conditions
	Day 5 (D5)	
	Day 8 (D8)	
Size-based fractionation experiment – Day 5	Fraction < 40 μm	Only size effect
	Fraction 40-85 μm	
	Fraction > 85 μm	
Size-based fractionation experiment – Day 8	Fraction < 40 μm	Only size effect
	Fraction 40-85 μm	
	Fraction > 85 μm	
Positive control for hypoxic conditions based on Daster *et al.* (2017)	Organoids > 200 μm	Organoids hand-picked from cultures grown from triturated samples for 5 days

Data presented in the following sections contains the results from the differential gene expression analysis of Iso50 CRC organoids cultured during different times and/or fractionated with PluriStrainers of 40 μm and 85 μm. Details regarding the isolation and purification of RNA from organoid samples are described in Section 2.3.1. Concentration of RNA samples was assessed by Qubit RNA BR Assay Kit and RNA integrity was determined with TapeStation 2200 RNA ScreenTape (see Section 2.4.1). Samples with a RNA concentration below 10 ng/mL were discarded, as well as, samples with RNA Integrity Number equivalent (RIN^e) value below 8. Subsequently, library preparation and sequencing was performed by Angela Marchbank from the Genome Research Hub at Cardiff University. Sequencing was carried out using the Illumina NextSeq 500 to generate single-end reads of 75bp in length. Two runs of 1x75 bp were necessary to ensure all samples have the same number of reads (30 million reads per sample). Raw data (FastQ files) obtained from the sequencing contained information about the frequency in which cDNA fragments sequences (reads) are represented in each sample. Bioinformatics processing steps prior to differential expression analysis are described in Section 2.44, which include trimming, mapping and normalizations based on the total RNA sequenced (counts per million, CPM) and based on the gene length (fragments per kilobase of transcript per million mapped reads, FPKM). A pre-filtering step performed in R was included

to remove lowly expressed genes. Genes with less than 5-15 raw counts are usually considered as non-expressed. However, by probability long genes are expected to generate more reads than short genes, therefore non-expressed long genes might not be adequately removed using this criterion and to be able to compare the expression levels across different genes the FPKM need to be considered, which reflects the abundance of each gene normalised based on the gene length. Genes with a FPKM value lower than 0.2-1 are usually considered as non-expressed. Following Bioconductor recommendations, genes with an average of raw counts below 10 and an average of FPKM below 0.5 were removed from all the dataset analysed in this work.
Finally, the differential gene expression analysis between samples was performed with R using DESeq package. DESeq fits a generalised linear model of the negative binomial family to test for significant differences in signals between conditions (Love et al. 2019). For each gene, fold changes and P values (pval), as well as P values adjusted (padj) for multiple testing with the Benjamini-Hochberg procedure, were used to control false discovery rate (FDR) (Benjamini & Hochberg 1995). The genes with adjusted p-value of less than 0.01 were deemed to be significantly differentially expressed, which indicated that 1% of significant tests will result in false positives. Below are shown the results obtained from the different experiments included in Table 5.1.

5.2.3.1 Time course experiment

Iso50 CRC organoids cultured for 3, 5 and 8 days showed clear size differences (Figure 5.3A) and RNA of each sample was extracted for subsequent sequencing using Illumina NextSeq 500. As described above, a pre-filtering step was included to remove lowly expressed genes and only genes with average of raw counts ≥ 10 and average of FPKM ≥ 0.5 in all biological groups were considered as expressed and included in the analysis. This resulted in 16732 "expressed" genes from the 41517 total genes, which were included in the differential gene expression analysis using DESeq package in R, in which every sample was compared against every other sample, i.e. D3 vs. D5, D3 vs. D8 and D5 vs. D8.
Results obtained from the differential gene expression analysis between D3, D5 and D8 samples were evaluated by principal component analysis (PCA) in R. PCA allowed the identification of strong patterns considering the expressed genes within samples D3, D5 and D8 (further details on PCA are described in Section 2.4.4). PCA results were plotted along the first two components, which explained the majority of the variance presented in the dataset

(PC1 89% and PC2 4%). As shown in Figure 5.3B, samples grouped based on the day of culture, since D3, D5 and D8 samples were clearly positioned in coordinates different from each other, with D5 being closer to D3 than to D8. This could be due to the shorter elapsed time between D3 and D5 than between D5 and D8. A similar hierarchical clustering was obtained with the analysis of the sample-to-sample Euclidean distances between D3, D5 and D8 samples (Figure 5.3C). Moreover, the great similarity between samples D3 and D5 was confirmed with the results obtained in MA-plots (Figure 5.3D). Briefly, these plots enable the visualisation of variation of gene expression ratio ($M=\log_2 ratio$) as a function of average signal intensity (A). Each gene is represented with a dot and red dots show the differentially expressed genes (p-value below 0.1) and black dots show the non-differentially expressed genes (p-value above 0.1). MA-plots in Figure 5.3C showed a low number of differentially expressed genes between D3 and D5 samples compared with the huge number of differentially expressed genes between D3 and D8 samples.

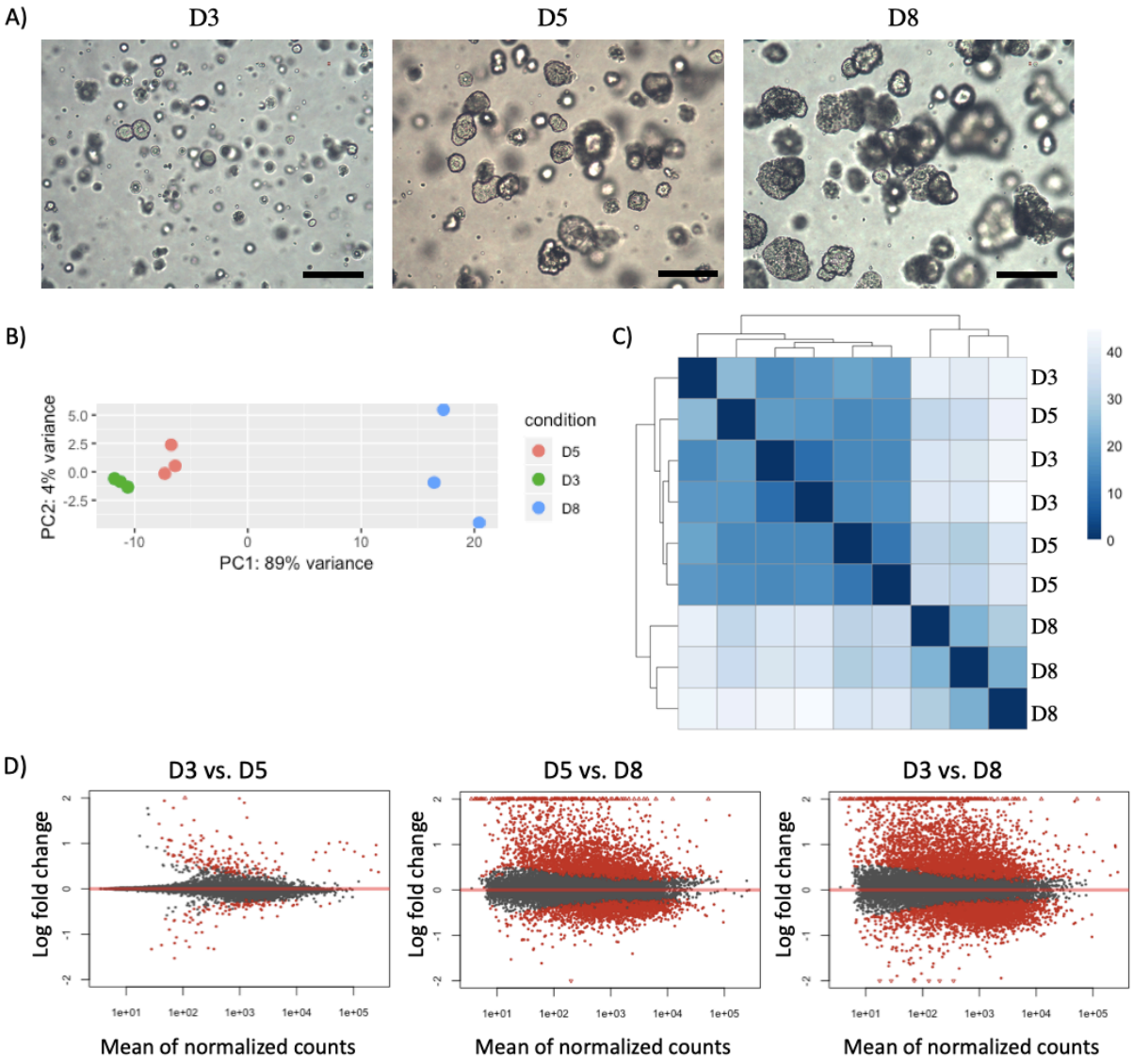

Figure 5.3 Time course experiment – Sample clustering and MA-plots

Total cellular RNA from Iso50 CRC organoids cultured for 3 (D3), 5 (D5) and 8 (D8) days was purified and reverse transcribed (N=3). **A.** Representative images of D3, D5 and D8 samples after each cultivation time. Scale bars correspond to 100 µm. **B-D.** RNA-seq was performed using Illumina NextSeq 500 and only "expressed" genes were considered for analysis (16732 from 41517 total genes). **B.** Results were analysed by PCA plot along first two components. **C.** Heatmap of sample-to-sample Euclidean distances and hierarchical clustering based on the sample distances. **D.** The Mean Average (MA) plot represents each gene with a dot. The x axis is the average expression over all samples, the y axis the log2 fold change between each pair of samples. Genes with adjusted p-value below 0.1 are shown in red.

Next, gene expression of organoids cultured for 3, 5 and 8 days was compared, considering only the differentially expressed genes obtained with the DESeq analysis from the comparison of every sample against every other sample (5014 genes, with adjusted p-value<0.01, obtained from the three possible pairwise comparisons between D3, D5 and D8 samples). As stated

above, DESeq corrects for multiple hypothesis testing via the Benjamini-Hochberg procedure (Benjamini & Hochberg 1995) and for each gene an adjusted p-value was calculated to control the number of false discoveries in those tests that result in a discovery (i.e. a significant result). In this work, genes with an adjusted p-value <0.01 were considered as differentially expressed, which indicated that only 1% of these genes resulted in false positives. This strict FDR allowed to be 99% sure that such genes did not arise as differentially expressed by chance.

Hierarchical clustering and heatmap generation with the genes differentially expressed for each of the pairwise comparisons between D3, D5 and D8 samples, were performed applying one minus Pearson correlation clustering method using the Broad Institute online tool Morpheus. Figure 5.4A shows that organoids cultured for 3 days (D3) hierarchically clustered together with organoids cultured for 5 days (D5). Moreover, the vertical branch lengths of the sample dendrogram (not gene dendrogram) reflect the distance, i.e. the similarity, between samples or sample clusters, being the most similar samples connected by short branches. This length can be used as a parameter to quantify the gene expression variability between the three biological replicates of D3, D5 and D8 samples. Interestingly, the shortest branch lengths were obtained for organoids cultured for 5 days (D5), whilst organoids grown for 8 days (D8) showed the longest branch length, thus emphasizing the importance of cultivation time for reduced batch-to-batch variability. Furthermore, two different clusters of genes were clearly defined: a top cluster with 2315 genes upregulated mainly on D3 samples and a bottom cluster with 2699 genes, consisting of genes upregulated on D8 samples. Furthermore, gene expression profile of D5 samples was at an intermediate level between D3 and D8 for most of the genes. To identify in which biological processes genes of top and bottom cluster were involved, GO (gene ontology) term enrichment analysis was performed in AmiGO with the genes included in each cluster and the results were visualised in REVIGO (Figure 5.4B). Treemaps of top and bottom clusters showed the most represented pathways for each group of genes, and sizes of the rectangles were proportional to the frequency of the GO term in the AmiGO database. Top cluster was upregulated in D3 samples and it comprised genes involved in RNA metabolism and heterocycle metabolism. This high level of transcription activity indicated the predominance of cell proliferation at the early stage of the culture. Instead, bottom cluster was mainly upregulated in D8 samples and it included genes involved in regulation of lipid metabolism and detection of chemical stimulus involved in sensory perception. Lipid metabolism is known to be altered under hypoxic conditions or in tumour cells, contributing

significantly to the pathogenesis and/or progression of cancer and metabolic disorders (Mylonis et al. 2019). All these processes are more deeply studied below.

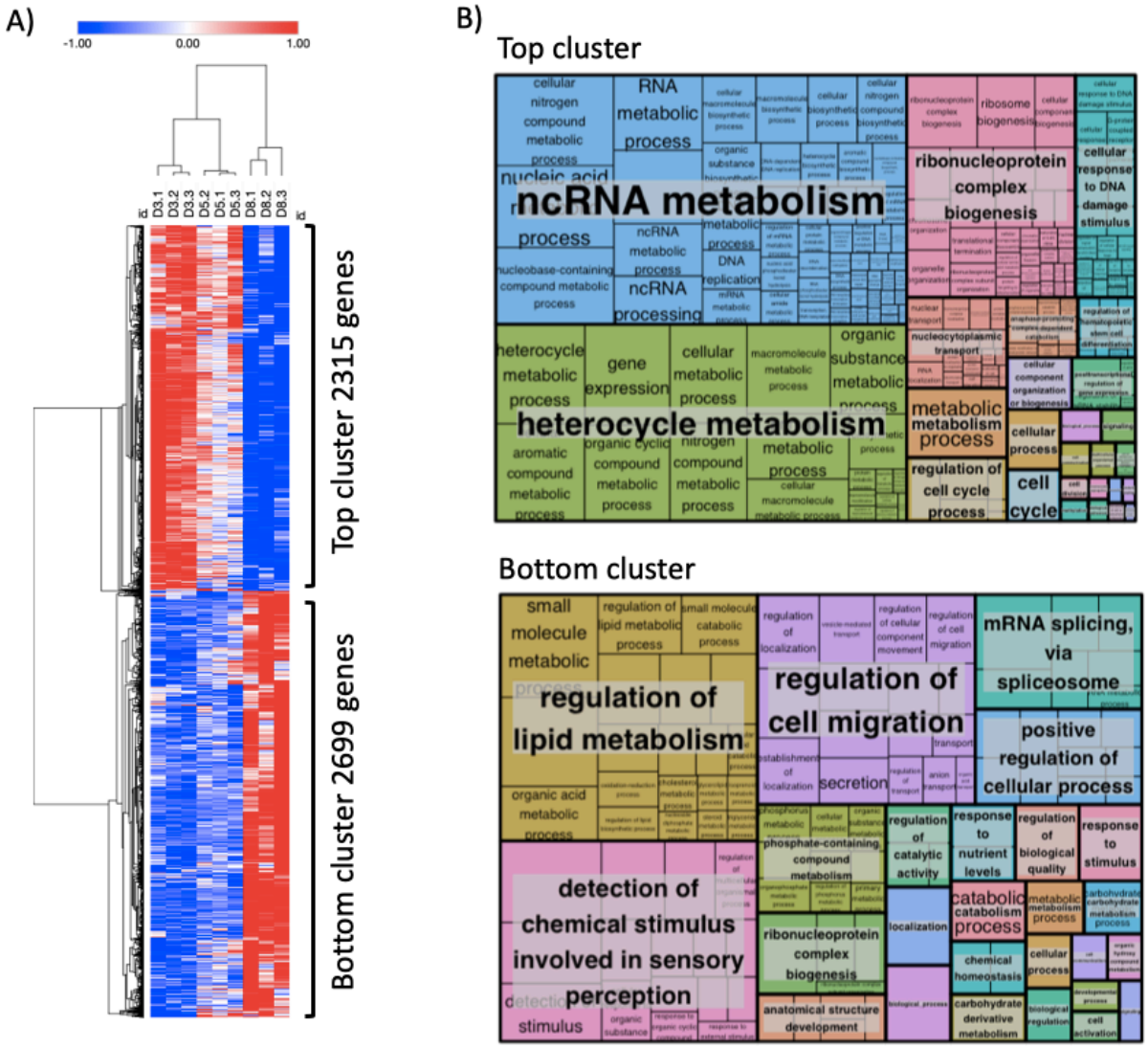

Figure 5.4 Time course experiment - Clustering and functional analysis of genes

A. Heatmap of differentially expressed genes (5014 genes, p-value<0.01) and hierarchical clustering (one minus Pearson correlation) was performed on Morpheus. Two clusters of genes were differentiated: Top cluster contained 2315 genes upregulated in D3 samples and Bottom cluster contained 2699 genes upregulated in D8 samples. **B.** Genes of each cluster were assessed for pathway enrichment analysis in AmiGO and treemaps were generated with REVIGO to visualise the most represented pathways in the GO term list. Each rectangle is a single cluster representative. The representatives are joined into superclusters of loosely related terms, visualised with different colours. The size of each rectangle is proportional to the frequency of the GO term in the database.

Further analysis was performed in AmiGO and Ingenuity Pathway Analysis (IPA) to identify potential biological processes and canonical pathways differentially expressed between larger organoids (D8) and smaller ones (D3). For that, the top 200 most differentially expressed genes, that resulted from the DESeq analysis of the pairwise comparison between D3 and D8 samples, were selected for gene enrichment analysis. The top 200 genes were chosen for the analysis based on Gene Ontology recommendations (http://geneontology.org/docs/faq/), which suggested that for a 25000 interrogated transcripts, the number of genes included in a functional analysis should be between 150 and 3000 genes (it would be difficult to observe enrichment when analysing less than 150 genes, and it would be difficult to obtain a meaningful enrichment when analysing more than 3000 genes). Therefore, considering that D3 and D8 presented 4795 differentially expressed genes (with adjusted p-value<0.01), the number of genes recommended for a functional analysis was between 30 and 575 genes in order to maintain the same ratio of minimum and maximum number of genes per number of interrogated transcripts as recommended by Gene Ontology. Taking into account this range, the top 200 most differentially expressed between D3 and D8 genes were selected for AmiGO and IPA analyses. Furthermore, these top 200 genes corresponded to an adjusted p-value<3.57×10^{-19} based on DESeq results, which indicated a relevant statistical significance.

The results obtained from the gene set enrichment analysis are shown in Figure 5.5. Among the most enriched GO terms from AmiGO database, it is worth highlighting carbohydrate derivative metabolic process, response to hypoxia and lipid metabolic process (Figure 5.5A). On the other hand, IPA correlations showed that PXR/RXR activation, glycolysis and acetate conversion to acetyl-CoA were some of the top functions and canonical pathways associated with the most differentially expressed genes between D3 and D8 (Figure 5.5B). Expression level of significantly different genes involved in these processes and listed in AmiGO and IPA results is discussed below.

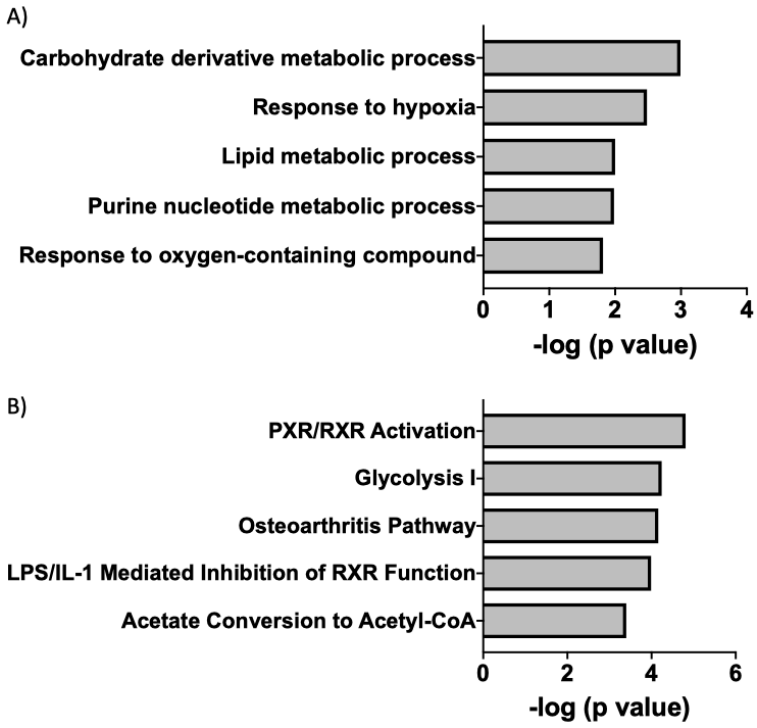

Figure 5.5 Top biological processes enriched in Iso50 CRC organoids cultured for 8 days compared to Iso50 CRC organoids cultured for 3 days

Top 200 genes most differentiated (adj p-value < $3.57x10^{-19}$) between organoids cultured for 3 and 8 days were used for **A.** GO term enrichment analysis using the AmiGO tool and **B.** canonical pathways enrichment through IPA. The 5 most enriched processes for each analysis are indicated, p-value< $1.53x10^{-2}$ and p-value< $3.98x10^{-4}$ for AmiGO and IPA, respectively.

Some of the gene expression changes that were observed in large (D8) versus small (D3) organoids might be related to hypoxia and they are discussed below. First, it is well known that hypoxic tumour cells undergo a significant shift from oxidative phosphorylation in mitochondria towards anaerobic glycolysis (Kucharzewska et al. 2015; Mylonis et al. 2019; Lyssiotis & Kimmelman 2017). During glycolysis, glucose is broken down to pyruvate, which is then converted into lactate by lactate dehydrogenase A (LDHA) instead of being oxidise via the tricarboxylic acid (TCA) cycle and oxidative phosphorylation. Glycolysis is less efficient in ATP production than oxidative phosphorylation (2 ATP vs. 38 ATP per mol of glucose), thus tumour cells need to consume more glucose to maintain its energy requirements for growth and survival (Huang et al. 2014). This was evidenced in D8 samples by transcription induction of glucose transporters, e.g. *GLUT1* (3.2-fold), *GLUT3* (3.3-fold), glycolytic enzymes, e.g. *PGK1* (1.9-fold), *ENO2* (10.9-fold), *ALDOC* (9.8-fold) and proteins that facilitate the synthesis and excretion of lactate, e.g. *LDHA* (1.8-fold) and *SLC16A3* (23.3-fold), respectively. The

reported genes upregulated in D8 samples when compare to D3 samples have been previously described as HIF1-target genes and their biology is known to be upregulated in response to hypoxia (Mylonis et al. 2019; Kucharzewska et al. 2015; Fedorova et al. 2019; Benita et al. 2009; Wang et al. 2018; Pisarsky et al. 2016; Allen et al. 2016; Chi et al. 2006; Fang & Fang 2016; He 2019a). Also, multiple mitochondrial ribosomal proteins (MRPs), translocases of the inner and outer mitochondria membrane (TIMM/TOMMs) and enzymes of the citric acid cycle were found to be downregulated in late-harvested organoids (D8) when compared to early-harvested organoids (D3). Some examples are: *MRPL1* (0.6-fold), *TIMM50* (0.6-fold), *TOMM40* (0.5-fold) and *IDH3A* (0.6-fold). Downregulation of mitochondrial proteins and citric acid cycle enzymes after 72 h of hypoxia has previously been reported for HeLa cells (Bousquet et al. 2015). Relevant overexpression of *SLC16A3*, a gene involved in rapid lactic acid transport across the plasma membrane, was in accordance with the high level of glycolysis and lactate production. Importantly, lactate has to be protonated to be transported across the plasma membrane, thus intracellular acidification influences homeostatic pH_i (intracellular pH) (Halestrap 2011). In order to minimise this acid stress, cells probably overexpressed genes involved in lactic acid excretion, such as *SLC16A3*, to maintain homeostatic pH_i. Acidosis in the tumour microenvironment has also been attributed to cellular CO_2 production and subsequent hypercapnic acidosis in the extracellular space of tumours. This has been explained by carbonic anhydrase *CA9* overexpression, which catalyses the hydration of CO_2 to form H^+ and HCO_3^-, and this gene is regulated by HIF1 in poorly differentiated cancers (Parks et al. 2017). As regards the latter, D8 organoids showed a 91.4-fold higher expression of *CA9* than D3 organoids, which evidenced the essential role of HIF1 in larger organoids when compared to smaller ones.

Second, activation of carbohydrate derivative metabolic processes, which include overexpression of *PFKP* (2.7-fold), *PFKFB4* (8.2-fold), *PGK1* (1.9-fold), *ALDOA* (1.9-fold) and *ALDOC* (9.8-fold) in D8 samples compared to D3 results, have been previously identified as hypoxia-inducible genes (Chi et al. 2006; Gao et al. 2018; He 2019b; Kawai et al. 2016; Fedorova et al. 2019).

Third, acetate conversion to acetyl-CoA is carried out by acetyl-CoA synthetase, *ACSS2*, whose expression was upregulated (2.8-fold) in D8 samples compared to D3 samples. Acetyl-CoA is widely used in macromolecule biosynthesis, such as lipid synthesis, and energy production to support cell growth and proliferation (Gao et al. 2016). It is mainly produced from oxidation of glucose, however, several studies have revealed that under hypoxic

conditions, *ACSS2* expression increases in cancer cells to capture acetate, as an alternative carbon source to glucose, to maintain cellular acetyl-CoA pool under stress conditions (Kamphorst et al. 2014; Gao et al. 2016). The high expression of *ACSS2* suggested that Iso50 CRC organoids cultured for 8 days experienced hypoxic conditions and converted acetate, present in B-27 Supplement (50X) (concentration unknown), into acetyl-CoA, due to the impaired flux from glucose to acetyl-CoA. Moreover, in non-tumour cells under normoxia, acetyl-CoA produced from pyruvate enters the TCA cycle, reaction mediated by pyruvate dehydrogenase (PDH). However, in order to reduce mitochondrial function during hypoxia for decreasing consumption of oxygen and ROS production, cancer cells induce the expression of pyruvate dehydrogenase kinase 1 (*PDK1*), which is a suppressor of *PDH* that blocks the conversion of pyruvate to acetyl-CoA (Mylonis et al. 2019). The expression level of *PDK1* was 5.4-fold higher in D8 samples than D3 samples, and contributed to reinforce the idea of the possible insufficient oxygen supply in larger organoids.

Fourth, AmiGO identified lipid metabolism as a biological process differentially expressed between D3 and D8. Some studies have demonstrated disorders of lipid metabolism in solid tumours, such as pancreatic cancer (Swierczynski 2014), liver cancer (De Huang et al. 2014), breast cancer (Alo et al. 1999), colon cancer (Accioly et al. 2008), and ovarian cancer (Nomura et al. 2010). Moreover, recent evidences have indicated that many aspects of lipid metabolism are modified during hypoxia, contributing significantly to the progression of cancer and metabolic disorders (Shen & Li 2017b; Mylonis et al. 2019). As conversion of glucose into citrate, the major source of cytoplasmic acetyl-CoA and fatty acids precursors, is prohibited under hypoxia due to the inhibition of the TCA cycle, hypoxia-mediated changes in lipid metabolism are required to maintain the high proliferation rate that characterises cancer cells. For instance, increase of fatty acids uptake under hypoxia has been described by several authors through the upregulation of FABPs (fatty acid binding proteins) (Ni et al. 2017; Mylonis et al. 2019), e.g. high level of *FABP1* expression has been demonstrated in colon cancer cell line under hypoxia, as well as, high level of *FABP3* expression in breast cancer, ovarian cancer and gliobastoma cells (Iwamoto et al. 2018; Munir et al. 2019). In concordance, D8 samples presented a 3.8-fold higher expression of *FABP1* and 3.3-fold higher expression of *FABP3* than D3 samples, which could indicate the promoted fatty acids uptake in larger organoids. Moreover, it had been reported that hypoxia significantly increased the uptake of low- and very-low-density lipoproteins revealed by the upregulation of *LDLR* and *VLDLR* (Shen & Li 2017a). In fact, Iso50 CRC organoids cultured for 8 days experimented a 1.5-fold and 6.1-fold

increase of *LDLR* and *VLDLR* expression, respectively, when compared with organoids cultured for 3 days. Similarly, overexpression of *LRP1*, which is the key receptor for cholesterol uptake, has been described under hypoxia in vascular smooth muscle cells and in cardiomyocytes (Cal et al. 2012a; Shen & Li 2017b; Mylonis et al. 2019) and it was also upregulated in D8 samples (5.4-fold) in this study. Furthermore, *ABCA1*, the ATP-binding cassette transporter A1 that plays a major role in cholesterol efflux, showed a 6.1-fold increase in the expression of D8 samples compared to D3 samples. *ABCA1* upregulation has previously been described for vascular endothelial cells (Manalo et al. 2005) and for human macrophages (Ugocsai et al. 2010) under hypoxia. In contrast, other authors have described that hypoxia reduces ABCA1-mediated cholesterol efflux, due to subcellular redistribution of ABCA1 protein under acute hypoxia and decreased protein level under prolonged hypoxia (Parathath et al. 2011).

Fifth, Pregnane X receptor/Retinoid X receptor (PXR/RXR) activation resulted as an overexpressed pathway in late-harvested Iso50 CRC organoids compared to early-harvested Iso50 CRC organoids. PXR is activated by sterols, bile acids, and > 60% of clinical drugs and heterodimerises with RXR to upregulate the expression of proteins involved in the detoxification and clearance of these substances from the body (Li et al. 2007). The previously described increase of cholesterol uptake in D8 samples via LRP1 receptor could explain the activation of *PXR* (8.4-fold). Moreover, Li *et al*. (2007) have demonstrated that *PXR* plays an important role in the detoxification of cholesterol in the intestine through CYP27A1 activation, which induces LXRA and its target genes, such as *ABCA1* and *ABCG1*, involved in cholesterol efflux (Li et al. 2007). The PXR/CYP27A1/LXRA pathway suggested by Li *et al*. (2007) could explain the overexpression of the implicated genes in regulation of cholesterol efflux in D8 samples, i.e. *PXR* (8.4-fold), *CYP27A1* (2.6-fold), *LXRA* (1.4-fold), *ABCA1* (6.1-fold) and *ABCG1* (27.5-fold).

Taken together, the evidences showed above suggested that hypoxia as well as carbohydrate and lipid metabolism were the most important differences detected between organoids grown for 3 and 8 days. Adaptation to hypoxia involves hypoxia inducible factor 1 (HIF1α), which was the main upstream regulator found by IPA in D8 samples. HIF1α is unstable under normoxia but becomes stable in hypoxic conditions and translocates into the nucleus, heterodimerises with HIF1β and the complex binds to HREs within the promoter regions of target genes. *HIF1α* expression in D3 and D8 samples was analysed and no significant differences were detected (adj p-value: 0.026). Indeed, larger Iso50 CRC organoids showed a

slight decrease (0.79-fold) of *HIF1α* expression compared to smaller ones. This observation agreed with reported results that indicate that HIF1α protein is transiently upregulated in hypoxia, but mRNA is frequently found to be unaffected or repressed (Cavadas et al. 2015; Abraham et al. 2004; Wenger et al. 1997). Further analysis of HIF1α protein level over culture time and other hypoxia markers, such as CA9, GLUT1, MCT1 and MCT4, by immunohistochemistry would be required to confirm the suggested lack of oxygen availability in organoids cultured for 8 days. Moreover, oxygen gradients in organoids could be measured with an electron paramagnetic resonance oximetry method that could be implemented similarly to the methodology applied by Langan *et al*. 2016 to measure the oxygen gradients in spheroid culture systems (Langan et al. 2016).

Apart from low oxygen availability, nutrient depletion has also been reported in the TME. The lack of glucose, amino acids and lipids in the TME has been described in literature and processes related to the supply of these nutrients are often upregulated in cancer cells (Nazemi & Rainero 2020; Finicle et al. 2018; Sullivan & Heiden 2019). Since nutrient diffusion distance varies in organoids of different size, it was hypothesized that the core of larger organoids might present lower nutrient availability, which could induce the expression of genes involved in nutrient uptake in D8 samples. For example, glucose transporters, e.g. *GLUT1* (3.2-fold) and *GLUT3* (3.3-fold), were overexpressed in larger organoids (D8) when compared to smaller ones (D3). Also, fatty acid uptake was induced in D8 samples over D3 samples, i.e. *FABP1* (3.8-fold) and *FABP3* (3.3-fold). Moreover, although the expression of the amino acid transporter *LAT1* was not upregulated in D8 samples (0.80-fold) when compared to D3 samples, the synthesis of amino acids was upregulated in organoids cultured for 8 days through the activation of the enzymes involved in the serine synthesis pathway, such as phosphoglycerate dehydrogenase (*PHGDH*, 1.6-fold) and phosphoserine aminotransferase (*PSAT1*, 1.2-fold). In summary, overexpression of genes involved in glucose and fatty acids uptake and serine synthesis suggested that larger Iso50 CRC organoids (D8) might present lower access to nutrients than smaller ones (D3). In agreement with that, it has been reported that the total uptake of nutrients (oxygen and glucose) is proportional to the spheroid diameter (Hu & Li 2007).

Finally, it is worth mentioning that differences detected in the gene expression profiles of organoids cultured during different days might be affected by other factors than their size. These include organoid age and depletion of certain nutrients along the cultivation time, although this was unlikely because the medium was replaced every 2-3 days. In order to avoid

possible time effects, another strategy to generate heterogeneous organoid size distributions consisted of filtering an organoid population at a specific day of culture and the gene expression results are shown below.

5.2.3.2 Size-based fractionation experiment

To avoid possible effects of time-dependent alterations of culture conditions on the study of the organoid transcriptome, a size-based fractionation experiment was suggested with organoids cultured for 5 and 8 days. For that, Iso50 CRC organoids were fractionated using PS of 40 μm and 85 μm to generate: Fraction < 40 μm, Fraction 40-85 μm and Fraction > 85 μm. Firstly, gene expression of different size fractions of organoids cultured for 5 days was investigated. Secondly, the same analysis was performed with fractionated organoids cultured during 8 days.

5.2.3.2.1 Size-based fractionation experiment - Day 5

Organoids cultured for 5 days were fractionated with PS of 40 μm and 85 μm and representative images of each fraction are shown in Figure 5.6A. Size differences were observed as expected between Fraction < 40 and Fraction 40-85, although the absolute number of organoids in Fraction > 85 was very low. RNA of each fraction (Fraction < 40 μm, Fraction 40-85 μm and Fraction > 85 μm) was extracted from three biological replicates and sequenced with Illumina NextSeq 500 with a coverage of 30 million reads per sample. Bioinformatics analysis included the pre-filtering step previously described to remove lowly expressed genes. Once the filtering was applied, only 16532 "expressed" genes from 41517 total genes were included in the DESeq analysis in R, in which every sample was compared against every other sample, i.e. Fraction < 40 vs. Fraction 40-85, Fraction < 40 vs. Fraction > 85 and Fraction 40-85 vs. Fraction > 85.

First, clustering was performed considering paired samples by PCA (Figure 5.6B) and hierarchical clustering with sample-to-sample Euclidean distance (Figure 5.6C). PCA results showed that the three fractions coming from biological replicate s1 grouped clearly together but clusters of s2 and s3 were not as well defined. Moreover, organoid size did not explain the higher variability between samples, as they did not group based on this parameter (Figure 5.6B). Similarly, hierarchical clustering with sample-to-sample Euclidean distances showed

that the three fractions coming from each biological replicate (s1, s2 and s3) were more similar to each other than between biological replicates of the same size fraction (Figure 5.6C). This suggested that cell origin had a higher influence on the transcriptome than the organoid size (within the range of sizes examined). Furthermore, red dots of MA-plots (Figure 5.6D) represented the differentially expressed genes between fractions, and it can be highlighted that the amount of differentially expressed genes was highly reduced when compared to differences between samples harvested on day 3, day 5 and day 8 (Figure 5.3D). This indicated that gene expression across different size fractions of organoids cultured for 5 days was statistically similar. Nevertheless, differentially expressed genes between these samples were further investigated.

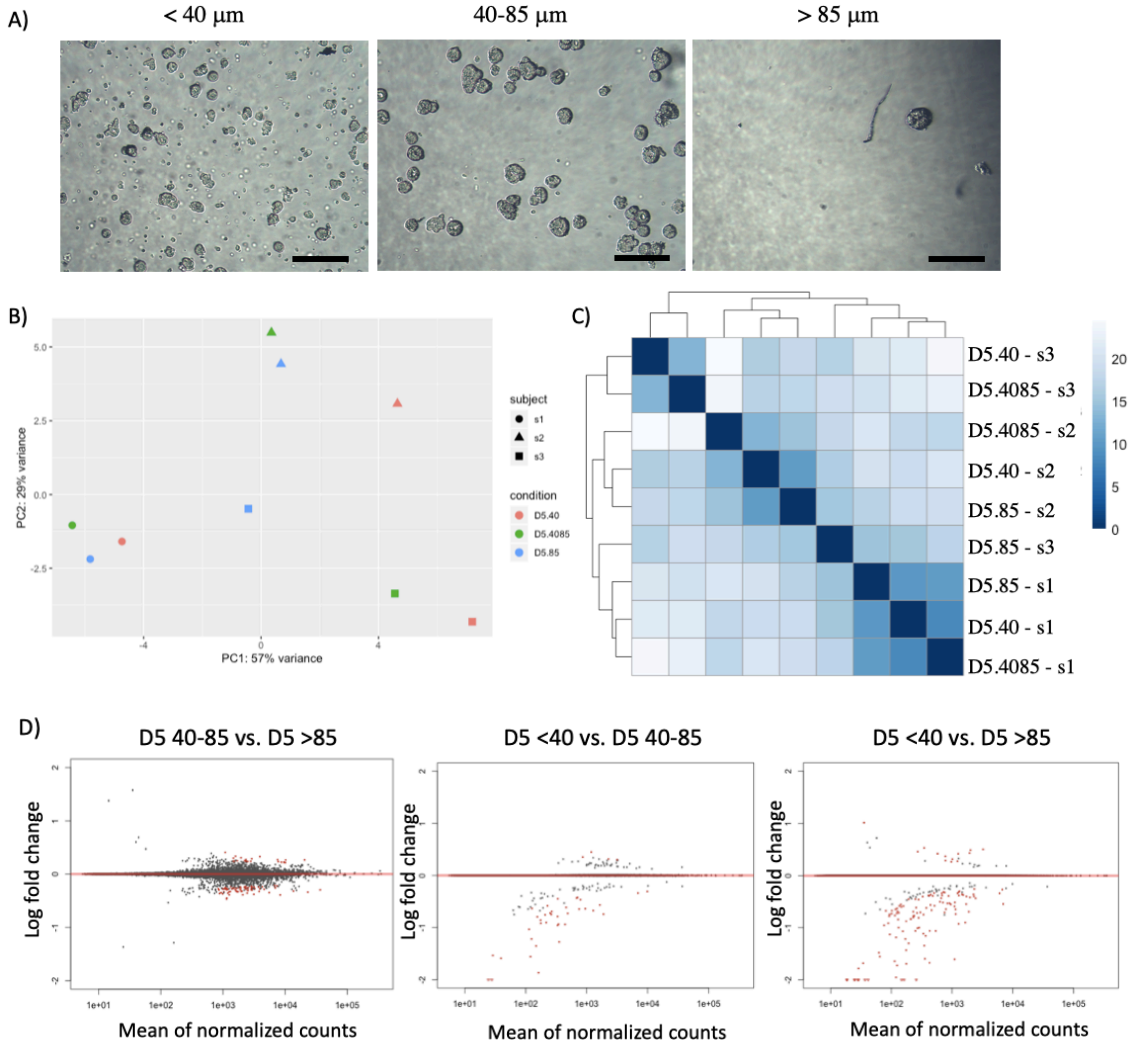

Figure 5.6 Size-based fractionation experiment - Day 5. Sample clustering and MA-plots

Iso50 CRC organoids cultured for 5 days were fractionated with PS of 40 µm and 85 µm. RNA from Fraction < 40, Fraction 40-85 and Fraction > 85 was extracted and subsequently sequenced (N=3). **A.** Representative images of Fraction < 40, Fraction 40-85 and Fraction > 85 samples after filtration. Scale bars correspond to 100 µm. **B-D.** RNA-seq was performed using Illumina NextSeq 500 and only "expressed" genes were considered for paired analysis (16532 from 41517 total genes). **B.** Results were analysed by PCA plot along first two components. Fraction size is represented by colour. Biological repeat, i.e. subject, is represented by shape. **C.** Heatmap of sample-to-sample Euclidean distances and hierarchical clustering based on the sample distances. **D.** MA-plots of the three possible sample comparisons. Genes with adjusted p-value below 0.1 are shown in red.

Next, only differentially expressed genes between Fraction < 40, Fraction 40-85 and Fraction > 85 were considered for the comparative analysis of gene expression profile between these fractionated organoids harvested after 5 days of culture. Differently expressed genes were obtained from DESeq results of the comparison of every sample against every other sample (94 genes, p-value<0.01, obtained from the three possible pairwise comparisons between

Fraction < 40, Fraction 40-85 and Fraction > 85 samples). It is worth mentioning that the number of differentially expressed genes was reduced 50 times when compared to the number of differentially expressed genes obtained in Time course experiment (5014 genes). This indicated that transcriptome of different size Iso50 CRC organoids cultured during 5 days did not show as many differences as the transcriptome of organoids cultured for different times. Hierarchical clustering (one minus Pearson correlation) of differentially expressed genes by Morpheus (Figure 5.7A) showed that the three size fractions of biological repeat 1 grouped together. However, clustering was not so defined with biological repeats 2 and 3. Moreover, samples did not cluster based on organoid size. Regarding the heatmap, gene expression grouping as a function of organoid size was not accomplished. Then, the 94 differentially expressed genes between Fraction < 40, Fraction 40-85 and Fraction > 85 were considered for pathway enrichment analysis in AmiGO and results were visualised with REVIGO. As shown in Figure 5.7B, regulation of locomotion, tube development and response to wounding were the most differentiated biological processes between the three size fractions obtained after 5 days of culture. Based on the heatmap (Figure 5.7A), the differentially expressed genes involved in that processes were overexpressed mainly in Fraction < 40 of biological repeats 2 and 3 and in Fraction 40-85 of biological repeat 3. However, Fraction < 40 of biological repeat 1 did not show the same pattern of expression, which could hamper the establishment of a strong relation between organoid size and the upregulated biological processes found in AmiGO. Nonetheless, results suggested that small organoids and single cells showed an activation of regulation of locomotion pathway compared to larger organoids. This could be explained due to the higher specific surface area of single cells and small organoids in contact with the extracellular matrix than cells forming larger organoids. Thus, the influence of the mechanical properties of Matrigel was expected to be greater in small organoids than in larger ones. It has been described that cell locomotion and focal adhesions are regulated by mechanical properties of extracellular matrix, such as the elasticity and stiffness. For instance, *ANXA1*, *CAV1*, *CAV2*, *ETS1* and *LAMC2* are genes involved in the regulation of extracellular matrix integrity (Bizzarro et al. 2012; Aga et al. 2014; Span et al. 2002; Xiong & Xu 2016) and these showed significant differences in expression levels between organoids in Fraction < 40 and organoids in Fraction 40-85, i.e. *ANXA1* (0.6-fold), *CAV1* (0.5-fold), *CAV2* (0.7-fold), *ETS1* (0.4-fold) and *LAMC2* (0.6-fold), repressed in Fraction 40-85 in all cases.

In summary, different size Iso50 CRC organoids generated by filtration after 5 days of culture did not show notable differences in gene expression profiles. In order to increase organoid size

variability and a probable induction of organoid transcriptome differences, the same filtration experiment was performed with Iso50 CRC organoids cultured for 8 days and results are shown in next section.

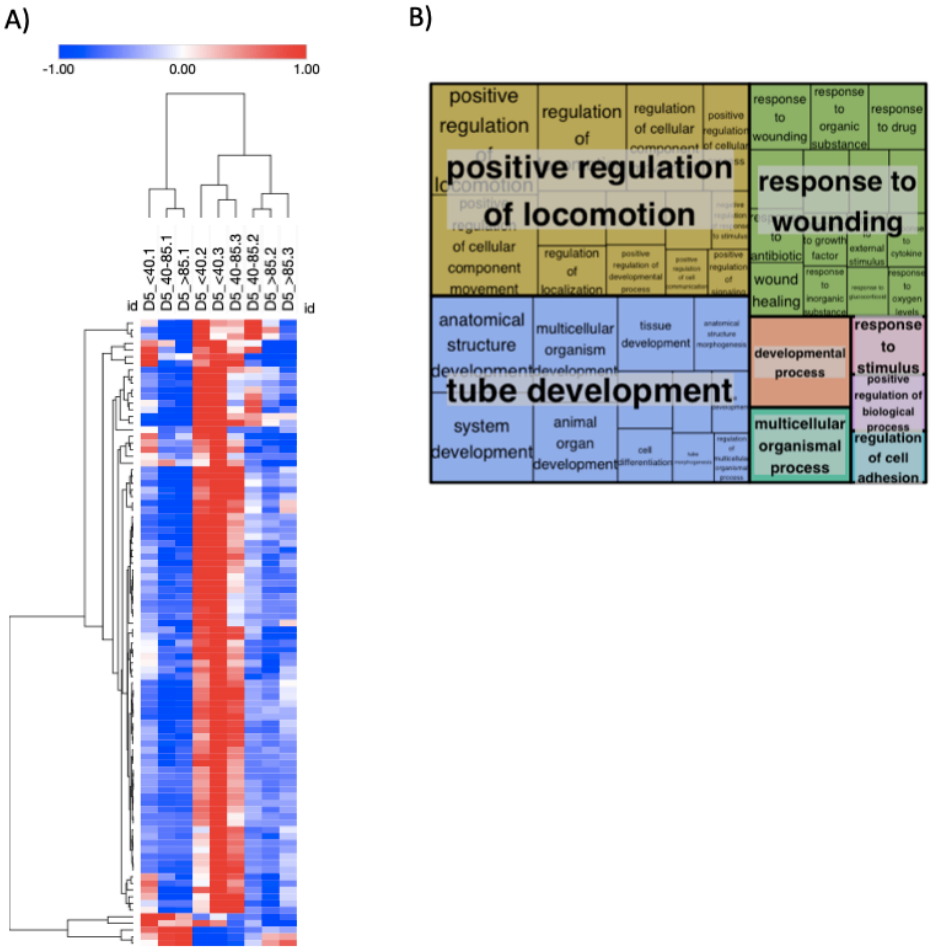

Figure 5.7 Size-based fractionation experiment - Day 5. Clustering and functional analysis of genes

A. Heatmap of differentially expressed genes (94 genes, p-value<0.01) and hierarchical clustering (one minus Pearson correlation) was performed on Morpheus. **B.** The 94 differentially expressed genes were assessed for pathway enrichment analysis in AmiGO and treemap was generated with REVIGO to visualise the most represented pathways in the GO term list. Each rectangle is a single cluster representative. The representatives are joined into superclusters of loosely related terms, visualised with different colours. The size of each rectangle is proportional to the frequency of the GO term in the database.

5.2.3.2.2 Size-based fractionation experiment - Day 8

Iso50 CRC organoids cultured for 8 days were fractionated with PS of 40 μm and 85 μm to generate Fraction < 40 μm, Fraction 40-85 μm and Fraction > 85 μm, whose size differences are clearly shown in Figure 5.8A. RNA was extracted from each fraction and subsequently sequenced using the Illumina NextSeq 500. Gene expression analysis included the same pre-filtering step as in Time course experiment to remove lowly expressed genes. Thus, for DESeq analysis in R, only 16942 "expressed" genes were considered from 41517 total genes, in which every sample was compared against every other sample, i.e. Fraction < 40 vs. Fraction 40-85, Fraction < 40 vs. Fraction > 85 and Fraction 40-85 vs. Fraction > 85.

First, clustering of paired samples was performed to find patterns in the data and to identify possible outliers. Two different unsupervised methods were used for clustering the data: PCA (Figure 5.8B and Figure 5.8C) and hierarchical clustering with sample-to-sample Euclidean distance (Figure 5.8D). PC1 and PC2 explained 56% and 23% of the variability of the data, respectively, and Figure 5.8B shows that sample clustering was not as clear as in Time course experiment (Figure 5.3B). At first sight, samples grouped based on subject, which corresponded to the experimental repeat, rather than grouping by size fraction. Again, this indicated that sample origin had a stronger influence in sample clustering than size fraction. Organoids of three consecutive passages were used for the three biological replicates of this experiment, thus passage influence was expected to be minimal. Other culture conditions, such as culture length, media composition, changes of media, temperature and CO_2 level were tried to be kept equal between the three repeats, but slight variations could induce differences in gene expression that are more significant than variations detected in organoids of different size. One important observation from the PCA plot in Figure 5.8B was that samples from the same replicates subject were positioned in a triangular shape in principal component space maintaining the position of each size fraction within the triangle. This could indicate that organoid size had an effect on sample clustering but that PC1 and PC2 might not be the best components to visualise this contribution. For that, PC3 (9.8%) was included in a 3D plot along with PC1 and PC2 (Figure 5.8C) and sample clustering according to the size fraction was more easily visualised. This suggested that some genes might present an expression pattern depending on organoid size, but these were separated from the major axes of variability between samples in this experiment. Furthermore, hierarchical clustering based on sample-to-sample distance showed that samples coming from the same initial mixture of organoids, i.e.

same subject, were more similar regardless of the size fraction (Figure 5.8D). Moreover, MA-plots showed that the number of differentially expressed genes between Fraction 40-85 and Fraction > 85 was low but, as expected, this number increased when comparing Fraction < 40 and Fraction > 85. Differentially expressed genes between these samples are studied more deeply below. Importantly, organoids present in the different fractions were cultured together, thus all organoids, regardless of their size, experienced the same environment during the cultivation period. This means that biological processes specific to an organoid size, such as medium acidification in large organoids or excretion of certain compounds, could affect the gene expression profile of organoids of a different size, thus increasing the similarity between size fractions.

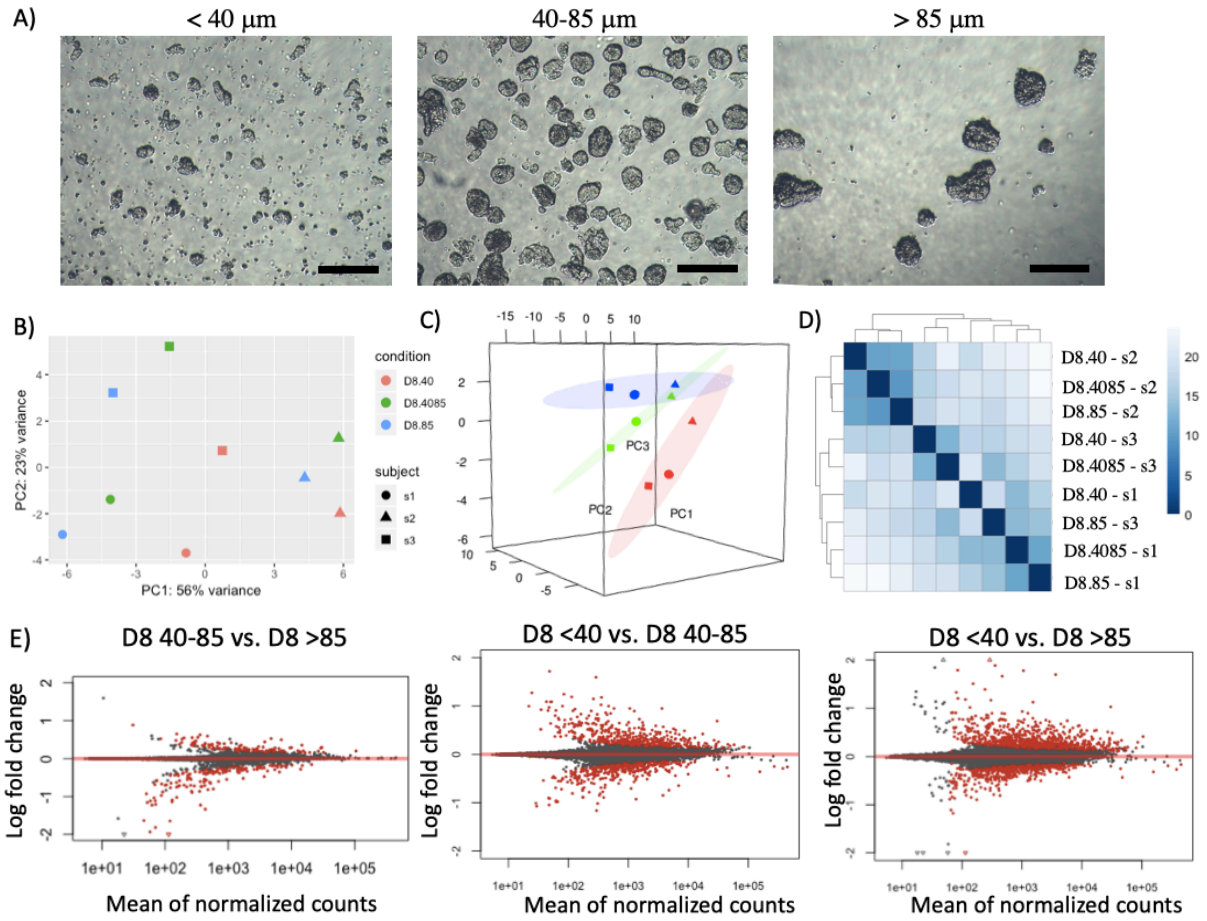

Figure 5.8 Size-based fractionation experiment - Day 8. Sample clustering and MA-plots

Iso50 CRC organoids cultured for 8 days were fractionated with PS of 40 µm and 85 µm. RNA from Fraction < 40, Fraction 40-85 and Fraction > 85 was extracted and subsequently sequenced (N=3). **A.** Representative images of Fraction < 40, Fraction 40-85 and Fraction > 85 samples after filtration. Scale bars correspond to 100 µm. **B-E.** RNA-seq was performed using Illumina NextSeq 500 and only "expressed" genes were considered for paired analysis (16942 from 41517 total genes). **B.** Results were analysed by PCA plot along first two components or **C.** first three components. **B-C.** share the same legend. Fraction size is represented by colour, whilst biological repeat, i.e. subject, is represented by shape. **D.** Heatmap of sample-to-sample Euclidean distances and hierarchical clustering based on the sample distances. **E.** MA-plots of the three possible sample comparisons. Genes with adjusted p-value below 0.1 are shown in red.

Next, differentially expressed genes between Fraction < 40, Fraction 40-85 and Fraction > 85 were considered for the comparative analysis of gene expression profile between these different-size organoids harvested after 8 days of culture. Differently expressed genes were obtained from DESeq results of the comparison of every sample against every other sample (894 genes, p-value<0.01, obtained from the three possible pairwise comparisons between Fraction < 40, Fraction 40-85 and Fraction > 85 samples). It should be noted that the number of differentially expressed genes in this analysis was considerably reduced when compared to

the number of differentially expressed genes in Time course experiment (5014 genes), but increased when compared to the number of differentially expressed genes in Size fractionation – Day 5 experiment (94 genes). This indicated that cultivation time induced major variations in gene expression profiles than the differences observed between the size fractions generated with PS. Furthermore, as previously hypothesised, transcriptome heterogeneity was higher in samples cultured for 8 days than in samples cultured for 5 days.

Hierarchical clustering (one minus Pearson correlation) of differentially expressed genes using the online tool Morpheus (Figure 5.9A) showed that the three biological repeats of Fraction < 40 grouped together, unlike Fraction 40-85 and Fraction > 85 that clustered in pairs. Moreover, three clusters of genes were identified, i.e. top cluster contained 527 genes mainly upregulated in Fraction > 85, medium cluster comprised of 87 genes overexpressed in Fraction 40-85 and bottom cluster consisted of 218 genes upregulated in Fraction < 40. GO term enrichment analysis was performed in AmiGO with the genes included in each cluster to identify which biological processes were mainly expressed in a specific size fraction, then results were visualised as a treemap with REVIGO (Figure 5.9B). On the one hand, top cluster contained genes upregulated in larger organoids that were involved in cholesterol metabolism, cellular response to organic cyclic compounds, epithelial cell differentiation and response to hypoxia, among others. Increase in cellular cholesterol levels has previously been correlated with hypoxia (Ramakrishnan et al. 2014; Shen & Li 2017b) due to the overexpression of genes involved in cholesterol uptake in cardiomyocytes and vascular smooth muscle cells (Cal 2012b; Shen & Li 2017b; Mylonis et al. 2019), as well as the induction of cholesterol synthesis in murine atherosclerotic plaques (Parathath et al. 2011). Therefore, deregulation of cholesterol metabolism in larger Iso50 CRC organoids might be explained due to a possible limited oxygen diffusion in organoids larger than 85 μm. Expression level of genes involved in cholesterol metabolism are further discussed below. Furthermore, the deregulated response to organic cyclic compounds could be related to steroid efflux, such as cholesterol. Regarding epithelial cell differentiation, previous reports have demonstrated the effect of aggregate size on cell differentiation because of its impact on the microenvironmental parameters, including the spatial gradient and cell-matrix interactions (Chen et al. 2015; Fonoudi et al. 2015; Bauwens et al. 2008; Silva et al. 2019). On the other hand, medium cluster contained genes upregulated in Fraction 40-85 that were involved in regulation of cell differentiation, cell migration and response to stimulus. In normal intestinal organoids, cell differentiation comes together with cell migration as organoids increase their size, since transit amplifying cells migrate upward

out of the crypt towards the lumen and they move along signalling gradients that trigger them to differentiate, giving rise to mature cell types (Spit et al. 2018). However, loss of APC in tumours results in cells that migrate aberrantly or less efficiently towards the crypt base in which they accumulate and form polyps (Narayan & Roy 2003). Bagley *et al*. (2017) showed that as cerebral organoids increased in size with age, the density of migrating cells increased, i.e. it was small around day 30, then increased from day 30 to 46, but they did not observe a significant increase from day 46 to 80 (Bagley et al. 2017). Taking this result into account, the migrating cell density might show a similar trend in different size Iso50 CRC organoids, but further studies including immunostaining with cell migration markers, such as matrix metalloproteinase-2 (MMP-2), matrix metalloproteinase-9 (MMP-9) and vascular endothelial growth factor (VEGF) could be perform to analyse the cell migration in organoids of different size (Yang et al. 2017). Finally, bottom cluster contained genes overexpressed in smaller organoids that were involved in RNA processing and cellular metabolism. These data suggested a higher proliferative capacity of small Iso50 CRC organoids when compared to larger ones, similar to previously described pattern in small spheroids (Laurent et al. 2013).

In summary, hierarchical clustering of differentially expressed genes between Fraction < 40, Fraction 40-85 and Fraction > 85 harvested after 8 days of culture showed that small organoids presented high transcriptional activity typical of proliferating cells, and larger organoids contained differentiated cells with high migration capacity, an active lipid metabolism and a gene expression profile affected by hypoxia. Expression of genes involved in those processes is further discussed below.

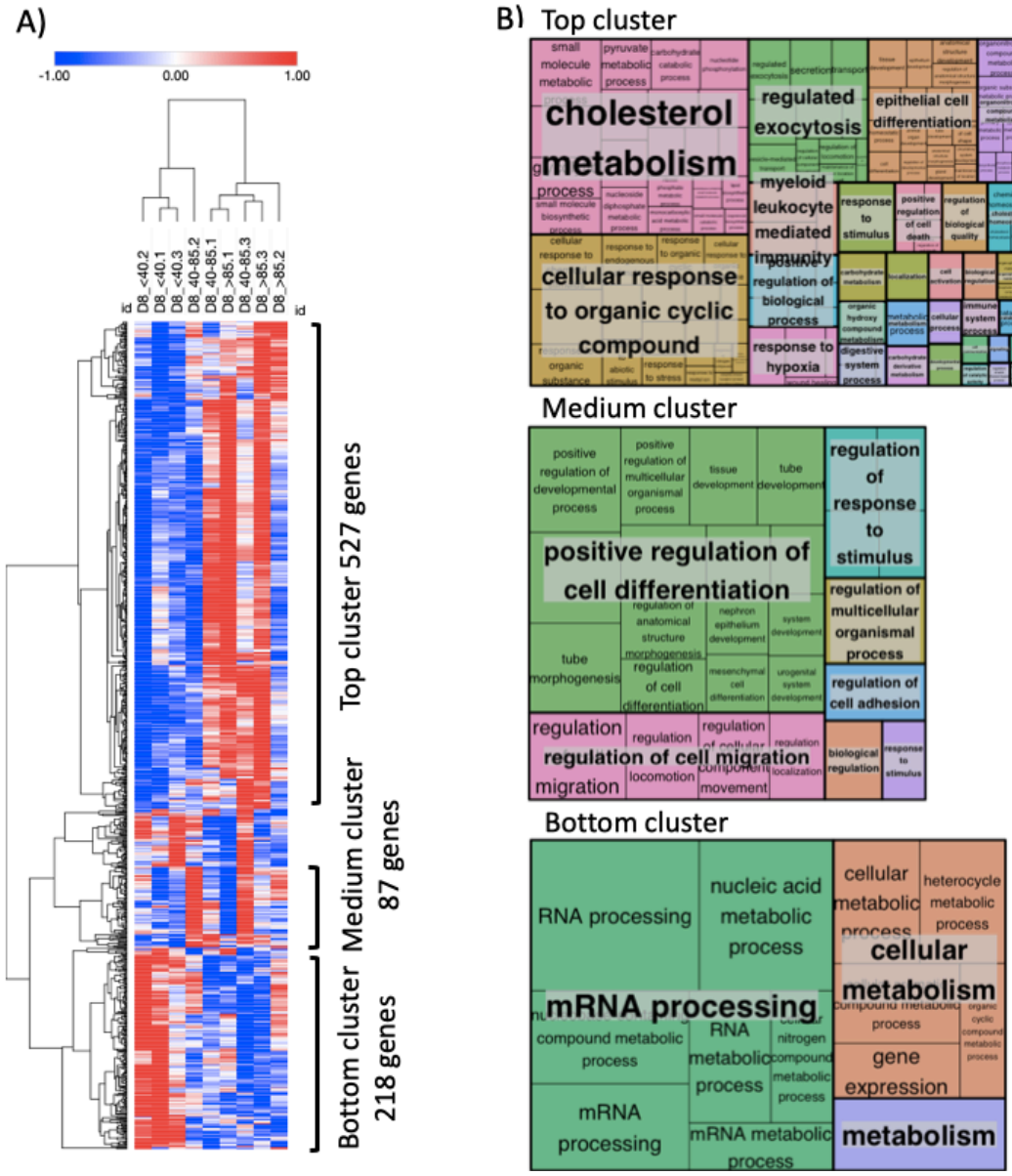

Figure 5.9 Size-based fractionation experiment - Day 8. Clustering and functional analysis of genes

A. Heatmap of differentially expressed genes (894 genes, p-value<0.01) and hierarchical clustering (one minus Pearson correlation) was performed on Morpheus. Three clusters of genes were differentiated: Top cluster contained 527 genes upregulated in Fraction > 85, Medium cluster contained 87 genes upregulated in Fraction 40-85 and Bottom cluster contained 218 genes upregulated in Fraction < 40. **B.** Genes of each cluster were assessed for pathway enrichment analysis in AmiGO and treemaps were generated with REVIGO to visualise the most represented pathways in the GO term list. Each rectangle is a single cluster representative. The representatives are joined into superclusters of loosely related terms, visualised with different colours. The size of each rectangle is proportional to the frequency of the GO term in the database.

Since gene expression profiles of Fraction < 40 and Fraction > 85 showed the highest divergence, further analysis with the most differentially expressed genes between these two fractions was performed with AmiGO and IPA to determine the most differentiated pathways between large and small organoids after 8 days of culture. The top 200 most differently expressed genes, that resulted from the DESeq analysis of the pairwise comparison between Fraction < 40 and Fraction > 85 samples, were selected for gene enrichment analysis in AmiGO and IPA software. These top 200 genes corresponded to an adjusted p-value < $6.8x10^{-5}$ based on DESeq results, which indicated a relevant statistical significance.

The results obtained from the gene enrichment analysis are shown in Figure 5.10 and both databases revealed upregulation of similar biological processes. Glycolysis, cholesterol biosynthesis, tight junction signalling and sirtuin signalling pathway were some of the biological processes upregulated in large organoids compared to smaller ones. Expression level of genes involved in these processes and listed in AmiGO and IPA results is discussed below.

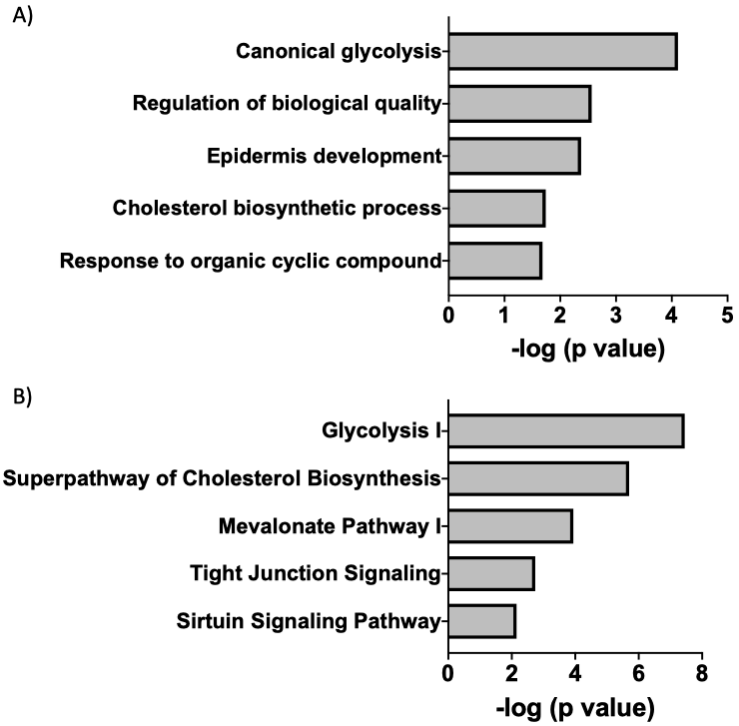

Figure 5.10 Top biological processes enriched in Iso50 CRC organoids present in Fraction > 85 compared to Iso50 CRC organoids present in Fraction < 40 after 8 days of culture

Top 200 genes most differentiated (adj p-value < $6.8x10^{-5}$) between organoids present in Fraction < 40 and Fraction > 85 were used for **A.** GO term enrichment analysis using the AmiGO tool and **B.** canonical pathways enrichment through IPA. The 5 most enriched processes for each analysis are indicated, p-value< $2.08x10^{-2}$ and p-value< $1.82x10^{-3}$ for AmiGO and IPA, respectively.

First, it is well established that hypoxic tumour cells reduce their reliance on mitochondrial oxygen-dependent ATP production in favour of cytoplasmic glycolysis (Wang et al. 2018; Nijhuis et al. 2017; Fang & Fang 2016; Li et al. 2018). The effect of organoid size on this metabolic shift was assessed by studying the expression of genes involved in glycolysis. Iso50 CRC organoids present in Fraction > 85 showed a 1.3-fold increase of *GLUT1* expression when compared to organoids present in Fraction < 40, which indicated that glucose uptake was enhanced in larger organoids. Overexpression of *GLUT1* under glucose deprivation has previously been shown for prostate cancer cells and fibroblast cells (Gonzalez-Menendez et al. 2018; Roelofs et al. 2006), which could indicate that organoids in Fraction > 85 suffered from nutrient deprivation at a larger extent than organoids in Fraction < 40. Furthermore, some glycolytic enzymes were upregulated in larger organoids, such as *PGK1* (1.3-fold), *ALDOA* (1.4-fold), *ALDOC* (1.7-fold), *PFKP* (1.3-fold), *PFKFB4* (1.5-fold) and *ENO2* (1.5-fold). Moreover, *LDHA*, *SLC16A3* and *CA9* expression presented a 1.3-fold, 1.6-fold and 1.9-fold increase, respectively, in Fraction > 85 in comparison to Fraction < 40. Lactate synthesis by LDHA is important to generate NAD^+, which is required to maintain the high glycolytic metabolism of large organoids, and SLC16A3 regulates lactic acid excretion to maintain homeostatic pH_i. Acidosis in the tumour microenvironment is also due to CO_2 hydration by the hypoxia-inducible gene *CA9*. Overexpression of this set of glycolytic genes indicated that larger organoids relied on glycolysis for energy production, thus suggesting that organoids in this fraction were probably under stronger hypoxic and/or nutrient deprivation conditions than smaller ones. This relation between organoid size and expression level of glycolytic genes has previously been described in Time course experiment (Section 5.2.3.1). References to published studies that demonstrate the upregulation of genes involve in glycolysis, and synthesis and excretion of lactate under hypoxia can be found in Section 5.2.3.1. In order to validate whether larger Iso50 CRC organoids adopted a glycolytic metabolic state, further studies to determine glucose consumption and lactate production levels by spectrophotometric enzyme assay are required (Wierenga et al. 2019).

Second, as previously detected in late-harvested organoids when compared to early-harvested organoids, cholesterol metabolism differed depending on organoid size. Organoids in Fraction > 85 showed upregulation of genes involved in fatty acid uptake (*FABP1*, 1.4-fold), and low- and very low-density lipoproteins uptake (*LDLR* and *VLDLR*, 1.4-fold each gene and *LRP1*, 1.6-fold). Overexpression of these genes has previously been described for larger organoids in the Time course experiment (see Section, 5.2.3.1), but unlike in Time course experiment, genes

involved in cholesterol biosynthesis also showed significantly higher expression in large organoids (Fraction > 85) when compared to small organoids (Fraction < 45) harvested after 8 days of culture. Cholesterol biosynthesis begins with the condensation of acetyl-CoA with acetoacetyl-CoA to form HMG-CoA, reaction catalysed by *HMGCS2*, which presented a 1.5-fold increase of expression in Fraction > 85 compared to Fraction < 40. Then, *HMGCR*, upregulated 1.3-fold, reduces HMG-CoA to mevalonate, which is converted to squalene through a series of reactions catalysed by *MVK* (1.3-fold), *MVD* (1.4-fold) and *FDFT1* (1.3-fold) genes, overexpressed in large organoids. Squalene is then converted into lanosterol by *SQLE* and *LSS*, whose expression increased 1.3-fold in large organoids in comparison to smaller ones. Finally, lanosterol serves as a precursor of cholesterol through several reactions and *DHCR7* encodes the terminal enzyme in the pathway of cholesterol biosynthesis, that catalyses the reduction of 7-dehydrocholesterol to cholesterol. Organoids present in Fraction > 85 displayed a *DHCR7* expression 1.3-fold higher than organoids present in Fraction < 40. These results indicated that pathway of cholesterol biosynthesis was induced in organoids larger than 85 μm when compared to organoids smaller than 40 μm. Increase in cellular cholesterol levels has previously been correlated with hypoxia (Ramakrishnan et al. 2014; Shen & Li 2017b) and this could explain the high cholesterol synthesis in large organoids. The increase of organoid diameter could generate oxygen gradients that trigger metabolic changes to adapt to the lack of oxygen and presumably cells located in organoid core became more hypoxic, as observed in tumours *in vivo*. Reports have described the increase of sterols synthesis depending on HIF1 activity (Shen & Li 2017b; Mylonis et al. 2019). For example, *HMGCR* has been identified as HIF1α target gene and hypoxic conditions showed a 2-fold increase in *HMGCR* mRNA relative to the corresponding results in normoxic murine macrophages (Parathath et al. 2011) and 1.3-fold in HepG2 cells (Pallottini et al. 2008). Moreover, it has been reported that cancer cells often gain the ability to synthesize lipids and show enhanced lipid uptake upon nutrient deprivation (Lisec et al. 2019; Munir et al. 2019; Parrales & Iwakuma 2016). Therefore, the overexpression of genes involved in lipid uptake and cholesterol biosynthesis in Fraction > 85 when compared to Fraction < 40 could indicate the presence of a nutrient-poor environment in the core of larger Iso50 CRC organoids. It would be necessary to study the effects of oxygen and nutrient deprivation, as separate parameters and in combination, on various aspects of lipid metabolism in different size Iso50 CRC organoids. For that, CRC organoids would need to be fed with different concentration of nutrients while ensuring an excess of oxygen or applying different oxygen concentration while

maintaining a high nutrient concentration. To study oxygen gradients in organoids, an electron paramagnetic resonance oximetry method could be implemented similarly to the methodology applied by Langan *et al*. 2016 to measure the oxygen gradients in spheroid culture systems (Langan et al. 2016). Moreover, lipid spatial distribution can be revealed with Oil-Red-O staining, which is a non-specific stain for any neutral lipid, and the Cholesterol/Cholesterol Ester-Glo assay kit from Promega could be used to measure the cholesterol by association with NADH production and proluciferin activation that produces light with a luciferase enzyme.

Third, tight junction signalling appeared as a differentially expressed process between small and large Iso50 CRC organoids. Recently, Tirier *et al*. showed that big CRC spheroids (70-100 μm) were characterised by the expression of genes involved in the formation of cell-cell junctions (Tirier et al. 2019). Expression pattern of genes related to tight junctions was compared between organoids present in Fraction < 40 and Fraction > 85. Tight junction proteins ZO-1, ZO-2 and ZO-3, encoded in humans by *TJP1*, *TJP2* and *TJP3* genes, respectively, belong to the family of zona occludens proteins and link tight junction transmembrane proteins, such as claudins or occludins, to the actin cytoskeleton (Itoh et al. 1999). Literature related to the expression of the ZO family proteins under hypoxic conditions is different depending on each protein. On the one hand, Brown *et al*. (2002) observed that ZO-1 expression levels were not significantly affected by hypoxic stress in brain microvessel endothelial cells (Brown 2002). On the other hand, Jenkins *et al*. (2016) showed the downregulation of ZO-2 in cyanotic patient's myocardium and cultured rat cardiomycytes when treated with hypoxic conditions (Jenkins et al. 2016). Furthermore, no literature has been found about ZO-3 expression under hypoxia. Here, *TJP1* expression was not significantly different between Iso50 CRC organoids in Fraction < 40 and organoids in Fraction > 85 (p-value = 0.9), *TJP2* expression was slightly upregulated (1.2-fold) in large organoids and *TJP3* expression showed a 1.4-fold increase in organoids of Fraction > 85 in comparison with organoids in Fraction < 40. Moreover, it has been described that *TJP3* was more highly expressed in differentiated organoids derived from biliary tract carcinomas than in poorly differentiated tumours (Lau et al. 2019). Also, *TJP3* expression was highly expressed in colon tops rather than in colon crypts, indicating that this gene is more expressed in mature intestinal epithelial cells (Kosinski et al. 2007). This could indicate that large Iso50 CRC organoids might experience hypoxic conditions and present a more differentiated phenotype than smaller organoids. Furthermore, the tight junction protein ZO-2 associates with the transcription factor AP-1 to control gene expression of processes related with differentiation, proliferation and

apoptosis (Betanzos et al. 2004; Matter & Balda 2007). The structure of AP-1 is a heterodimer composed of proteins c-Jun, encoded by the *JUN* gene, and c-Fos, encoded by the *FOS* gene. It has been reported that hypoxia stimulates expression of *JUN* and AP-1 activity in a HIF1α dependent manner in a variety of cell lines including mouse embryonic fibroblasts (Laderoute et al. 2002), F9 murine teratocarcinoma cells (Alfranca et al. 2002), rat pheochromocytoma 12 (PC12) cells (Mishra et al. 1998) and HT29 colon cancer cells (Yao et al. 1994). *FOS* was also induced by hypoxia (8 hours exposure) in HT29 colon cancer cells, but at a lower grade than *JUN* induction (5-fold vs. 30-fold) (Yao et al. 1994). In this work, large Iso50 CRC organoids showed a 1.4-fold and 1.8-fold upregulation of *JUN* and *FOS* over small organoids, respectively, which could indicate the presence of hypoxic cells in large organoids. Furthermore, non-muscle myosin heavy chains, encoded by *MYH9*, *MYH10* and *MYH14* genes, are involved in various physiological activities, such as cell migration, adhesion, and gene transcription. Lv *et al*. (2019) showed that under oxygen-glucose-deprivation, *MYH9* was activated in brain endothelial cells and exhibited a key role in tight junction expression (Lv 2019). *MYH9* and *MYH14* expression in large Iso50 CRC organoids was 1.2-fold and 1.4-fold higher than in smaller ones, respectively. Also, myosin light chain kinase (*MYLK*) regulates the integrity of tight junctions, and mRNA and protein levels of MYLK are significantly increased when HIF1α is overexpressed in rat monolayer epithelial cells (Meng et al. 2019) and human endothelial cells (Wang et al. 2013). Here, *MYLK* expression was increased 1.5-fold in large organoids compared to smaller organoids. Furthermore, the tight junction protein cingulin, encoded by *CGN* gene, is associated with differentiation of epithelial cells (Guillemot et al. 2013) and organoids in Fraction > 85 showed a 1.4-fold increase in *CGN* expression over organoids in Fraction < 40. In summary, tight junction proteins expression was affected by hypoxic conditions and results shown above suggested that Iso50 CRC large organoids experienced a more hypoxic environment than smaller organoids. Also, upregulation of certain genes (*TJP3* and *CGN*) could be an indicator of a more differentiated phenotype of larger Iso50 CRC organoids than in smaller ones.

Fourth, sirtuin signalling pathway has been identified by IPA as a differentially expressed biological process between large and small organoids. Sirtuin proteins possess either mono-ADP ribosyltransferase or deacylase activity, and they are implicated in glycolipid metabolism, lifespan regulation, stress response, inflammatory response and tumour formation (Satoh et al. 2013; Zhu et al. 2017). Moreover, some reports have linked sirtuins and HIF1 by demonstrating that sirtuins can regulate HIF1α activity (Laemmle et al. 2012; Lim et al. 2010). Lim *et al*.

(2010) concluded that SIRT1 binds to HIF1α and deacetylates it at Lys 674. By doing so, SIRT1 inactivates HIF1α by blocking p300 recruitment and consequently represses HIF1α target genes. Under hypoxia SIRT1 was downregulated due to decreased NAD^+ levels, which allowed the acetylation and activation of HIF1*a* in human kidney and colon cancer cells (Lim et al. 2010). Nevertheless, Laemmle *et al*. (2012) demonstrated that there was no change in SIRT1 protein or mRNA levels in hepatocellular carcinoma cells exposed to 1% O_2. Moreover, they showed that SIRT1 was not regulating HIF1α at the transcriptional level, but was required for the post-translational stabilisation and accumulation of HIF1α protein (Laemmle et al. 2012). In this work, *SIRT1* mRNA level was not significantly different between small and large Iso50 CRC organoids (p-value = 0.91) but expression of certain genes regulated by SIRT1 was increased. For example, the expression of *NDRG1* was increased more than 2-fold in larger organoids. Luo *et al*. (2014) showed the upregulation of this gene under hypoxia via HIF1α and Chen *et al*. (2006) concluded that its expression is enhanced by *SIRT1* (Luo et al. 2014; Cangul 2004; Chen et al. 2006). Also, *ACSS2* expression was induced 1.5-fold in organoids of Fraction > 85 compared to organoids in Fraction < 40. This gene is induced by hypoxia and acts in conjunction with SIRT1 and CBP to regulate the expression of HIF2α target genes under hypoxia. Acetylation and deacetylation of HIF2α are required for its efficient signalling during hypoxia in Hep3B cells. HIF2α acetylation is mediated by CBP, whereas SIRT1 deacetylases HIF2α that facilitates reengagement of HIF2α by CBP (Xu et al. 2014; R. Chen et al. 2015; Chen et al. 2017). Moreover, it has been described that HMGCS2 (3-hydroxy-3-methylglutaryl CoA synthase 2), involved in regulation of ketone bodies production, is deacetylated by SIRT3 in response to fasting in order to enhance its enzymatic activity. Ketogenesis is activated during fasting, which upregulates *HMGCS2* gene expression by accumulation of glucagon and cyclic-AMP (Shimazu et al. 2010; Hegardt 1999). Cells in the core of large Iso50 CRC organoids might experience fasting conditions due to possible diffusional limitation of glucose to the centre of the organoid and this could explain the upregulation of *HMGCS2* expression in large organoids by 1.5-fold. Taken together, sirtuins play an important role in response to stress conditions, such as hypoxia or fasting, by increasing stability of proteins like HIF1α, HIF2α and HMGCS2, which are involved in hypoxia-inducible signalling pathway, and ketogenesis to provide lipid-derived energy during times of carbohydrate deprivation.

In summary, results obtained from gene enrichment analysis using the Gene Ontology's browser AmiGO and the IPA software, showed that the top 200 most differentially expressed genes between Fraction < 40 and Fraction > 85 of organoids harvested after 8 days of culture, were enriched in GO terms related with glycolysis, lipid metabolism, tight junction signalling and sirtuin signalling pathway. Moreover, genes involved in the aforementioned processes, which were significantly upregulated in Fraction > 85, have been previously linked to nutrient deprivation and hypoxic conditions (see references above). This suggested that organoids present in Fraction > 85 might experience limitations of oxygen and nutrient supply to the cells located at the organoid core.

When comparing the results obtained in the Time course experiment and in the Size-based fractionation (Day 8) experiment, the similarities found between both analyses were of the most interest. Association of biological processes, such as glycolysis and lipid uptake and biosynthesis, with large organoids seemed to be hypoxia-linked and nutrient deprivation-linked in both, Time course experiment and Size-based fractionation (Day 8) experiment. This suggested that their biology differences were intrinsically due to size, rather than culture time. It is worth mentioning, that fold change values obtained in Size-based fractionation (Day 8) experiment were notably lower than in the Time course experiment. This could be explained due to the fact that samples of fractionated organoids were obtained from the same initial mixture of organoids, i.e. shared origin, which could reduce the gene expression variability. However, samples for Time-course experiment were generated from three independent cultures harvested at different times, which might present higher variability in gene expression levels.

5.2.3.2.3 Gene expression profile of > 200 μm Iso50 CRC organoids

Daster *et al*. (2017) detected hypoxic areas in CRC spheroids larger than 200 μm, but not in smaller ones (Daster et al. 2017). However, as described above, hypoxia related genes were already upregulated in Iso50 CRC organoids larger than 85 μm. In order to study whether a more pronounced change in gene expression profile occurred in considerably larger organoids, Iso50 CRC organoids with a diameter larger than 200 μm were generated. As demonstrated in Figure 5.1C, Iso50 CRC organoids cultured for 8 days from single cells did not reach this size so organoids larger than 200 μm detected under the microscope were hand-picked from cultures that had been grown from triturated samples for 5 days. The option of filtering with a membrane of 200 μm pore size was discarded because, based on previous experience, Iso50

CRC organoids with diameters larger than 100 μm were very fragile and easily broken during filtration process. Gene expression profile of organoids larger than 200 μm was compared with the gene expression profile of Fraction < 40 of organoids cultured from single cells during 5 days. Figure 5.11A shows representative images of both samples and it can be noted that the largest organoids suffered from oxygen and nutrients diffusional limitations, as evidenced by dark necrotic cells at the centre of the organoids. RNA of each sample was extracted from three biological replicates and sequenced with Illumina NextSeq 500 with a coverage of 30 million reads per sample. Before starting the bioinformatics analysis, the same pre-filtering step described for previous experiments was applied here to remove lowly expressed genes, which resulted with 16774 "expressed" genes from 41517 total genes. These "expressed" genes were selected for DESeq analysis in R, in which gene expression of organoids larger than 200 μm was compared against gene expression of organoids in Fraction < 40.

First, sample clustering was performed by two methods: PCA (Figure 5.11B) and hierarchical clustering with sample-to-sample Euclidean distance (Figure 5.11C). On the one side, PC1 and PC2 explained 81% and 9% of the variability of the data, respectively, and two groups of samples were identified corresponding to each condition (Figure 5.11B). On the other side, same groups were obtained for the hierarchical clustering analysis based on Euclidean distances (Figure 5.11C). Moreover, Euclidean distance between samples of organoids smaller than 40 μm and larger than 200 μm, was higher than any reported in previously described size-based fractionation experiments, which suggested that transcriptome of organoids larger than 200 μm was notably distinct from the Fraction < 40. Furthermore, MA-plot in Figure 5.11D showed that the number of differentially expressed genes between organoids smaller than 40 μm and organoids larger than 200 μm was high and the following section focuses on these differentially expressed genes.

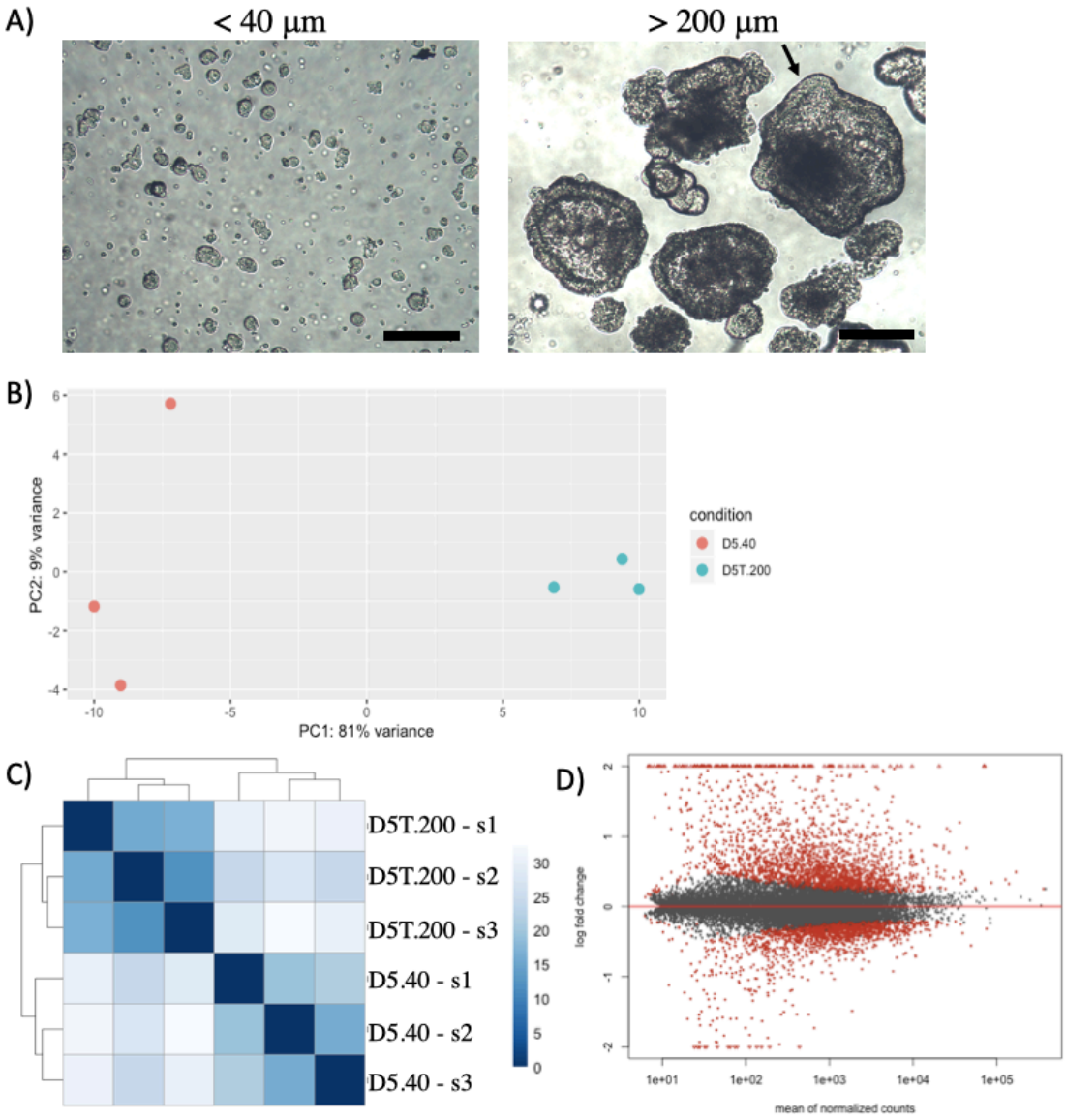

Figure 5.11 Larger than 200 µm Iso50 CRC organoids experiment. Sample clustering and MA-plots

Iso50 CRC organoids cultured for 5 days from single cells were fractionated with PS of 40 µm and RNA of Fraction < 40 was extracted. Also, organoids larger than 200 µm, detected under the microscope, were manually pipetted from a pull of Iso50 CRC organoids cultured for 5 days from trituration and RNA of these large organoids was extracted. RNA of both samples was sequenced (N=3). **A.** Representative images of Fraction < 40 after filtration of organoids (on the left) and organoids population after 5 days of culture from trituration (on the right). Black arrow indicates a representative organoid with a diameter larger than 200 µm, which was pipetted for RNA-seq experiment. Scale bars correspond to 100 µm. **B-D.** RNA-seq was performed using Illumina NextSeq 500 and only "expressed" genes were considered for analysis (16774 from 41517 total genes). **B.** Results were analysed by PCA plot along first two components. **C.** Heatmap of sample-to-sample Euclidean distances and hierarchical clustering based on the sample distances. **D.** MA-plot of organoids < 40 µm vs. organoids > 200 µm. Genes with adjusted p-value below 0.1 are shown in red.

Then, differentially expressed genes between organoids smaller than 40 μm and organoids larger than 200 μm were considered for the comparative analysis of gene expression profile. Differently expressed genes (1849 genes, p-value<0.01) were obtained from DESeq results of the comparison of organoids smaller than 40 μm and organoids larger than 200 μm. This number was lower than in Time course experiment (5014 genes), but higher than in Size-based fractionation experiment (94 for Day 5 and 894 for Day 8), which indicated that, the higher the organoid size range, the more variable the transcriptome was. Moreover, differences induced by the day of cultivation were more pronounced than differences detected in various size fractions harvested on the same day of culture. Differentially expressed genes were analysed by Morpheus, as previously described, for hierarchical clustering applying one minus Pearson correlation clustering method (Figure 5.12A) and it can be noted that samples clustered together based on their size. Moreover, two clear gene clusters were identified and they are specified in Figure 5.12A. On the one hand, top cluster contained 580 genes and they were upregulated in organoids smaller than 40 μm and downregulated in organoids larger than 200 μm. On the other hand, bottom cluster was formed by 1269 genes mainly upregulated in organoids larger than 200 μm and downregulated in organoids smaller than 40 μm. Genes of each cluster were analysed by AmiGO for GO term enrichment analysis and results were visualised with REVIGO to generate a treemap for top and bottom clusters. As shown in Figure 5.12B, genes forming the top cluster were mainly involved in biological processes related to RNA metabolism, cellular aromatic compound metabolism, biosynthesis of constituent RNA and proteins, and cell cycle. All these processes could explain the high transcriptional activity and differential proliferative potential of small organoids, as compared to larger ones. Instead, genes grouped in the bottom cluster were involved in monocarboxylic acid metabolism, lipid transport, detection of chemical stimulus involved in sensory perception, cholesterol homeostasis, response to nutrient level and response to decreased oxygen levels. These data underlie the divergent metabolism obtained for different size organoids.

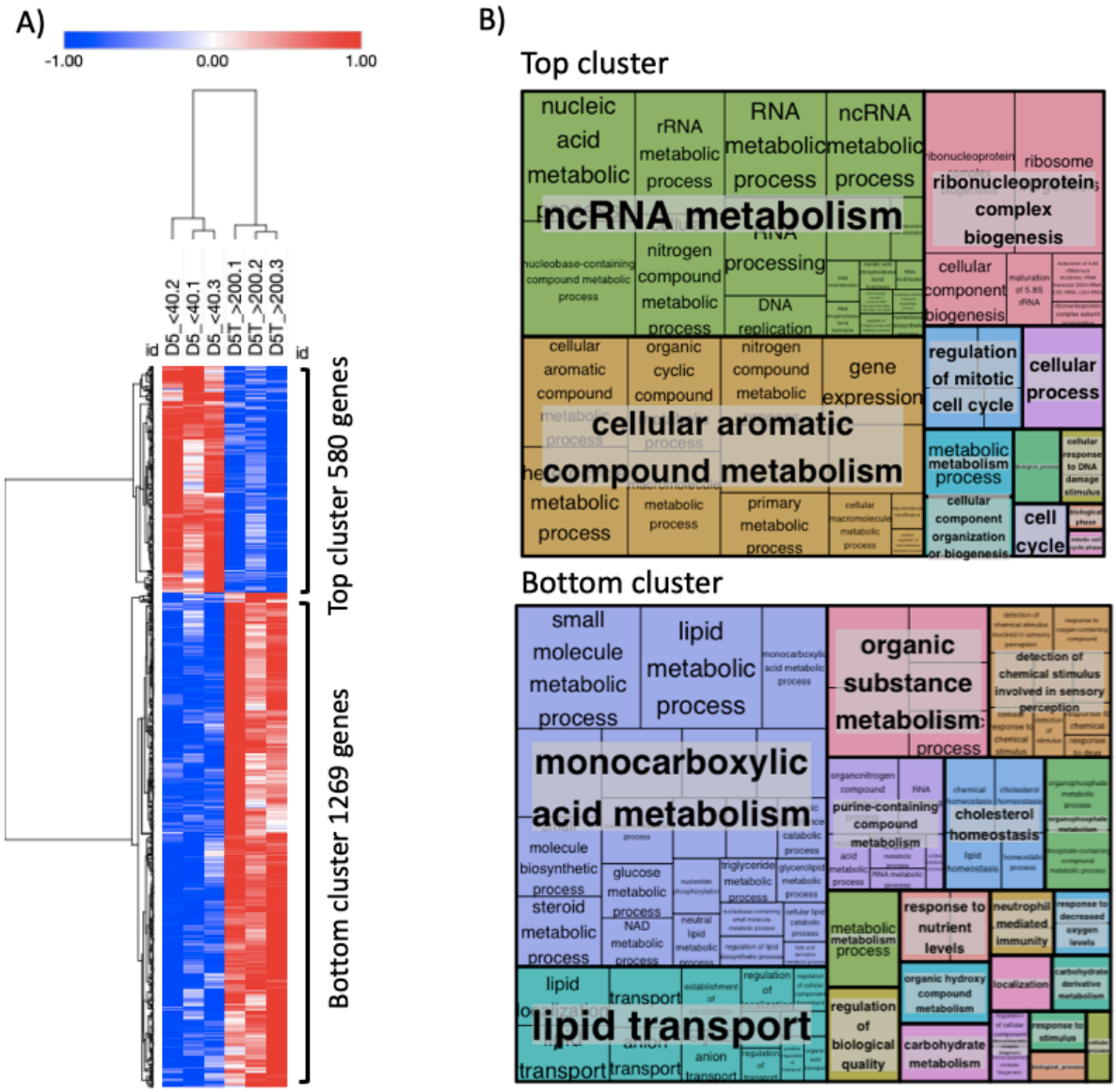

Figure 5.12 Larger than 200 µm Iso50 CRC organoids experiment. Clustering and functional analysis of genes

A. Heatmap of differentially expressed genes (1849 genes, p-value<0.01) and hierarchical clustering (one minus Pearson correlation) was performed on Morpheus. Two clusters of genes were differentiated: Top cluster contained 580 genes upregulated in Fraction < 40 of organoids cultured for 5 days from single cells and fractionated with PS of 40 µm, and Bottom cluster contained 1269 genes upregulated in organoids > 200 µm cultured for 5 days from trituration and manually pipetted those structures larger than 200 µm. **B.** Genes of each cluster were assessed for pathway enrichment analysis in AmiGO and treemaps were generated with REVIGO to visualise the most represented pathways in the GO term list. Each rectangle is a single cluster representative. The representatives are joined into superclusters of loosely related terms, visualised with different colours. The size of each rectangle is proportional to the frequency of the GO term in the database.

First, the monocarboxylic acid metabolism includes those pathways in which monocarboxylic acids, such as lactate and pyruvate, are involved. Thus, anaerobic glycolysis with conversion of glucose into lactate via pyruvate as intermediate could be a differentially expressed pathway between organoids smaller than 40 µm and organoids larger than 200 µm. Expression of specific genes involved in glycolysis was compared between small and large organoids. GLUT1 involved in glucose uptake, was upregulated by 2.8-fold in organoids larger than 200 µm compared to organoids smaller than 40 µm. Moreover, most of the glycolytic enzymes were upregulated in larger organoids compared to smaller ones, i.e. *HK1* (1.3-fold), *HK2* (1.5-fold), *GPI* (1.5-fold), *PFKP* (2.4-fold), *PFKL* (1.5-fold), *ALDOA* (2.1-fold), *ALDOC* (9.0-fold), *TPI1* (1.4-fold), *PGK1* (2.2-fold), *PGAM1* (1.4-fold), *ENO1*(1.4-fold) and *ENO2* (8.7-fold), as well as, genes involved in lactate synthesis (*LDHA*, 2.3-fold) and lactic acid transport across the plasma membrane (*SLC16A3*, 14.5-fold). These results indicated the higher reliance on glycolysis of organoids larger than 200 µm compared to smaller ones, and also the importance of lactate production to regenerate NAD^+ from NADH, required in glycolysis, and its subsequent translocation to the extracellular space. Stimulation of glycolysis, and lactate synthesis as well as its release under hypoxia has been described in numerous publications (Lyssiotis & Kimmelman 2017; Mylonis et al. 2019; Kucharzewska et al. 2015; Chi et al. 2006; Fang & Fang 2016; He 2019b; Kawai et al. 2016; Fedorova et al. 2019; Wang et al. 2018). Thus, the induction of the glycolytic metabolism in Iso50 CRC organoids larger than 200 µm could be explained due to the limitation of oxygen diffusion in such large structures. This fact was also observed under the microscope, where the largest organoids developed a necrotic core due to the lack of oxygen and nutrients (Figure 5.11A).

Second, differential expression of genes involved in cholesterol synthesis and homeostasis was studied for Iso50 CRC organoids smaller than 40 µm and larger than 200 µm. Mainly, all genes involved in cholesterol biosynthesis were upregulated in larger organoids, i.e. *HMGCS1*(1.9-fold), *HMGCS2* (5.1-fold), *HMGCR* (1.5-fold), *MSMO1* (1.8-fold), *MVD* (1.7-fold), *IDI1* (1.6-fold), *FDPS* (1.6-fold), *FDFT1* (1.5-fold), *SQLE* (1.4-fold) and *LSS* (1.7-fold). Increase of cholesterol synthesis under hypoxia has previously been reported (Ramakrishnan et al. 2014; Shen & Li 2017b). For instance, Dai *et al*. (2016) demonstrated that the mRNA level of *HMGCR* was upregulated in hypoxic HepG2 cells (Dai et al. 2016). Besides biosynthesis, cholesterol uptake and efflux have a key role in maintaining cholesterol homeostasis. Cholesterol uptake is regulated by *LRP1* and *LDLR*, which mediate the endocytosis of low-density lipoproteins, and large organoids displayed an increase of their expression by 3.9-fold

and 1.5-fold, respectively, when compared to smaller organoids. These results were in agreement with published data, where *LRP1* mRNA and *LDLR* mRNA expression was increased in cardiomyocytes under hypoxia (Cal et al. 2012b). Furthermore, *INSIG1* and *INSIG2* expression displayed a 2.2-fold and 1.6-fold increase in larger organoids, respectively, and it has been described that these genes have a crucial role in cholesterol homeostasis, since they negatively regulate HMGCR transcription by supressing activation of the endoplasmic reticulum membrane bound transcription factor SREBP (Dong et al. 2012). Furthermore, *ABCA1* is involved in cholesterol efflux, and its expression was 3.9-fold increased in organoids larger than 200 μm compared to organoids smaller than 40 μm. *ABCA1* upregulation has previously been described for vascular endothelial cells (Manalo et al. 2005) and for human macrophages (Ugocsai et al. 2010) under hypoxia. In summary, cholesterol metabolism was highly activated in Iso50 CRC organoids larger than 200 μm which suggested that hypoxia-signalling pathways activated an adaptive response important in cholesterol homeostasis.

Third, fatty acid transport appeared as a differentially expressed pathway between small and large Iso50 CRC organoids. Expression of genes involved in that process are studied below. Upregulation of fatty acid transport-related genes, such as, *FABP1* (5.8-fold), *FABP2* (3.6-fold) and *SLC27A2* (1.3-fold), was observed in large organoids compared to smaller ones. This observation has previously been described for MC38 CRC cell line (Iwamoto et al. 2018) and human trophoblast (Biron-Shental et al. 2007) exposed to hypoxia. Apart from alterations of fatty acid transport, it is worth noting that fatty acid catabolism is impaired during hypoxia, since oxidation takes place in mitochondria and requires oxygen, and accumulation of free fatty acids could cause lipotoxicity (Mylonis et al. 2019). To avoid this, cells can convert fatty acids to neutral triacylglycerols, that are stored in lipid droplets and can serve as the main form of energy depots. *AGPAT2* and *LPIN1*, have been shown to mediate hypoxia-induced lipid droplets accumulation, since both genes are direct targets of HIF1α. Formation of lipid droplets under hypoxia is further favoured by the hypoxic induction of essential constituents of lipid droplet membranes, such as expression of *PLIN2* stimulated by HIF2, and induction of *HILPDA* by HIF1 (Mylonis et al. 2019; Bildirici et al. 2018). All these genes involved in lipid droplets formation were upregulated in larger Iso50 CRC organoids when compared to smaller ones, i.e. *AGPAT2* (1.5-fold), *LPIN1* (1.8-fold), *PLIN2* (1.7-fold) and *HILPDA* (2.0-fold). These results were in agreement with published data that describe the involvement of HIFs in the regulation of lipid metabolism.

In summary, Iso50 CRC organoids larger than 200 μm showed more drastic metabolic responses associated to hypoxic conditions than those larger than 85 μm investigated before. These results suggested the importance of considering organoid size in drug sensitivity screens using Iso50 CRC organoids. Moreover, the study performed in this chapter should be expanded to other CRC organoid lines and other tumour organoid models in order to confirm the relation between organoid size and the lack of oxygen and nutrients availability.

5.2.3.3 RNA-seq data validation

A subset of RNA-seq results were validated by qRT-PCR. For that, fold change of certain genes was compared between both methodologies. The gene panel selected for the analysis contained: stem cell markers (*LGR5*, *SOX9*, *OLFM4*, *CD44* and *OCT4*), differentiation markers (*LYZ*, *KRT20*), hypoxia markers (*HIF1A* and *GLUT1*), proliferation markers (*KI67*, *PCNA* and *MCM2*) and polarity markers (*ITGA6* and *CLDN1*). Moreover, Actin and *GAPDH* were used as housekeeping genes. Figure 5.13A shows the qRT-PCR results for Iso50 CRC organoids cultured for 3, 5 and 8 days with biological triplicates (same samples as in Time-course RNA-seq experiment, i.e. D3, D5 and D8). Importantly, gene expression of Actin and *GAPDH* was not significantly different between the three days of culture studied. Moreover, stem cell genes and proliferation genes decreased their expression along the culture time, instead, differentiation markers seemed to be slightly upregulated over time although their expression was not significantly different between the three days of culture studied. These results are in accordance with previously described data in this work, where small organoids showed a higher expression of proliferation genes than larger ones, which presented a more differentiated phenotype than organoids < 40 μm. Regarding hypoxia markers, it has been described that HIF1α protein is transiently upregulated in hypoxia, but the mRNA is frequently found to be repressed (Cavadas et al. 2015; Abraham et al. 2004; Wenger et al. 1997). Although this pattern was observed here, this gene was not an appropriate hypoxia marker to be analysed by qRT-PCR. On the other hand, *GLUT1* expression increased over time due to activation of glycolysis in larger organoids. Finally, polarity markers were downregulated along the cultivation time. Iso50 CRC organoids are multicellular structures and assuming that they are spheres, the expression of *ITGA6*, a gene that encodes α-6-integrin, was expected to be lower as the organoid size increased, because the larger the organoid, the lower the proportion of cells attached to Matrigel.

Gene expression fold change was calculated using qRT-PCR results obtained for samples harvested on Day 3 and Day 8 of culture, and results were compared with fold change estimated by RNA-seq for the same conditions (Day 8 vs. Day 3, Time-course experiment). As shown in Figure 5.13B, a linear correlation ($R^2 = 0.735$) was obtained between both techniques, which indicated that about 73.5% of the genes selected showed consistent results between RNA-seq and qRT-PCR data. In summary, RNA-seq results were validated by qRT-PCR, so that, differences in gene expression profiles analysed in RNA-seq experiments discussed in this thesis were confirmed.

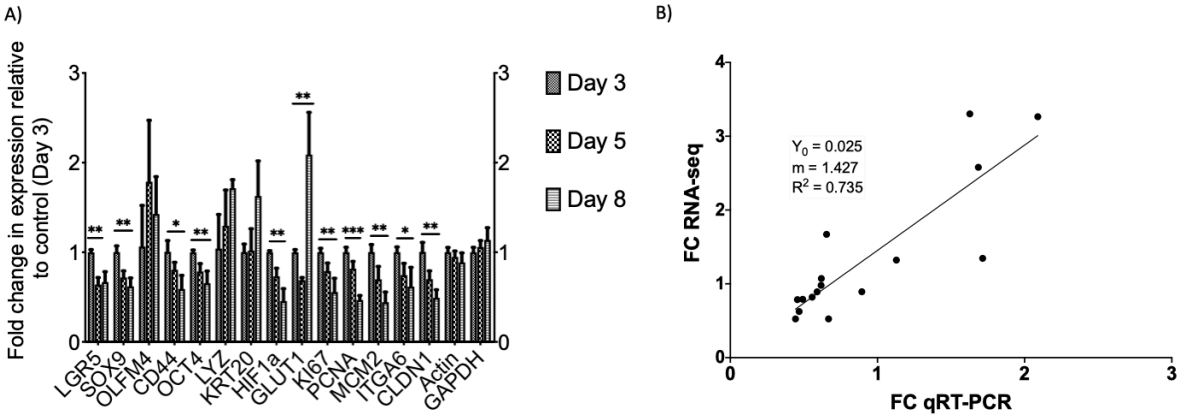

Figure 5.13 RNA-seq results validation with qRT-PCR

A. qRT-PCR results obtained for Iso50 CRC organoids cultured for 3, 5 and 8 days. Data presented as fold change vs. Day 3 sample control, means ± standard error of the mean, N=3 independent experiments. Statistical analysis was performed using one-way Anova test whereby * indicates $p \leq 0.05$, ** indicates $p \leq 0.01$, *** indicates $p \leq 0.001$. **B.** Comparison of fold change (FC), estimated by qRT-PCR, with FC estimated by RNA-seq of Day 8 and Day 3 samples. Data was fitted to a linear model function ($Y = Y_0 + mX$).

5.3 Summary

In this chapter, the impact of organoid size in its biology has been studied. From the experiments outlined in this chapter it has been concluded:

v) Iso50 CRC organoid diameter increased exponentially with the cultivation time allowing their volume doubling time of 3.2 days.

vi) Cultivation time was optimised to maximise the volume of Iso50 CRC organoids with a size range between 40 μm and 85 μm, resulting in a 5 days culture.

vii) The relationship between number of cells per organoid (Y) and organoid diameter (X) followed a power function ($Y = AX^B$, A = 0.0009316, B = 2.544, $R^2 = 0.9451$, CI(A) = 0.0004640 to 0.001815, CI(B) = 2.391 to 2.703). It was calculated that Iso50 CRC organoids with a diameter between 40-85 μm contained 11-76 cells per organoid.

viii) Gene expression profiles of Iso50 CRC organoids cultured for 3, 5 and 8 days showed significant differences. Small organoids, i.e. early-harvested, displayed higher cell proliferation activity than larger ones, i.e. late-harvested. Instead, larger organoids showed an upregulation of anaerobic glycolysis and lipid metabolism, when compared to smaller organoids.

ix) The transcriptome of size-fractionated organoids cultured for 5 days and filtrated with PluriStrainers did not show many significant differences, only 94 genes from 16532 "expressed" genes were differentially expressed between Fraction < 40, Fraction 40-85 and Fraction > 85.

x) Differences in gene expression profiles were more relevant when organoids were cultured for 8 days and fractionated with PluriStrainers. Metabolism of organoids smaller than 40 μm was directed to RNA processing and transcriptional activity. However, organoids larger than 85 μm showed an activation of glycolysis and cholesterol biosynthesis together with processes associated with differentiation of epithelial cells, such as tight junction formation.

xi) Activation of these biological processes (i.e. glycolysis, cholesterol biosynthesis and fatty acid transport) were confirmed culturing Iso50 CRC organoids larger than 200 μm, which showed a higher fold-change when compared to Fraction < 40.

xii) Glycolysis, cholesterol biosynthesis, fatty acid transport, among others were upregulated in organoids larger than 85 μm, which could be responses to hypoxic and nutrient deprivation conditions probably suffered in the core of large organoids due to limitation of oxygen and nutrient diffusion in such large structures.

This chapter shows that organoid biology is clearly affected by their size, as previously demonstrated for spheroids (Daster et al. 2017; Tirier et al. 2019), and reinforces the importance of considering and controlling organoid size in their applications. Drug testing is one of their major applications and organoid response to certain compounds could be affected by this parameter. Thus, it is necessary to take into account organoid size during the planning

phase of drug testing. For instance, the efficiency of drugs (e.g. doxorubicin, 5-FU, cisplatin and irinotecan) that need oxygen to induce an effective anticancer effect through the formation of ROS, might be hindered in large organoids. On the other side, hypoxia-activated prodrugs would need to be tested in larger organoids, since they present a hypoxic core where the electron reduction required to form the active toxic drug could occur. In conclusion, organoid size needs to be accordingly selected in drug testing depending on the mechanism of action of the drug. Although this work has been performed with the Iso50 CRC organoid line, other CRC organoid lines and other tumour organoid models should be included in further studies to confirm the observed trends related to the upregulation of glycolytic and lipid metabolism with the increase of organoid size.

6. Conclusions and future perspectives

6.1 Conclusions

Since organoids mimic the original tissue architecture of the corresponding organ and recapitulate some functions of that organ, they represent an excellent model for drug discovery and regenerative medicine. Therefore, organoids have the potential to become an alternative to 2D cultures for drug discovery, but there is a bottleneck to their widespread utilisation. Currently, organoids are produced in small amounts through a manual process, which results in organoids of varied size, thus possibly affecting drug response reproducibility. However, organoids need to be produced at a large scale to supply end users, and importantly, batch-to-batch variability should be reduced. So far, Cellesce Ltd has developed a new bioprocessing technology for the scale up of organoid production. Nevertheless, a size-based fractionation step after the organoid expansion process was missing. In this work, a size-based organoid separation approach was proposed in order to reduce batch-to-batch variability of large scale organoid production, and to increase drug assays reproducibility. To address this, the main aims of this project were to design a fluidised bed for organoid size-based fractionation, and to study the size-based phenotypic heterogeneity using the biophysically-purified organoid subpopulations. To achieve these aims, the study had the following objectives addressed throughout the chapters of this thesis. Firstly, Chapter 3 sought (i) to perform a hydrodynamic characterisation of a fluidised bed containing organoids, (ii) to optimise the fluidised bed design and operating conditions for the size-based organoid separation and (iii) to validate the design of the fluidised bed for size-based separation. Then, Chapter 4 attempted (i) to assess the organoid size-based separation performance using the designed fluidised bed, (ii) to compare the fluidisation results with a membrane organoid filtration and (iii) to determine whether drug response variability was reduced when drug treatment was performed with organoids having a more uniform size. Finally, Chapter 5 focused on the phenotypic heterogeneity of organoids of different size, (i) to evaluate physiological characteristics of different size organoids (e.g. organoid size alongside culture time and the number of cells per organoid) and (ii) to assess whether the organoid gene expression profile was altered accordingly to their size.

The hydrodynamics characterisation of a fluidised bed containing Iso50 CRC organoids enabled the determination of the fluidisation velocity range required for the size-based

separation of organoids. The results obtained for Iso50 CRC organoids cultured for 5 days were: u_{mf} = 7.90 x 10^{-5} m/s and u_0 = 1.67 x 10^{-4} m/s. Furthermore, organoid aggregation in the system (inside the FB column and in the pump tubing) was found as the major challenge to overcome. For that, the fluidised bed design was assessed based on the fundamentals of physics, chemistry and biology, with particular consideration for organoid aggregation and flow distribution inside the column. The study concluded with a FB design and set up conditions that were validated with polystyrene beads with similar physical properties to Iso50 CRC organoids. The acceptable purity (96% for 20 μm beads in Top fraction and 66% for 60 μm beads in Column fraction) and recovery (94% of the 20 μm loaded beads and 86% of the 60 μm loaded beads) results obtained with polystyrene beads, confirmed that the fluidised bed was able to separate different size particles (within the size and density range of Iso50 CRC organoids grown for 5 days).

By contrast, the fractionation of Iso50 CRC organoids with the designed fluidised bed resulted in poor purity fractions, low separation efficiencies and recoveries above 100%, based on MS3 Coulter Counter results. These results did not agree with the microscope pictures of the different size fractions obtained after fluidisation, which showed clear size differences between fractions. Particle overcounting with the MS3 Coulter Counter and organoid aggregation/breakage during the fluidisation and/or during the counting/sizing process with MS3 Coulter Counter were suggested as possible causes of the discrepancies between microscope images and MS3 Coulter Counter sizing data.

The separation performance of the fluidised bed for Iso50 CRC organoids was compared with membrane organoid filtration, the latter of which exhibited better performance. PluriStrainers were able to remove more single cells and generate homogeneously sized organoid populations. This work suggests that organoid size-based fractionation may improve drug (LGK974, 5-FU and Trametinib) response reproducibility as shown by a lower coefficient of variation in IC_{50} results when compared to non-fractionated organoids. Importantly, IC_{50} values obtained with fractionated organoids were statistically equivalent to IC_{50} values of non-fractionated organoids, which indicated that size-based fractionation did not affect the drug response in terms of IC_{50} values but improved the reproducibility of the results.

Finally, the results of the RNA-seq experiment revealed that the gene expression profile of Iso50 CRC organoids was altered accordingly to organoid size. More specifically, small Iso50 CRC organoids (< 40 μm) displayed higher transcriptional activity, typical of proliferating cells, whilst large Iso50 CRC organoids (> 85 μm) showed an activation of glycolysis,

cholesterol biosynthesis and fatty acid transport transcriptional programmes. Upregulation of these processes have been associated with hypoxic and nutrient deprivation conditions, which suggests that oxygen and nutrients diffusion in the core of large organoid may be limited. This is of special interest since organoids have the potential to revolutionise drug discovery and personalised medicine, but the results found in this thesis showed the importance of considering and controlling organoid size in assessment of their function. Limited drug penetration, lack of oxygen and acidosis (as a result of high glycolytic flux), have been previously linked with drug resistance in cancer cells, and this work points to the necessity to consider the organoid size during the planning phase of drug testing and select this parameter accordingly to the mechanism of action of the drug.

6.2 Future perspectives

Although data generated in this work supports the increase of drug response reproducibility when a size-based fractionation step is included after organoid expansion, the separation performance would need to be improved for organoid fluidisation considering design aspects, operating conditions and the implementation of process analytical tools for the better separation monitoring and performance assessment. Moreover, further drug assay and gene expression-related studies would be necessary to confirm some of the results observed in this thesis and therefore additional considerations are suggested below.

6.2.1 Column design

Apart from, distributor design, organoid loading strategy and other design parameters described in Chapter 3.2.2, additional considerations such as aspect ratio of the column, introduction of parallel inclined plates, height of the inlet side port, could also be studied for the improvement of the separation efficiency. Also, further research might study the addition of a bottom exit to continuously extract large organoids from the lower part of the column, thus ensuring the target size range inside the fluidised bed after the separation process. Furthermore, future studies including a computational fluid dynamics (CFD) approach should be employed to predict the influence of several parameters on the separation efficiency *in silico*. For that, organoid density needs to be experimentally determined to accurately model the fluidisation.

6.2.2 Operating conditions

Different operating conditions such as, higher fluidising flowrate or a longer fluidisation experiment to increase single cell removal, should be tested in future work following a design of experiments, thus also studying interactions between factors. Moreover, a two-stage process including a loading step and a fluidisation step should be explored to reduce the undesired effect of the lateral loading on the upwards flow. Additionally, organoid aggregation has been identified as the major challenge during their fluidisation and, although it was reduced, but not completely removed, the precise mechanism of organoid aggregation in the fluidised bed would need to be elucidated to successfully separate organoids based on their size.

6.2.3 Process analytical tools

The limiting resolution of the microscope video camera used to record organoid movement inside the column has hindered the separation monitoring. Thus, further investigation and experimentation into a better non-intrusive measurement technique (e.g. a charge coupled device camera) is strongly recommended.
Moreover, organoid counting and sizing with MS3 Coulter Counter has been identified as a limitation on the assessment of separation metrics and thus alternative measurement techniques need to be tested in order to accurately count and size organoids in a high-throughput and label-free fashion. For instance, using OrgaQuant, a publicly available trained neural network analysis platform that can automatically measure organoid number and diameter in 3D cultures from brightfield images.

6.2.4 Drug testing

Regarding drug testing with fractionated organoids, further experiments using a broader range of compounds, could shed more light on how relevant is organoid uniformity for the reduction of drug response variability and which is the relation between organoid size and drug resistance. Also, this work has been focused on Iso50 CRC line and more organoid lines need to be included in future studies to confirm that conclusions achieved with Iso50 organoids are applicable also for other organoid lines. Furthermore, drug response reproducibility has been assessed from IC_{50} values calculated with a metabolic assay in this thesis, and further work

needs to be done to assess response reproducibility of size-fractionated organoids from a morphometric analysis. For instance, using the aforementioned platform OrgaQuant, or more sophisticated software offered by private companies e.g. OMiner from OcellO.

Moreover, stem cell content might differ with organoid size, since it would be expected a higher ratio of stem cells in smaller organoids and thus, the response of drugs targeting cancer stem cells could differ in smaller and larger organoids. Therefore, it would be interesting to determine the population of stem cells of different size organoids by Lgr5 staining and investigate whether larger organoids experience an increase of cancer stem cell drug resistance. Furthermore, to mimic more closely the TME it would be interesting to include in future work drug sensitivity studies with the co-culture of size-fractionated organoids and cancer-associated fibroblast or immune infiltrates in order to assess the drug response reproducibility in both the epithelial and stromal compartments when a more homogeneous in size organoid population is used in the assays.

6.2.5 Gene expression profile

HIF1α has been identified by IPA as the main upstream regulator that can explain the observed gene expression differences between small and large organoids. However, it has been described that the mRNA level of HIF1α is unaffected under hypoxia and thus the RNA-seq experiment performed in this work could not show the upregulation of HIF1α protein. Further analysis of HIF1α at the protein level by immunohistochemistry is necessary to confirm the suggested lack of oxygen availability in large organoids. This could be complemented with the measurement of oxygen gradients in organoids with an electron paramagnetic resonance oximetry method, which is a non-invasive method to measure oxygen levels in biological systems using implanted and soluble paramagnetic probes (Langan et al. 2016). Moreover, considering that gene expression analysis was performed on RNA from whole Iso50 CRC organoids, biologically important processes could mask events occurring in defined areas. Therefore, other strategies, as for example single-cell RNA-seq and immunohistochemistry, should be included in future studies because they might reveal the existence of other relevant biological processes that are specific of an organoid zone. In addition, functional assays would be needed to confirm the upregulation of glycolytic and lipid metabolism in larger organoids. For that, further studies to determine the glucose consumption and lactate production levels in different size organoids using spectrophotometric enzyme assays would be required, as well as

the measurement of lipid spatial distribution by Oil-Red-O staining, and cholesterol content using the Cholesterol/Cholesterol Ester-Glo assay kit.

Finally, the target size range of organoid diameter considered in this thesis was 40-85 μm, based on OcellO recommendations, however gene expression profile of different size organoids should be compared with the profile of *in vivo* tumours, in order to determine the organoid size range that most closely mimics the gene expression profile of tumour cell *in vivo*.

7. References

Abraham, D. et al., 2004. Upregulated hypoxia-inducible factor-1 DNA binding activity to the vascular endothelial growth factor-A promoter mediates increased vascular permeability in donor lung grafts. *The Annals of Thoracic Surgery*, 77(5), pp.1751–1755.

Accioly, M.T. et al., 2008. Lipid bodies are reservoirs of cyclooxygenase-2 and sites of prostaglandin-E2 synthesis in colon cancer cells. *Cancer Research*, 68(6), pp.1732–1740.

Aga, M. et al., 2014. Differential Effects of Caveolin-1 and -2 Knockdown on Aqueous Outflow and Altered Extracellular Matrix Turnover in Caveolin-Silenced Trabecular Meshwork Cells. pp.1–13.

Ahonen, I. et al., 2017. A high-content image analysis approach for quantitative measurements of chemosensitivity in patient-derived tumor microtissues. *Scientific Reports*, pp.1–18.

Alfranca, A. et al., 2002. c-Jun and Hypoxia-Inducible Factor 1 Functionally Cooperate in Hypoxia-Induced Gene Transcription. *Molecular and Cellular Biology*, 22(1), pp.12–22.

Allen, E. et al., 2016. Metabolic Symbiosis Enables Adaptive Resistance to Anti-angiogenic Therapy that Is Dependent on mTOR Signaling. *CellReports*, 15(6), pp.1144–1160.

Alo, P.L. et al., 1999. Fatty acid synthase (FAS) predictive strenght in poorly differentiated early breast carcinomas. pp.1–6.

Antoni, D. et al., 2015. Three-Dimensional Cell Culture: A Breakthrough in Vivo. *International Journal of Molecular Sciences*, 16(12), pp.5517–5527.

Ao, Z. et al., 2020. One-Stop Microfluidic Assembly of Human Brain Organoids To Model Prenatal Cannabis Exposure. pp.1–9.

Arendt, L.M., Keller, P.J., et al., 2014. Anatomical localization of progenitor cells in human breast tissue reveals enrichment of uncommitted cells within immature lobules. *Breast Cancer Research*, 16(5), pp.229–16.

Arendt, L.M., St Laurent, J., et al., 2014. Human Breast Progenitor Cell Numbers Are Regulated by WNT and TBX3 Y. Li, ed. *PLOS ONE*, 9(10), pp.e111442–14.

Arora, N. et al., 2017. A process engineering approach to increase organoid yield. *Development*, 144(6), pp.1128–1136.

Ashley, N., 2013. Regulation of intestinal cancer stem cells. *Cancer Letters*, 338(1), pp.120–126.

Ashley, N. et al., 2014. Rapidly derived colorectal cancer cultures recapitulate parental cancer characteristics and enable personalized therapeutic assays. *The Journal of Pathology*, 234(1), pp.34–45.

Asif, M., 1991. Distributor effects in liquid fluidized beds of low-density particles. pp.1–8.

Asif, M., 1992. Hydrodynamics of liquid fluidized beds including the distributor region. pp.1–12.

Au, S.H. et al., 2017. Microfluidic Isolation of Circulating Tumor Cell Clusters by Size and Asymmetry. *Scientific Reports*, 7(1), pp.373–10.

Azamathulla, H.M. & Ahmad, Z., 2013. Estimation of Critical Velocity for Slurry Transport through Pipeline Using Adaptive Neuro-Fuzzy Interference System and Gene-Expression Programming. *Journal of Pipeline Systems Engineering and Practice*, 4(2), pp.131–137.

B, O., V, OcellO B.V. *ocello.nl*. Available at: https://ocello.nl/ [Accessed December 7, 2019].

Badder, L.M., 2017a. *Developing stem-cell containing organoids as a pre-clinical model for colorectal cancer therapeutics*.

Badder, L.M., 2017b. *Developing stem-cell containing organoids as a pre-clinical model for colorectal cancer therapeutics*.

Badder, L.M. et al., 2019. 3D imaging of colorectal cancer organoids identifies responses to Tankyrase inhibitors. *bioRxiv*, pp.1–42.

Bagheri, M. et al., 2019. Evaluation of antitumor effects of aspirin and LGK974 drugs on cellular signaling pathways, cell cycle and apoptosis in colorectal cancer cell lines compared to oxaliplatin drug. *Fundamental & Clinical Pharmacology*, 34(1), pp.51–64.

Bagley, J.A. et al., 2017. Fused cerebral organoids model interactions between brain regions. *Nature Methods*, 14(7), pp.743–751.

Bao, J. et al., 2016. Enhanced hepatic differentiation of rat bone marrow-derived mesenchymal stem cells in spheroidal aggregate culture on a decellularized liver scaffold. *International Journal of Molecular Medicine*, 38(2), pp.457–465.

Barker, N. et al., 2007. Identification of stem cells in small intestine and colon by marker gene Lgr5. *Nature*, 449(7165), pp.1003–1007.

Barker, N. et al., 2010. Lgr5+ve Stem Cells Drive Self-Renewal in the Stomach and Build Long-Lived Gastric Units In Vitro. *Stem Cell*, 6(1), pp.25–36.

Bauwens, C.L. et al., 2008. Control of Human Embryonic Stem Cell Colony and Aggregate Size Heterogeneity Influences Differentiation Trajectories. pp.1–11.

Bello, M.M., Raman, A.A.A. & Purushothaman, M., 2016. Applications of fluidized bed reactors in wastewater treatment - A review of the major design and operational parameters. pp.1–23.

Benita, Y. et al., 2009. An integrative genomics approach identifies Hypoxia Inducible Factor-1 (HIF-1)-target genes that form the core response to hypoxia. *Nucleic Acids Research*, 37(14), pp.4587–4602.

Benjamini, Y. & Hochberg, Y., 1995. Controlling the False Discovery Rate: A Practical and Powerful Approach to Multiple Testing. *Journal of the Royal Statistical Society: Series B (Methodological)*, 57(1), pp.289–300.

Bergmann, S. et al., 2018. Blood–brain-barrier organoids for investigating the permeability of CNS therapeutics. *Nature Protocols*, 13(12), pp.2827–2843.

Betanzos, A. et al., 2004. The tight junction protein ZO-2 associates with Jun, Fos and C/EBP transcription factors in epithelial cells. *Experimental Cell Research*, 292(1), pp.51–66.

Betge, J. et al., 2019. Multiparametric phenotyping of compound effects on patient derived organoids. 14, pp.849–39.

Bildirici, I. et al., 2018. PLIN2 Is Essential for Trophoblastic Lipid Droplet Accumulation and Cell Survival During Hypoxia. *Endocrinology*, 159(12), pp.3937–3949.

Biron-Shental, T. et al., 2007. Hypoxia regulates the expression of fatty acid binding proteins in primary term human trophoblasts

. pp.1–14.

Bizzarro, V., Petrella, A. & Parente, L., 2012. Annexin A1: Novel roles in skeletal muscle biology. *Journal of Cellular Physiology*, 227(8), pp.3007–3015.

Bodmer, W.F. et al., 1987. Localization of the gene for familial adenomatous polyposis on chromosome 5. pp.1–3.

Boj, S.F. et al., 2015. Organoid Models of Human and Mouse Ductal Pancreatic Cancer. *Cell*, 160(1-2), pp.324–338.

Boretto, M. et al., 2017. Development of organoids from mouse and human endometrium showing endometrial epithelium physiology and long-term expandability. *Development*, 144(10), pp.1775–1786.

Borten, M.A. et al., 2018. Automated brightfield morphometry of 3D organoid populations by OrganoSeg. *Scientific Reports*, pp.1–10.

Bousquet, P.A. et al., 2015. Hypoxia Strongly Affects Mitochondrial Ribosomal Proteins and Translocases, as Shown by Quantitative Proteomics of HeLa Cells. *International Journal of Proteomics*, 2015(23), pp.1–9.

Box, G.E.P., 1979. *Robustness in the Strategy of Scientific Model Building*, ACADEMIC PRESS, INC.

Boycott, A.E., 1920. Sedimentation of blood corpuscles. pp.1–1.

Brophy, C.M. et al., 2008. Rat hepatocyte spheroids formed by rocked technique maintain differentiated hepatocyte gene expression and function. *Hepatology*, 49(2), pp.578–586.

Brown, E. et al., 2003. Dynamic imaging of collagen and its modulation in tumors in vivo using second-harmonic generation. pp.1–5.

Brown, R.C., 2002. Protection against hypoxia-induced increase in blood-brain barrier permeability: role of tight junction proteins and NFkappaB. *Journal of Cell Science*, 116(4), pp.693–700.

Burdon, R.H., van Knippenberg, P.H. & Sharpe, P.T., 1988. Chapter 4: Unit gravity sedimentation. In *Methods of Cell Separation*. Laboratory Techniques in Biochemistry and Molecular Biology. Elsevier, pp. 70–90.

Busek, M. et al., 2016. Hypoxia-on-a-chip. *Current Directions in Biomedical Engineering*, 2(1), pp.71–75.

Cal, R., Castellano, J., Revuelta-López, E., Aledo, R., Barriga, M., Farré, J., Vilahur, G., Nasarre, L., Hove-Madsen, L., Badimon, L. & Llorente-Cortés, V., 2012a. Low-density lipoprotein receptor-related protein 1 mediates hypoxia-induced very low density lipoprotein-cholesteryl ester uptake and accumulation in cardiomyocytes. *Cardiovascular Research*, 94(3), pp.469–479.

Cal, R., Castellano, J., Revuelta-López, E., Aledo, R., Barriga, M., Farré, J., Vilahur, G., Nasarre, L., Hove-Madsen, L., Badimon, L. & Llorente-Cortés, V., 2012b. Low-density lipoprotein receptor-related protein 1 mediates hypoxia-induced very low density lipoprotein-cholesteryl ester uptake and accumulation in cardiomyocytes. *Cardiovascular Research*, 94(3), pp.469–479.

Campbell, Q.P., le Roux, M. & Smith, I.G.T., 2015. Water-only laboratory coal fractionation using the reflux classifier. *Minerals Engineering*, 83(C), pp.59–63.

Cangul, H., 2004. Hypoxia upregulates the expression of the NDRG1 gene leading to its overexpression in various human cancers. *BMC Genetics*, 5(1), pp.27–11.

Cavadas, M.A.S. et al., 2015. REST mediates resolution of HIF-dependent gene expression in prolonged hypoxia. *Scientific Reports*, pp.1–12.

Cernaro, V. et al., 2013. Relaxin: New Pathophysiological Aspects and Pharmacological Perspectives for an Old Protein. *Medicinal Research Reviews*, 34(1), pp.77–105.

Chen, B., Nelson, D.M. & Sadovsky, Y., 2006. N-Myc Down-regulated Gene 1 Modulates the Response of Term Human Trophoblasts to Hypoxic Injury. pp.1–10.

Chen, C. & Lou, T., 2017. Hypoxia inducible factors in hepatocellular carcinoma. pp.1–13.

Chen, R. et al., 2017. Coordinate regulation of stress signaling and epigenetic events by Acss2 and HIF-2 in cancer cells A. Imhof, ed. *PLOS ONE*, 12(12), pp.e0190241–31.

Chen, R. et al., 2015. The Acetate/ACSS2 Switch Regulates HIF-2 Stress Signaling in the Tumor Cell Microenvironment S. Rocha, ed. *PLOS ONE*, 10(2), pp.e0116515–24.

Chen, V.C. et al., 2015. Development of a scalable suspension culture for cardiac differentiation from human pluripotent stem cells. *Stem Cell Research*, 15(2), pp.365–375.

Chi, J.-T. et al., 2006. Gene Expression Programs in Response to Hypoxia: Cell Type Specificity and Prognostic Significance in Human Cancers E. T. Liu, ed. *PLoS Medicine*, 3(3), pp.e47–15.

Choi, I.-K. et al., 2013. Strategies to increase drug penetration in solid tumors. pp.1–18.

Clevers, H., 2016. Modeling Development and Disease with Organoids. pp.1–12.

Collins, A. et al., 2020. Patient-derived explants, xenografts and organoids: 3-dimensional patient-relevant pre-clinical models in endometrial cancer. *Gynecologic Oncology*, 156(1), pp.251–259.

Cook, D. et al., 2014. Lessons learned from the fate of AstraZeneca's drug pipeline: a five-dimensional framework. *Nature Publishing Group*, 13(6), pp.419–431.

Coulson, J.M. & Richardson, J.F., 1999. *Chemical Engineering Vol 1 Fluid flow, heat transfer and mass transfer*,

Coulson, J.M. & Richardson, J.F., 2002. *Chemical engineering. Particle technology and separation processes* 5 ed.,

Cruz-Gil, S. et al., 2018. A more physiological approach to lipid metabolism alterations in cancer: CRC-like organoids assessment. 35, pp.4–34.

Dagogo-Jack, I. & Shaw, A.T., 2017. Tumour heterogeneity and resistance to cancer therapies. *Nature Reviews Clinical Oncology*, 15(2), pp.81–94.

Dai, X. et al., 2019. Zoledronic acid enhances the efficacy of the MEK inhibitor trametinib in KRAS mutant cancers. *Cancer Letters*, 442, pp.202–212.

Dai, X.-Y. et al., 2016. Nuclear translocation and activation of YAP by hypoxia contributes to the chemoresistance of SN38 in hepatocellular carcinoma cells. *Oncotarget*, 7(6), pp.1–16.

Dainiak, M.B. et al., 2007. Methods in Cell Separations. In *Cell Separation: fundamentals, analytical and preparative methods*. Advances in Biochemical Engineering/Biotechnology. Berlin, Heidelberg: Springer Berlin Heidelberg, pp. 1–18.

Dalili, A., Samiei, E. & Hoorfar, M., 2019. A review of sorting, separation and isolation of cells and microbeads for biomedical applications: microfluidic approaches. *The Analyst*, 144(1), pp.87–113.

Daster, S., 2017. Induction of hypoxia and necrosis in multicellular tumor spheroids is associated with resistance to chemotherapy treatment. pp.1–12.

De Huang et al., 2014. HIF-1-Mediated Suppression of Acyl-CoA Dehydrogenases and Fatty Acid Oxidation Is Critical for Cancer Progression. *CellReports*, 8(6), pp.1930–1942.

de Lau, W. et al., 2014. The R-spondin/Lgr5/Rnf43 module: regulator of Wnt signal strength. *Genes & Development*, 28(4), pp.305–316.

Dee, K.U., Shuler, M.L. & Wood, H.A., 1997. Inducing Single-Cell Suspension of BTI-TN5B1-4 Insect Cells: I. The Use of Sulfated Polyanions to Prevent Cell Aggregation and Enhance Recombinant Protein Production. pp.1–15.

Dengler, V.L., Galbraith, M.D. & Espinosa, J.M., 2014. Transcriptional regulation by hypoxia inducible factors. *Critical Reviews in Biochemistry and Molecular Biology*, 49(1), pp.1–15.

Denko, N.C., 2008. Hypoxia, HIF1 and glucose metabolism in the solid tumours. pp.1–9.

do Nascimento, O.L., Reay, D.A. & Zivkovic, V., 2016. Influence of surface forces and wall effects on the minimum fluidization velocity of liquid-solid micro-fluidized beds. *Powder Technology*, 304, pp.55–62.

Dong, X.-Y., Tang, S.-Q. & Chen, J.-D., 2012. Dual functions of Insig proteins in cholesterol homeostasis. *Lipids in Health and Disease*, 11(1), pp.1–1.

Doroodchi, E. et al., 2006. Particle size classification in a fluidized bed containing parallel inclined plates. *Minerals Engineering*, 19(2), pp.162–171.

Doroodchi, E., Galvin, K.P. & Fletcher, D.F., 2005. The influence of inclined plates on expansion behaviour of solid suspensions in a liquid fluidised bed—a computational fluid dynamics study. *Powder Technology*, 156(1), pp.1–7.

Edmondson, R., Broglie, J.J., Adcock, A.F. & Yang, L., 2014a. Three-Dimensional Cell Culture Systems and Their Applications in Drug Discovery and Cell-Based Biosensors. *ASSAY and Drug Development Technologies*, 12(4), pp.207–218.

Edmondson, R., Broglie, J.J., Adcock, A.F. & Yang, L., 2014b. Three-Dimensional Cell Culture Systems and Their Applications in Drug Discovery and Cell-Based Biosensors. *ASSAY and Drug Development Technologies*, 12(4), pp.207–218.

Ellis, M.J., Chaudhuri, J. & Dale, T.C., 2018. Methods for culturing organoids Cellesce, ed., pp.1–25.

Erdmann, W.S. & Gos, T., 1990. Density of trunk tissues of young and medium age people. pp.1–3.

Fang, S. & Fang, X., 2016. Advances in glucose metabolism research in colorectal cancer. *Biomedical Reports*, 5(3), pp.289–295.

Fatehullah, A., Appleton, P.L. & Nathke, I.S., 2013. Cell and tissue polarity in the intestinal tract during tumourigenesis: cells still know the right way up, but tissue organization is lost. *Philosophical Transactions of the Royal Society B: Biological Sciences*, 368(1629), pp.20130014–20130014.

Fatehullah, A., Tan, S.H. & Barker, N., 2016. Organoids as an in vitro model of human development and disease. *Nature Publishing Group*, 18(3), pp.246–254.

Fearon, E.R. & Vogelstein, B., 1990. A Genetic Model for Colorectal Tumorigenesis. pp.1–9.

Fedorova, M.S. et al., 2019. The CIMP-high phenotype is associated with energy metabolism alterations in colon adenocarcinoma. *BMC Medical Genetics*, 20(S1), pp.330–13.

Figaro, S. et al., 2017. Optimizing the fluidized bed bioreactor as an external bioartificial liver. *The International Journal of Artificial Organs*, 40(4), pp.196–203.

Finicle, B.T., Jayashankar, V. & Edinger, A.L., 2018. Nutrient scavenging in cancer. *Nature Reviews Cancer*, pp.1–15.

Firdaus, M. et al., 2012. Beneficiation of Coarse Coal Ore in an Air-Fluidized Bed Dry Dense-Medium Separator. *International Journal of Coal Preparation and Utilization*, 32(6),

pp.276–289.

Flanagan, D. et al., 2018. Wnt Signalling in Gastrointestinal Epithelial Stem Cells. *Genes*, 9(4), pp.178–32.

Fonoudi, H. et al., 2015. A Universal and Robust Integrated Platform for the Scalable Production of Human Cardiomyocytes From Pluripotent Stem Cells. *STEM CELLS Translational Medicine*, 4(12), pp.1482–1494.

Foscolo, P.U., Gibilaro, L.G. & Waldram, S.P., 1983. A unified model for particulate expansion of fluidised beds and flow in fixed porous media. pp.1–10.

Freshney, R.I., 2010. *Culture of Aninmal Cells*,

Freyer, J.P., Wilder, M.E. & Jett, J.H., 1987. Viable Sorting of Intact Multicellular Spheroids by Flow Cytometry. pp.1–10.

Furuta, E. et al., 2008. Fatty Acid Synthase Gene Is Up-regulated by Hypoxia via Activation of Akt and Sterol Regulatory Element Binding Protein-1. *Cancer Research*, 68(4), pp.1003–1011.

Gabardo, S. et al., 2014. Dynamics of ethanol production from whey and whey permeate by immobilized strains of Kluyveromyces marxianus in batch and continuous bioreactors. *Renewable Energy*, 69(C), pp.89–96.

Gabardo, S. et al., 2015. Dynamics of yeast immobilized-cell fluidized-bed bioreactors systems in ethanol fermentation from lactose-hydrolyzed whey and whey permeate. *Bioprocess and Biosystems Engineering*, 39(1), pp.141–150.

Gabardo, S., Rech, R. & Ayub, M.A.Z., 2012. Performance of different immobilized-cell systems to efficiently produce ethanol from whey: fluidized batch, packed-bed and fluidized continuous bioreactors. *Journal of Chemical Technology & Biotechnology*, 87(8), pp.1194–1201.

Galvin, K.P. & Dickinson, J.E., 2013. Particle transport and separation in inclined channels subject to centrifugal forces. *Chemical Engineering Science*, 87(c), pp.294–305.

Galvin, K.P. et al., 2005. Performance of the reflux classifier for gravity separation at full scale. *Minerals Engineering*, 18(1), pp.19–24.

Galvin, K.P. et al., 2016. Single-stage recovery and concentration of mineral sands using a REFLUX™ Classifier. *Minerals Engineering*, 93, pp.32–40.

Galvin, K.P., Callen, A., et al., 2010. Gravity Separation of Coal in the Reflux Classifier – New Mechanisms for Suppressing the Effects of Particle Size. *International Journal of Coal Preparation and Utilization*, 30(2-5), pp.130–144.

Galvin, K.P., Zhou, J. & Walton, K., 2010. Application of closely spaced inclined channels in gravity separation of fine particles. *Minerals Engineering*, 23(4), pp.326–338.

Ganapathy-Kanniappan, S. & Geschwind, J.-F.H., 2013. Tumor glycolysis as a target for cancer therapy: progress and prospects. pp.1–11.

Gao, D. et al., 2014. Organoid Cultures Derived from Patients with Advanced Prostate Cancer. *Cell*, 159(1), pp.176–187.

Gao, R. et al., 2018. PFKFB4 Promotes Breast Cancer Metastasis via Induction of Hyaluronan Production in a p38-Dependent Manner. pp.1–16.

Gao, X. et al., 2016. Acetate functions as an epigenetic metabolite to promote lipid synthesis under hypoxia. *Nature Communications*, pp.1–14.

Gauthier, D., 1999. Infuence of the particle size distribution of powders on the velocities of minimum and complete ¯uidization. pp.1–16.

Geldart, D., 1972. The Effect of Particle Size and Size Distribution on the Behaviour of Gas-Fluidised Beds. pp.1–15.

Gerlee, P. & Anderson, A.R.A., 2009. Evolution of cell motility in an individual-based model of tumour growth. *Journal of Theoretical Biology*, 259(1), pp.67–83.

Gill, S., Thomas, R.R. & Goldberg, R.M., 2003. Colorectal cancer chemotherapy. *Alimentary Pharmacology and Therapeutics*, 18(7), pp.683–692.

Gillet, J.P., Varma, S. & Gottesman, M.M., 2013. The Clinical Relevance of Cancer Cell Lines. *JNCI Journal of the National Cancer Institute*, 105(7), pp.452–458.

Gonzalez-Menendez, P. et al., 2018. GLUT1 protects prostate cancer cells from glucose deprivation-induced oxidative stress. *Redox Biology*, 17, pp.112–127.

Gossett, D.R. et al., 2010. Label-free cell separation and sorting in microfluidic systems. *Analytical and Bioanalytical Chemistry*, 397(8), pp.3249–3267.

Goto-Silva, L. et al., 2019. Computational fluid dynamic analysis of physical forces playing a role in brain organoid cultures in two different multiplex platforms. pp.1–10.

Grimes, D.R., Fletcher, A.G. & Partridge, M., 2014. Oxygen consumption dynamics in steady-state tumour models. *Royal Society Open Science*, 1(1), pp.140080–13.

Guillaumond, F. et al., 2013. Strengthened glycolysis under hypoxia supports tumor symbiosis and hexosamine biosynthesis in pancreatic adenocarcinoma. pp.1–6.

Guillemot, L., Spadaro, D. & Citi, S., 2013. The Junctional Proteins Cingulin and Paracingulin Modulate the Expression of Tight Junction Protein Genes through GATA-4 M. Koval, ed. *PLOS ONE*, 8(2), pp.e55873–8.

Hakim, L.F. et al., 2005. Aggregation behavior of nanoparticles in fluidized beds. *Powder Technology*, 160(3), pp.149–160.

Halestrap, A.P., 2011. The monocarboxylate transporter family-Structure and functional characterization. *IUBMB Life*, 64(1), pp.1–9.

Hartman, M., Trnka, O. & Svoboda, K., 1994. Free Settling of Nonspherical Particles. *Industrial & Engineering Chemistry Research*, 33(8), pp.1979–1983.

He, J. et al., 2016. Density-based segregation/separation performances of dense medium gas-solid fluidized bed separator (DMFBS) for coal cleaning and upgrading. *Journal of the Taiwan Institute of Chemical Engineers*, 59(C), pp.252–261.

He, Y., Luo, Y., Zhang, D., Wang, X., Zhang, P., Li, H., Ejaz, S. & Liang, S., 2019a. PGK1-mediated cancer progression and drug resistance. pp.1–23.

He, Y., Luo, Y., Zhang, D., Wang, X., Zhang, P., Li, H., Ejaz, S. & Liang, S., 2019b. Review Article PGK1-mediated cancer progression and drug resistance. pp.1–23.

Hegardt, F.G., 1999. Mitochondrial 3-hydroxy-3-methylglutaryl-CoA synthase: a control enzyme in ketogenesis. pp.1–14.

Hinderliter, P.M. et al., 2010. ISDD: A computational model of particle sedimentation, diffusion and target cell dosimetry for in vitro toxicity studies. pp.1–20.

Hirenallur-Shanthappa, D.K., Ramírez, J.A. & Iritani, B.M., 2017. *Immunodeficient Mice: The Backbone of Patient-Derived Tumor Xenograft Models*, Elsevier Inc.

Hu, G. & Li, D., 2007. Three-dimensional modeling of transport of nutrients for multicellular tumor spheroid culture in a microchannel. *Biomedical Microdevices*, 9(3), pp.315–323.

Hu, J.L. et al., 2017. Opportunities for organoids as new models of aging. *Journal of Cell Biology*, 217(1), pp.39–50.

Hu, X. & Calo, J.M., 2006. Plastic particle separation via liquid-fluidized bed classification. *AIChE Journal*, 52(4), pp.1333–1342.

Huang, D., Li, C. & Zhang, H., 2014. Hypoxia and cancer cell metabolism. *Acta Biochimica et Biophysica Sinica*, 46(3), pp.214–219.

Hubert, C.G. et al., 2016. A Three-Dimensional Organoid Culture System Derived from Human Glioblastomas Recapitulates the Hypoxic Gradients and Cancer Stem Cell Heterogeneity of Tumors Found In Vivo. *Cancer Research*, 76(8), pp.2465–2477.

Huch, M., Bonfanti, P., et al., 2013. Unlimited in vitro expansion of adult bi-potent pancreas progenitors through the Lgr5/R-spondin axis. *The EMBO Journal*, pp.1–14.

Huch, M., Dorrell, C., et al., 2013. In vitro expansion of single Lgr5+ liver stem cells induced by Wnt-driven regeneration. *Nature*, 494(7436), pp.247–250.

Hwang, T.J. et al., 2016. Failure of Investigational Drugs in Late-Stage Clinical Development and Publication of Trial Results. *JAMA Internal Medicine*, 176(12), pp.1826–8.

IMAMURA, Y. et al., 2015. Comparison of 2D- and 3D-culture models as drug-testing platforms in breast cancer. *Oncology Reports*, 33(4), pp.1837–1843.

Itoh, M. et al., 1999. Direct Binding of Three Tight Junction-associated MAGUKs, ZO-1, ZO-2, and ZO-3, with the COOH Termini of Claudins. pp.1–13.

Iversen, P.W. et al., 2012. HTS Assay Validation. pp.1–31.

Iveson, S.M., Mason, M. & Galvin, K.P., 2014. Gravity Separation and Desliming of Fine Coal: Pilot-Plant Study Using Reflux Classifiers in Series. *International Journal of Coal Preparation and Utilization*, 34(5), pp.239–259.

Iwamoto, H. et al., 2018. Cancer Lipid Metabolism Confers Antiangiogenic Drug Resistance. *Cell Metabolism*, 28(1), pp.104–117.e5.

Jack W Scannell, J.B., 2016. When Quality Beats Quantity: Decision Theory, Drug Discovery, and the Reproducibility Crisis. *PLOS ONE*, pp.1–21.

Jain, R., 2014. *The evaluation of the hindered settling behavior of the ground calcium carbonate suspension*.

Jamieson, L.E., Harrison, D.J. & Campbell, C.J., 2019. Raman spectroscopy investigation of biochemical changes in tumor spheroids with aging and after treatment with staurosporine. *Journal of Biophotonics*, 12(5), pp.e201800201–11.

Jeffries, R.E. et al., 2013. Effect of Oxygen Concentration on Viability and Metabolism in a Fluidized-Bed Bioartificial Liver Using 31P and 13C NMR Spectroscopy. *Tissue Engineering Part C: Methods*, 19(2), pp.93–100.

Jenkins, E.L. et al., 2016. Chronic hypoxia down-regulates tight junction protein ZO-2 expression in children with cyanotic congenital heart defect. *ESC Heart Failure*, 3(2), pp.131–137.

Jiliang, M., Xiaoping, C. & Daoyin, L., 2013. Minimum fluidization velocity of particles with wide size distribution at high temperatures. *Powder Technology*, 235(C), pp.271–278.

Jiménez-Valerio, G. et al., 2016. Resistance to Antiangiogenic Therapies by Metabolic Symbiosis in Renal Cell Carcinoma PDX Models and Patients. *CellReports*, 15(6), pp.1134–1143.

Jin, M.-Z. et al., 2018. Organoids: An intermediate modeling platform in precision oncology. *Cancer Letters*, 414, pp.174–180.

Johnson, M. et al., 2016. Characterization of Multiple Hindered Settling Regimes in Aggregated Mineral Suspensions. *Industrial & Engineering Chemistry Research*, 55(37), pp.9983–9993.

Jung, D.J. et al., 2019. A one-stop microfluidic-based lung cancer organoid culture platform for testing drug sensitivity. *Lab on a Chip*, 19(17), pp.2854–2865.

Jung, J., Seol, H.S. & Chang, S., 2018. The Generation and Application of Patient-Derived Xenograft Model for Cancer Research. *Cancer Research and Treatment*, 50(1), pp.1–10.

Kaiser, P. et al., 2014. Cell Retention by Encapsulation for the Cultivation of Jurkat Cells in Fixed and Fluidized Bed Reactors. pp.1–9.

Kaiser, P. et al., 2018. Scale-up of the ex vivo expansion of encapsulated primary human T lymphocytes. *Biotechnology and Bioengineering*, 115(10), pp.2632–2642.

Kalaga, D.V. et al., 2014. Particle-liquid mass transfer in solid–liquid fluidized beds. *Chemical*

Engineering Journal, 245(C), pp.323–341.

Kamphorst, J.J. et al., 2014. Quantitative analysis of acetyl-CoA production in hypoxic cancer cells reveals substantial contribution from acetate. *Cancer & Metabolism*, 2(1), pp.54–8.

Kapałczyńska, M. et al., 2016. 2D and 3D cell cultures – a comparison of different types of cancer cell cultures. *Archives of Medical Science*, pp.1–10.

Karolak, A., Poonja, S. & Rejniak, K.A., 2019. Morphophenotypic classification of tumor organoids as an indicator of drug exposure and penetration potential S. M. Peirce, ed. *PLoS computational biology*, 15(7), pp.e1007214–21.

Karthaus, W.R. et al., 2014. Identification of Multipotent Luminal Progenitor Cells in Human Prostate Organoid Cultures. *Cell*, pp.1–13.

Kaushik, S., Pickup, M.W. & Weaver, V.M., 2016. From transformation to metastasis: deconstructing the extracellular matrix in breast cancer. *Cancer and Metastasis Reviews*, 35(4), pp.655–667.

Kavsan, V.M., Iershov, A.V. & Balynska, O.V., 2011. Immortalized cells and one oncogene in malignant transformation: old insights on new explanation. *BMC Cell Biology*, 12(1), p.23.

Kawai, K. et al., 2016. Fructose-bisphosphate aldolase A is a key regulator of hypoxic adaptation in colorectal cancer cells and involved in treatment resistance and poor prognosis. *International Journal of Oncology*, 50(2), pp.525–534.

Keller, P.J. et al., 2012. Defining the cellular precursors to human breast cancer. *Proceedings of the National Academy of Sciences*, 109(8), pp.2772–2777.

Kendall, K., Kendall, M. & Rehfeldt, F., 2011. *Adhesion of Cells, Viruses and Nanoparticles*,

Keysselt, K. et al., 2019. Different in vivo and in vitro transformation of intestinal stem cells in mismatch repair deficiency. pp.1–12.

Khan, A.R. & Richardson, J.F., 1989. Fluid-particle interactions and flow characteristics of fluidized beds and settling suspensions of spherical particles. *Chemical Engineering Communications*, 78(1), pp.111–130.

Khan, M.S. et al., 2017. Expansion behaviour of a binary solid-liquid fluidised bed with different solid mass ratio. *Advanced Powder Technology*, 28(12), pp.3111–3129.

Kiani, A., Zhou, J. & Galvin, K.P., 2015. Enhanced Recovery and Concentration of Positively Buoyant Cenospheres from Negatively Buoyant Fly Ash Particles using the Inverted Reflux Classifier. *Minerals Engineering*, 79(C), pp.1–9.

Kim, J.A., Hong, S. & Rhee, W.J., 2019. Microfluidic three-dimensional cell culture of stem cells for high-throughput analysis. *World J Stem Cells*, 11(10), pp.803–816.

Kondo, J. & Inoue, M., 2019. Application of Cancer Organoid Model for Drug Screening and Personalized Therapy. *Cells*, 8(5), pp.470–16.

Kopparthi, P. et al., 2019. Beneficiation of coal fines using the Reflux™ Classifier. *Minerals Engineering*, 136, pp.110–119.

Kosinski, C. et al., 2007. Gene expression patterns of human colon tops and basal crypts and BMP antagonists as intestinal stem cell niche factors. pp.1–6.

Kourkoumpetis, T. et al., 2018. Differential Expression of Tight Junctions and Cell Polarity Genes in Human Colon Cancer. *Exploratory Research and Hypothesis in Medicine*, 3(1), pp.14–19.

Kowalczuk, P.B. & Drzymala, J., 2016. Physical meaning of the Sauter mean diameter of spherical particulate matter. *Particulate Science and Technology*, 34(6), pp.645–647.

Kucharzewska, P., Christianson, H.C. & Belting, M., 2015. Global Profiling of Metabolic Adaptation to Hypoxic Stress in Human Glioblastoma Cells N. K. Karamanos, ed. *PLOS ONE*, 10(1), pp.e0116740–22.

Kuo, H.P., Hsiao, Y.C. & Shih, P.Y., 2006. A study of the axial segregation in a rotating drum using deformable particles. *Powder Technology*, 166(3), pp.161–166.

Laderoute, K.R. et al., 2002. The Response of c-Jun/AP-1 to Chronic Hypoxia Is Hypoxia-Inducible Factor 1 Dependent. *Molecular and Cellular Biology*, 22(8), pp.2515–2523.

Laemmle, A. et al., 2012. Inhibition of SIRT1 Impairs the Accumulation and Transcriptional Activity of HIF-1α Protein under Hypoxic Conditions M. V. Blagosklonny, ed. *PLOS ONE*, 7(3), pp.e33433–12.

Lancaster, M.A. et al., 2013. Cerebral organoids model human brain development and microcephaly. *Nature*, pp.1–18.

Langan, L.M. et al., 2016. Direct Measurements of Oxygen Gradients in Spheroid Culture System Using Electron Parametric Resonance Oximetry D. Hinderberger, ed. *PLOS ONE*, 11(2), pp.e0149492–13.

Langhans, S.A., 2018. Three-Dimensional in Vitro Cell Culture Models in Drug Discovery and Drug Repositioning. *Frontiers in Pharmacology*, 9, pp.1657–14.

Laskovski, D. et al., 2006. Segregation of hydraulically suspended particles in inclined channels. *Chemical Engineering Science*, 61(22), pp.7269–7278.

Lau, D.K. et al., 2019. Genomic Profiling of Biliary Tract Cancer Cell Lines Reveals Molecular Subtypes and Actionable Drug Targets. *ISCIENCE*, 21, pp.624–637.

Laurent, J. et al., 2013. Multicellular tumor spheroid models to explore cell cycle checkpoints in 3D. *BMC Cancer*, 13(1), pp.1–1.

Lazzari, G., Couvreur, P. & Mura, S., 2017. Multicellular tumor spheroids: a relevant 3D model for the in vitro preclinical investigation of polymer nanomedicines. *Polymer Chemistry*, 8(34), pp.4947–4969.

Leckband, D. & Israelachvili, J., 2001. Intermolecular forces in biology. *Quarterly Reviews of Biophysics*, 34(2), pp.105–267.

Lee, F. et al., 2018. *Constrained spheroids/ organoids in perfusion culture* 1st ed., Elsevier Inc.

Li, J. et al., 2014. Recovery and concentration of buoyant cenospheres using an Inverted Reflux Classifier. *Fuel Processing Technology*, 123(C), pp.127–139.

Li, Q. et al., 2018. Klotho negatively regulated aerobic glycolysis in colorectal cancer via ERK/HIF1α axis. pp.1–11.

Li, T., Chen, W. & Chiang, J.Y.L., 2007. PXR induces CYP27A1 and regulates cholesterol metabolism in the intestine. *Journal of Lipid Research*, 48(2), pp.373–384.

Li, Y. et al., 2018. Motion characteristics of binary solids in a liquid fluidised bed with inclined plates. *Particuology*, 39, pp.48–54.

Liberti, M.V. & Locasale, J.W., 2017. The Warburg Effect: How Does it Benefit Cancer Cells? *Trends in Biochemical Sciences*, 41(3), pp.211–218.

Lim, J.-H. et al., 2010. Sirtuin 1 Modulates Cellular Responses to Hypoxia by Deacetylating Hypoxia-Inducible Factor 1α. *Molecular Cell*, 38(6), pp.864–878.

Lim, W. et al., 2018. Formation of size-controllable tumour spheroids using a microfluidic pillar array (μFPA) device. *The Analyst*, 143(23), pp.5841–5848.

Linnekamp, J.F. et al., 2018. Consensus molecular subtypes of colorectal cancer are recapitulated in in vitro and in vivo models. *Cell Death & Differentiation*, pp.1–18.

Lisec, J. et al., 2019. Cancer cell lipid class homeostasis is altered under nutrient-deprivation but stable under hypoxia. pp.1–11.

Liu, J. et al., 2013. Targeting Wnt-driven cancer through the inhibition of Porcupine by LGK974. pp.1–6.

Liu, W. et al., 2012. Review Article Targeted genes and interacting proteins of hypoxia inducible factor-1. pp.1–14.

Love, M.I., Anders, S. & Huber, W., 2019. Analyzing RNA-seq data with DESeq2. pp.1–87.

Lu, J. et al., 2016. A New Fluidized Bed Bioreactor Based on Diversion-Type Microcapsule Suspension for Bioartificial Liver Systems E. Laconi, ed. *PLOS ONE*, 11(2), pp.e0147376–18.

Luby, C.J., Coughlin, B.P. & Mace, C.R., 2017. Enrichment and Recovery of Mammalian Cells from Contaminated Cultures Using Aqueous Two-Phase Systems. *Analytical Chemistry*, 90(3), pp.2103–2110.

Lucas, A. et al., 1986. Improved Equation for the Calculation of Minimum Fluidization Velocity. pp.1–4.

Luke, J.J., Ott, P.A. & Shapiro, G.I., 2014. The Biology and Clinical Development of MEK Inhibitors for Cancer. *Drugs*, 74(18), pp.2111–2128.

Luo, E.-C. et al., 2014. MicroRNA-769-3p Down-regulates NDRG1 and Enhances Apoptosis in MCF-7 Cells During Reoxygenation. *Scientific Reports*, 4(1), pp.328–8.

Lv, B. et al., 2015. Effect of the secondary air distribution layer on separation density in a dense-phase gasâ€“solid fluidized bed. *MINING SCIENCE AND TECHNOLOGY (CHINA)*, pp.1–5.

Lv, B. et al., 2018. Particle mixing and separation performance of gas-solid separation fluidized beds containing binary mixtures. *FUEL*, 226, pp.462–471.

Lv, G. et al., 2011. Bioartificial liver system based on choanoid fluidized bed bioreactor improve the survival time of fulminant hepatic failure pigs. *Biotechnology and Bioengineering*, 108(9), pp.2229–2236.

Lv, Y., 2019. Myosin IIA Regulated Tight Junction in Oxygen Glucose-Deprived Brain Endothelial Cells Via Activation of TLR4/PI3K/Akt/JNK1/2/14-3- 3ε/NF-ϰB/MMP9 Signal Transduction Pathway. *Cellular and Molecular Neurobiology*, 39(2), pp.301–319.

Lyssiotis, C.A. & Kimmelman, A.C., 2017. Metabolic Interactions in the Tumor Microenvironment. *Trends in Cell Biology*, 27(11), pp.863–875.

M Gholizadeh, H. et al., 2016. Bacillussp. DSM 2523 entrapped within chitosan beads used as the whole cell biocatalyst for the production of cyclodextrin glucanotransferase in a fluidized bed bioreactor. *Starch - Stärke*, 68(9-10), pp.989–998.

Ma, N. et al., 2004. Quantitative studies of cell-bubble interactions and cell damage at different Pluronic F-68 and cell concentrations. *Biotechnology Progress*, 20(4), pp.1183–1191.

Ma, Y. et al., 2017. The MAPK Pathway Regulates Intrinsic Resistance to BET Inhibitors in Colorectal Cancer. *Clinical Cancer Research*, 23(8), pp.2027–2037.

Maharaj, L., Pocock, J. & Loveday, B.K., 2007. The effect of distributor configuration on the hydrodynamics of the teetered bed separator. *Minerals Engineering*, 20(11), pp.1089–1098.

Manalo, D.J. et al., 2005. Transcriptional regulation of vascular endothelial cell responses to hypoxia by HIF-1. *Blood*, 105(2), pp.659–669.

Marshall, H., 2018. *Environmental Nanotechnology*, Scientific e-Resources.

Mathieu, J. et al., 2011. HIF Induces Human Embryonic Stem Cell Markers in Cancer Cells. *Cancer Research*, 71(13), pp.4640–4652.

Matter, K. & Balda, M.S., 2007. Epithelial tight junctions, gene expression and nucleo-junctional interplay. *Journal of Cell Science*, 120(9), pp.1505–1511.

Mazzucchelli, S. et al., 2019. Establishment and Morphological Characterization of Patient-Derived Organoids from Breast Cancer. pp.1–13.

McCabe, W.L., Smith, J.C. & Harriott, P., 1993. *Unit Operations of Chemical Engineering. Fifth Edition*,

Mcintosh, r.l. & anderson, v., 2010. a comprehensive tissue properties database provided for the thermal assessment of a human at rest. *Biophysical Reviews and Letters*, 05(03), pp.129–151.

Meijer, T.G. et al., 2017. Ex vivotumor culture systems for functional drug testing and therapy response prediction. *Future Science OA*, 3(2), pp.FSO190–13.

Meng, C. et al., 2019. Effects of hypoxia inducible factor-1α on expression levels of MLCK, p-MLC and ZO-1 of rat endothelial cells. *Biochemical and Biophysical Research Communications*, 519(3), pp.591–596.

Meng, D.D., Kim, J. & Kim, C.-J., 2006. A degassing plate with hydrophobic bubble capture and distributed venting for microfluidic devices. *Journal of Micromechanics and Microengineering*, 16(2), pp.419–424.

Meng, F.-Y. et al., 2010. An improved purification approach with high cell viability and low cell loss for cryopreserved hepatocytes. *Cryobiology*, 60(2), pp.238–239.

Merenda, A., Fenderico, N. & Maurice, M.M., 2020. Wnt Signaling in 3D: Recent Advances in the Applications of Intestinal Organoids. *Trends in Cell Biology*, 30(1), pp.60–73.

Michelini, E. et al., 2010. Cell-based assays: fuelling drug discovery. *Analytical and Bioanalytical Chemistry*, 398(1), pp.227–238.

Mishra, R.R. et al., 1998. Role of c-fos in hypoxia-induced AP-1 cis-element activity and tyrosine hydroxylase gene expression. pp.1–10.

Mohd-Sahib, A.-A. et al., 2017. Lipid for biodiesel production from attached growth Chlorella vulgaris biomass cultivating in fluidized bed bioreactor packed with polyurethane foam material. *Bioresource Technology*, 239, pp.127–136.

Moreira, M.T. et al., 1995. Control of pellet morphology of filamentous fungi in fluidized bed bioreactors by means of a pulsing flow. Application to Aspergillus niger and Phanerochaete chrysosporium. pp.1–6.

Mueller-Klieser, W., 1984. Method for the determination of oxygen consumption rates and diffusion coefficients in multicellular spheroids. *Biophysical Journal*, 46(3), pp.343–348.

Mueller-Klieser, W.F. & Sutherland, R.M., 1982. Oxygen tensions in multicell spheroids of two cell lines. pp.1–9.

Munir, R. et al., 2019. Lipid metabolism in cancer cells under metabolic stress. *British Journal of Cancer*, pp.1–9.

Murayama & Gotoh, 2019. Patient-Derived Xenograft Models of Breast Cancer and Their Application. *Cells*, 8(6), pp.621–17.

Mylonis, I., Simos, G. & Paraskeva, E., 2019. Hypoxia-Inducible Factors and the Regulation of Lipid Metabolism. *Cells*, 8(3), pp.214–16.

Naghib, S.D. et al., 2017. Expansion properties of alginate beads as cell carrier in the fluidized bed bioartificial liver. *Powder Technology*, 316(C), pp.711–717.

Narayan, S. & Roy, D., 2003. Role of APC and DNA mismatch repair genes in the development of colorectal cancers. *Molecular Cancer*, 2(1), pp.41–15.

Nazemi, M. & Rainero, E., 2020. Cross-Talk Between the Tumor Microenvironment, Extracellular Matrix, and Cell Metabolism in Cancer. *Frontiers in Oncology*, 10, pp.302–7.

Nelson, M.J., Nakhla, G. & Zhu, J., 2017. Fluidized-Bed Bioreactor Applications for Biological Wastewater Treatment: A Review of Research and Developments. *Engineering*, 3(3), pp.330–342.

Nelson, S.R. et al., 2020. Modelling of pancreatic cancer biology: transcriptomic signature for 3D PDX-derived organoids and primary cell line organoid development. *Scientific Reports*, pp.1–12.

Ng, W.K. & Tan, R.B.H., 2006. Investigation of Drying Geldart D and B Particles in Different Fluidization Regimes. pp.1–7.

Nguyen, H. & Duong, H.Q., 2018. The molecular characteristics of colorectal cancer: Implications for diagnosis and therapy (Review). *Oncology Letters*, pp.1–10.

Nguyentranlam, G. & Galvin, K.G., 2001. Particle classification in the reflux classifier. pp.1–11.

Nguyentranlam, G. & Galvin, K.P., 2004. Applications of the Reflux Classifier in solid–liquid operations. *International Journal of Mineral Processing*, 73(2-4), pp.83–89.

Ni, T. et al., 2017. Oroxylin A suppresses the development and growth of colorectal cancer through reprogram of HIF1α-modulated fatty acid metabolism. *Nature Publishing Group*, pp.1–12.

Nijhuis, A. et al., 2017. Remodelling of microRNAs in colorectal cancer by hypoxia alters metabolism profiles and 5-fluorouracil resistance. *Human Molecular Genetics*, 26(8), pp.1552–1564.

Nikravesh, N. et al., 2017. Encapsulation and Fluidization Maintains the Viability and Glucose Sensitivity of Beta-Cells. *ACS Biomaterials Science & Engineering*, 3(8), pp.1750–1757.

Nirmala, C. et al., 2001. Growth characteristics of glioblastoma spheroids. pp.1–7.

Nomura, D.K. et al., 2010. Monoacylglycerol Lipase Regulates a Fatty Acid Network that Promotes Cancer Pathogenesis. *Cell*, 140(1), pp.49–61.

Novellasdemunt, L., Antas, P. & Li, V.S.W., 2015. Targeting Wnt signaling in colorectal cancer. A Review in the Theme: Cell Signaling: Proteins, Pathways and Mechanisms. *American Journal of Physiology-Cell Physiology*, 309(8), pp.C511–C521.

Nunes, A.S. et al., 2018. 3D tumor spheroids as in vitro models to mimic in vivo human solid tumors resistance to therapeutic drugs. *Biotechnology and Bioengineering*, 116(1), pp.206–226.

Nusse, R., 2008. Wnt signaling and stem cell control. *Cell Research*, 18(5), pp.523–527.

Ohta, Y. & Sato, T., 2014. Intestinal tumor in a dish. pp.1–4.

Okkelman, I.A. et al., 2019. A deeper understanding of intestinal organoid metabolism revealed by combining fluorescence lifetime imaging microscopy (FLIM) and extracellular flux analyses. 15, pp.497–28.

Oliver, A.J. et al., 2018. Tissue-Dependent Tumor Microenvironments and Their Impact on Immunotherapy Responses. *Frontiers in Immunology*, 9, pp.309–8.

Özkaya, B. et al., 2019. Fluidized bed bioreactor for multiple environmental engineering solutions. *Water Research*, 150, pp.452–465.

Pallottini, V. et al., 2008. Regulation of HMG-CoA reductase expression by hypoxia. *Journal of Cellular Biochemistry*, 104(3), pp.701–709.

Pammolli, F., Magazzini, L. & Riccaboni, M., 2011. The productivity crisis in pharmaceutical R&D. *Nature Publishing Group*, pp.1–11.

Pan, X., 2018. *Scale-down of CHO Cell Fed-batch Cultures*.

Parathath, S. et al., 2011. Hypoxia Is Present in Murine Atherosclerotic Plaques and Has Multiple Adverse Effects on Macrophage Lipid Metabolism. *Circulation Research*, 109(10), pp.1141–1152.

Park, J.S. et al., 2018. VK-phantom male with 583 structures and female with 459 structures, based on the sectioned images of a male and a female, for computational dosimetry. *Journal of Radiation Research*, 59(3), pp.338–380.

Parks, S.K., Cormerais, Y. & Pouysségur, J., 2017. Hypoxia and cellular metabolism in tumour pathophysiology. *The Journal of Physiology*, 595(8), pp.2439–2450.

Parrales, A. & Iwakuma, T., 2016. p53 as a Regulator of Lipid Metabolism in Cancer. *International Journal of Molecular Sciences*, 17(12), pp.2074–11.

Pearce, S.C. et al., 2018. Marked differences in tight junction composition and macromolecular permeability among different intestinal cell types. pp.1–16.

Perry, R.H. & Green, D.W., 2008. *Perry"s Chemical Engineers" Handbook, 8th Edition*,

Pertoft, H. et al., 1978. Density gradients prepared from Colloidal silica particles coated by Polyvinylpyrrolidone (Percoll). pp.1–12.

Picco, G. et al., 2017. Loss of AXIN1 drives acquired resistance to WNTpathway blockade in colorectal cancer cells carrying RSPO3 fusions. *EMBO Molecular Medicine*, 9(3), pp.293–303.

Pisarsky, L. et al., 2016. Targeting Metabolic Symbiosis to Overcome Resistance to Anti-angiogenic Therapy. *CellReports*, 15(6), pp.1161–1174.

Ponder, E., 1925. On sedimentation and rouleaux formation. pp.1–18.

Powley, I.R. et al., 2020. Patient-derived explants (PDEs) as a powerful preclinical platform

for anti-cancer drug and biomarker discovery. *British Journal of Cancer*, pp.1–10.

Pradip Shahi Thakuri, S.L.H.G.D.L.A.H.T., 2016. Multiparametric Analysis of Oncology Drug Screening with Aqueous Two-Phase Tumor Spheroids. pp.1–12.

Prudent, M. et al., 2016. Small-Scale Perfusion Bioreactor of Red Blood Cells for Dynamic Studies of Cellular Pathways: Proof-of-Concept. *Frontiers in Molecular Biosciences*, 3(214), pp.S39–11.

Przepiorski, A. et al., 2018. A Simple Bioreactor-Based Method to Generate Kidney Organoids from Pluripotent Stem Cells. *Stem Cell Reports*, 11(2), pp.470–484.

Putnam, D.D., Namasivayam, V. & Burns, M.A., 2003. Cell affinity separations using magnetically stabilized fluidized beds: Erythrocyte subpopulation fractionation utilizing a lectin-magnetite support. *Biotechnology and Bioengineering*, 81(6), pp.650–665.

Qian, X. et al., 2018. Generation of human brain region–specific organoids using a miniaturized spinning bioreactor. *Nature Protocols*, 13(3), pp.565–580.

Qiu, G.-Z. et al., 2017. Reprogramming of the Tumor in the Hypoxic Niche: The Emerging Concept and Associated Therapeutic Strategies. *Trends in Pharmacological Sciences*, 38(8), pp.669–686.

Rademakers, T. et al., 2019. Oxygen and nutrient delivery in tissue engineering: Approaches to graft vascularization. *Journal of Tissue Engineering and Regenerative Medicine*, 13(10), pp.1815–1829.

Radisic, M., Iyer, R.K. & Murthy, S.K., 2006. Micro- and nanotechnology in cell separation. pp.1–12.

Ramakrishnan, S.K. et al., 2014. Loss of von Hippel-Lindau Protein (VHL) Increases Systemic Cholesterol Levels through Targeting Hypoxia-Inducible Factor 2 and Regulation of Bile Acid Homeostasis. *Molecular and Cellular Biology*, 34(7), pp.1208–1220.

Rasteh, M., Farhadi, F. & Ahmadi, G., 2018. Empirical models for minimum fluidization velocity of particles with different size distribution in tapered fluidized beds. *Powder Technology*, p.#startpage#.

Reddy, S.N. & Sai, P.S.T., 2018. Continuous segregation of binary mixture of solids in liquid fluidised beds: influence of feed entry location. *Indian Chemical Engineer*, 61(2), pp.153–166.

Reichard, A. & Asosingh, K., 2018. Best Practices for Preparing a Single Cell Suspension from Solid Tissues for Flow Cytometry. *Cytometry Part A*, 95(2), pp.219–226.

Richardson, J.F. & Zaki, W.N., 1997. Sedimentation and fluidisation: Part I. *Chemical Engineering Research and Design*, 75(Supplement), pp.S82–S100.

Rijal, G. & Li, W., 2018. Native-mimicking in vitro microenvironment: an elusive and seductive future for tumor modeling and tissue engineering. pp.1–22.

Rock, J.R. et al., 2009. Basal cells as stem cells of the mouse trachea and human airway

epithelium. pp.1–5.

Roelofs, B. et al., 2006. Acute activation of glucose uptake by glucose deprivation in L929 fibroblast cells. *Biochimie*, 88(12), pp.1941–1946.

Rofstad, E.K. et al., 1986. Growth Characteristics of Human Melanoma Multicellular Spheroids In Liquid-Overlay Culture: Comparisons With the Parent Tumour Xenografts. pp.1–12.

Roscigno, G. et al., 2019. Breast cancer organoids: a new model tool for the prediction of drug penetration and patient outcome. *Annals of Oncology*, 30(Supplement_5), pp.1–2.

Rowe, P.N. & Nienow, W., 1975. Minimum fluidisation velocity of multi-component particle mixtures. pp.1–5.

Saglam-Metiner, P., Gulce-Iz, S. & Biray-Avci, C., 2019. Bioengineering-inspired three-dimensional culture systems_ Organoids to create tumor microenvironment. *Gene*, 686, pp.203–212.

Salafi, T., Zhang, Y. & Zhang, Y., 2019. A Review on Deterministic Lateral Displacement for Particle Separation and Detection. *Nano-Micro Letters*, 11(1), pp.1–33.

Sandercock, A.M. et al., 2015. Identification of anti-tumour biologics using primary tumour models, 3-D phenotypic screening and image-based multi-parametric profiling. *Molecular Cancer*, pp.1–18.

Santarelli, R., Pierre, F. & Corpet, D., 2008. Processed Meat and Colorectal Cancer: A Review of Epidemiologic and Experimental Evidence. *Nutrition and Cancer*, 60(2), pp.131–144.

Sarrouh, B.F. & da Silva, S.S., 2008. Evaluation of the Performance of a Three-Phase Fluidized Bed Reactor with Immobilized Yeast Cells for the Biotechnological Production of Xylitol. pp.1–17.

Sato, T. & Clevers, H., 2013. Growing Self-Organizing Mini-Guts from a Single Intestinal Stem Cell: Mechanism and Applications. pp.1–6.

Sato, T. et al., 2011. Long-term Expansion of Epithelial Organoids From Human Colon, Adenoma, Adenocarcinoma, and Barrett's Epithelium. *Gastroenterology*, 141(5), pp.1762–1772.

Sato, T. et al., 2009. Single Lgr5 stem cells build crypt-villus structures in vitro without a mesenchymal niche. *Nature*, 459(7244), pp.262–265.

Satoh, A., Stein, L. & Imai, S., 2013. The Role of Mammalian Sirtuins in the Regulation of Metabolism, Aging, and Longevity. In *Histone Deacetylases: the Biology and Clinical Implication*. Handbook of Experimental Pharmacology. Berlin, Heidelberg: Springer Berlin Heidelberg, pp. 125–162.

Scannell, J.W. et al., 2012. Diagnosing the decline in pharmaceutical R&D efficiency. *Nature Publishing Group*, 11(3), pp.191–200.

Schatoff, E.M., Leach, B.I. & Dow, L.E., 2017. WNT Signaling and Colorectal Cancer.

Current Colorectal Cancer Reports, 13(2), pp.101–110.

Selden, C. et al., 2017. A clinical-scale BioArtificial Liver, developed for GMP, improved clinical parameters of liver function in porcine liver failure. *Scientific Reports*, pp.1–19.

Selden, C. et al., 2013. Evaluation of Encapsulated Liver Cell Spheroids in a Fluidised-Bed Bioartificial Liver for Treatment of Ischaemic Acute Liver Failure in Pigs in a Translational Setting M. Yamamoto, ed. *PLOS ONE*, 8(12), pp.e82312–12.

Semenza, G.L., 2008. Tumor metabolism: cancer cells give and take lactate. *Journal of Clinical Investigation*, 60, pp.7075–3.

Sha, J. et al., 2011. Hydrodynamics of Coarse Coal Slime and Quartz Particles in a Liquid-Solid Fluidized Bed Separator. *Advanced Materials Research*, 279, pp.350–355.

Shen, G. & Li, X., 2017a. The Multifaceted Role of Hypoxia-Inducible Factor 1 (HIF1) in Lipid Metabolism. In *Hypoxia and Human Diseases*. InTech, pp. 1–31.

Shen, G. & Li, X., 2017b. The Multifaceted Role of Hypoxia-Inducible Factor 1 (HIF1) in Lipid Metabolism. In *Hypoxia and Human Diseases*. InTech, pp. 1–31.

Shields, C.W., IV, Reyes, C.D. & López, G.P., 2015. Microfluidic cell sorting: a review of the advances in the separation of cells from debulking to rare cell isolation. *Lab on a Chip*, pp.1–20.

Shimazu, T. et al., 2010. SIRT3 Deacetylates Mitochondrial 3-Hydroxy-3-Methylglutaryl CoA Synthase 2 and Regulates Ketone Body Production. *Cell Metabolism*, 12(6), pp.654–661.

Silva, T.P. et al., 2019. Review Article Design Principles for Pluripotent Stem Cell-Derived Organoid Engineering. *Stem Cells International*, pp.1–17.

Sonveaux, P. et al., 2008. Targeting lactate-fueled respiration selectively kills hypoxic tumor cells in mice. *Journal of Clinical Investigation*, 234, pp.1036–14.

Span, P.N. et al., 2002. Expression of the transcription factor Ets-1 is an independent prognostic marker for relapse-free survival in breast cancer. pp.1–4.

Spit, M., Koo, B.-K. & Maurice, M.M., 2018. Tales from the crypt: intestinal niche signals in tissue renewal, plasticity and cancer. *Open Biology*, 8(9), pp.180120–14.

Stadler, M. et al., 2015. Increased complexity in carcinomas: Analyzing and modeling the interaction of human cancer cells with their microenvironment. *Seminars in Cancer Biology*, 35(C), pp.107–124.

Sullivan, M.R. & Vander Heiden Matthew G, 2019. Determinants of nutrient limitation in cancer. *Critical Reviews in Biochemistry and Molecular Biology*, 0(0), pp.1–15.

Swierczynski, J., 2014. Role of abnormal lipid metabolism in development, progression, diagnosis and therapy of pancreatic cancer. *World Journal of Gastroenterology*, 20(9), pp.2279–26.

Swietach, P. et al., 2012. Importance of Intracellular pH in Determining the Uptake and

Efficacy of the Weakly Basic Chemotherapeutic Drug, Doxorubicin V. Saks, ed. *PLOS ONE*, 7(4), pp.e35949–9.

Tan, S. & Barker, N., 2014. Epithelial stem cells and intestinal cancer. *Seminars in Cancer Biology*, pp.1–14.

Tatemoto, Y. et al., 2005. Separation of Solid Particles by Density Difference in a Liquid–Solid Fluidized Bed. pp.1–7.

Tentler, J.J. et al., 2012. Patient-derived tumour xenografts as models for oncology drug development. *Nature Reviews Clinical Oncology*, 9(6), pp.338–350.

Testa, U., Pelosi, E. & Castelli, G., 2018. Colorectal Cancer: Genetic Abnormalities, Tumor Progression, Tumor Heterogeneity, Clonal Evolution and Tumor-Initiating Cells. *Medical Sciences*, 6(2), pp.31–113.

Tharmalingam, T. et al., 2008. Pluronic Enhances the Robustness and Reduces the Cell Attachment of Mammalian Cells. *Molecular Biotechnology*, 39(2), pp.167–177.

The Cancer Genome Atlas Network, 2012. Comprehensive molecular characterization of human colon and rectal cancer. *Nature*, 487(7407), pp.330–337.

Thielicke, W. & Stamhuis, E.J., 2014. PIVlab – Towards User-friendly, Affordable and Accurate Digital Particle Image Velocimetry in MATLAB. *Journal of Open Research Software*, 2, pp.1202–10.

Tikunov, A.P. et al., 2017. Dose-response in a high density three-dimensional liver device with real-time bioenergetic and metabolic flux quantification. *Toxicology in Vitro*, 45(Part 1), pp.119–127.

Tirier, S.M. et al., 2019. Pheno-seq – linking visual features and gene expression in 3D cell culture systems. *Scientific Reports*, pp.1–15.

Tottori, N. & Nisisako, T., 2020. Particle/cell separation using sheath-free deterministic lateral displacement arrays with inertially focused single straight input. *Lab on a Chip*, 17, pp.1–38.

Tredan, O. et al., 2007. Drug Resistance and the Solid Tumor Microenvironment. *JNCI Journal of the National Cancer Institute*, 99(19), pp.1441–1454.

Tripathy, A. et al., 2017. Study of particle hydrodynamics and misplacement in liquid–solid fluidized bed separator. *Chemical Engineering Research and Design*, 117, pp.520–532.

Tripathy, S.K. et al., 2015. A short review on hydraulic classification and its development in mineral industry. *Powder Technology*, 270(PA), pp.205–220.

Tsuyoshi Takagi, 2005. Dextran Sulfate Suppresses Cell Adhesion and Cell Cycle Progression of Melanoma Cells. pp.1–8.

Turton, R. & Clark, N.N., 1987. An explicit relationship to predict spherical particle terminal velocity. *Powder Technology*, pp.1–3.

Ugocsai, P. et al., 2010. HIF-1beta determines ABCA1 expression under hypoxia in human macrophages. *International Journal of Biochemistry and Cell Biology*, 42(2), pp.241–252.

Vadivelu, R. et al., 2017. Microfluidic Technology for the Generation of Cell Spheroids and Their Applications. *Micromachines*, 8(4), pp.94–23.

Van Liedekerke, P. et al., 2019. Quantitative cell-based model predicts mechanical stress response of growing tumor spheroids over various growth conditions and cell lines N. L. Komarova, ed. *PLoS computational biology*, 15(3), pp.e1006273–40.

Van Norman, G.A., 2016. Drugs, Devices, and the FDA: Part 1. *JACC: Basic to Translational Science*, 1(3), pp.170–179.

van Tienderen et al., 2019. Recreating Tumour Complexity in a Dish: Organoid Models to Study Liver Cancer Cells and their Extracellular Environment. *Cancers*, 11(11), pp.1706–18.

van Zessen, E. et al., 2005. Fluidized-bed and packed-bed characteristics of gel beads. *Chemical Engineering Journal*, 115(1-2), pp.103–111.

Vito, A., El-Sayes, N. & Mossman, K., 2020. Hypoxia-Driven Immune Escape in the Tumor Microenvironment. *Cells*, 9(4), pp.992–20.

Wallace, D.I., 2013. Properties of tumor spheroid growth exhibited by simple mathematical models. pp.1–9.

Walsh, N.C. et al., 2017. Humanized Mouse Models of Clinical Disease. *Annual Review of Pathology: Mechanisms of Disease*, 12(1), pp.187–215.

Walton, K., Zhou, J. & Galvin, K.P., 2010. Processing of fine particles using closely spaced inclined channels. *Advanced Powder Technology*, 21(4), pp.386–391.

Wang, G. et al., 2018. New strategies for targeting glucose metabolism-mediated acidosis for colorectal cancer therapy. *Journal of Cellular Physiology*, 234(1), pp.348–368.

Wang, H., Li, Z., et al., 2011. Multimerization of Adenovirus Serotype 3 Fiber Knob Domains Is Required for Efficient Binding of Virus to Desmoglein 2 and Subsequent Opening of Epithelial Junctions. *Journal of Virology*, 85(13), pp.6390–6402.

Wang, H., Li, Z.-Y., et al., 2011. Desmoglein 2 is a receptor for adenovirus serotypes 3, 7, 11 and 14. *Nature Medicine*, 17(1), pp.96–104.

Wang, P. et al., 2013. Overexpression of Hypoxia-Inducible Factor-1a Exacerbates Endothelial Barrier Dysfunction Induced by Hypoxia. *Cellular Physiology and Biochemistry*, 32(4), pp.859–870.

Wei, L. & Sun, M., 2016. Numerical studies of the influence of particles' size distribution characteristics on the gravity separation performance of Liquid-solid Fluidized Bed Separator. *International Journal of Mineral Processing*, 157(C), pp.111–119.

Weigmann, B. et al., 2007. Isolation and subsequent analysis of murine lamina propria mononuclear cells from colonic tissue. *Nature Protocols*, 2(10), pp.2307–2311.

Weinhouse, S., 1956. On Respiratory Impairment in Cancer Cells. *Science*, 124, pp.1–6.

Wek, R.C. & Staschke, K.A., 2010. How do tumours adapt to nutrient stress&quest. *The EMBO Journal*, 29(12), pp.1946–1947.

Wenger, R.H. et al., 1997. Hypoxia-inducible factor-1α is regulated at the post-mRNA level. *Kidney international*, 51(2), pp.560–563.

West, C.M.L., 1989. Size-dependent resistance of human tumour spheroids to photodynamic treatment. pp.1–5.

Wierenga, A.T.J. et al., 2019. HIF1/2-exerted control over glycolytic gene expression is not functionally relevant for glycolysis in human leukemic stem/ progenitor cells. pp.1–17.

Wilding, J.L. & Bodmer, W.F., 2014. Cancer Cell Lines for Drug Discovery and Development. *Cancer Research*, 74(9), pp.2377–2384.

Williamson, I.A. et al., 2018. A High-Throughput Organoid Microinjection Platform to Study Gastrointestinal Microbiota and Luminal Physiology. *Cellular and Molecular Gastroenterology and Hepatology*, 6(3), pp.301–319.

Wojtkowiak, J.W. et al., 2011. Drug Resistance and Cellular Adaptation to Tumor Acidic pH Microenvironment. *Molecular Pharmaceutics*, 8(6), pp.2032–2038.

Wolfe, J. & Bryant, G., 1999. Freezing, drying and/orvitrification of membrane-solute-water systems. pp.1–25.

Wu, J. et al., 2014. Oxygen Transport and Stem Cell Aggregation in Stirred-Suspension Bioreactor Cultures F. Pappalardo, ed. *PLOS ONE*, 9(7), pp.e102486–12.

Xiong, G.-F. & Xu, R., 2016. Function of cancer cell-derived extracellular matrix in tumor progression. *Journal of Cancer Metastasis and Treatment*, 2(9), pp.357–8.

Xu, C. et al., 2018. Patient-derived xenograft mouse models: A high fidelity tool for individualized medicine (Review). *Oncology Letters*, pp.1–8.

Xu, M. et al., 2014. An acetate switch regulates stress erythropoiesis. *Nature Medicine*, 20(9), pp.1018–1026.

Yan, K.S. et al., 2017. Non-equivalence of Wnt and R-spondin ligands during Lgr5+ intestinal stem-cell self-renewal. *Nature*, 545(7653), pp.238–242.

Yang, Qian et al., 2010. Fluidized-bed bioartificial liver assist devices (BLADs) based on microencapsulated primary porcine hepatocytes have risk of porcine endogenous retroviruses transmission. *Hepatology International*, 4(4), pp.757–761.

Yang, Qingqiang et al., 2017. H19 promotes the migration and invasion of colon cancer by sponging miR-138 to upregulate the expression of HMGA1. *International Journal of Oncology*, 50(5), pp.1801–1809.

Yang, W.-C., 2003. Handbook of Fluidization and Fluid-Particle Systems. pp.1–851.

Yang, Y. et al., 2013. Co-Culture With Mesenchymal Stem Cells Enhances Metabolic Functions of Liver Cells in Bioartificial Liver System. pp.1–11.

Yao, K.-S. et al., 1994. Activation of AP-1 and of a Nuclear Redox Factor, Ref-1, in the response of HT29 Colon Cancer Cells to Hypoxia. pp.1–7.

Yin, X. et al., 2016. Engineering Stem Cell Organoids. *Stem Cell*, 18(1), pp.25–38.

Young, M. & Reed, K.R., 2016. Organoids as a Model for Colorectal Cancer. *Current Colorectal Cancer Reports*, pp.1–7.

Yu, C.-B., 2014. Evaluation of a novel choanoid fluidized bed bioreactor for future bioartificial livers. *World Journal of Gastroenterology*, 20(22), pp.6869–10.

Yu, F., Hunziker, W. & Choudhury, D., 2019. Engineering Microfluidic Organoid-on-a-Chip Platforms. *Micromachines*, 10(3), pp.165–12.

Zang, R. et al., 2012. Cell-Based Assays in High-Throughput Screening for Drug Discovery. *International Journal of Biotechnology for Wellness Industries*, pp.1–22.

Zhan, T. et al., 2019. MEK inhibitors activate Wnt signalling and induce stem cell plasticity in colorectal cancer. *Nature Communications*, pp.1–17.

Zhang, J, 2005. Actin at cell-cell junctions is composed of two dynamic and functional populations. *Journal of Cell Science*, 118(23), pp.5549–5562.

Zhang, Yuanqing et al., 2015. Utilizing a high-throughput microfluidic platform to study hypoxia-driven mesenchymal-mode cell migration. *Integrative Biology*, 7, pp.672–680.

Zhang, Zhe et al., 2019. A new drug carrier with oxygen generation function for modulating tumor hypoxia microenvironment in cancer chemotherapy. *Colloids and Surfaces B: Biointerfaces*, 173, pp.335–345.

Zhang, Zhiyun et al., 2012. Quality control of cell-based high-throughput drug screening. *Acta Pharmaceutica Sinica B*, 2(5), pp.429–438.

Zhao, H. et al., 2019. Sphere-forming assay vs. organoid culture: Determining long-term stemness and the chemoresistant capacity of primary colorectal cancer cells. *International Journal of Oncology*, pp.1–12.

Zhao, P. et al., 2015. Dry cleaning of fine lignite in a vibrated gas-fluidized bed: Segregation characteristics. *FUEL*, 142(C), pp.274–282.

Zhou, E. et al., 2018. Effect of vibration energy on fluidization and 1–6 mm coal separation in a vibrated dense medium fluidized bed. *Separation Science and Technology*, 53(14), pp.2297–2313.

Zhou, J. et al., 2006. Enhanced separation of mineral sands using the Reflux Classifier. *Minerals Engineering*, 19(15), pp.1573–1579.

Zhou, P. et al., 2016. Efficacy of Fluidized Bed Bioartificial Liver in Treating Fulminant Hepatic Failure in Pigs: A Metabolomics Study. *Scientific Reports*, pp.1–9.

Zhu, A., Ibrahim, J.G. & Love, M.I., 2019. Heavy-tailed prior distributions for sequence count data: removing the noise and preserving large differences. pp.1–9.

Zhu, Y. et al., 2017. Metabolic regulation of Sirtuins upon fasting and the implication for cancer. *Current Opinion in Oncology*, 25(6), pp.630–636.

Zigrang, D.J. & Sylvester, N.D., 1981. An Explicit Equation for particles settling velocities in solid-liquid systems. *AIChE Journal*, pp.1–2.

Zimmerman, J.J., Saint André-von Arnim, von, A. & McLaughlin, J., 2011. *Chapter 74 – Cellular Respiration* Fourth Edition, Elsevier.

8. Appendices

8.1 Appendix A

Development of Carman-Kozeny equation

Many attempts have been made to obtain general expression to calculate the pressure drop and mean velocity for flow through the bed of particles. Coulson Richardson suggested an analogy between streamline flow through a tube and streamline flow through the pores in a bed of particles as a starting point for deriving a general expression (Coulson & Richardson 1999). This analogy is presented below.

A horizontal pipe with a concentric element ABCD is shown in Figure 8.1. The forces acting are the normal pressures over the ends and shear forces over the curved sides.

The force over AB = $P\pi s^2$ Equation A.1

The force over CD = $-(\mathrm{P} + \Delta\mathrm{P})\pi s^2$ Equation A.2

And the force over curved surface = $2\pi s l R_y$ Equation A.3

Where the shear stress $R_y = \mu \frac{du_x}{ds}$ Equation A.4

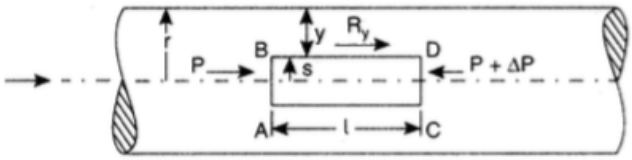

Figure 8.1 Flow through pipe

Taking a force balance:

$$P\pi s^2 - (P + \Delta\mathrm{P})\pi s^2 + 2\pi s l \mu \frac{du_x}{ds} = 0 \quad \text{Equation A.5}$$

$$\left(-\frac{\Delta P}{l}\right) s + 2\mu \frac{du_x}{ds} = 0 \quad \text{Equation A.6}$$

the velocity at any distance s from the axis of the pipe may be found by integrating Equation A.6:

$$u_x = \frac{1}{2\mu}\left(\frac{\Delta P}{l}\right)\frac{s^2}{2} + constant \qquad \text{Equation A.7}$$

At the walls of the pipe, where s = r, the velocity u_x must be zero in order to satisfy the condition of zero wall slip, then:

$$constant = \frac{1}{2\mu}\left(\frac{-\Delta P}{l}\right)\frac{r^2}{2} \qquad \text{Equation A.8}$$

and,

$$u_x = \frac{1}{4\mu}\left(\frac{-\Delta P}{l}\right)(r^2 - s^2) \qquad \text{Equation A.9}$$

thus the velocity over the cross-section varies in a parabolic manner with the distance from the axis of the pipe.
The velocity of flow is seen to be a maximum when s = 0, that is at the pipe axis.

$$u_{max} = u_{CL} = \frac{1}{4\mu}\left(\frac{-\Delta P}{l}\right)r^2 \qquad \text{Equation A.10}$$

Hence:

$$\frac{u_x}{u_{CL}} = 1 - \frac{s^2}{r^2} \qquad \text{Equation A.11}$$

If the velocity is taken as constant over an annulus of radii s and (s + ds), the volumetric rate of flow dQ through the annulus is given by:

$$dQ = 2\pi s\, ds\, u_x = 2\pi\, u_{CL}\, s\left(1 - \frac{s^2}{r^2}\right)ds \qquad \text{Equation A.12}$$

The total flow over the cross-section is then given by integrating Equation A.12:

$$Q = 2\pi\, u_{CL} \int_0^r s\left(1 - \frac{s^2}{r^2}\right) ds = \frac{\pi}{2} r^2 u_{CL} \qquad \text{Equation A.13}$$

Thus the average velocity (u) is given by:

$$u = \frac{Q}{(\pi d^2/4)} \qquad \text{Equation A.14}$$

Combining Equation A.10, Equation A.13 and Equation A.14, the flow through a circular tube is obtained:

$$u = \left(\frac{-\Delta P}{l}\right)\frac{r^2}{8\mu} = \left(\frac{-\Delta P}{l}\right)\frac{d^2}{32\mu} \qquad \text{Equation A.15}$$

Now, the flow through the pores in a bed is considered analogous to Equation A.15 and it can be rewritten for flow through a bed as:

$$u_1 = \left(\frac{-\Delta P}{l'}\right)\frac{{d'_m}^2}{K'\mu} \qquad \text{Equation A.16}$$

where: d'_m is some equivalent diameter of the pore channels, K' is a dimensionless constant whose value depends on the structure of the bed, l' is the length of channel, and u_1 is the average velocity through the pore channels.

Dupuit related the average velocity of the flow of the fluid (u_c) and u_1 by the following argument. In a cube of side X, the volume of free space is εX^3 so that the mean cross-sectional area for flow is the free volume divided by the height, or εX^2 (Coulson & Richardson 2002). The volume flowrate through this cube is $u_c X^2$, so that the average linear velocity through the pores, u_1, is given by:

$$u_1 = \frac{u_c X^2}{\varepsilon X^2} = \frac{u_c}{\varepsilon} \qquad \text{Equation A.17}$$

Kozeny proposed that d'_m from Equation A.16 may be taken as (Coulson & Richardson 2002):

$$d'_m = \frac{\varepsilon}{S_B} = \frac{\varepsilon}{S(1-\varepsilon)} \qquad \text{Equation A.18}$$

where:

$$\frac{\varepsilon}{S_B} = \frac{volume\ of\ voids\ filled\ with\ fluid}{specific\ surface\ area\ of\ the\ bed} \qquad \text{Equation A.19}$$

Combining Equation A.17 and Equation A.18, Equation A.16 becomes:

$$u_c = \frac{\varepsilon {d'_m}^2}{K'\mu}\left(\frac{-\Delta P}{l}\right) = \frac{1}{K''}\frac{\varepsilon^3}{S_B^2\mu}\left(\frac{-\Delta P}{l}\right) = \frac{1}{K''}\frac{\varepsilon^3}{S^2(1-\varepsilon)^2}\frac{1}{\mu}\left(\frac{-\Delta P}{l}\right) \qquad \text{Equation A.20}$$

where: S is the specific surface area of the particles and $K''$is generally known as Kozeny's constant and a commonly accepted value for K'' is 5:

$$u_c = \frac{1}{5}\frac{\varepsilon^3}{(1-\varepsilon)^2}\frac{-\Delta P}{S^2\mu l} \qquad \text{Equation A.21}$$

Considering particles as spheres, S is calculated as:

$$S = \frac{Surface\ area\ of\ a\ particle}{Particle\ volume} = \frac{4\pi\left(\frac{d}{2}\right)^2}{\frac{4}{3}\pi\left(\frac{d}{2}\right)^3} = \frac{6}{d} \qquad \text{Equation A.22}$$

and Carman-Kozeny equation is obtained:

$$u_c = \frac{1}{180}\frac{\varepsilon^3}{(1-\varepsilon)^2}\frac{-\Delta P\ d^2}{\mu l} \qquad \text{Equation A.23}$$

8.2 Appendix B

Primer test results

A)

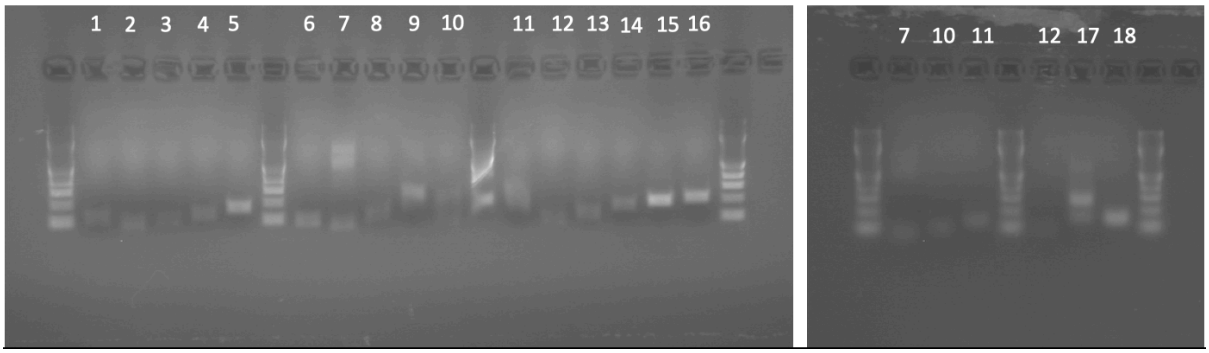

B)

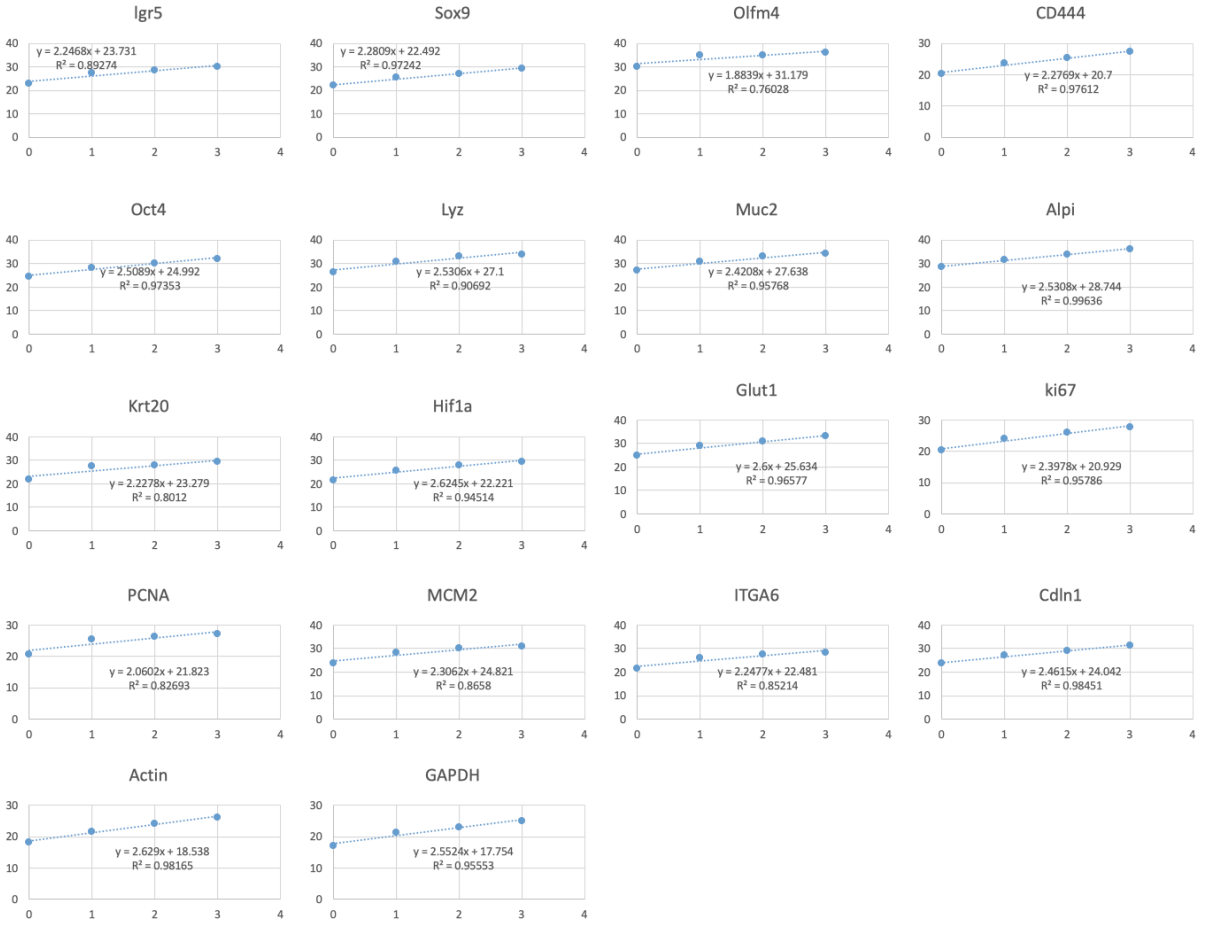

C)

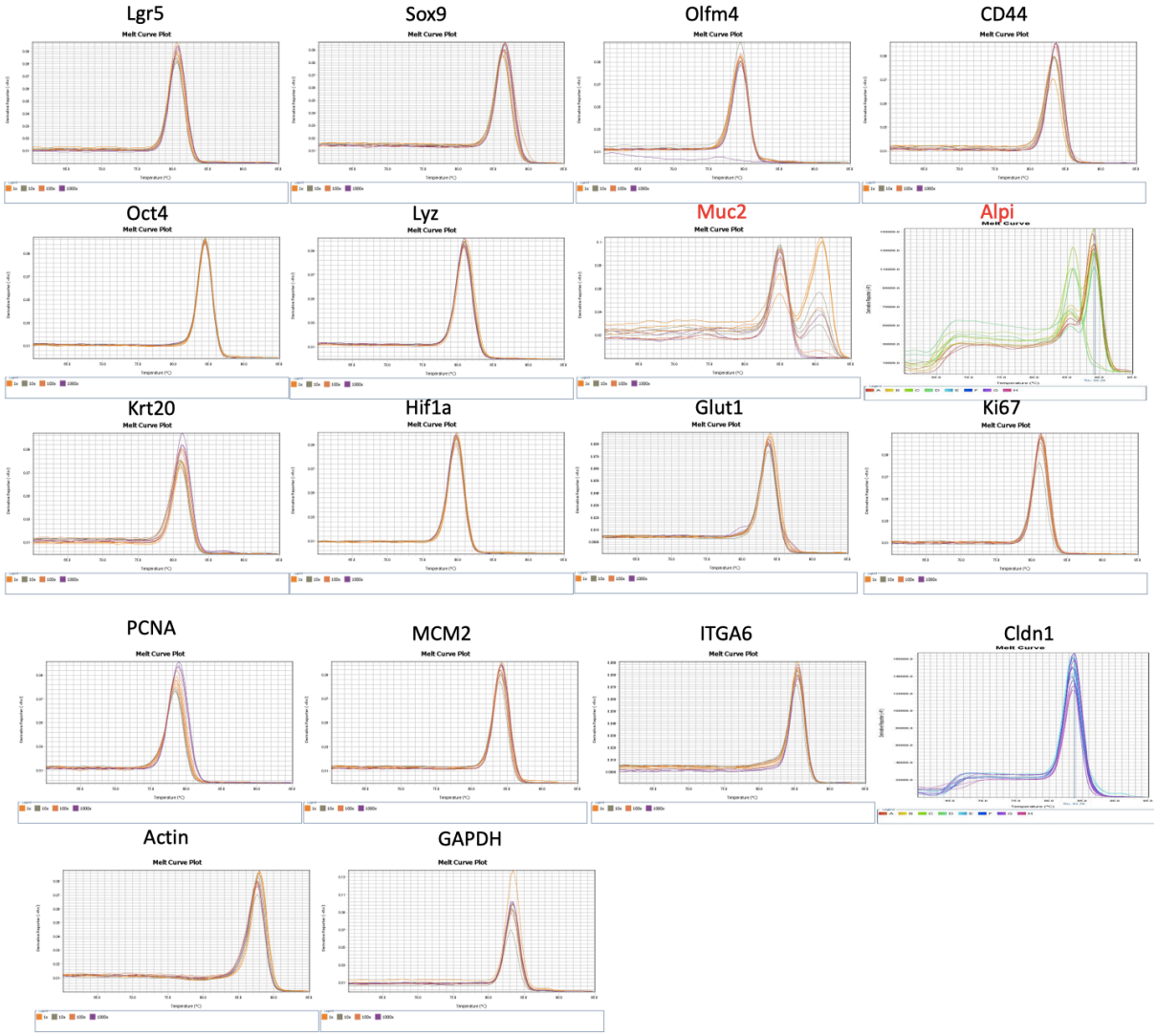

Figure 8.2 Primer test results

LGR5 (1), *SOX9* (2), *OLFM4* (3), *CD44* (4), *OCT4* (5), *LYZ* (6), *MUC2* (7), *KRT20* (8), *HIF1a* (9), *GLUT1* (10), *KI67* (11), *PCNA* (12), *MCM2* (13), *ITGA6* (14), *ACTIN* (15), *GAPDH* (16), *ALPI* (17), *CLDN1* (18).

A. RT-qPCR amplicon bands in agarose gel. **B.** Linear relationship between Ct value and the cDNA dilution number. **C.** qRT-PCR melt curve.

MUC2 and *ALPI* were discarded because a single peak in the qRT-PCR melt curve was not obtained.

8.3 Appendix C

Ratio of absorbance at 260 nm and 280 nm to assess the quality of RNA samples included in the qRT-PCR.

Table 8.1 Ratio of absorbance at 260 nm and 280 nm and concentration of RNA samples included in the qRT-PCR

Sample description	260/280	Conc. (ng/µL)
D3 Biological replicate 1	2.00	102.9
D3 Biological replicate 2	1.95	58.9
D3 Biological replicate 3	1.83	30.1
D5 Biological replicate 1	2.06	262.2
D5 Biological replicate 2	2.03	319.3
D5 Biological replicate 3	2.07	362.2
D8 Biological replicate 1	2.04	252.4
D8 Biological replicate 2	2.04	443.9
D8 Biological replicate 3	1.99	181.4

RNA Screen Tape RNI[e] results to assess the quality of RNA samples included in the RNA-seq experiment.

Table 8.2 RNA Screen Tape RNI[e] results of RNA samples included in the RNA-seq experiment

Sample description	RIN[e]	28s/18s (Area)	Conc. (ng/µL)
Ladder	-	-	135
1- (NF-D3)	10.0	2.4	62.5
2- (NF-D3)	10.0	2.5	46.3
3- (NF-D3)	10.0	2.4	12.1
4- (NF-D5)	10.0	2.8	156
5- (NF-D5)	10.0	2.8	206
6- (NF-D5)	10.0	1.9	374
7- (NF-D8)	10.0	3.0	267
8- (NF-D8)	9.9	3.0	329
9- (NF-D8)	9.6	2.5	264
10-(F-D5-<40)	9.8	2.6	271
11-(F-D5-4085)	9.8	2.7	626
12-(F-D5->85)	10.0	1.9	25.8
13-(F-D5-<40)	9.4	2.5	165
14-(F-D5-4085)	10.0	2.0	323
15-(F-D5->85)	10.0	2.0	5.26
16-(F-D5-<40)	9.9	2.4	108
17-(F-D5-4085)	9.8	3.0	455
18-(F-D5->85)	10.0	2.4	16.9
19-(F-D5-<40)	9.8	2.6	144
20-(F-D5-4085)	9.9	2.8	396

21-(F-D5->85)	10.0	2.2	29.3
22-(F-D8-<40)	9.1	2.3	224
23-(F-D8-4085)	8.2	2.0	2330
24-(F-D8->85)	8.9	1.4	927
25-(F-D8-<40)	9.0	2.4	286
26-(F-D8-4085)	9.4	1.5	462
27-(F-D8->85)	9.5	2.8	1180
28-(F-D8-<40)	8.6	3.1	892
29-(F-D8-4085)	9.3	3.3	776
30-(F-D8->85)	8.9	1.7	988
31-(F-D5T->200)	9.9	2.8	254
32-(F-D5T->200)	9.3	1.7	463
33-(F-D5T->200)	9.6	2.7	311

The group of samples 13, 14 and 15 were discarded from the RNA-seq experiment due to the low RNA concentration in sample 15-(F-D5-<40).

8.4 Appendix D

Relationship between Iso50 CRC organoid area and number of cells per organoid

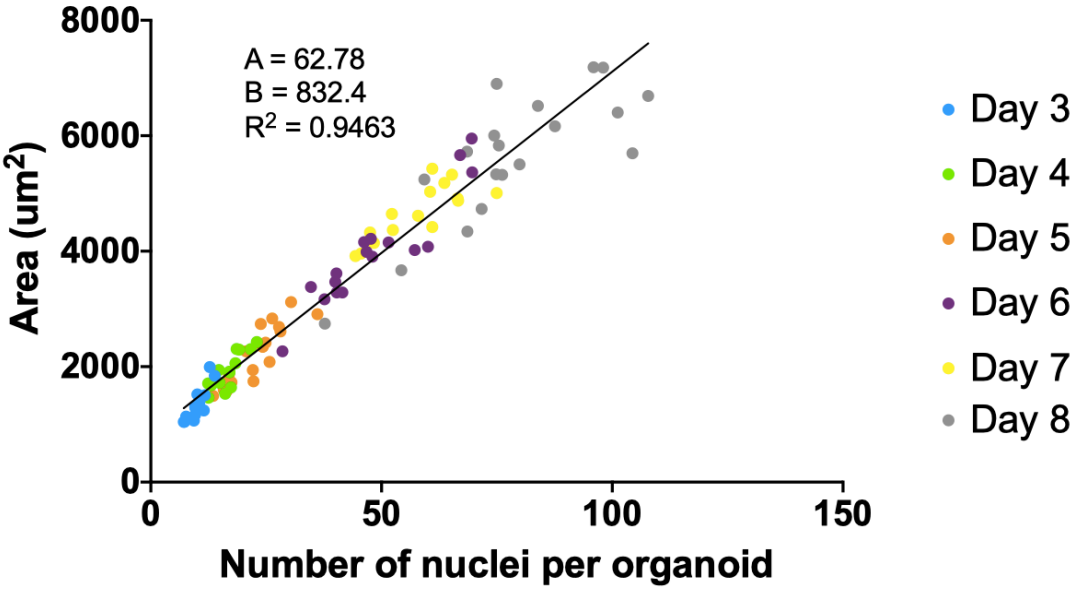

Figure 8.3 Relationship between Area of Iso50 CRC organoid and number of cells per organoid

Iso50 CRC organoids cultured during 3, 4, 5, 6, 7, and 8 days of culture were fixed and stained with Hoechst (nuclei stain) at the end of each culture time span. Then, organoids were imaged with Opera Phenix High Content Screening microscope and images were analysed with Harmony software to calculate the average number of cells per organoids and the average ellipsoid medium axis length per well, which was used to calculate the area of the 2D maximum projection. A linear regression was applied to the data and the fitted equation was the expression Y= AX+B, where Y is the area of the organoid 2D maximum projection and X is the number of nuclei per organoid.